Matti Liukkonen

Adopting a Multi-stage Modeling Approach to Series-Hybrid Powertrain Design

School of Electrical Engineering

Thesis submitted for examination for the degree of Licentiate of Science in Technology.

Espoo 15.11.2012

Thesis supervisor:

Prof. Seppo J. Ovaska

Thesis instructor:

Prof. Jussi Suomela

Aalto University
School of Electrical
Engineering

AALTO UNIVERSITY
SCHOOL OF ELECTRICAL ENGINEERING

ABSTRACT OF THE
LICENTIATE'S THESIS

Author: Matti Liukkonen

Title: Adopting a Multi-stage Modeling Approach to Series-Hybrid Powertrain Design

Date: 15.11.2012 Language: English Number of pages:10+123

Department of Electrical Engineering

Professorship: Industrial Electronics Code: S-81

Supervisor: Prof. Seppo J. Ovaska

Instructor: Prof. Jussi Suomela

This research concentrates on the modeling, design, and control of series-hybrid powertrains in Non-Road Mobile Machineries (NRMMs). Hybridization of mobile machinery powertrains is a topical subject due to needs to decrease CO_2 emissions and energy consumption, and the possibility of using alternative power sources. This research proposes a combination of backward, functional, static, quasi-static, and dynamic modeling methods as an approach for the systematic series-hybrid powertrain design. As a result, this research introduces an efficient and systematic modeling approach for the design of series-hybrid powertrains in NRMMs, and investigates the accuracies of the approach. In addition, the research proposes an energy management algorithm for an ultracapacitor buffered diesel series-hybrid powertrain. The results significantly benefit NRMM powertrain designers and scholars by providing an efficient approach with computationally light and easy to adapt modeling tools for similar studies. The study was conducted due to a need for system-design guidelines for different powertrain options, which are somewhat lacking in the literature. Thus, research into hybridizing or introducing fuel cell powertrain to NRMMs still needs persistent attention by many researchers and engineers for several years until the feasibilities and design principles of different powertrain options will be thoroughly explored and concluded.

Keywords: Diesel-electric, Energy buffering, Fuel cell,
Powertrain design, Series-hybrid, Mobile work machine, Modeling

AALTO-YLIOPISTO
SÄHKÖTEKNIIKAN KORKEAKOULU

LISENSIAATINTUTKIMUKSEN
TIIVISTELMÄ

Tekijä: Matti Liukkonen

Työn nimi: Monivaiheisen mallinnustavan hyödyntäminen sähköisen sarjahybridivoimansiirron suunnittelussa

Päivämäärä: 15.11.2012 Kieli: Englanti Sivumäärä:10+123

Sähkötekniikan laitos

Professuuri: Teollisuuselektroniikka Koodi: S-81

Valvoja: Prof. Seppo J. Ovaska

Ohjaaja: Prof. Jussi Suomela

Tutkimus keskittyy liikkuvien työkoneiden sarjahybridivoimansiirron mallintamiseen, suunnitteluun ja ohjaukseen. Liikkuvien työkoneiden hybridisointi on ajankohtaista, koska se mahdollistaa CO_2-päästöjen ja energiankulutuksen pienentämisen sekä erilaiset tehontuottomuodot. Tutkimus esittää sarjahybridivoimansiirron systemaattiseen mallintamiseen lähestymistapaa, jonka laskentasuunta on kuormasta takaperin lähteisiin. Lisäksi mallinnustapaa voidaan kuvata toiminnallisen, staattisen, näennäisstaattisen, ja dynaamisen mallinnustavan yhdistelmäksi. Lopputulemana työ esittelee tehokkaan ja systemaattisen mallinnuslähestymistavan liikkuvien työkoneiden voimansiirrolle, sekä tarkastelee menetelmän mallinnustarkkuutta. Lisäksi tutkimus käsittelee aktiivisella superkondensaattorilla puskuroidun diesel-sähköisen voimansiirron tehonohjausalgoritmeja. Tutkimus hyödyttää liikkuvien työkoneiden voimansiirron suunnittelijoita sekä tutkijoita ja opiskelijoita vastaavan aiheen parissa. Työ lisää sovellusalueeseensa järjestelmätason suunnittelumenetelmiä, jotka ovat tähän saakka puuttuneet tai olleet vaillinaisia. Liikkuvien työkoneiden hybridisointi tai polttokennotehontuoton hyödyntäminen vaatii vielä monien tutkijoiden sekä insinöörien pitkäjänteistä työtä useiden vuosien ajan, kunnes eri voimansiirtotopologioiden hyödyllisyys ja suunnitteluperiaatteet on selvitetty.

Avainsanat: Diesel-sähköinen, Energian puskurointi, Liikkuva työkone, Mallintaminen, Polttokenno, Sarjahybridi, Voimansiirron suunnittelu

Preface

The series-hybrid electric vehicle powertrain study at Aalto University facilities started in the year 2002, with the demonstrator for the interest of industrial partners. My contribution to the topic started in the mid-2007, when the work continued with the development of the series-hybrid Hardware-in-the-Loop test environment. My work with powertrain components efficiency measurements, power control experiments, and modeling of the system components, progressed in 2008 and 2009. Analysis of the results lasted until 2010 and writing of the thesis until the mid-2012. The created modeling platform has been in my own and colleagues' design use since 2009, and adopted for teaching purposes in 2012.

I would like to thank all my colleagues for their support, and the good working atmosphere.

This study has been carried out in the HybDrive, TopDrive and ECV/Tubridi projects, financed by the Doctoral Program of Electrical Energy Engineering (DPEEE), the Finnish Funding Agency for Technology and Innovations (Tekes), and the Multidisciplinary Institute of Digitalization and Energy (MIDE) of Aalto University, respectively. Furthermore, grants given by the Henry Ford and Fortum foundations have supported progression of this thesis.

Otaniemi, 15.11.2012

Matti Liukkonen

Contents

List of Publications

This thesis consists of an overview and the following publications which are referred to in the text by their Roman numerals:

I M. Liukkonen, A. Hentunen, J. Suomela, and J. Kyyrä, "Functional Simulations of Power Electronics Components in Series-Hybrid Machinery for the needs of OEM," in *Proc. Nordic Workshop on Power and Industrial Electronics* (Norpie 2008), Espoo, Finland, June 9-11, 2008.

II M. Liukkonen, A. Hentunen, J. Suomela, and J. Kyyrä, "Low-pass Filtered Power-flow Control in Series Hybrid Electric Vehicle," in *Proc. 24th Electric Vehicle Symposium* (EVS24), Stavanger, Norway, May 13-16, 2009.

III M. Liukkonen, A. Hentunen, and J. Suomela, "Validation of quasi-static Series Hybrid Electric Vehicle Simulation model," in *Proc. IEEE Vehicle Power and Propulsion Conference* (VPPC 2010), Lille, France, Sept. 1-3, 2010.

IV M. Liukkonen, A. Hentunen, and J. Suomela, "Analysis of the Ultracapacitor Module in Power Buffering," in *Proc. 4th European Symposium on Super Capacitors and Applications* (ESSCAP 2010), Bordeaux, France, Oct. 21-22, 2010.

V M. Liukkonen, A. Lajunen, and J. Suomela, "Comparison of Different Buffering Topologies in FC-hybrid Non-Road Mobile Machineries," in *Proc. IEEE Vehicle Power and Propulsion Conference* (VPPC 2011), Chicago, IL, Sept. 6-9, 2011.

The author has written Publications I and II under the supervision of Prof. Jorma Kyyrä, and all publications under the instruction of Prof. Jussi Suomela, respectively. Second authors Lic.Sc. Ari Hentunen and M.Sc. Antti Lajunen have given their important feedback and advices during the work and publishing phase, and the thesis supervisor Prof. Seppo Ovaska helped clarifying contents while compiling all publications together.

The author has contributed the design and validation measurements of presented plant models, as well as analysis and supervisory control algorithms design for the system level studies. The thesis is based on his own contributions within the HybDrive (mid-2007 to 2009), TopDrive (2010 to 2012), and ECV/Tubridi research projects carried out at Aalto University. In addition, the thesis contributed research in the MIDE Hyblab-project which was carried out from 2008 to 2012.

Symbols and abbreviations

Symbols

In general, the electrical variables with subscripts written in upper case refer to the quantities on the DC-link voltage potential and subscripts written with lower case refer to the quantities on the energy storage voltage potential, respectively.

A	Battery exponential voltage
B	Battery exponential capacity
C	Battery nominal current
C_{DC}	Constant capacitance of a DC link
C_{uc}	Constant capacitance of an ultracapacitor pack
$\mathbf{C}_{\mathrm{uc}}$	Variable capacitance map of an ultracapacitor pack
D	Current direction for a DC-DC converter
e_{n}	Speed error term of a proportional-integral controller
e_{u}	Voltage error term of a proportional-integral controller
E_{bat}	Battery pack energy content
$E_{\mathrm{losses\_}i}$	Energy losses of a component i
E_{uc}	Ultracapacitor pack energy content
i_{AFE}	Direct current of an active front-end converter
i_{bat}	Battery current
i_{BRK}	Brake unit current
i_{ES}	Energy storage current on a DC-link voltage potential
$i_{\mathrm{ES}'}$	Energy storage system current reference on a DC-link voltage potential
i_{es}	Energy storage current
i_{fc}	Fuel cell current
i_{LOAD}	Load current on a DC link
$i_{\sum \mathrm{PCC}}$	Sum current on a point of common coupling
I_{max}	Maximum current of a DC-DC converter
I_{min}	Minimum current of a DC-DC converter
i_{ref}	Current reference
$i_{\mathrm{ref}'}$	Current reference before limitations
$i_{\lvert\mathrm{ref}\rvert}$	Absolute current reference
i_{uc}	Ultracapacitor pack current
i^*	Battery low-frequency current dynamics
it	Battery extracted capacity
J_{tot}	Total inertia on engine shaft
K_{I}	Integral coefficient of a proportional-integral controller
K_{P}	Proportional coefficient of a proportional-integral controller
$\dot{m}$	Engine fuel quantity in milligrams per stroke
n_{EM}	Electric machine speed
$n_{\mathrm{e\_ref}}$	Engine speed reference
n_{G}	Generator speed
n_{VSDG}	Engine actual speed

p_{ij}	Surface polynomial coefficient
p_{LOAD}	Load power, electrical
P_{MAX}	Tuning parameter of an energy management algorithm
p_{mech}	Load power, mechanical
p_{ref}	Load power reference
Q	Battery maximum capacity
R_{bat}	Battery resistance
R_{DC}	Equivalent series resistance of DC-link capacitors
R_{uc}	Equivalent series resistance of an ultracapacitor pack
t_{k}	Discrete-time sample with an index k
u_{bat}	Battery nonlinear output voltage
u_{DC}	DC-link voltage
$u_{\mathrm{DC\_ref}}$	DC-link voltage reference
u_{es}	Energy storage voltage
u_{fc}	Fuel cell cource output voltage
U_{max}	Ultracapacitor maximum voltage
U_{nom}	Battery minimum voltage value of the linear area
u_{ratio}	Voltage conversion ratio, energy storage respect to DC-link voltage
u_{uc}	Ultracapacitor pack voltage
U_0	Battery maximum voltage value of the linear area
$\eta(i_{\mathrm{es}}, u_{\mathrm{ratio}})$	Efficiency map of a DC-DC converter
$\eta(n_{\mathrm{G}}, \boldsymbol{\tau}_{\mathbf{req}})$	Combined efficiency map of an active front-end converter and generator
η_{boost}	Efficiency map of a DC-DC converter in a discharge operation mode
η_{buck}	Efficiency map of a DC-DC converter in a charge operation mode
$\eta_{\mathrm{ED}}(n_{\mathrm{EM}}, \boldsymbol{\tau}_{\mathbf{EM}})$	Efficiency map of an electric drive
$\boldsymbol{\tau}_{\mathbf{EM}}$	Torque of an electric machine
$\boldsymbol{\tau}_{\mathbf{e}}$	Output torque of a diesel engine
$\boldsymbol{\tau}_{\mathbf{load}}$	Load torque of a diesel engine
$\boldsymbol{\tau}_{\mathbf{map}}$	Torque data mapping of a diesel engine
$\boldsymbol{\tau}_{\mathbf{req}}$	Generator requested torque
τ_{AFE}	Control delay time-constant of an active front-end converter
$\tau_{\mathrm{DC/DC}}$	Control delay time-constant of a DC-DC converter
τ_{e}	Control delay time-constant of a diesel engine
ω_{G}	Generator angular speed
ω_{VSDG}	Engine angular speed

Abbreviations

AC/DC	AC to DC rectifier
AFE	Active Front-End converter
AOC	Adaptive Optimal-Control
CO_2	Carbon dioxide
DC/AC	DC to AC inverter
DC/DC	DC to DC converter
ED	Electric Drive
EM	Electric Machine
EMS	Energy Management Strategy
ES	Energy Storage
EUT	Equipment Under Test
FC	Fuel Cell
G	Generator
HE	High Energy
HP	High Power
ICE	Internal Combustion Engine
MABX	dSpace MicroAutoBox
MPC	Model Predictive Control
NRMM	Non-Road Mobile Machinery
OEM	Original Equipment Manufacturer
PE	Power Electronics
PEM	Polymer Electrolyte Membrane or Proton Exchange Membrane fuel cell
PI	Proportional-Integral controller
SHEV	Series Hybrid Electric Vehicle
UC	Ultracapacitor
VSDG	Variable Speed Diesel Generator-set

1 Introduction

Non-road mobile machineries (NRMMs) are vehicles whose aim is to produce effective work in mobile positions. This category includes devices such as, harbor straddle carriers; mine loaders; forest work machineries, for instance, harvesters and forwarders; and military vehicles. Complementary terms for an NRMM are an off-road heavy vehicle [1]−[2], or even a heavy-duty vehicle [3]. The powertrain, which is the focus of this research, functions as a part of NRMMs.

Thus, a powertrain refers to the part of a vehicle which generates power and provides a path for power from the source to its load. In general, a powertrain may consist of various different components, due to the diverse purposes of NRMMs as illustrated in example Fig. 1. A harbor straddle carrier is used to lift, move, and descend containers in a harbor area. An underground mining loader charges a bucket at the end of an underground mine and hauls ore to a point from where an underground truck carries ore the rest of the way up. A forwarder collects logs with a boom and delivers logs next to the road from where a truck is able to pick up logs for road transportation.

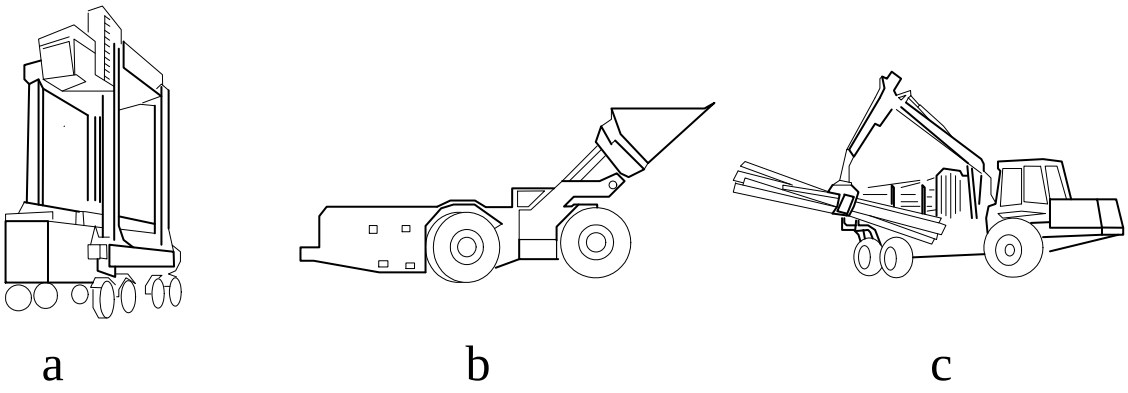

Figure 1: Different non-road mobile machineries; (a) harbor straddle carrier, (b) mine loader, and (c) forwarder.

The powertrain, for instance in a passenger car, consists of an internal combustion engine (ICE), a gearbox, driveshafts, and differentials. In this vehicle, the ICE operates as a source, and the wheels operate as loads. Another example of powertrain design can be found in a diesel-electric train, which consists of an ICE, generator, rectifier, inverters, and traction machines. This type of a powertrain transforms rotational movement into an electric current and back to rotational movements. The third example of powertrain design is hydraulic, which is usually operated in hydro-static means. In that powertrain, the ICE rotates a hydraulic generator that in turn is connected via hydraulic hoses to hydraulic motors. In such cases, the fluid pressure of the hoses is kept constant. Furthermore, this thesis uses the word "powertrain" as described in the context of these three aforementioned examples. Synonyms are used to denote the powertrain [1]−[2], such as drivetrain [2]−[4], drive line, and transmission.

In the conventional car powertrain, the ICE operates as a source, and the wheels to the environment contacts operate as loads. Thus, a two-wheel drive has two bodies which create a load for the ICE, and a four-wheel drive has four. The ICE usually couples mechanically to loads and, thus, always operates at a speed defined by a vehicle speed and a gear ratio. In practice, loads define the torque and speed of the ICE and therefore, it cannot be operated in the best efficiency operation area. Moreover, the ICE cannot absorb more regenerative power than the parasitic loads on the ICE shaft consume, and therefore, during deceleration the kinetic energy from the vehicle body is consumed as heat in the brakes. On the other hand, some trains and ships have adopted the diesel-electric powertrain which relieves the ICE from the mechanical speed of a load. Furthermore, in trains the diesel-electric powertrain is needed if the railway line is lacking power lines. Such high cost high power applications as these have conventionally used electric powertrains. However, the diesel-electric powertrain cannot provide regenerative energy recuperation, although electric traction machines and inverters could provide such an operation. In practice, the diesel-electric powertrain only lacks a suitable energy storage system.

In comparison to cars, heavy-duty vehicle powertrains are more diverse. Besides the need for kinetic energy, heavy-duty vehicles often need linear movement for actuators, such as, buckets, hoists, and booms, which are usually operated with hydraulic cylinders. The movements and payloads of hydraulic actuators yield another load for the ICE, and may demand high peak powers. Conventionally, hydraulic actuators have introduced partly or fully hydrostatic power transfer to the powertrain of a heavy-duty vehicle. The hydrostatic power transfer has traditionally had low overall energy efficiency which is in range of less than 10 % due to partial loading of an ICE with high constant speed. Furthermore, in conventional designs, the hydraulic transmission has transferred power in only one direction, thus preventing regenerative energy recuperation.

Heavy-duty vehicles are a diverse group as described earlier. Trucks, cranes, tractors, bucket loaders, and trains among others can be included in this category. Some of these vehicles operate only on bounded sites, and thus are called non-road mobile machineries. Traditionally, NRMMs have been built with a mechanical, hydraulic, or diesel-electric powertrain. The conventional designs of NRMM powertrains have not usually enabled regenerative energy recuperation, which is available in most NRMM work cycles as kinetic and potential energy forms. In the traditional design, regenerative energy has been converted into heat in mechanical brakes, hydraulic valves or in brake resistors. Moreover, system efficiency is low during engine idling, i.e. partial loading of an ICE. These reasons together lead to low overall energy efficiency in a system. For instance, the corresponding system efficiency in a conventional passenger car application is in the range of 14 - 22 %, and with a hybridized system 29 - 30 %, respectively [5]. Furthermore, through hybridization, low emission by-production in power generation, and lower or even locally zero-emission powertrains can be succesfully achieved [3]. Therefore, different hybrid powertrain topologies are studied for the regenerative energy recuperation of the NRMM powertrain.

A hybrid vehicle powertrain can be realized in many different ways. In gen-

eral, different combinations of mechanical, hydraulic and electrical power transfer components may come into question for the right drivetrain topology choice for a specific case. For example, series, parallel, series-parallel, and complex hybrid electric vehicle architectures have been defined in [4]. However, feasible powertrain topology choices are predefined based on the application field, and thus, the study for hybridizing a powertrain in the NRMM concentrates on the series-hybrid electric vehicle (SHEV) topology [1]−[2].

This series-hybrid electric powertrain can consist of several different energy sources and storages, see Fig. 2. These energy sources usually are engine and fuel cell, whereas the usual energy storage options are battery, ultracapacitor, and flywheel [6]. Additionally, the drive line demands controllable electric power conversions with power electronics devices. Such devices change the form of the current from alternate to direct, and vice versa, for the use of generator and electric machine. DC-DC converters control electric power through different voltage levels in the drive line, for the utilization of energy storage full capacity [7]. The amount of options for the design of a hybrid drive line makes it an undoubtedly complex process. The degrees of freedom in design arise because of several energy storage options and their combinations, the sizing of energy sources and storages, the energy source and storage interface options, e.g. active or passive, and the control of active interfaces. Thus, feasibilities and design procedures of series hybrid powertrains are studied for the needs of NRMM manufacturer product development [8]. The importance of the study arises—specifically, due to the complexity of the subject, implementation of a new design, lack of already known design principles, and the education of new engineers. Therefore, efficient modeling principles for the NRMM powertrain design are considered in this research.

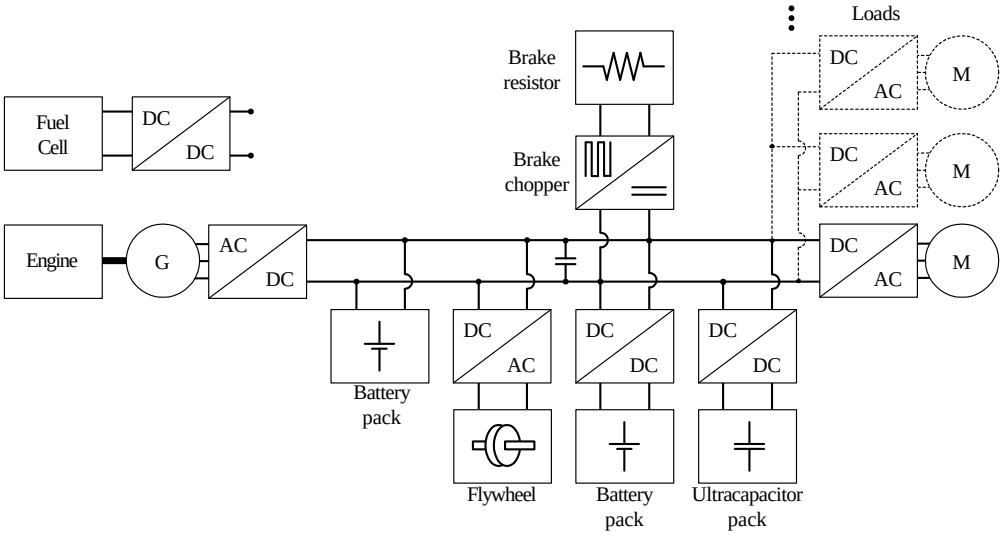

Figure 2: Different series-hybrid electric vehicle powertrain component options.

Thus, this study concentrates on the series-hybrid electric powertrain, which

has all system loads connected to the common DC-bus. In other words, all system loads are treated as one load which is consumed from the common DC-bus. This simplification neglects the realization of the load, since this would lead to an overly diverse research area.

As a summary, the goal of this thesis is to provide design knowledge, and tools for engineering series-hybrid powertrains in NRMM applications. In some NRMM applications, conventional powertrains needs to be re-designed due to low-energy efficiency, and lack of regenerative energy recuperation. As a design options, there exist various types of powertrains, as different types of hybrids, and as different types of series-hybrids which are discussed in Chapter 2. In practice, the engineer should be capable of choosing the right powertrain for a specific application. Therefore, contributions have been made in order to reach previous common goals. Firstly, the research concentrates on a series-hybrid electric powertrain modeling from known loads of the DC-bus to actual values of powertrain variables (such as currents and voltages) in different voltage potentials, and primary energy source outputs. The primary energy source actual output values for the fuel cell stack are current, voltage and hydrogen, and for the diesel generator-set, speed, torque, and fuel consumption. Secondly, the research focuses on power control for an ultracapacitor (UC) buffered series-hybrid electric powertrain. Thirdly, developed modeling and simulation tool are used to analyze the cost, size, weight, and efficiency of different fuel cell series-hybrid powertrain topologies [8].

The main scope of this thesis is on series-hybrid electric powertrain modeling and energy management for the design of non-road mobile machineries.

This thesis is organized as follows: Chapter 1 defines the background, scope, and structure of the thesis; Chapter 2 previews the history and the State-of-the-Art of the topic; Chapter 3 presents the development of different series-hybrid powertrain component plant models, describes test setups for plant model validations and presents mathematical descriptions of the models; Chapter 4 summarizes and reviews publications; and Chapter 5 summarizes the thesis.

The publications included in this thesis are reprinted at the end.

2 State-of-the-Art

2.1 History

Development Milestones of an Early Electric Vehicle

The invention of the electric vehicle has been attributed to various people from the 1820s to 1900s. Named contributions began with Ányos Jedelik in 1828, who demonstrated an early type of electric motor. After several other contributions, in 1881, French inventor Gustave Trouvé demonstrated a working three-wheeled automobile at the International Exhibition of Electricity in Paris, which was powered by 0.1 horsepower DC motor and weighted 160 kg.

The 1890s was an era of rapid development of an electric vehicle. The first commercially succesful electric car, able to carry six passengers at 16 km/h, was made in 1893 by Paul Pouchain. Later, the 100 km/h speed barrier with an electric vehicle was broken in 1899 for the first time by Camille Jenatzy. Development was rapid due to a series of competitions that promoted technical improvements.

The first hybrid vehicles reported were shown at the Paris Salon in 1899 with a presentation of parallel and series-hybrid concepts. The series-hybrid was derived from a pure electric vehicle, and built by the French firm Vendovelli and Priestly.

During 1900-1910, electric cars reached the height of their success, and manufacturing amounts peaked in the United States by 1912. As gasoline automobiles became more powerful, more flexible, and above all easier to handle—electric vehicles started to disappear. Their high cost, limited range and performance impaired them against the gasoline vehicles. In nearly 60 years, the only electric vehicles sold were forklifts, delivery vehicles, and golf carts. [9]−[12]

Fuel Cell

The first contributions for the fuel cell invention were made as early as 1839 by Sir William Grove, who discovered that it might be possible to generate electricity by reversing the electrolysis of water. It took until 1889 before the term “fuel cell” came into use while Charles Langer and Ludwig Mond tried to engineer the first practical fuel cell using air and coal gas.

It was remarkably later, in the 1950s, that Francis Bacon successfully produced the first practical alkaline fuel cell. In the 1960s, an alkaline fuel cell power plant was developed for the Apollo spacecraft. The plant provided both electricity (1.5 kW) as well as drinking water for the astronauts on their journey to the moon. A drawback in previous fuel cells was that carbon dioxide would react with the alkaline electrolyte, and thus reduce the overall efficiency of the fuel cell. Technologies with the non-alkaline electrolytes became more attractive for terrestrial applications, such as, solid oxide fuel cells, phosphoric acid fuel cells, molten carbonate fuel cells and proton exchange membrane (PEM) fuel cells which were later considered to be the power source in vehicles.

Already in the early 1960s, Thomas Grubb and Leonard Niedrach developed the first PEM fuel cell while working in General Electric. The PEM fuel cell technology

was interesting but not immediately adopted by NASA's space flights. The era of PEM fuel cells on space flights started with Gemini 6 to 12, between 1965 and 1966. Then in 1979, the company Ballard Power Systems was established, and it has since grown to become recognised as a world leader in PEM fuel cell technology. [11], [13]

Evolvement of a Diesel-Electric Powertrain in Heavy Vehicles

The diesel-electric powertrain has long been used in some applications, such as in locomotives [14], and ships [15]. In the 1900s, electric propulsion was introduced to ships. In those days, electrical systems were various kinds of AC or DC systems, and a power source in the beginning was a turbine, and later on diesel engines were also utilized [15]. In about 1925, the diesel-electric traction began to compete with other propulsion systems in locomotives [14]. Some decades later, in 1947, a braking resistor system was proposed for a locomotive to prevent the need for brake shoe maintenance, wheel wear, and to increase faster schedules for operation [16].

Concerns about the environment triggered more research on electric vehicles between 1955-1965, and as a result, a new thyristor inverter technology with advantages, including the use of asynchronous motors, was adopted to traction motor considerations [12]. Simultaneously, an earth-moving DC electric drive vehicle, the 100-ton with 1100-horsepower ore truck, was in commercial use. In those days, an ore truck powertrain consisted of a gas turbine as a power source, DC generators and motors. The motors were integrated in wheels with gearings [17].

Research continued to adopt "commutator-less" AC-drives for locomotives, military vehicles, battery powered electric vehicles, and other types of NRMMs. In the middle of the century, NRMM powertrains were realized by diesel engines with gearshift and torque-converter transmissions [17]. By 1973, the new converter technology with asynchronous traction motors had been introduced to diesel-electric locomotives. At that time, a diesel-electric powertrain consisted of a diesel generator-set with a passive diode rectifier, DC intermediate circuit with a braking resistor, and thyristor based inverters operating asynchronous traction motors [18].

A Rise of New Interest in Electric Vehicles

In the 1970s, the period of energy crises increased the interest of vehicle manufacturers towards electric vehicle research. The energy crisis was a period in which the major industrial countries of the world faced substantial shortages of petroleum. The two worst crises of this period were the 1973 oil crisis, and the 1979 energy crisis. Oil prices first rose in the early 1970s, and then declined during the late 1970s, thus leaving electric vehicle research interest dependent on its environmental impacts [19].

In the beginning of the 20th century, battery capacities were around 0.02-0.07 kWh/kg, and by 1988, it was understood that theoretical battery capacities would stay under 0.3-2.8 kWh/kg [11]−[12]. On the contrary, gasoline and diesel energy densities are in the range of 12 kWh/kg. Thus, it was agreed that electric vehicles could never compete with gasoline automobiles in the driving range. The automobile industry begun to concentrate on research on hybrid and fuel cell vehicles for

long-range vehicular purposes [11]. Furthermore, energy densities of batteries are currently still within 0.05-0.15 kWh/kg [20].

In the 1960s, GM resurrected its research (since the 1910s) on electric and hybrid vehicle propulsion systems. For instance, in 1966, the first fuel cell van was demonstrated. At that time, the fuel cell system was reported to be too expensive and complicated.

In 1968, an electrically powered six-wheel military vehicle was demonstrated with an IC engine, AC generator, inverters, and wheel motors. That same year a series-hybrid powertrain, with the stirling engine providing power to a passive battery pack, was tested in a small size passenger car [19]. Thus, by 1983, research for hybridizing vehicle powertrains had already a long history. Meantime, development of a parallel hybrid powertrain test vehicle was reported in [21].

By the 1990s, automobile manufacturers became interested in hybrid and fuel cell applications. Several demonstrations were made for both in the 1990s. Commercial markets of hybrid vehicles were initiated in 1997 by Toyota Prius [4], and the commercialization of the fuel cell vehicle is still waiting to begin. Fuel cell vehicles currently exist for all modes of transport. The most prevalent fuel cell vehicles are forklifts and material handling vehicles. However, there are currently no fuel cell cars available for commercial sale. The major challenges for fuel cell technology commercialization are on lowering the cost of volume production, and increasing reliability as well as durability. [22]

2.2 State of the Research

The previous section states the long history of electric, hybrid and fuel cell powertrains. Despite this lengthy history, the field of hybrid powertrain research is in a relatively early phase. An increase in publicly available publications related to the topic began in the late 1990s. However, this section concentrates on recent proceedings on the field, thus covering the early 2000s.

By the year 2007, Terminal Systems Inc. reported completion of the preliminary testing of their first ECO Crane with a diesel/battery hybrid powertrain [23]. The application is similar as in Fig. 1 (a), and studied in Publication V. Other proceedings relating to a comparable system have been reported in [24] and [25].

Publication [24] reviews six different energy management strategies (EMS) for a diesel-electric system with energy storage. Furthermore, that publication focuses on providing design rules for different series-hybrid powertrains with a passive high power (HP) battery pack or an active ultracapacitor pack as possible energy storage. The research proposes methods with which to compare different EMS strategies, and compares the HP battery powertrain topology cost sensitivities with different EMSs, but will not proceed to conclusions on the supremacy of either an active ultracapacitor buffering or an HP battery buffering. Furthermore, the study neglects weights and sizes of different powertrain options; moreover, the proposed methods for design are simple, but superficial.

Publication [25] presents power control for a powertrain with diesel-engine, separately excited generator with diode rectifier, and DC-DC converter between low

capacitance intermediate circuit and UC energy storage. Tuning variables for power control in the system-level are generator excitation and intermediate voltage reference of a DC-DC converter.

In 2007, the journal *Proceedings of the IEEE* published a special issue related to the hybridization of vehicles, which reviewed the State-of-the-Art of the field. Therefore, it is publicly known that for vehicles driven on fixed routes and with a cyclic pattern, i.e. stop-and-go means, the fuel saving potential is an average of 50 % or more, with either parallel or series-hybrid powertrains [4]. Furthermore, it is self-explanatory that for many vehicles, including hybrids, the most energy efficient path from fuel conversion to vehicle propulsion is the most direct path. For combustion engine driven vehicles, this means mechanical coupling; for fuel cell vehicles, this means directly through an intermediate bus without passing through an energy storage media, because every energy conversion generates losses [7]. Therefore, general considerations are made to choose either a mechanical or a hybridized powertrain for each vehicle applications.

The following review classifies different powertrains with the control possibility of power electronics converters. In this context, a converter or energy storage (ES) coupling is termed passive, if it allows no controllability provided by e.g. hard-switching of semi-conductors, or when a component is directly coupled. On the other hand, they are defined as active, if controllable semi-conductor technology is utilized. Furthermore, the fuel cell (FC) or the ICE primary source is another basis of classification for powertrains. Based on this categorising, recently studied different series-hybrid powertrains are described in the following paragraphs.

A powertrain with an engine generator-set, active rectifier, and passive battery pack

The powertrain topology presented in Fig. 3 and earlier covered in [1], [4], [11], [24], [26], and [27]; is the first step forward from diesel-electric powertrains which are commonly utilized in trains and heavy high power ore trucks. The powertrain provides engine operation steadily on the chosen operating point, with commands of operation speed ω, and torque $\boldsymbol{\tau}$, which together define power p to a battery pack in the intermediate circuit.

Furthermore, passive HP batteries are proposed—specifically for charge-sustaining operation of series-hybrid powertrains [24].

Publication [26] presents dynamic modeling which takes into account both electrical and mechanical phenomena in the powertrain with actively loaded ICE and passive battery pack.

Publication [27] reviews different hybrid powertrain topologies, including series-hybrid, as well as heavy-duty FC hybrid; and states the need for high power-density batteries in hybrid vehicles.

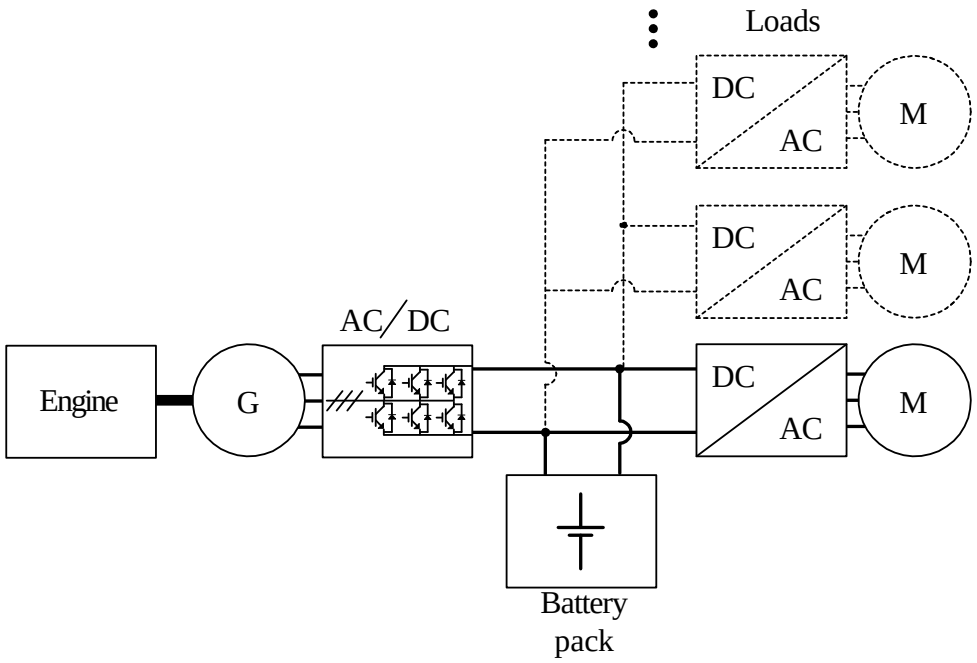

Figure 3: The powertrain with an engine generator-set, active rectifier, and passive battery pack.

A powertrain with an engine generator-set, active rectifier, and active battery pack

The powertrain topology presented in Fig. 4 is proposed in studies [2], [4], and [28]. The active battery pack refers to a battery which is controlled with a DC-DC converter.

In this topology, the powertrain control strategy becomes similar to the earlier powertrain case, if the DC-DC converter regulates voltage of a low capacitance intermediate circuit. However, there is another possibility for the powertrain control strategy which derives from the diesel-electric powertrain without energy storage. In such a case, voltage of the low capacitance intermediate circuit is regulated with the active rectifier, and the DC-DC converter primarily commands the current of the energy storage.

Publication [28] states needed operation modes to control power flows in all relevant directions. Furthermore, a sizing method is proposed for traction motor, engine, and energy storage system. The sizing method is based on the maximum power needed from components of the powertrain. An energy storage system design is discussed and the design of a hybrid energy storage explained, i.e. combined battery and UC. It is noted that the hybrid energy storage has much less weight than a battery alone as the energy storage. In addition, both passive and active hybridizations of the energy storage system are proposed.

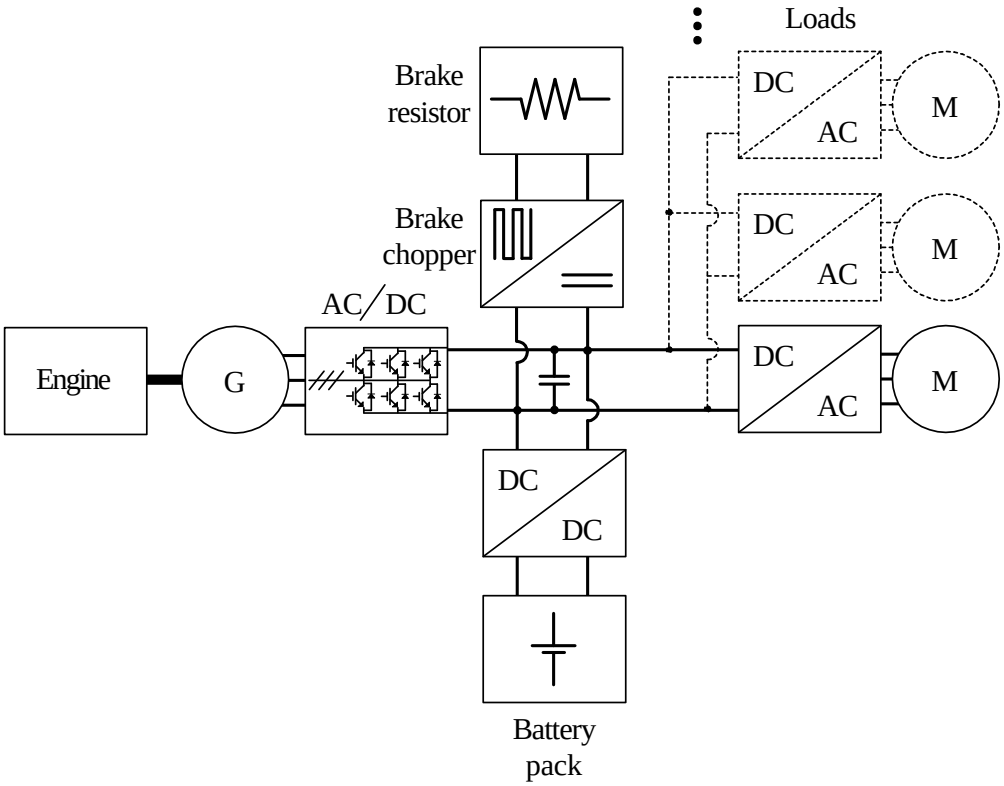

Figure 4: The powertrain with an engine generator-set, active rectifier, and active battery pack.

A powertrain with an engine generator-set, active rectifier, and active UC pack

The powertrain with an engine and a UC energy storage is shown in Fig. 5 and proposed in [4], [24], [29], and [30]. Power control strategies in this case can include intermediate circuit voltage regulation features, the DC-DC converter regulation, and the active rectifier regulation. However, the voltage operation range of an UC pack delimits its control freedom in respect to the battery buffering case.

Publication [24] proposes UC buffering for the crane application, suggests six different power management strategies and compares their costs. The study does not consider the sizes and weights of such systems.

Publication [29] presents thoroughly the characteristics of the UC buffered powertrain with its parameters. In the case presented, the control strategy is such that the DC-DC converter regulates voltage of the low capacitance intermediate circuit; moreover, the active rectifier generates power flow from an engine depending on the state-of-charge (SOC) of a UC, current derivative limitations, and the efficiency map of a combined active rectifier generator unit.

Publication [30] proposes an energy management strategy to save both the power

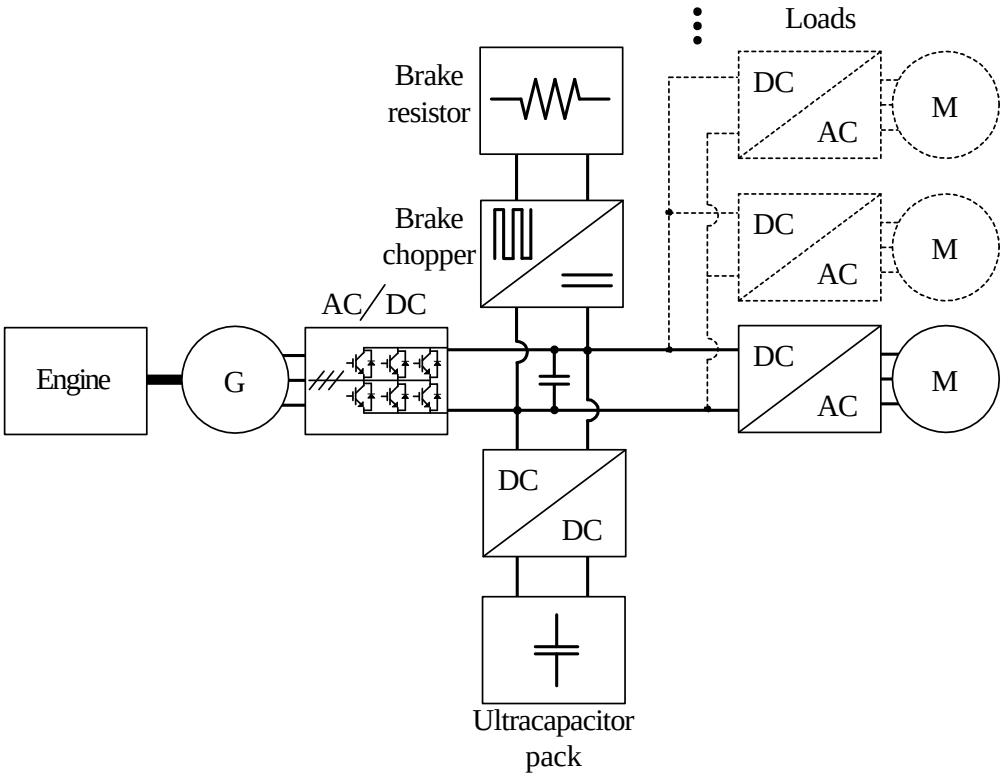

Figure 5: The powertrain with an engine generator-set, active rectifier, and active ultracapacitor pack.

losses in the hybrid system, and capacitance of the UC pack. The strategy is based on keeping the summation of the kinetic energy and the UC energy constant. It is proposed that the engine is controlled in three steps: maximum, optimum, and auxiliary power regions. Furthermore, the study proposes a method to design appropriate capacitance for the UC buffered diesel-electric powertrain in local or express train applications.

A powertrain with an engine generator-set, active rectifier, passive battery, and active UC pack

The powertrain with an engine, a passive battery as an intermediate circuit, and an active UC energy storage system as a peak power unit is presented in Fig. 6 and studied in [31]−[32].

The objective of the publication [31] is on the dynamic control strategy of the DC-DC converters for energy management between the batteries and supercapacitors. The dynamic modeling describes phenomena occurring on the intermediate circuit, which has parallel smoothing capacitors (1.5 mF) and a lead-acid battery pack with current smoothing inductor (25 μH) in series. The circuit creates the same

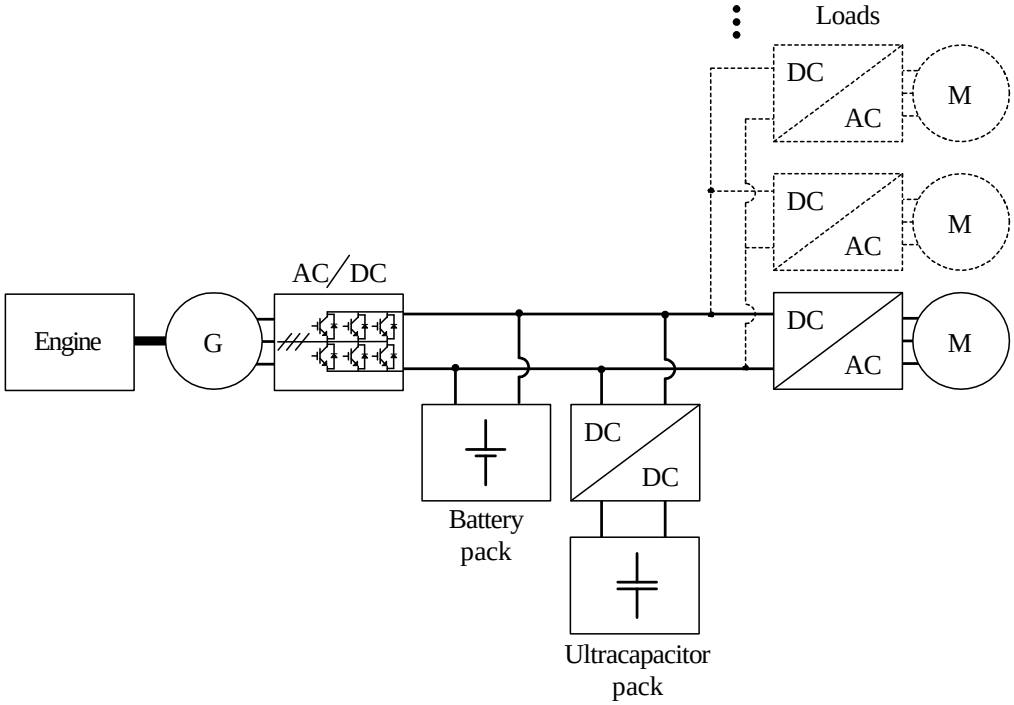

Figure 6: The powertrain with an engine generator-set, active rectifier, passive battery, and active ultracapacitor pack.

phenomenon which can occur in the intermediate circuit with long cabling between different power electronics components, or between a power electronic component and a battery pack.

Publication [32] continues the research on the control laws of DC-DC converters in the energy management between battery and UC by polynomial control strategy, and by dynamic modeling of such systems. Both studies concentrate on optimizing the system by designing the switching event time-scale operation.

A powertrain with an engine generator-set, passive rectifier, and active UC pack

The UC buffered diesel-electric powertrain with a passive rectifier is presented in Fig. 7 and studied in [25], and [33].

Publication [25] proposes improvements to an EMS, which is based on both the DC-link voltage regulation and the engine generator-set droop frequency regulation. In the EMS, the DC-link voltage regulation is used when primary power is fed by the active UC pack, thus, the DC-link voltage can be regulated to a value which does not allow the passive rectifier to conduct. Furthermore, while using regenerative braking, the voltage control mode transfers power to the UC pack. In contrast, in the event of the UC pack being exhausted or the load too high, the engine generator-

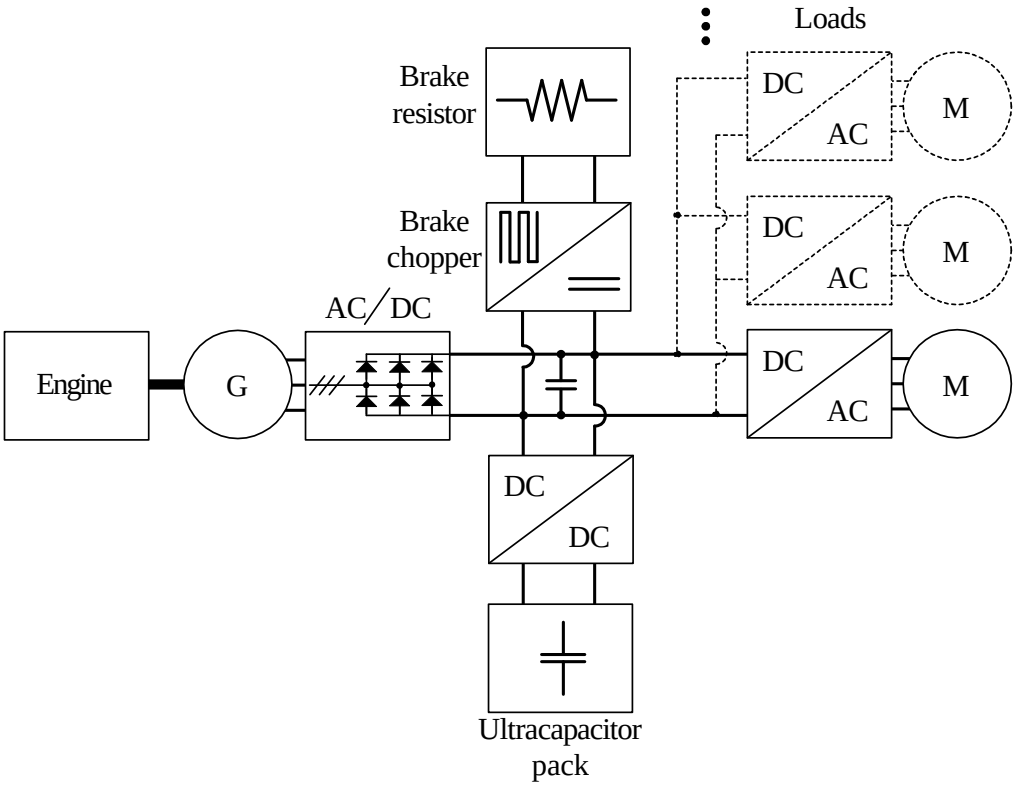

Figure 7: The powertrain with an engine generator-set, passive rectifier, and active ultracapacitor pack.

set droop frequency regulation is chosen. Then, primary power is fed by the engine generator-set. If the droop frequency reference cannot be met, the UC pack assists the operation. The contribution of the study itself is on the generator frequency estimator algorithm for the EMS operation. The study presents a hybrid powertrain with engine size decreased to one-third of the original. However, a drawback of the system is that the engine is used to charge the UC pack to ensure operation.

Publication [33] concentrates accurately on electrical behaviors, and power electronics (PE) control in the system, thus neglecting system level operation issues outside the study. The paper proposes use of a bidirectional three-level DC-DC converter with energy storage, and a control algorithm for the converter to perform power control which affects the system level power flow. The proposed control algorithm seems to result in the ON-OFF operation of the two power sources. However, the contribution of the study is on the UC based energy storage design guidelines for such a system which has a ride-through capability against voltage sags (or dips, i.e., an instantaneous decrease in the RMS voltage with a range of 10 % - 90 % and duration up to a minute) in the mains. Furthermore, the study is exact and systematic in its analysis, as well as discussing deeply issues relating to converter technology

possibilities in such a system. The proposed power flow control algorithm is based on DC-link voltage from which UC voltage and current references are calculated.

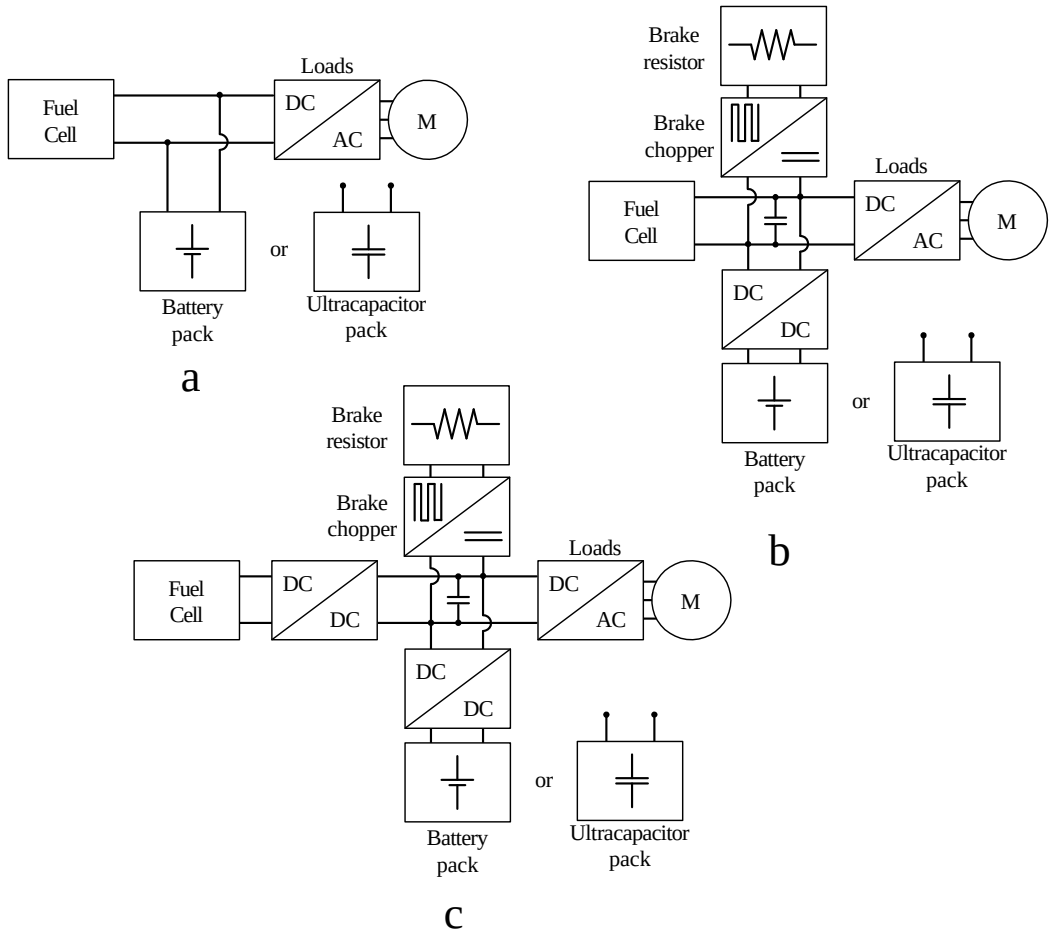

Figure 8: Different fuel cell source powertrain cases; (a) the powertrain with a passively coupled FC source and passive ES, (b) the powertrain with a passively coupled FC source and active ES, and (c) the powertrain with an actively coupled FC source and active ES.

A powertrain with passive or active coupling of a fuel cell source and a battery pack

Basic fuel cell source powertrain topologies with battery buffering are illustrated in Figs. 8 (a)-(c), and studied in [7], [20], [27], [34], and [35].

Publication [7] proposes FC powertrains with: passive coupling of FC and UC [Fig. 8 (a)], passive coupling of FC and active coupling of battery pack [Fig. 8 (b)], as well as active coupling of FC with an energy storage system [Fig. 8 (c)]. In the study, the passive coupling of the FC source is justified by fewer losses on the primary power path, and the active coupling of the FC source is justified only

by a matching of the intermediate circuit voltage. Thus, the efficiency of the FC-converter is extremely important due to its direct effect on vehicle fuel efficiency.

Publication [20] investigates a modern tramway as a hybridization target. In such a system the powertrain is doubled, the tram is equipped with both, a generator sized based on the peak load power, as well as overhead lines for supply and regenerative power. By hybridization, overhead lines can be removed and generator size decreased to supply only average power, which in this case is less than a third of the peak load power. The average power operated generator is reversible with the FC source, and thus, an actively coupled FC with passive battery pack is proposed as well as an actively coupled FC with active UC. The energy management algorithm for the active FC and passive battery pack case is based on the battery SOC which is maintained with control of the FC source. Additionally, the algorithm consists of battery current limitations, and current slope limitations for the FC source. The energy management for the active FC and active UC powertrain is realized with the DC-link voltage regulation (PI-controlled) by the UC-converter, while the FC-converter is controlled to maintain the UC state-of-charge (P-controlled). Both controller outputs are limited to ensure usage within a safe operation area of the sources. Design examples of both energy storages are presented, and algorithm operations are verified by experiments.

Publication [27] reviews schematics of fuel cell based powertrains for passenger cars and heavy-duty transit buses.

Publication [34] presents a reduced scale Hardware-in-the-Loop test system for a powertrain with passive FC coupling, and passive battery pack. The study proposes a low-cost, effective, and easy to adapt design environment which combines parts of real hardware, and parts replaced by emulating tools.

Publication [35] compares three powertrain cases, a passively coupled FC with an active battery pack, a passively coupled FC with an active UC pack, and a passively coupled FC with both active battery and active UC packs. The publication concludes that the case with both battery and UC packs is the most promising powertrain topology for passenger car applications. The conclusion is affected by the fact that calculation parameters for a battery are based on lead acid technology instead of other types of batteries with higher specific power. The profitability of the combined active HE battery and active UC buffering with respect to battery or UC only topologies was also concluded in Publication V. Furthermore, in some applications, the combined battery-UC pack ES is replaceable with the proper design of an HP battery. However, features of these powertrain cases are dissimilar due to different amounts of energy in the ES system, and thus, they might become suitable for different applications.

A FC powertrain with an UC pack buffering

The FC powertrain with UC buffering (Fig. 8) is considered in studies [7], [20], [35]−[41]; and buffering with a flywheel in [41]. Issues discussed in Publications [7], [20], and [35]; were reviewed in the previous section.

Publication [36] compares two different EMSs for a powertrain with an actively

coupled FC source and active UC pack. Compared EMSs are a rule-based method and a model predictive control (MPC) method. Both EMS cases are based on a low-level control strategy in which DC-bus voltage is regulated with the FC-converter, and the UC-converter is controlled with the current reference. In both cases, the low-level control strategies are the same as those proposed for the diesel-electric series-hybrid powertrain in Section 3.11, and in Publications II−IV; i.e., the DC-bus voltage regulation with the primary source converter, and the current controlled UC pack. The rule-based EMS relies on a high-pass filtering of the load current, which defines the UC current reference with compensation of power losses and change of voltage potential. Furthermore, the FC source is targeted to be operated near the optimal operation point. The MPC approach utilizes a model of the system to project the future response as a function of control inputs and known disturbances. The designs of both controllers are briefly explained, and the behaviors of design examples compared. Conclusions between behaviors are drawn, but no real differences on performances were comprehensively reported.

Publication [37] presents an approach for the design and analysis of FC-UC hybrid systems oriented to automotive applications. The design issues of the powertrain with an actively coupled FC and active UC are discussed, and a presentation then made of the powertrain design approach based on drive cycle parameters resulting in proper FC and UC source sizing. The study concludes that the most suitable hybridization degree of the FC-UC powertrain for an automotive application is 79 %, which is a suitable value for urban driving cycles, as stated in Publication [38]. The proposed result in [37] is based on calculations with different driving cycles. The hybridization degree (HD) is defined, as

$$\mathrm{HD} = \frac{P_{\mathrm{ess,max}}}{P_{\mathrm{fcs,max}} + P_{\mathrm{ess,max}}} \cdot 100[\%],$$

where $P_{\mathrm{ess,max}}$ refers to the maximum energy storage system power, and $P_{\mathrm{fcs,max}}$ to the maximum fuel cell system power, respectively.

Publication [38] studies proper sizings for FC-battery and FC-UC topologies (considering the degree of hybridization), and discusses approvable design domains, as in [24]. Furthermore, Publication [38] concludes different hybridization degrees for powertrains depending on a driving cycle. In both powertrain cases, the hybridization degree varies between 20 % to 80 %, depending on whether the driving cycle represents sub-urban or urban driving, respectively.

Publication [39] proposes an adaptive optimal-control (AOC) method as the EMS for the powertrain with an actively coupled FC and active UC pack. The design and learning routine of the neural network based AOC method is presented, and comparison against a fuzzy logic based EMS has been assessed. Conclusions favour the AOC-EMS method in respect to the fuzzy logic based method designed by an expert. The tuned AOC algorithm takes load power and SOC as inputs, and gives the fuel cell power reference as output to a low-level control algorithm. The idea of the AOC-EMS is similar as in the EMS designed in Publications II−III, and presented in Section 3.11.

Publication [40] is an earlier study of neural networks usage (in respect to Publication [39]) for an EMS of a powertrain buffered with the active UC pack. The study proposes a more complex neural network with eight inputs, and with one output as the UC pack current reference. Moreover, the study neglects operating points of a primary energy source, since it concentrates on active UC buffering in general.

Publication [41] reviews feasibilities of a hybrid powertrain in different train applications. It is noted that a hybrid powertrain is not advantageous in all train application cases, such as in locomotives for high-speed, heavy freight, and switcher applications. The reasons for previous cases are either extended periods of maximum power (high-speed, heavy freight), or low-speed (switcher) operations where power provided by the powertrain is less of an issue due to the limitations of wheel adhesion. On the other hand, a hybrid powertrain may be beneficial in subways, mass transit, commuter, and intercity rail applications.

A FC powertrain with combined battery and UC buffering

As the last group of introduced topologies, a FC powertrain with two energy storages has been investigated in [42]−[46]. Different methods exist to realize a FC powertrain with two energy storages, as shown in Fig. 9.

Publication [42] presents predictive controllers for different converters in the powertrain with FC source, active battery, and active UC packs [Fig. 9 (a)]. The proposed predictive controllers are for low-level controls, and they are proposed to replace classical PI-regulators from each converter. Predictive controllers have been demonstrated to be faster with simulations and validation measurements in a reduced scale testbed. Use of predictive controllers in each converter low-level control results in faster dynamic system responses.

Publication [43] presents an energy management strategy based on the flatness control technique and the fuzzy logic control. The studied EMS is proposed for the generic battery and UC buffered topology, but the study presents a design example for a powertrain with two DC busses from which one connects to a FC source and active UC pack, and via other DC-DC converter to a higher voltage DC bus, and to loads, and to an active battery pack [Fig. 9 (b)]. The main property of the proposed EMS is that, power flow of the system in different operating modes is managed with the same control algorithm without any algorithm commutation or prediction of the system behavior. Furthermore, the flatness control is utilized to divide load power between the FC source and the ES system, and the fuzzy logic control is used to divide the ES system current between the battery and UC packs.

Publication [44] studies a powertrain with a passively coupled FC source, active battery, and active UC pack [in the control point of view as Fig. 9 (c)]. The study proposes use of a three-port isolated triple-half-bridge DC-DC converter for ESs, and proposes two different EMSs for the powertrain. Furthermore, a design routine is provided to size the battery and UC in order to achieve the lightest mass at the 95 % efficiency. The study concludes that the constant operation of the FC source leads to higher system efficiency in the studied case than the ON-OFF operation of the FC source.

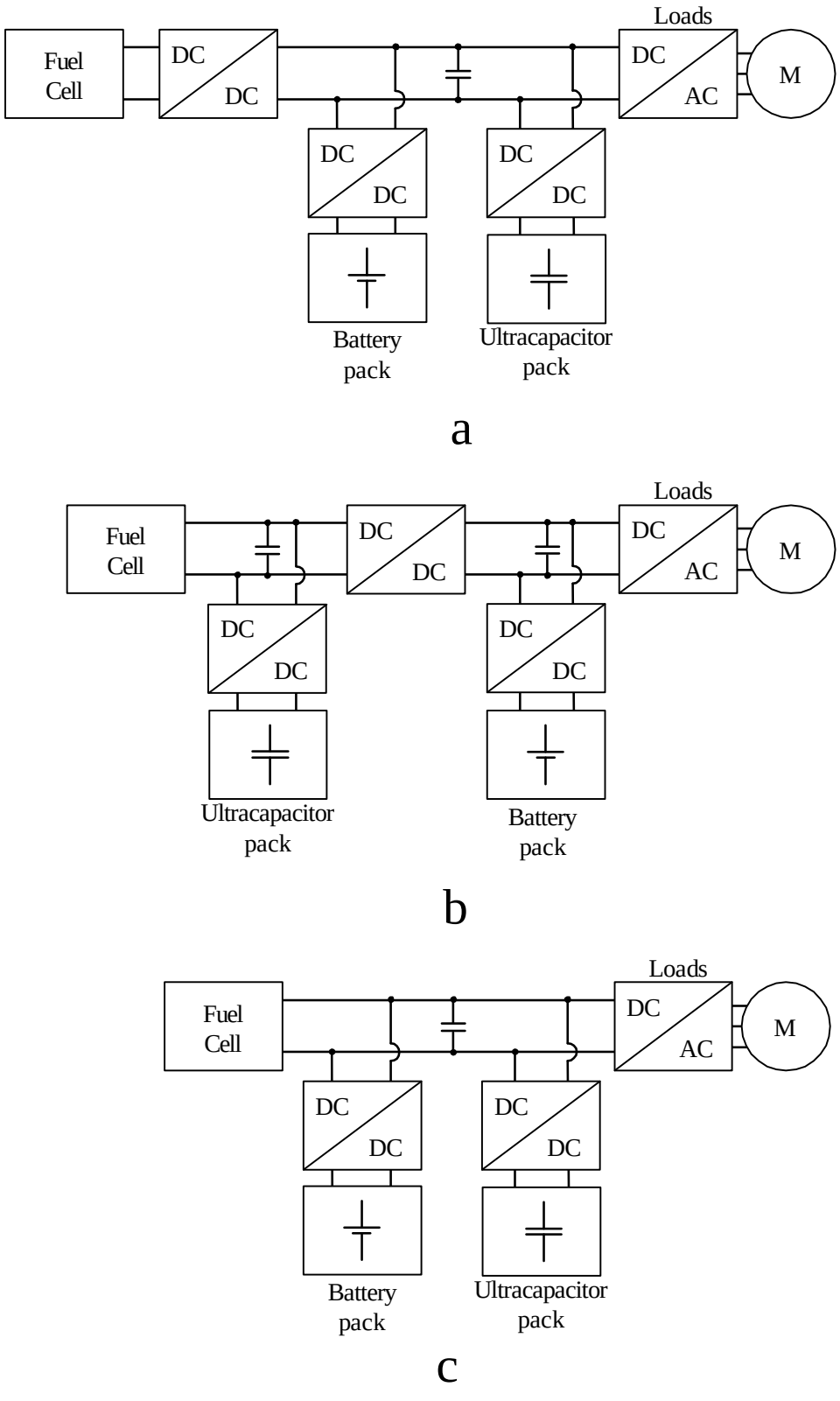

Figure 9: (a) The powertrain with an actively coupled FC source, active battery, and active UC, (b) the powertrain with a passively coupled FC source, and active ESs in two different DC-buses, and (c) the powertrain with a passively coupled FC source, active battery, and active UC. For the sake of simplicity, possible brake units have been left out of the Figure.

Publication [45] proposes a dynamic power distribution between the FC source, battery, and UC [Fig. 9 (a)]. The powers between the FC source and ES system, as well as active battery and active UC are individually controlled; and a proposal made for a global optimization controller with real-time capability. Simulations have been used to prove feasibility of the proposed control against common thermostatic controls. Results suggest a great benefit over urban driving, and lesser benefit to sub-urban driving. Furthermore, the study presents cost functions for optimization of both controllers.

Publication [46] presents the design of a wavelet-transform-based power management for a powertrain with an actively coupled FC source, active battery, and active UC packs. The proposed wavelet-transform algorithm is capable of identifying the high-frequency transient and real-time power demand of the HEV, and allocating power components with different frequency contents to corresponding sources. Simulations of the proposed control were presented, and experimental data for verification and validation of results have been created with a reduced scale test bed.

Hardware-in-the-Loop environments

State of the research in the design of different powertrains has been presented in previous paragraphs based on Publications [24]−[46]. Furthermore, different approaches for Hardware-in-the-Loop environments for supporting research have been presented in Publications [34], [47], and [48].

The ideas of Publication [34] were discussed in an earlier section. A full-scale Hardware-in-the-Loop environment which is used for research in this thesis is presented in Publication [47]. In addition, useful test setups regarding performed research and relating to Publication [47] are presented in Section 3.1.

Publication [48] presents an idea of two reverse-coupled electric machines emulating a driving cycle for use of the traction unit testing in different hybrid powertrains. In such a system, one of the electric machines is controlled with speed, and the other with torque command based on driving cycle and vehicle parameters.

Different modeling methods

The dynamic forward map-based modeling represents a more complete vehicle powertrain system model, contradictory to the proposed multi-stage modeling approach, which concentrates only on the powertrain design beginning from the tractive effort or the drive cycle.

The dynamic forward system models have been presented and validated for the series-hybrid powertrain in Publication [26], and for the power-split hybrid powertrain in Publication [49]. Furthermore, forward and backward, as well as dynamic and quasi-static modeling approaches are widely discussed in [1], [48], and [50].

Therefore, in the modeling approach framework, this study concentrates on how to combine different modeling methods—specifically for the design of different series-hybrid powertrains.

The framework of this study in the State-of-the-Art context

The framework of this study is on the guidelines of systematic and effective series-hybrid NRMM powertrain modeling for designing powertrain hardware dimensions and software algorithms.

In the early phase of the study, the focus was on finding suitable modeling methods. Then, this focus switched to the UC buffered diesel-electric series-hybrid powertrain with indirect primary source power buffering. Finally, the proposed modeling approach was used for the comparison of different FC series-hybrid powertrains in an NRMM application.

3 Development of Series-Hybrid Powertrain Plant Models

An introduction to the studied series-hybrid drive lines, their variables, and principles of plant models are presented in Figs. 10 and 11.

The basis of plant models are control delays of sub-systems and mappings of quantities, such as efficiency and fuel consumption. The control delays are either constant or variable. In this study, the control delays τ_{AFE} and $\tau_{\mathrm{DC/DC}}$ are constant, whereas τ_{e} is dependent on speed, and fuel quantity controlled by a speed PI-regulator.

The power conversion losses are considered with efficiency mappings. Efficiency affects the magnitude of a variable on the unregulated side of a sub-system component. For example, the active front-end (AFE) converter-generator combination efficiency mapping $\eta(n_{\mathrm{G}}, \boldsymbol{\tau}_{\mathrm{req}})$ is a function of generator speed (n_{G}), and requested torque ($\boldsymbol{\tau}_{\mathrm{req}}$). Furthermore, the DC-DC converter efficiency mapping $\eta(i_{\mathrm{es}}, u_{\mathrm{ratio}})$ is a function of energy storage current (i_{es}), and voltage conversion ratio (u_{ratio}).

In Fig. 10, the primary control signal for the variable speed diesel generator-set (VSDG) is speed value (n_{VSDG}), which speed regulator gives fuel quantity ($\dot{m}$) as an output. The AFE converter is controlled with the DC-link voltage reference, which voltage regulator gives i_{AFE} as an output. The DC-DC converter is controlled with the current (i_{es}) reference.

In addition, Fig. 10 presents a plant model for the ultracapacitor pack. It consists of either constant (C_{uc}) or variable capacitance ($\mathbf{C}_{\mathrm{uc}}$) value, and the equivalent series resistance (R_{uc}).

The existence of the tractive electric drive plant model is dependent on the starting point of the simulation, mechanical or electrical load, p_{mech} or p_{LOAD}, respectively.

An example of the fuel cell series hybrid powertrain is presented in Fig. 11. It introduces a battery pack and a fuel cell source plant models and their variables. This figure presents the active battery and UC pack buffered electric powertrain.

3.1 Test Setups for Experimental Identifications and Validations of the Sub-system Models

The identification of the DC-DC converter and the UC module plant models can be performed with the test setup presented in Fig. 12 which is reviewed from Publication IV. The test setup consists of the AFE converter connected to the mains, the DC-DC converter connected between the AFE converter and the UC module, as well as measuring and data-acquisition systems. The devices in the test setup were *NXA_0460 5* (Vacon Plc.) for AC/DC conversion, *MSc200DCDC750* (MSc Electronics Plc.) for DC-DC conversion, *BMOD0018 P390* (17.8 F, 390 V, Maxwell Technologies Inc.) as the UC module, *Norma D6100* (LEM) as the measuring device with 6 to 300 A current shunts, and dSpace *MicroAutoBox 1401/1501/1507* (MABX) as the data-acquisition and control hardware.

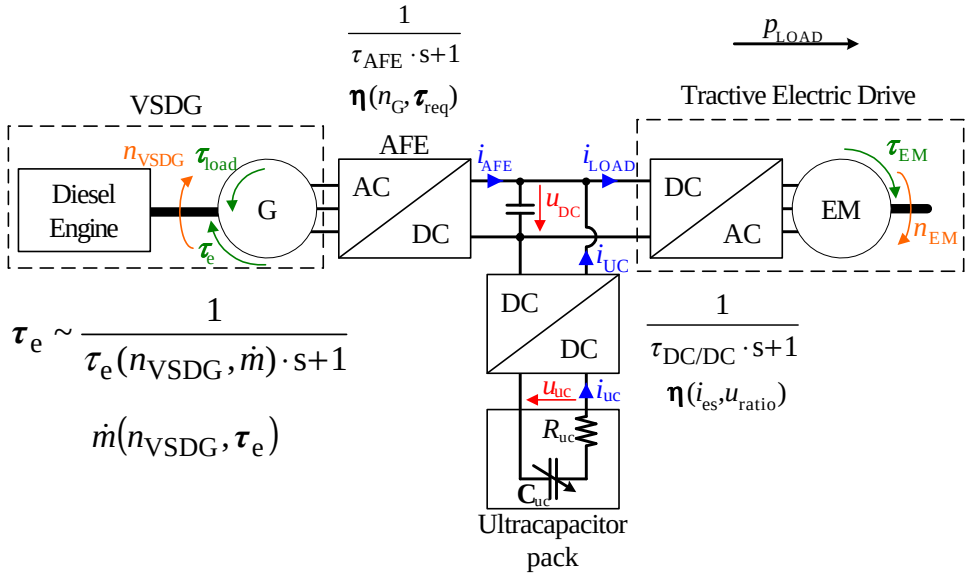

Figure 10: The active UC buffered electric powertrain with the ICE. Powertrain variables and principles of plant models.

The identification of the VSDG plant model speed control responses can be performed with the test setup presented in Fig. 13. The test setup consists of VSDG, diode rectifier, DC-DC converter, and load resistor with parallel capacitors. The VSDG in the test setup was *49 DTAG* (AGCO Corporation Plc.) with the custom made axial flux permanent magnet machine *PMG120-2000* (Axco-Motors Plc.) as a generator.

The validation test setup (utilized in Publication III) for the DC-DC converter and the UC plant models, and for the supervisory control algorithms is presented in Fig. 14. The tractive electric drive in the test setup consisted of a Siemens *ELFA 1PV5135-4WS28* traction electric machine and a *G650 D44/170/170 M7-1* inverter. The braking electric drive consisted of the same asynchronous machine model, and an industrial frequency converter (Vacon Plc.) with a braking resistor. The AFE converter *NXA_0460 5* (Vacon Plc.) regulated the DC-link voltage around 650 V and supplied the primary source current i_{AFE}. The DC-DC converter between the DC link and the UC module had a continuous current (i_{es}) of 120 A, maximum current of 200 A and minimum current of 20 A in the ES voltage level.

Fig. 15 presents the full series-hybrid powertrain system test setup which is not considered in this thesis.

3.2 Basis of Plant Models

The target of the plant models is to envisage mean values of powertrain variables with 20 Hz-bandwidth. The targeted bandwidth is in the range of a DC-link volt-

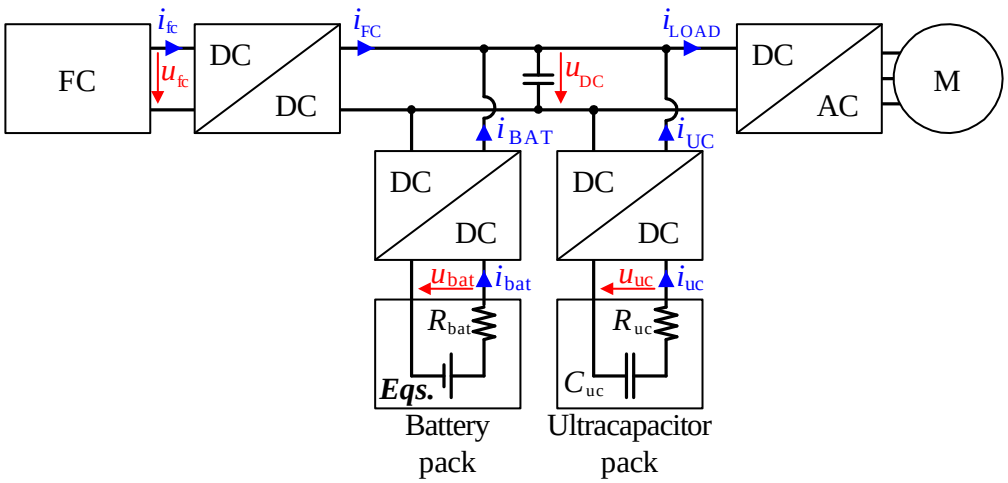

Figure 11: The active battery and UC pack buffered electric powertrain with the fuel cell source. Powertrain variables.

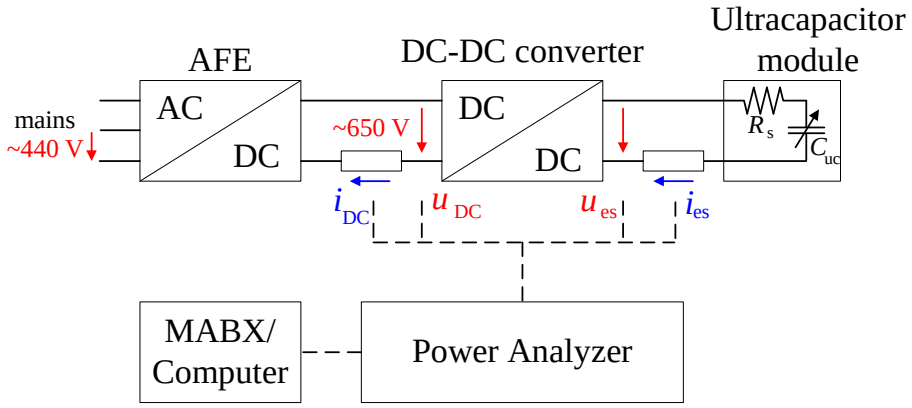

Figure 12: The test setup for the DC-DC converter and the ultracapacitor module identification.

age controller, whereas a chosen time-step for simulator is in the range of current-controllers within such a system. Furthermore, the designed sub-system models should be 'fast' to provide efficient rapid control prototyping of an energy management [51]. In this context, the word 'fast' refers to system models which finish a whole driving cycle in a time-period of 5 to 30 minutes rather than within several hours to days. Therefore, the backward functional modeling from the imposed load cycle towards the primary energy sources power delivery is appropriate, which is computationally lighter, for example, than the forward modeling method. The

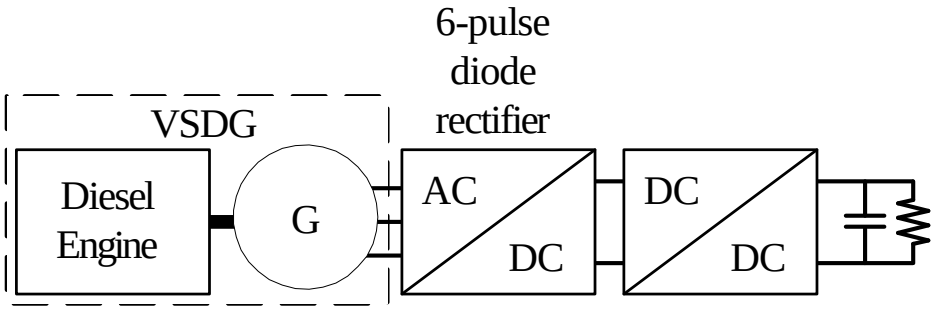

Figure 13: The test setup for the variable speed diesel generator-set plant model identification.

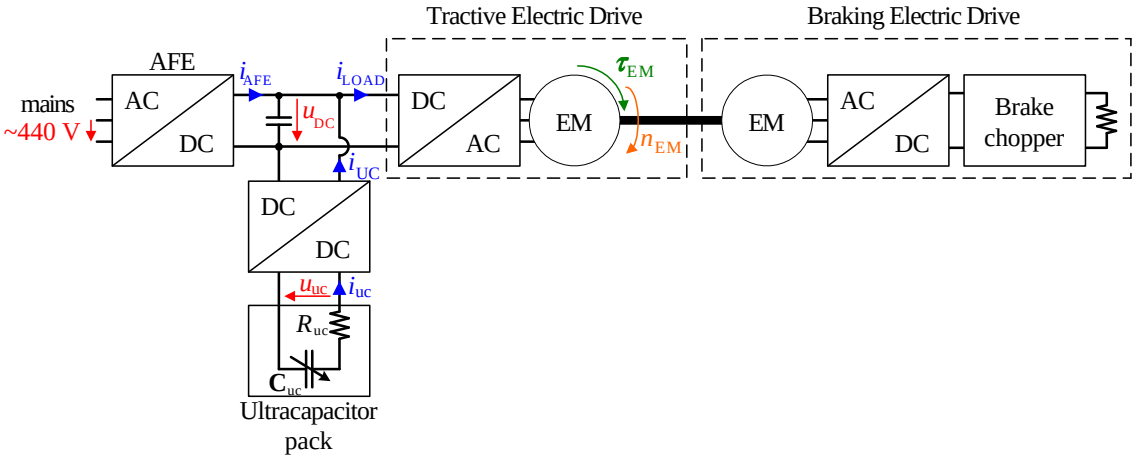

Figure 14: The Hardware-in-the-Loop test setup for validations of the DC-DC converter and the ultracapacitor module plant models.

backward model approach is also known as the wheel-to-engine and the front-to-rear modeling [1]. The differences to the forward modeling are that the backward model lacks "Driver model", "Environmental model", "Tire interface model", and "Traction control algorithms", as the starting point of the proposed model is the load cycle of the existing NRMM.

In the proposed modeling approach, different descriptions for plant models are used, such as static, quasi-static, dynamic, and functional. In this context, the static model or a part of a model refers to one or two dimensional mappings of subsystem behavior. Thus, efficiency mapping of an electric drive or FC output voltage behavior [$u_{\mathrm{fc}} = \mathrm{f}(i_{\mathrm{fc}})$] are considered as static models. The quasi-static definition is used when a model uses a static mapping with some dynamics description, but

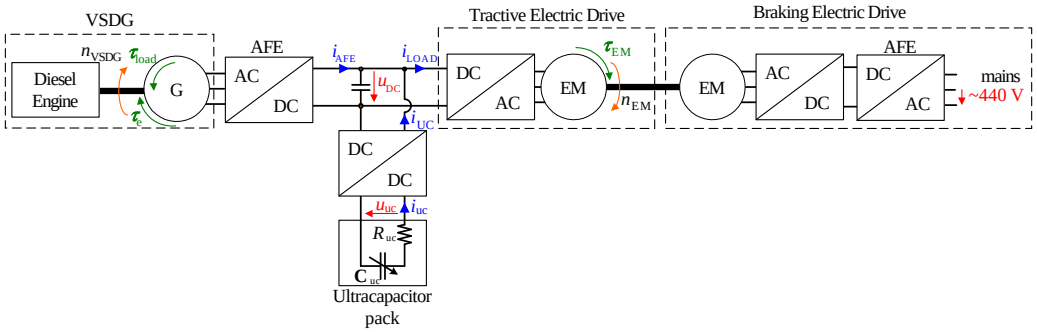

Figure 15: The full UC buffered diesel-electric series-hybrid powertrain Hardware-in-the-Loop test setup.

does not influence the up-stream of calculation direction, i.e., a quasi-static model assumes backward calculation and a dynamic model forward calculation, respectively [50, p. 70]. In the proposed approach, there are quasi-static characteristics in several sub-system models, such as in load power, fuel consumption, and energy losses calculations. The dynamic definition is used when the model influences the up-stream of calculation direction, and thus, is considered as a sub-model of forward calculation [50, p. 70]. This is the case, for instance, with a DC-DC converter model, since it defines an energy storage current, whereas the ES state affects its operation. In this context, the dynamic definition does not consider the accuracy of transients. Eventually, the functional definition is used when a plant model primarily imitates operation of a sub-model, as when an EM is controllable with an inverter.

The system-level simulation speed depends much on the chosen simulation time-step. The time-step of simulations is determined by the fastest dynamically modelled variable, such that the time-step should be smaller than the time-constant of such variable. In this study, the shortest modeled time-constant is τ_{AFE}, which refers to the AFE converter current response time. Therefore, the length of the simulation time-step, i.e. $t_{\mathrm{k}} - t_{\mathrm{k}-1}$, is chosen as 1 ms, where t_{k} refers to a discrete-time sample with an index k. Furthermore, the time-step should be a multiple of one in order to operate with both even and odd time-step long discrete operations, and thus the next possible option for the time-step is 10 ms which is already too long. In addition, the time-step selection gives space for the modeling functional characteristics of plant models.

3.3 Electric Drive Plant Model

In the presented modeling approach, the static electric drive plant model is used if the starting point for simulations is the mechanical load (p_{mech}). Conversely, it is not used if the starting point is the electrical load (p_{LOAD}).

Fig. 16 presents a measured one-quadrant efficiency map of an electric drive [47] for the proposed static electric drive plant model. A measured efficiency map is

used to scale mechanical load to electrical. The efficiency map describes the input and output power relation of an electric drive as functions of speed and torque. This figure illustrates that combined efficiency of an inverter and a traction electric machine, in this case, reaches a 92 % efficiency in a certain operation region.

Realization of the load power scaling can be expressed, as

$$p_{\mathrm{LOAD}} = \begin{cases} p_{\mathrm{mech}} \Big/ \eta_{\mathrm{ED}}(n_{\mathrm{EM}}, \boldsymbol{\tau}_{\mathrm{EM}}), & \text{if} \quad p_{\mathrm{mech}} > 0, \\ p_{\mathrm{mech}} \cdot \eta_{\mathrm{ED}}(n_{\mathrm{EM}}, \boldsymbol{\tau}_{\mathrm{EM}}), & \text{if} \quad p_{\mathrm{mech}} < 0, \end{cases} \tag{1}$$

where power is defined as positive towards the load.

However, the presented one-quadrant efficiency map is well defined only for the motoring mode operation, and mirroring the efficiency map to the generator mode operation affects the load scaling accuracy [50, p. 75]. Thus, a two-quadrant efficiency mapping of an electric drive is a more convenient choice for the static electric drive plant model.

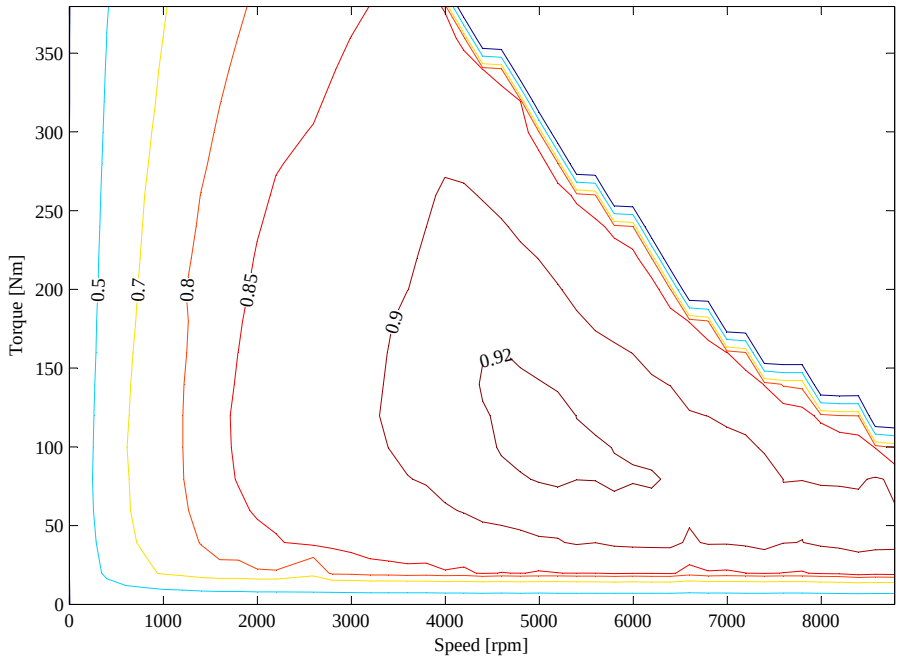

Figure 16: Combined measured efficiency map of Siemens *ELFA 1PV5135-4WS28* traction electric machine and *G650 D44/170/170 M7-1* inverter.

Furthermore, energy losses on the electric drive ($E_{\mathrm{losses\_ED}}$) can be expressed, as

$$E_{\mathrm{losses\_ED}} = \int_0^t (1 - \eta_{\mathrm{ED}}) \cdot p_{\mathrm{mech}} \cdot \mathrm{d}t. \tag{2}$$

In the dynamic modeling approach [52], an electric drive plant model is realized with inverter efficiency mapping, and the dynamic equations of a specific traction motor. However, dynamic modeling of a traction motor is not essential, if the powertrain design concentrates on power transfer from a source to loads, and does not concentrate on the traction control. Furthermore, dynamic modeling of different electric motor types have been introduced in [50, pp. 76-90].

Functionalities of the Electric Drive Plant Model

It is known that the active load can behave as negative resistance. This behavior, in a large-signal meaning, may cause the DC-link voltage to collapse if the load power is not derated. The collapse of the DC-link voltage occurs due to saturated power transfer from energy sources or storages via DC-DC converters to the DC link. The effect can be avoided with the load power deration, which can be expressed, as

$$p_{\mathrm{act}}(t_{\mathrm{k}}) = \begin{cases} p_{\mathrm{ref}}(t_{\mathrm{k}}), & \text{if} \quad u_{\mathrm{DC}}(t_{\mathrm{k-1}}) \geq U_{\mathrm{DC}}^{\mathrm{low}}, \\ p_{\mathrm{ref}}(t_{\mathrm{k}}) \cdot f(u_{\mathrm{DC}}(t_{\mathrm{k-1}})), & \text{if} \quad U_{\mathrm{DC}}^{\mathrm{low}} > u_{\mathrm{DC}}(t_{\mathrm{k-1}}) > U_{\mathrm{DC}}^{\mathrm{min}}, \\ 0, & \text{if} \quad U_{\mathrm{DC}}^{\mathrm{min}} \geq u_{\mathrm{DC}}(t_{\mathrm{k-1}}). \end{cases} \tag{3}$$

In Eq. 3, p_{act} refers to the actual load power, and p_{ref} to the load power reference. In addition, $U_{\mathrm{DC}}^{\mathrm{low}}$ and $U_{\mathrm{DC}}^{\mathrm{min}}$ refer to a region where $f(u_{\mathrm{DC}})$ changes e.g. linearly from 1 to 0. Furthermore, such a deration function can be expressed, as

$$f(u_{\mathrm{DC}}) = \min\left[1, \max\left(0, \left(u_{\mathrm{DC}} - U_{\mathrm{DC}}^{\mathrm{min}}\right) \Big/ \left(U_{\mathrm{DC}}^{\mathrm{low}} - U_{\mathrm{DC}}^{\mathrm{min}}\right)\right)\right]. \tag{4}$$

However, utilization of the proposed functionality in the ED sub-system, changes the approach from static to functional quasi-static in sense of the sub-system input interface and behavior. [50, pp. 70-76]

3.4 DC-DC Converter Plant Model

This section proposes a modeling approach for a non-isolated multiphase interleaved bi-directional DC-DC converter, as in [7], and [47].

The power electronic converters typically achieve very high efficiency values in their best operation area. In this context, a very high efficiency refers to a power conversion with efficiency in the range of 97 % to 98 %. On the contrary, the efficiency of the PE converter may decrease remarkably to between 50 % and 90 %, if an inappropriate operation area is used. This thesis proposes efficiency mapping and a functional description approach for the DC-DC converter modeling, due to the limitations of the chosen simulation time-step (1 ms), and the need for exact full-system efficiency comparisons. The chosen simulation time-step restricts power semiconductor switching events, since modeling of the shortest semiconductor switching periods

would decrease the simulation time-step to a range of 10 μs. Furthermore, a shorter time-step would make a system model unnecessarily complex, and would lead to slower full driving cycle simulation times whose total lengths are in the range of 100 s to several 1000 s.

The efficiency of the DC-DC converter depends on the energy storage current (i_{es}), and the voltage conversion ratio (u_{ratio}) which is defined, as

$$u_{\mathrm{ratio}} = u_{\mathrm{es}}/u_{\mathrm{DC}}. \tag{5}$$

An example of the efficiency mapping of the DC-DC converter during charge mode is presented in Publication IV, and data is given on Appendix A.

The thesis proposes the first-order response function as an approximation of the DC-DC converter current control loop. A comparison of the first-order response behavior to a PI-controlled response is presented in Eq. 6 and in Fig. 17. Furthermore, a PI-controller tuning method and parameters for a comparison are given in Eqs. 7-9, and in Table 1.

$$\frac{i_{\mathrm{es}}}{i_{\mathrm{es,ref}}} = \frac{1}{\tau_{\mathrm{DC/DC}} \cdot \mathrm{s} + 1} \approx \frac{K_{\mathrm{P}} \cdot \mathrm{s} + K_{\mathrm{I}}}{L \cdot \mathrm{s}^2 + (K_{\mathrm{P}} + r_{\mathrm{L}} + r_{\mathrm{es}}) \cdot \mathrm{s} + K_{\mathrm{I}}}. \tag{6}$$

In Eq. 6, K_{P} refers to a proportional coefficient and K_{I} to an integral coefficient of the current PI-controller. In addition, L refers to a choke inductance and r_{L} to a choke resistance of a DC-DC converter, and r_{es} refers to an ES resistance, respectively.

In the comparison the PI-controller parameters are defined, as

$$K_{\mathrm{P}} = \alpha_{\mathrm{c}} \cdot L, \tag{7}$$

$$K_{\mathrm{I}} = \alpha_{\mathrm{c}}^2 \cdot L, \tag{8}$$

where

$$\alpha_{\mathrm{c}} = 2 \cdot \pi \cdot f_{\mathrm{c}}. \tag{9}$$

In Eqs. 7-9, α_{c} refers to the current-controller bandwidth in angular frequency [rad/s], and f_{c} to the bandwidth in frequency [1/s].

Table 1: Parameters for comparison of responses.

$\tau_{\mathrm{DC/DC}}$ [ms]	f_{c} [1/s]	L [mH]	r_{L} [mΩ]	r_{es} [mΩ]
10.0	20.0	1.0	13.5[a]	70.0[b]

[a] An approximate for a choke in low-frequencies. [b] Bases on 1.1 Ω/F for UCs, 500 V potential, and to the datasheet of *BMOD0063 P125* (Maxwell Technologies Inc.).

Fig. 17 illustrates errors between the first-order response and the PI-controlled response. A cumulative error (e_{Σ}) between the first-order response and the PI-controlled case is in range of 0.5 As for the 100 A current transient. For example,

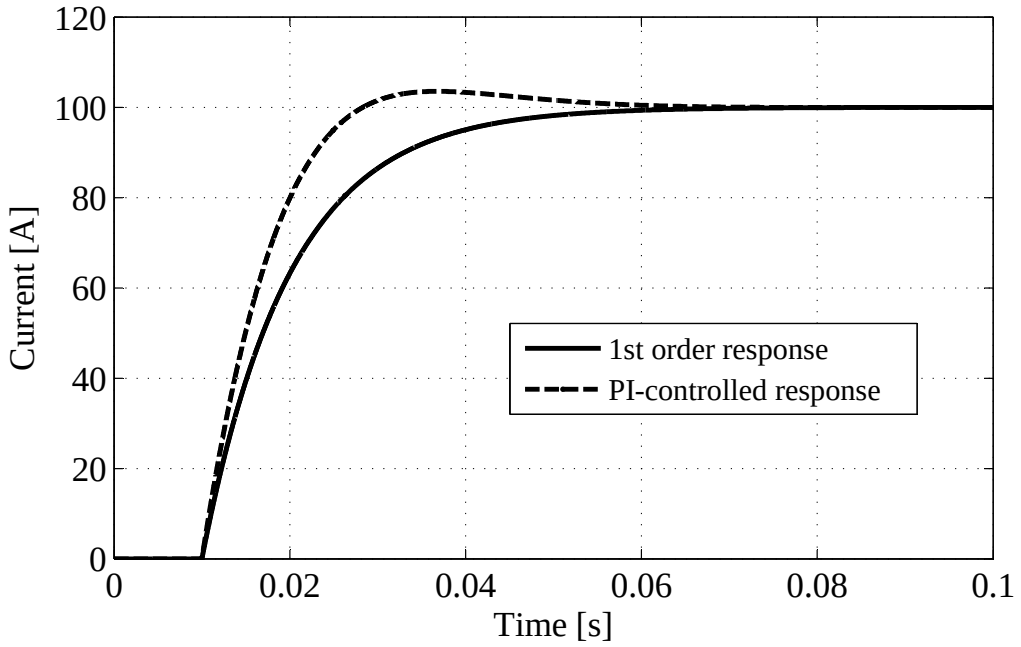

Figure 17: The comparison of the first-order response behavior to the PI-controlled response.

such an error in a transient occurring once in a time-period t would cause a total error to energy transfer, as

$$\frac{\Delta E_{\text{es}}}{E_{\text{es}}} \approx \frac{e_{\Sigma}}{i_{\text{es}} \cdot t} \cdot 100\ [\%]. \tag{10}$$

Eq. 10 results to the total error value between 0.05 % to 5.0 % when t is changed from 0.1 s to 10 s. Thus, the usage of the DC-DC converter highly affects the energy transfer accuracy of the proposed modeling method, in other words, an insignificant error occurs when a converter controls continuously constant powers. Conversely, significant error occurs if the converter transfers transient loads. However, internal controller parameters are not always known by system integrators, and therefore an approximation needs to be made with the described possible existence of an error.

Other essential functionalities of the plant model are minimum and maximum current limits (I_{min}, I_{max}), sub-system level proportional voltage controller, and conduction event of an upper anti-parallel diode.

The proposed approach for the DC-DC converter plant model can be expressed, as

$$i_{\text{ref}} = D \cdot i_{|\text{ref}|}, \qquad \text{when} \quad I_{\text{min}} \leq |D| \cdot i_{|\text{ref}|} \leq I_{\text{max}}, \tag{11}$$

$$i_{\text{es}} = i_{\text{bat}} = i_{\text{uc}} = i_{\text{fc}} = i_{\text{ref}} / (\tau_{\text{DC/DC}} \cdot \text{s} + 1), \tag{12}$$

$$i_{\mathrm{ES}}(t_{\mathrm{k}}) = \begin{cases} i_{\mathrm{es}}(t_{\mathrm{k}}) \cdot \eta_{\mathrm{boost}}(i_{\mathrm{es}}(t_{\mathrm{k-1}}), u_{\mathrm{ratio}}(t_{\mathrm{k-1}})) \cdot u_{\mathrm{ratio}}(t_{\mathrm{k-1}}), & \text{while discharging,} \\ i_{\mathrm{es}}(t_{\mathrm{k}}) / \eta_{\mathrm{buck}}(i_{\mathrm{es}}(t_{\mathrm{k-1}}), u_{\mathrm{ratio}}(t_{\mathrm{k-1}})) \cdot u_{\mathrm{ratio}}(t_{\mathrm{k-1}}), & \text{while charging.} \end{cases} \tag{13}$$

In Eq. 11, D (+1, 0, or −1) refers to current direction of the DC-DC converter. Note that $(t_{\mathrm{k}} - t_{\mathrm{k-1}}) << \tau_{\mathrm{DC/DC}}$.

The modeling approach neglects the exact behavior of converter dynamics, and therefore, it is unclear whether "dynamic model" or "quasi-static model" should be used. However, as described in [50, p. 70], the proposed approach fulfils dynamic description in sense of the interface and influence on adjacent components in the system level modeling.

Furthermore, energy losses on the DC-DC converter ($E_{\mathrm{losses\_DC/DC}}$) can be expressed, as

$$E_{\mathrm{losses\_DC/DC}} = \int_0^t (1 - \eta_{\mathrm{DC/DC}}) \cdot u_{\mathrm{es}} \cdot i_{\mathrm{es}} \cdot \mathrm{d}t. \tag{14}$$

Discussions of Accuracies in DC-DC Converter Efficiency Mapping

The accuracy of the measured efficiency mapping was first discussed in Publication IV. In efficiency measurements, the utilized power analyzer was *Norma D6100* (LEM) with its triaxial shunts for 6 to 300 A current measurements. The measuring accuracy for voltage channels in the frequency range of 0 to 15 Hz are ± (0.15 + 0.03) % for reading and range, respectively. The measuring accuracy for current shunts is ± 0.1 % within a frequency range of 0 to 100 kHz. Furthermore, measurements were taken at 70 kHz sampling frequency, and averaged over 1 s time-period. Table 2 illustrates voltage measurement accuracies depending on the operation point of an energy storage system.

Table 2: Voltage measurement maximum errors in different operation points.

u_{es} reading [V]	u_{es} range [V]	u_{es} error [V]	u_{es} error [%]	u_{DC} reading [V]	u_{DC} range [V]	u_{DC} error [V]	u_{DC} error [%]
200	340	± 0.402	± 0.201	650	670	± 1.176	± 0.181
380	670	± 0.771	± 0.203				

The maximum error of an efficiency measurement $\Delta\eta$ can be calculated with the partial differential equation, as

$$\Delta\eta = \left|\frac{\delta\eta}{\delta u_{\mathrm{out}}}\right| \Delta u_{\mathrm{out}} + \left|\frac{\delta\eta}{\delta i_{\mathrm{out}}}\right| \Delta i_{\mathrm{out}} + \left|\frac{\delta\eta}{\delta u_{\mathrm{in}}}\right| \Delta u_{\mathrm{in}} + \left|\frac{\delta\eta}{\delta i_{\mathrm{in}}}\right| \Delta i_{\mathrm{in}}, \tag{15}$$

where

$$\eta = \frac{u_{\mathrm{out}} \cdot i_{\mathrm{out}}}{u_{\mathrm{in}} \cdot i_{\mathrm{in}}},$$

thus

$$\Delta\eta = \frac{i_{\mathrm{out}}}{u_{\mathrm{in}} \cdot i_{\mathrm{in}}} \Delta u_{\mathrm{out}} + \frac{u_{\mathrm{out}}}{u_{\mathrm{in}} \cdot i_{\mathrm{in}}} \Delta i_{\mathrm{out}} + \frac{u_{\mathrm{out}} \cdot i_{\mathrm{out}}}{u_{\mathrm{in}}^2 \cdot i_{\mathrm{in}}} \Delta u_{\mathrm{in}} + \frac{u_{\mathrm{out}} \cdot i_{\mathrm{out}}}{u_{\mathrm{in}} \cdot i_{\mathrm{in}}^2} \Delta i_{\mathrm{in}}.$$

Table 3 illustrates efficiency measurement accuracies on four operation points. This table utilizes the measured values of current and voltage, and concludes that the total maximum error of the efficiency mapping is in the range $\pm$ 0.47...0.52 %. The total maximum error is a value for a case when all error components cumulate the same direction.

Table 3: Efficiency measurement maximum errors in different operation points.

u_{out} [V]	i_{out} [A]	u_{in} [V]	i_{in} [A]	$\Delta\eta$ [%]
254.8	29.2	650.4	12.2	$\pm$ 0.505
379.7	29.57	650.4	17.99	**$\pm$0.467**
256.7	194.4	650.3	79.5	**$\pm$0.519**
369.3	194.6	650.2	113.3	$\pm$ 0.478

In practise, an efficiency mapping needs a look-up table with a high number of cells, and in this case the introduced efficiency mapping needs a look-up table with 531 cells as for data in Appendix A. Thus, it is common to fit a polynomial function to represent such a data-set as the efficiency mapping. However, the measured efficiency mapping is non-linear, and therefore, introduction of a polynomial function for the efficiency surface creates an RMS error. The introduced error is dependent on the degree of a polynomial function which can be expressed e.g. for the DC-DC converter efficiency, as

$$\begin{aligned}\eta(i_{\text{es}}, u_{\text{ratio}}) \;=\; & p_{00} + p_{10}\cdot i_{\text{es}} + p_{01}\cdot u_{\text{ratio}} \\ & + p_{20}\cdot i_{\text{es}}^2 + p_{11}\cdot i_{\text{es}}\cdot u_{\text{ratio}} + p_{02}\cdot u_{\text{ratio}}^2 \\ & + \ldots \\ & + p_{\text{i0}}\cdot i_{\text{es}}^{\text{i}} + p_{(\text{i}-1)(\text{j}-1)}\cdot i_{\text{es}}^{\text{i}-1}\cdot u_{\text{ratio}}^{\text{j}-1} + p_{(\text{i}-1)(\text{j}-2)}\cdot i_{\text{es}}^{\text{i}-1}\cdot u_{\text{ratio}}^{\text{j}-2} + \ldots \\ & \ldots + p_{(\text{i}-2)(\text{j}-1)}\cdot i_{\text{es}}^{\text{i}-2}\cdot u_{\text{ratio}}^{\text{j}-1} + p_{0\text{j}}\cdot u_{\text{ratio}}^{\text{j}}.\end{aligned} \tag{16}$$

In Eq. 16, p_{ij} refers to a coefficient of a polynomial function, and indexes i and j define the degree of the surface function.

Table 4 illustrates decrease of an RMS error, and increase of a coefficient number, as functions of a surface polynomial degree numbers.

Furthermore, introduced RMS errors change if a polynomial function is defined only for a bounded region where in most operation of a converter occurs. These errors are illustrated in Table 5 within voltage conversion range of 0.3...0.59.

Tables 4 and 5 highlight that an introduced RMS error by a polynomial function is 0.41 % if the whole efficiency surface is estimated. However, an error decreases to 0.078 % if only suitable parts of the mapping are estimated. These values refer to cases with 18 and 12 coefficients for definition of a polynomial function.

To conclude, an efficiency mapping, if measured only once, has the total maximum error of $\pm$ 0.47...0.52 % due to principles of qualitative analysis. In practise, the total error limits would decrease if efficiency measurements would be repeated and quantitative analysis utilized. Furthermore, if the whole efficiency mapping

Table 4: Polynomial fittings for the efficiency surface within u_{ratio} of 0.07 ... 0.59.

RMS error [%]	coefficients	i	j
1.27	3	1	1
1.15	5	2	1
0.92	5	1	2
0.76	6	2	2
0.60	9	2	3
0.55	12	2	4
0.53	15	2	5
0.44	14	3	4
0.41	**18**	**3**	**5**
0.39	20	4	5
0.39	21	5	5

Table 5: Polynomial fittings for the efficiency surface within u_{ratio} of 0.3 ... 0.59.

RMS error [%]	coefficients	i	j
0.59	3	1	1
0.33	5	2	1
0.59	5	1	2
0.33	6	2	2
0.16	9	3	2
0.33	9	2	3
0.078	**12**	**4**	**2**
0.073	15	5	2

would be estimated with a surface polynomial function, then the total maximum error would increase, for instance, to ± 0.9 %, as stated in Table 4, or to ± 0.55...0.6 % (Table 5) if only a bounded area of the mapping is estimated. Thus, in this phase of research it is convenient to use only look-up table based efficiency mapping for the plant model of a DC-DC converter; and if measurements of a DC-DC converter efficiency would be made quantitatively, then, for instance, a surface polynomial function for suitable parts of the mapping could be considered as an option to result in a total maximum error e.g. in the range of ± 0.1 %.

In addition, the average of RMS errors between charge and discharge modes in a specific operation point is ± 0.3 %, when the efficiency data is compared in the range $(i_{\text{es}}, u_{\text{ratio}}) = (30\text{ A}...196\text{ A}, 0.2...0.6)$, and ± 0.2 % when $u_{\text{ratio}} = 0.3...0.6$. Thus, for more accurate energy transfer calculations, there is a need for different mappings of charge and discharge modes and quantitative analysis of efficiency measurements.

Control Interface of the DC-DC Converter Plant Model

The objective of the DC-DC converter is to control the current to the DC link (i_{ES}). However, energy storages have operation restrictions such as a charge for ultracapacitors and batteries, and speed for flywheels.

Specifically for ultracapacitors, there is a need for maximum and minimum voltage operation limits to avoid over-voltage, operation in unsuitable efficiency, and limited power areas. Therefore, a deration is introduced as a limitation for system control to prevent prohibited operation. The deration e.g. for the ultracapacitor pack, based on the voltage u_{uc}, can be expressed, as

$$i_{|\mathrm{ref}|} = \begin{cases} i_{|\mathrm{ref}'|} \cdot f_1(u_{\mathrm{uc}}), & \text{while} \quad \text{discharging}, \\ i_{|\mathrm{ref}'|} \cdot f_2(u_{\mathrm{uc}}), & \text{while} \quad \text{charging}. \end{cases} \tag{17}$$

Functions $f_1(u_{\mathrm{uc}})$ and $f_2(u_{\mathrm{uc}})$ are piecewise determined, for instance, as

$$f_1(u_{\mathrm{uc}}) = \min\Big[1, \max\Big(0, \big(u_{\mathrm{uc}} - U_{\mathrm{uc}}^{\mathrm{min}}\big) \Big/ \big(U_{\mathrm{uc}}^{\mathrm{low}} - U_{\mathrm{uc}}^{\mathrm{min}}\big)\Big)\Big], \tag{18}$$

$$f_2(u_{\mathrm{uc}}) = \min\Big[1, \max\Big(0, \big(U_{\mathrm{uc}}^{\mathrm{max}} - u_{\mathrm{uc}}\big) \Big/ \big(U_{\mathrm{uc}}^{\mathrm{max}} - U_{\mathrm{uc}}^{\mathrm{high}}\big)\Big)\Big]. \tag{19}$$

In Eqs. 18 and 19, $U_{\mathrm{uc}}^{\mathrm{max}}$ and $U_{\mathrm{uc}}^{\mathrm{min}}$ refer to the maximum and minimum voltages of the UC pack, $U_{\mathrm{uc}}^{\mathrm{high}}$ and $U_{\mathrm{uc}}^{\mathrm{low}}$ refer to the ES current limitation threshold high and low voltages, respectively.

Furthermore, a static inversion of the DC-DC converter is needed in order to achieve the objective to control the DC-link current reference $i_{\mathrm{ES}'}$. The static inversion can be expressed, as

$$i_{|\mathrm{ref}'|} = \begin{cases} |i_{\mathrm{ES}'}|/(u_{\mathrm{ratio}} \cdot \eta(i_{|\mathrm{ref}|}, u_{\mathrm{ratio}})), & \text{while} \quad \text{discharging}, \\ |i_{\mathrm{ES}'}| \cdot \eta(i_{|\mathrm{ref}|}, u_{\mathrm{ratio}})/u_{\mathrm{ratio}}, & \text{while} \quad \text{charging}. \end{cases} \tag{20}$$

Eventually, the current control direction D can be concluded based on a sign of the $i_{\mathrm{ES}'}$.

However, the static inversion is not necessarily suitable for the low capacitance intermediate circuits due to the risk of overcompensation. That is the case−specifically, in the proposed indirect primary source power buffering (Section 3.11), since overcompensation confuses the DC-link voltage PI-regulator of the AFE converter. Fig. 18 illustrates the cause for the problem. For instance, when i_{ES} is overcompensated, then u_{DC} becomes higher than its reference, and the AFE converter PI-regulator tries to compensate u_{DC} by transferring power to the primary source.

3.5 Ultracapacitor Pack Plant Model

This section proposes basic approaches for the ultracapacitor pack plant model.

In the basic approaches, the UC pack can be modeled with either constant or variable capacitance, and equivalent series resistance. The mapping of a variable capacitance, as functions of current and voltage, is presented in Publication IV. Furthermore, this study considers R_{uc} as a constant quantity, although it is dependent on temperature and voltage. The advantage of the proposed approaches is computational simplicity.

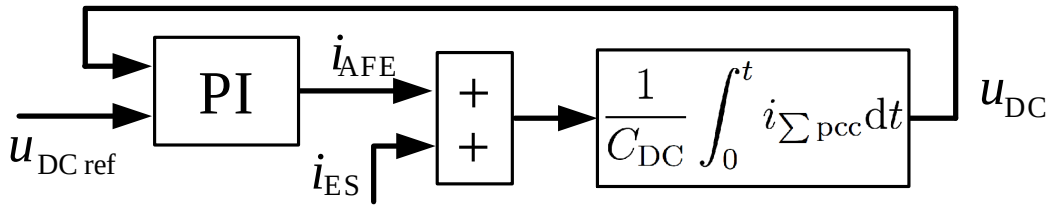

Figure 18: The AFE converter PI-regulator sign changes if i_{ES} is overcompensated.

Furthermore, there exists several electric circuit models for more accurate modeling of an ultracapacitor behavior. However, such models need parameter extraction from experimental tests, and might affect system-level simulation time-steps from operating as intended. For instance, three basic electric circuit models are: the RC parallel branch model, the RC transmission line model, and the RC series-parallel branch model. Fig. 19 illustrates different types of UC electric circuit models. [53]

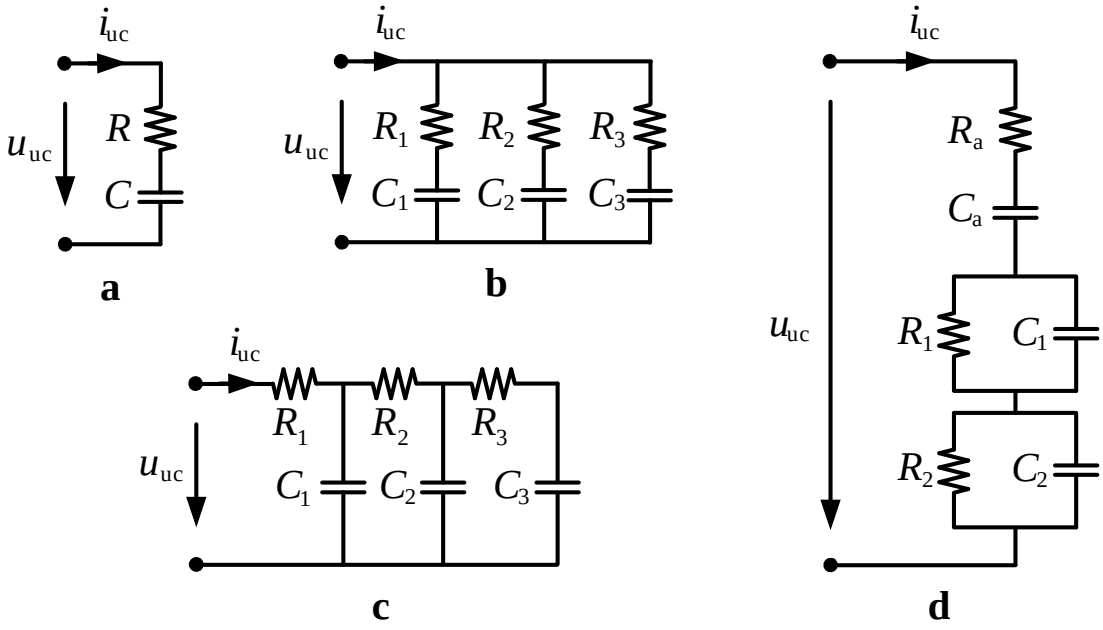

Figure 19: (a) Simple ultracapacitor model, (b) RC parallel branch model, (c) RC transmission line model, (d) RC series-parallel branches model.

In the basic dynamic approach, the UC pack output voltage can be expressed, as

$$u_{\mathrm{uc}} = \frac{1}{C_{\mathrm{uc}}}\int_0^t i_{\mathrm{uc}}\mathrm{d}t - R_{\mathrm{uc}} i_{\mathrm{uc}} + U_{\mathrm{uc\_initial}}. \tag{21}$$

The variable capacitance (as in Publication IV) can be expressed by a fitted polynomial function, as

$$\mathbf{C}_{\mathrm{uc}}(i_{\mathrm{uc}}, u_{\mathrm{uc}}) = p_{00} + p_{10} i_{\mathrm{uc}} + p_{01} u_{\mathrm{uc}}. \tag{22}$$

The polynomial fitting introduces an RMS error of 0.34 F with coefficients: $p_{00} = 14.42$, $p_{10} = -0.006072$, and $p_{01} = 0.01938$, for a *BMOD0018 P390* (17.8 F, 390 V, Maxwell Technologies Inc.) UC module.

Energy losses on the UC pack can be expressed, as

$$E_{\mathrm{losses\_uc}} = R_{\mathrm{uc}} \int_0^t i_{\mathrm{uc}}^2 \mathrm{d}t. \tag{23}$$

Furthermore, energy content for the weight, size, and cost calculations of the UC pack (E_{uc}) is calculated as,

$$E_{\mathrm{uc}} = (1/2) \cdot C_{\mathrm{uc}} \cdot U_{\mathrm{max}}^2, \tag{24}$$

where U_{max} refers to the maximum voltage of the ultracapacitor pack.

The local efficiency [50, p. 114] has been measured in Publication IV for the static modeling of the UC based ES systems. In this context, the static model refers to efficiency mapping, for instance, within a look-up table.

Capacitor Plant Model

Furthermore, the low-capacitance intermediate circuit voltage, i.e. the DC-link voltage, can be expressed, as

$$u_{\mathrm{DC}} = \frac{1}{C_{\mathrm{DC}}} \int_0^t i_{\sum \mathrm{PCC}} \mathrm{d}t - R_{\mathrm{DC}} i_{\sum \mathrm{PCC}} + U_{\mathrm{DC\_initial}}, \tag{25}$$

where C_{DC} refers to the DC-link capacitance, $i_{\sum \mathrm{PCC}}$ refers to the sum current on a point of common coupling, and R_{DC} refers to the equivalent series resistance of DC-link capacitors.

3.6 Battery Pack Plant Model

The modeling of a battery is a very complex procedure and requires a thorough knowledge of electro-chemistry. However, the simulation of complete systems, as the hybrid vehicle powertrains, does not require a high level of precision in electro-chemical phenomenons. Therefore, a generic Li-ion battery model, proposed in [54]−[55], with dynamic behavior was utilized in this research.

In general, there exist three basic types of battery models: experimental, electro-chemical, and electric circuit models. However, only electric circuit models are useful to represent electrical characteristics of batteries. The two basic electric circuit models are: a voltage source in series with an internal resistance, comparable to Fig. 19 (a), and an open-circuit voltage in series with resistance and parallel RC circuits, as in Fig. 19 (d). The second case of models needs a parameter extraction

based on experiments, and thus, in the first phase of the powertrain design the generic battery model derived from the first case is more suitable.

The main feature of the generic battery model is that parameters can be extracted from a manufacturer's discharge curve. On the other hand, the model has several assumptions, which are: the internal resistance is supposed to be constant, charge characteristics are assumed to be the same as for discharge, capacity of the battery is not dependent on current amplitude, temperature has no effect, no self-discharge, and no memory effect [54].

In the generic battery modeling method, the Li-ion battery pack discharge characteristics ($i^* > 0$) is modeled, as

$$u_{\text{bat}}(it, i^*, i_{\text{bat}}) = U_0 - K\frac{Q}{Q - it}i^* - K\frac{Q}{Q - it}it + Ae^{-B \cdot it} - R_{\text{bat}} \cdot i_{\text{bat}}, \tag{26}$$

and charge characteristics ($i^* < 0$), as

$$u_{\text{bat}}(it, i^*, i_{\text{bat}}) = U_0 - K\frac{Q}{it + 0.1 \cdot Q}i^* - K\frac{Q}{Q - it}it + Ae^{-B \cdot it} - R_{\text{bat}} \cdot i_{\text{bat}}. \tag{27}$$

In Eqs. 26 and 27, u_{bat} is non-linear output voltage (V), it is extracted capacity (Ah), i^* is low-frequency current dynamics (A), i_{bat} is battery current (A), U_0 is the maximum voltage value of the linear area (V), K is polarization constant (Ah^{-1}), Q is maximum battery capacity (Ah), A is exponential voltage (V), B is exponential capacity (Ah^{-1}), and R_{bat} is constant ESR (Ω) of the battery pack.

The battery internal resistance depends on several factors, such as state-of-charge, temperature, and age of the battery. Thus, manufacturer data-sheets do not always give any value for battery resistances. For such cases, the study [54] proposes use of an experiment based estimate value for the battery resistance. The proposed resistance is constant and represents the correct resistance in only the measured operation point, and thus includes an error in every other operation point. The battery resistance can be calculated as,

$$R_{\text{bat}} = (1 - \eta_{\text{bat}})\frac{U_{\text{nom}}}{\text{C}}, \tag{28}$$

where η_{bat} refers to the battery efficiency with the nominal battery current C, and U_{nom} is the minimum voltage of the battery packs linear voltage area. This study uses efficiency of 99 % for high-energy batteries. In other words, that means 1 % power losses on the battery pack with the 1C value for the both charge and discharge conditions. In case of a high power battery, the continuous current instead of the nominal current 1C should be used, e.g. 4C. This assumes thermal conduct of power losses for the high power battery pack to be equal with the high energy battery pack.

Energy losses on the battery pack can be expressed, as

$$E_{\text{losses\_bat}} = R_{\text{bat}} \int_0^t i_{\text{bat}}^2 \text{d}t. \tag{29}$$

Energy content (E_{bat}) for the weight, size, and cost calculations of the battery pack is calculated, as

$$E_{\text{bat}} = \frac{U_0 + U_{\text{nom}}}{2}Q. \tag{30}$$

3.7 Active Front-end Converter and Generator Plant Model

This section proposes a functional quasi-static approach for an active front-end converter and generator combination plant model—specifically, for series-hybrid powertrains with a low-capacitance intermediate circuit. A different type of modeling approach comes into question depending on the topology of the hybrid system. For instance, the article [52] proposes a functional method in which converter output current is empirically defined based on speed, field current, and output voltage of a generator, and by field current first-order dynamics, for a hybrid powertrain with a passive battery in an intermediate circuit.

The active-front-end converter, i.e. an inverter in a voltage control mode, and generator sub-system model can be realized with the efficiency mapping in the torque-speed plane, and with the DC-link voltage PI-regulator which controls the DC current to the intermediate circuit. The energy losses of power conversion from the DC link to the engine shaft are taken into consideration as in Eqs. 1 and 2, and Fig. 16 presents. The DC-link voltage regulator type, and parameter values, affect the realization of power transfer from the primary source.

In general, the plant model contains the DC-link voltage PI-regulator, and feed-forward value ($i_{\mathrm{f-f}}$) which is the difference between the load current, and the energy storage system current, as $i_{\mathrm{f-f}} = i_{\mathrm{LOAD}} - i_{\mathrm{ES}}$. Furthermore, the error term (e_{u}) for the PI-regulator is defined, as $e_{\mathrm{u}} = u_{\mathrm{DCref}} - u_{\mathrm{DC}}$.

The current reference before the limitations ($i_{\mathrm{ref}'}$) is defined, as

$$i_{\mathrm{ref}'}(t_{\mathrm{k}}) = i_{\mathrm{f-f}} + K_{\mathrm{P}} e_{\mathrm{u}} + K_{\mathrm{I}} \int_0^t \left[e_{\mathrm{u}} + K_{\mathrm{aw}} (i_{\mathrm{ref}}(t_{\mathrm{k-1}}) - i_{\mathrm{ref}'}(t_{\mathrm{k-1}})) \right] \mathrm{d}t, \tag{31}$$

where t_{k} refers to time index, K_{P} and K_{I} are PI-regulator coefficients, and K_{aw} is the anti-windup coefficient.

The current reference $i_{\mathrm{ref}'}$ must be limited to prevent stall and overspeed of the engine. Therefore, the current reference with the maximum and minimum limitations, is defined as

$$i_{\mathrm{ref}}(t_{\mathrm{k}}) = \begin{cases} i_{\mathrm{max}}(n_{\mathrm{G}}), & \text{if} \quad i_{\mathrm{ref}'}(t_{\mathrm{k}}) \geq i_{\mathrm{max}}(n_{\mathrm{G}}), \\ i_{\mathrm{ref}'}(t_{\mathrm{k}}), & \text{if} \quad i_{\mathrm{max}}(n_{\mathrm{G}}) > i_{\mathrm{ref}'}(t_{\mathrm{k}}) > i_{\mathrm{min}}(n_{\mathrm{G}}), \\ i_{\mathrm{min}}(n_{\mathrm{G}}), & \text{if} \quad i_{\mathrm{min}}(n_{\mathrm{G}}) \geq i_{\mathrm{ref}'}(t_{\mathrm{k}}), \end{cases} \tag{32}$$

where $i_{\mathrm{max}}(n_{\mathrm{G}})$ refers to a dynamic maximum current limit, and $i_{\mathrm{min}}(n_{\mathrm{G}})$ to a dynamic minimum current limit, respectively.

The study proposes a definition for the dynamic maximum current limit, as

$$i_{\mathrm{max}}(n_{\mathrm{G}}) = \vec{I}_{\mathrm{max}}(n_{\mathrm{G}}) - P(n_{\mathrm{G_{ref}}} - n_{\mathrm{G}}). \tag{33}$$

The dynamic maximum current limit consist of the static maximum DC current vector [$\vec{I}_{\mathrm{max}}(n_{\mathrm{G}})$] which is derived from the maximum power curve of the engine [$P_{\mathrm{e}}(n_{\mathrm{e}})$]. The load limitation decreases proportionally if the generator speed (n_{G}) fails to meet the reference ($n_{\mathrm{G_{ref}}}$). The purpose of the dynamic maximum current limit is to prevent stalling of the engine.

The dynamic minimum current limit [$i_{\min}(n_{\mathrm{G}})$] is proposed to be defined, as

$$i_{\min}(n_{\mathrm{G}}) = P(n_{\mathrm{G}} - n_{\mathrm{G_{max}}}), \tag{34}$$

where $n_{\mathrm{G_{max}}}$ refers to the maximum allowed speed, and the P-regulator limits the regenerative load to the engine shaft, and thus, prevents overspeed. The dynamic minimum current limit can have a value between zero to $I_{\min}$ which is a negative value, and derived based on the maximum parasitic shaft load. It is used to enable the regenerative braking to the engine shaft when the DC-link voltage arises over the reference, and the engine speed is low enough for the regenerative braking.

Eventually, the DC-link current of the AFE converter is defined, as

$$i_{\mathrm{AFE}} = i_{\mathrm{ref}}/(\tau_{\mathrm{AFE}} \cdot \mathrm{s} + 1), \tag{35}$$

where τ_{AFE} refers to the current control delay time-constant of the AFE-converter-generator combination. Therefore, the load torque $\boldsymbol{\tau}_{\mathrm{load}}$ for the engine can be derived from the DC-link current (i_{AFE}), as

$$\boldsymbol{\tau}_{\mathrm{load}} = \begin{cases} i_{\mathrm{AFE}} \cdot u_{\mathrm{DC}}/(\eta_{\mathrm{ED}}(n_{\mathrm{G}}, \boldsymbol{\tau}_{\mathrm{req}}) \cdot \omega_{\mathrm{G}}), & \text{if} \quad i_{\mathrm{AFE}} \geq 0, \\ i_{\mathrm{AFE}} \cdot u_{\mathrm{DC}} \cdot \eta_{\mathrm{ED}}(n_{\mathrm{G}}, \boldsymbol{\tau}_{\mathrm{req}})/\omega_{\mathrm{G}}, & \text{if} \quad 0 > i_{\mathrm{AFE}}. \end{cases} \tag{36}$$

In Eq. 36, $\eta_{\mathrm{ED}}(n_{\mathrm{G}}, \boldsymbol{\tau}_{\mathrm{req}})$ refers to the efficiency mapping of the electric drive, which consists of the permanent magnet machine and the AFE converter. ω_{G} refers to the generator angular speed, and $\boldsymbol{\tau}_{\mathrm{req}}$ refers to the requested torque, as $\boldsymbol{\tau}_{\mathrm{req}} = i_{\mathrm{AFE}} \cdot u_{\mathrm{DC}}/\omega_{\mathrm{G}}$.

Energy losses on the AFE-converter-generator combination ($E_{\mathrm{losses\_AFE\_gen}}$) can be calculated, as

$$E_{\mathrm{losses\_AFE\_gen}} = \int_0^t (1 - \eta_{\mathrm{ED}}) \cdot u_{\mathrm{DC}} \cdot i_{\mathrm{AFE}} \cdot \mathrm{d}t. \tag{37}$$

3.8 Diesel Engine Plant Model

The diesel engine modeling is an essential part of the powertrain design. The engine modeling can be very complicated due to the complexity and various subsystems of an engine [52]. However, more generalized fuel consumption mapping based engine models exist in order to decrease the amount of model parameters and their complexity.

In 1986, Tsai and Goyal presented a fuel consumption mapping based quasi-linear dynamic diesel engine model, which is suitable for testing the adequacy of its controller under all operating conditions [56]. Such a model is based on knowledge of output torque as functions of fuel injection and speed.

Although, the quasi-linear dynamic model is known and its construction is relatively simple, more simplified first and second-order torque response functions are proposed for modeling of diesel engine dynamics. In such cases, fuel consumption is derived based on experimental mapping of fuel consumption with different torque and speed [49]. The advantage of the latest model is that torque response and

fuel consumption mapping can be experimentally tested for any engine, with no knowledge needed of fuel injection dependency to output torque.

However, as this study has not achieved any experimental data of fuel consumption or emissions, use is made of a modified model based on the proposal and parameters presented by Tsai and Goyal [56].

In general, the diesel engine plant model includes Newton's second law for rotational dynamics, as

$$\omega_{\mathrm{VSDG}} = \frac{1}{J_{\mathrm{tot}}} \int_0^t (\boldsymbol{\tau}_{\mathrm{e}} - \boldsymbol{\tau}_{\mathrm{load}}) \cdot \mathrm{d}t + \omega_{\mathrm{VSDG\_initial}}. \tag{38}$$

In Eq. 38, J_{tot} refers to the inertia of the VSDG shaft, which includes both the inertia of the diesel engine and generator. The ω_{VSDG} refers to the angular speed of the variable speed diesel generator-set.

The VSDG is controlled with the speed reference and therefore, the sub-system PI-controller for speed is defined, as

$$e_{\mathrm{n}} = n_{\mathrm{VSDG\_ref}} - n_{\mathrm{VSDG}}, \tag{39}$$

$$\dot{m}' = K_{\mathrm{P}} \cdot e_{\mathrm{n}} + K_{\mathrm{I}} \int_0^t e_{\mathrm{n}} \cdot \mathrm{d}t, \tag{40}$$

$$\dot{m} = \begin{cases} \vec{M}_{\max}(n_{\mathrm{VSDG}}), & \text{if} \quad \dot{m}' \geq \vec{M}_{\max}(n_{\mathrm{VSDG}}), \\ \dot{m}', & \text{if} \quad \vec{M}_{\max}(n_{\mathrm{VSDG}}) > \dot{m}' > 0, \\ 0, & \text{if} \quad 0 \geq \dot{m}'. \end{cases} \tag{41}$$

In Eqs. 39-41, e_{n} refers to the error term of the speed reference and the actual value, $\dot{m}'$ refers to the unlimited fuel injection output value of the speed PI-controller, and $\vec{M}_{\max}(n_{\mathrm{VSDG}})$ refers to the maximum fuel quantity vector as a function of the VSDG speed. The $\vec{M}_{\max}(n_{\mathrm{VSDG}})$ defines the maximum torque curve for the diesel engine. The output $\dot{m}$ is the actual fuel quantity value [mg/stroke]. Furthermore, the model uses the speed reference change rate limiter.

The fuel consumption m of the engine can be expressed, as

$$m = K \int_0^t n_{\mathrm{VSDG}} \cdot \dot{m} \cdot \mathrm{d}t, \tag{42}$$

where the coefficient K is *piston amount / stroke cycle*.

The engine torque follows a nonlinear torque function of injected fuel and engine speed with a time delay which varies in length by the time between successive engine firings. The torque response delay for the four-stroke cycle, the six-cylinder high speed engine, can be expressed, as

$$\boldsymbol{\tau}_{\mathrm{e}} = \frac{\boldsymbol{\tau}_{\mathrm{map}}}{0.65 \cdot \tau_{\mathrm{e}} \cdot \mathrm{s} + 1}, \tag{43}$$

where the time-constant τ_{e} is given, as

$$\tau_{\mathrm{e}} = 20/n_{\mathrm{VSDG}}. \tag{44}$$

Fig. 20 presents the torque data ($\boldsymbol{\tau}_{\text{map}}$) for the turbocharged diesel engine as a mapping of speed, and fuel quantity per stroke. The torque mapping presented in this figure refers to the brake torque which is the indicated torque minus the parasitic losses of the water pump, fuel pump, oil pump, valve train, air filter, muffler, piston rings, and crank bearings [56].

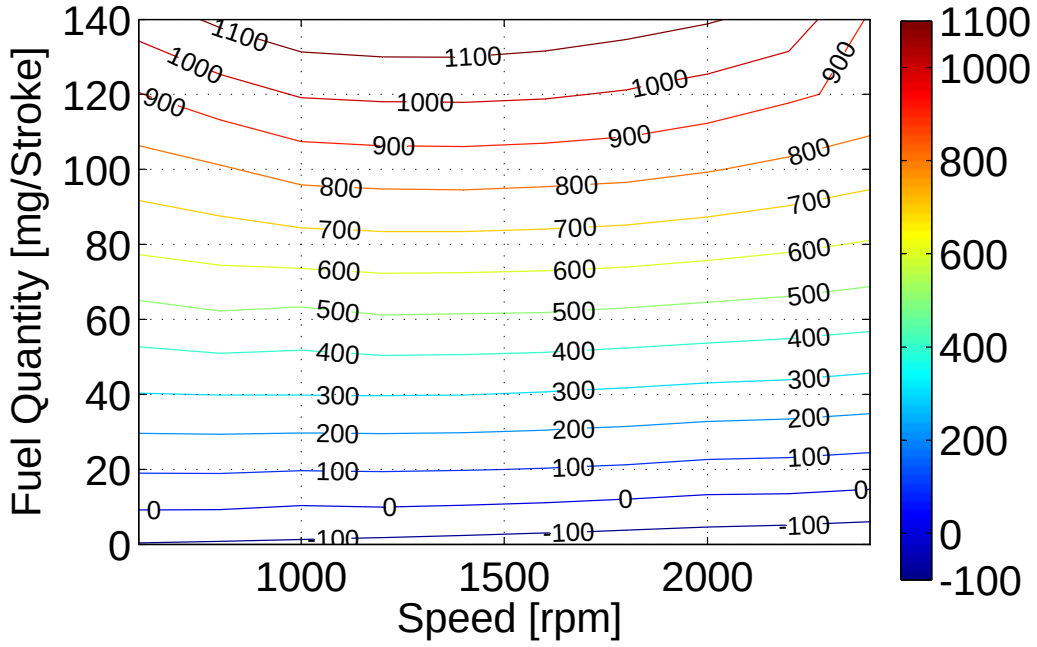

Figure 20: The torque data as a mapping of fuel quantity and speed of the engine.

The torque mapping can be expressed with a polynomial function of speed and fuel quantity. The surface fitting can be done with a surface fitting tool to achieve coefficients for the surface function, as

$$\begin{aligned}\boldsymbol{\tau}_{\text{map}}(n_{\text{VSDG}}, \dot{m}) \;=\; & p_{00} + p_{10}\cdot n_{\text{VSDG}} + p_{01}\cdot \dot{m} \\ & + p_{20}\cdot n_{\text{VSDG}}^2 + p_{11}\cdot n_{\text{VSDG}}\cdot \dot{m} + p_{02}\cdot \dot{m}^2 \\ & + p_{30}\cdot n_{\text{VSDG}}^3 + p_{21}\cdot n_{\text{VSDG}}^2\cdot \dot{m} + p_{12}\cdot n_{\text{VSDG}}\cdot \dot{m}^2 .\end{aligned} \tag{45}$$

The coefficients of Eq. 45 are presented in Table 6. The RMS error of the surface function respect to data is 13.4 Nm.

3.9 Fuel Cell Source Plant Model

This study proposes use of a static *ui*-curve model for a FC-stack. The FC-stack is modeled as a current-dependent voltage source, hence $u_{\text{fc}} = \text{f}(i_{\text{fc}})$, where u_{fc} is

Table 6: Coefficients of the torque data surface polynomial function.

Coefficients	Value
p_{00}	-39.28
p_{10}	-0.06109
p_{01}	6.34
p_{20}	-1.092e^{-5}
p_{11}	5.736e^{-3}
p_{02}	-3.565e^{-3}
p_{30}	6.791e^{-9}
p_{21}	-1.602e^{-6}
p_{12}	-7.244e^{-6}

the output voltage of the FC-stack, and i_{fc} is the FC-stack current, as well as the low-voltage side current of the boost converter. The fuel cell stack *ui*-curve imitates the output voltage, i.e., the polarization curve of a typical commercial fuel cell stack, which is usually given by a FC manufacturer. The easiest way to imitate the polarization curve is with a look-up table.

Furthermore, hydrogen and oxygen consumption calculation is needed for the powertrain design. The rates of conversion (utilizations) of hydrogen (u_{fH_2}) and oxygen (u_{fO_2}) are determined in [55], as

$$u_{\text{fH}_2} = \frac{n^{\text{r}}_{\text{H}_2}}{n^{\text{in}}_{\text{H}_2}} = \frac{R \cdot T \cdot N \cdot i_{\text{fc}}}{Z \cdot F \cdot P_{\text{fuel}} \cdot V_{lpm(\text{fuel})} \cdot x\%}, \tag{46}$$

$$u_{\text{fO}_2} = \frac{n^{\text{r}}_{\text{O}_2}}{n^{\text{in}}_{\text{O}_2}} = \frac{R \cdot T \cdot N \cdot i_{\text{fc}}}{2 \cdot Z \cdot F \cdot P_{\text{air}} \cdot V_{lpm(\text{air})} \cdot y\%}. \tag{47}$$

In the above equations, $n^{\text{r}}_{\text{H}_2}$ is relieved hydrogen, and $n^{\text{in}}_{\text{H}_2}$ hydrogen input, as well as $n^{\text{r}}_{\text{O}_2}$ refers to relieved air, and $n^{\text{in}}_{\text{O}_2}$ to air input, respectively. In addition, R is the gas constant and equals to 8.3145 J/(mol·K), T is operation temperature (K), and N is number of cells. Parameter Z refers to the number of moving electrons per mole of fuel, i.e., 2 for a single hydrogen−oxygen fuel cell reaction ($\text{H}_2 + \text{O}_2 \rightarrow \text{H}_2\text{O}$), but for multiple reactions it becomes an experimental decimal value (e.g. 2.967 for PEM FC - 6 kW - 45 V in Simulink™ models [55]). Furthermore, F is the Faraday constant and equals to 96485 A·s/mol, P_{fuel} is fuel absolute supply pressure (atm), P_{air} is air absolute supply pressure (atm), $V_{lpm(\text{fuel})}$ is fuel flow rate (l/min), $V_{lpm(\text{air})}$ is air flow rate (l/min), x is percentage of hydrogen in the fuel, and y is percentage of oxygen in the oxidant.

Dynamic modeling of a FC system have been discussed in articles [57], and [58]. The article [57] proposes a dynamic model extended by a static current-voltage description with temperature dependence. The proposed model captures the first-order physical phenomenas, and furthermore, it can be identified from electrical terminal measurements. The article [58] discusses in depth the modeling of a FC-system in general, and proposes a model which is targeted at the development of the PEM FC real-time control systems. However, such dynamic models are considered too complex for energy management and system design of the entire powertrain.

3.10 Brake Resistor and Chopper Plant Model

This section proposes a functional modeling approach of a brake resistor and chopper, i.e. a braking unit, in a low capacitance intermediate circuit. Based on the knowledge attained, modeling of a braking-unit in vehicle powertrain systems has not been recently discussed in the literature. However, other possibilities to model the braking-unit would be electrical circuit modeling with either ideal or non-ideal power semiconductor switches, or also by functionally with a constant voltage operation limit.

In any case, the braking-unit modeling method should not affect a system level simulation time-step, and thus, electrical circuit modeling is unviable. A simpler method with only a constant voltage operation limit would assume unlimited power capabilities in a braking-unit, and furthermore, it adds a computational discontinuity due to a state change in intermediate circuit variable. Thus, the proposed functional modeling method can be considered to be the most suitable method.

The braking unit is used to prevent excessive increase of voltage in low capacitance intermediate circuits. Functionality of the braking unit can be described, e.g. as

$$i_{\mathrm{BRK}}(t_{\mathrm{k}}) = \begin{cases} K_{\mathrm{P}} \cdot e_{\mathrm{u}}(t_{\mathrm{k-1}}) + K_{\mathrm{I}} \int_0^t e_{\mathrm{u}}(t_{\mathrm{k-1}}) \cdot \mathrm{d}t, & \text{if} \quad u_{\mathrm{DC}}(t_{\mathrm{k-1}}) > U_{\mathrm{DC}}^{\mathrm{brake}} \\ 0, & \text{if} \quad U_{\mathrm{DC}}^{\mathrm{brake}} \geq u_{\mathrm{DC}}(t_{\mathrm{k-1}}). \end{cases} \tag{48}$$

In Eq. 48, i_{BRK} refers to braking unit current, e_{u} refers to voltage error between $U_{\mathrm{DC}}^{\mathrm{brake}}$ and u_{DC}, as well as K_{P} and K_{I} are due to functional modeling of a braking unit. Furthermore, a power limitation saturates excessive values of i_{BRK}.

3.11 Energy Management Algorithm in the Hybrid Control Mode Validation

This section proposes an indirect primary source power buffering method for use in the active ultracapacitor buffered diesel series-hybrid powertrains. The method was used for validations of plant models in Publication III. The indirect power buffering, in this context, means the low capacitance intermediate circuit regulation with the AFE converter, while the DC-DC converter filters the load. On the contrary, the direct power buffering refers to the low capacitance intermediate circuit regulation with the DC-DC converter, while the primary source is controlled based on the averaged load.

A scheme of the proposed series-hybrid powertrain energy management is presented in Fig. 21. The control signals and actual values are the speed reference (n_{ref}) for the VSDG electronic control unit, the DC-link voltage reference for the AFE converter ($u_{\mathrm{DC\_ref}}$), the actual UC pack voltage (u_{uc}), the actual DC-link voltage (u_{DC}), the current reference ($i_{|\mathrm{ref}|}$) and direction (D) for the DC-DC converter, as well as the actual load power (p_{LOAD}).

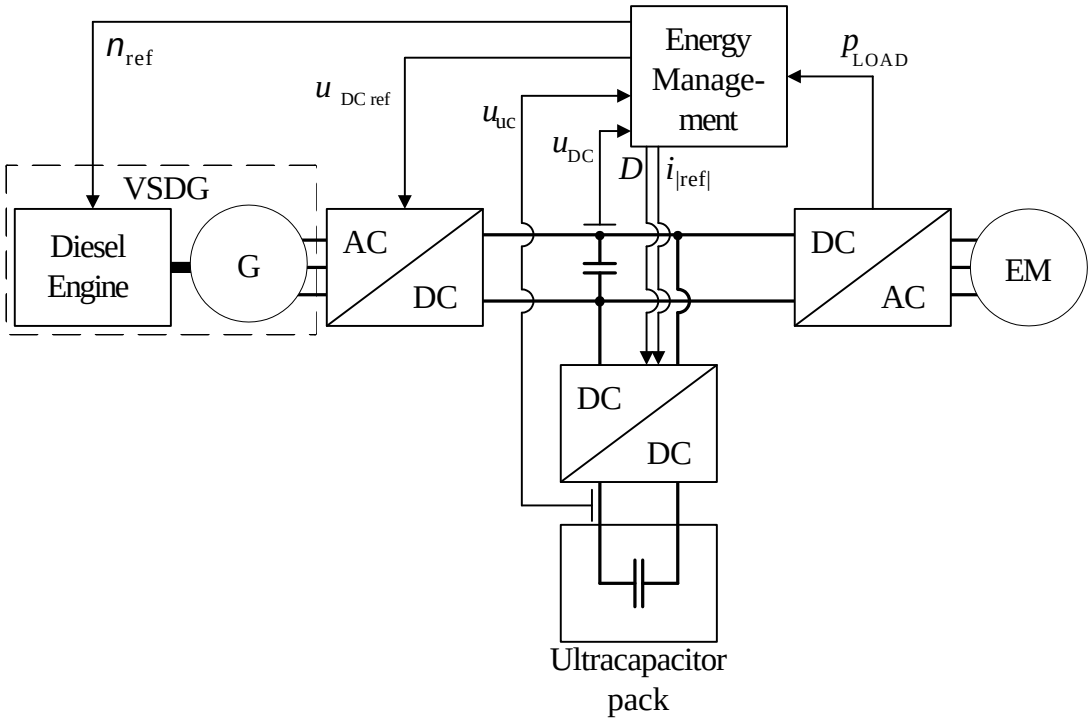

Figure 21: The energy management hierarchy of the series-hybrid powertrain with the ultracapacitor pack for power buffering.

The Energy Storage System Control in the Series-Hybrid Powertrain

In general, the energy storage system control design can be started on the energy storage system current to the DC link (i_{ES}), since the DC-link current relation to the energy storage current can be expressed as in Eq. 20. The energy storage system control depends on the whole powertrain control strategy and therefore, one general solution does not exist.

The ES System Control in the Plant Model Validation Experiment

This sub-section presents the energy management algorithm which was used in the ES system Hardware-in-the-Loop experiments.

The energy management algorithm has two parallel regulators. First, the P-regulator from DC-link voltage, as

$$i_{\mathrm{ES}'\_1} = P(u_{\mathrm{DC\_ref}} - u_{\mathrm{DC}}). \tag{49}$$

Second, the filter structure based on coefficients ($b_0 ... b_{\mathrm{n}}$) of a moving average function with values $1/(n+1)$, i.e. a discrete-time finite impulse response (FIR) filter. The study uses a 20-second averaging period with 0.1 s time-steps. The output of the

FIR filter is, as

$$p_{\mathrm{FIR}}(t_{\mathrm{k}}) = \sum_{t_{\mathrm{i}}=t_{\mathrm{k-n-1}}}^{t_{\mathrm{n}}=t_{\mathrm{k}}} [p_{\mathrm{LOAD}}(t_{\mathrm{k}})/(n+1)] \tag{50}$$

$$u_{\mathrm{FIR}}(t_{\mathrm{k}}) = 2 - \frac{p_{\mathrm{FIR}}(t_{\mathrm{k}})}{P_{\mathrm{MAX}}},$$

where t_{k} refers to a discrete time-step between initial t_{i} and ending t_{n} values, and furthermore, P_{MAX} refers to the tuning parameter of the energy management algorithm which is, e.g., 2...3 times the maximum primary source power. The output of the FIR filter is multiplied with the power reference for the primary source (u_{P}) which in the validation case is expressed, as

$$u_{\mathrm{P}}(t_{\mathrm{k}}) = P_{\mathrm{MAX}}\left(1 - \frac{u_{\mathrm{uc}}(t_{\mathrm{k}})}{U_{\mathrm{max}}}\right). \tag{51}$$

Furthermore, the filter output (p_{filter}) is piecewise determined, as

$$p_{\mathrm{filter}}(t_{\mathrm{k}}) = \begin{cases} u_{\mathrm{FIR}}(t_{\mathrm{k}}) \cdot u_{\mathrm{P}}(t_{\mathrm{k}}), & \text{if } u_{\mathrm{FIR}}(t_{\mathrm{k}}) \cdot u_{\mathrm{P}}(t_{\mathrm{k}}) > 0, \\ 0, & \text{if } 0 \geq u_{\mathrm{FIR}}(t_{\mathrm{k}}) \cdot u_{\mathrm{P}}(t_{\mathrm{k}}). \end{cases} \tag{52}$$

This prevents the negative output of the filter. Therefore, all regenerative load power is included in the filter output and subtracted from the actual load power of the DC link. The power regulator output is, as

$$i_{\mathrm{ES'\_2}} = \frac{p_{\mathrm{LOAD}} - p_{\mathrm{filter}}}{u_{\mathrm{DC}}}. \tag{53}$$

Thus, the ES system current reference on the DC-link voltage potential can be expressed, as

$$i_{\mathrm{ES'}} = i_{\mathrm{ES'\_1}} + i_{\mathrm{ES'\_2}}. \tag{54}$$

The sign of $i_{\mathrm{ES'}}$ determines the current control direction D.

The stability of the ES system control algorithm can be studied by deriving the $i_{\mathrm{ES'}}$ with all its inputs. The ES system current reference space on a static state is presented in Fig. 22 with the values $u_{\mathrm{DC\_ref}}$ 650 V, u_{DC} 600 V...700 V, P-regulator coefficient of 2, and p_{LOAD} between P_{MAX} to $-P_{\mathrm{MAX}}$ (100 kW...−100 kW). The static current reference space is the worst case in the sense of the filter output, since the maximum output occurs only if the maximum input lasts long enough.

The current reference space shows how parallel regulators affect the ES system current. With the high load, the full energy storage voltage, and the low DC-link voltage, the ES system gets the highest positive reference. On the contrary, the highest negative reference is given with the low ES voltage, the high regenerative load, and the high DC-link voltage. The positive linear function, described in Eq. 52, makes impossible negative output values of the filter and therefore, the negative load power weights the current reference towards negative values. The power buffering is performed based on the load power level and the ES voltage with the weighting depended on the actual DC-link voltage.

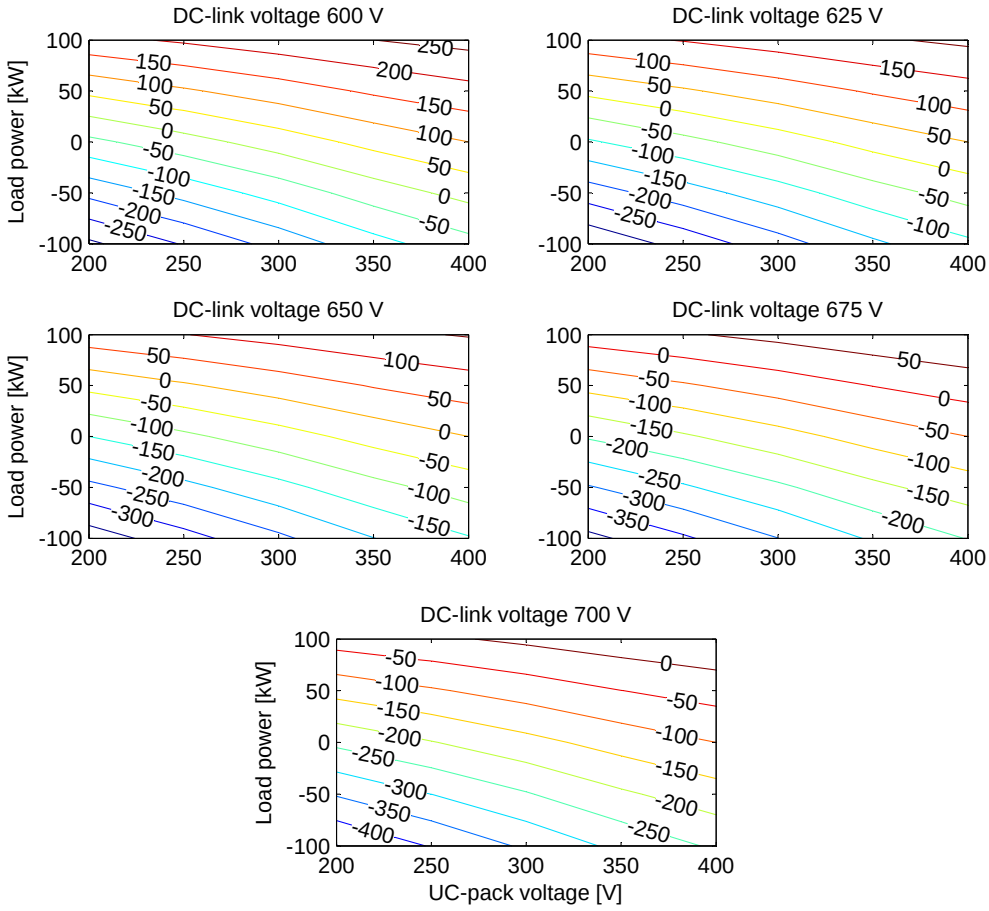

Figure 22: The static ES system current reference ($i_{\mathrm{ES}'}$) space presented in 5 piecewise charts with all inputs.

The Rule-Based Speed Control for the VSDG in the Series-Hybrid Powertrain

The variable speed diesel generator-set can be forced to operate on the minimum fuel consumption per kilowatt hour area, with the co-operation of the VSDG speed control, and the AFE converter control, as discussed in [59]. The rule-based speed control for the VSDG can be expressed, e.g. as

$$n_{\mathrm{e\_ref}} = \begin{cases} n_{\mathrm{e\_max}}, & \text{if} \quad p_{\mathrm{AFE}} > P_{\mathrm{lim\_max}}, \\ \vdots & \vdots \\ n_{\mathrm{e\_1}}, & \text{if} \quad P_{\mathrm{lim\_2}} > p_{\mathrm{AFE}} > P_{\mathrm{lim\_1}} + P_{\mathrm{hyst}}, \\ n_{\mathrm{e\_idle}}, & \text{if} \quad P_{\mathrm{lim\_1}} \geq p_{\mathrm{AFE}}, \end{cases} \tag{55}$$

which defines engine speed references depending on its load. In Eq. 55; $n_{\mathrm{e\_idle}}$, $n_{\mathrm{e\_1}}$, …, $n_{\mathrm{e\_max}}$ refer to different speed references for the engine; $P_{\mathrm{lim\_1}}$, $P_{\mathrm{lim\_2}}$, …,

$P_{\text{lim\_max}}$ refer to different power limits between speed reference transitions; P_{hyst} refers to the hysteresis between power transition limits; and p_{AFE} refers to the AFE converter power, as $i_{\text{AFE}} \cdot u_{\text{DC}}$. Simulated Fig. 23 illustrates the operation areas where the VSDG operation can be forced. Crowded operation point areas represent specific static speed $(n_{\text{e\_idle}}, n_{\text{e\_1}}, ..., n_{\text{e\_max}})$ values, and scattered operation points are due to transitions between static speed states.

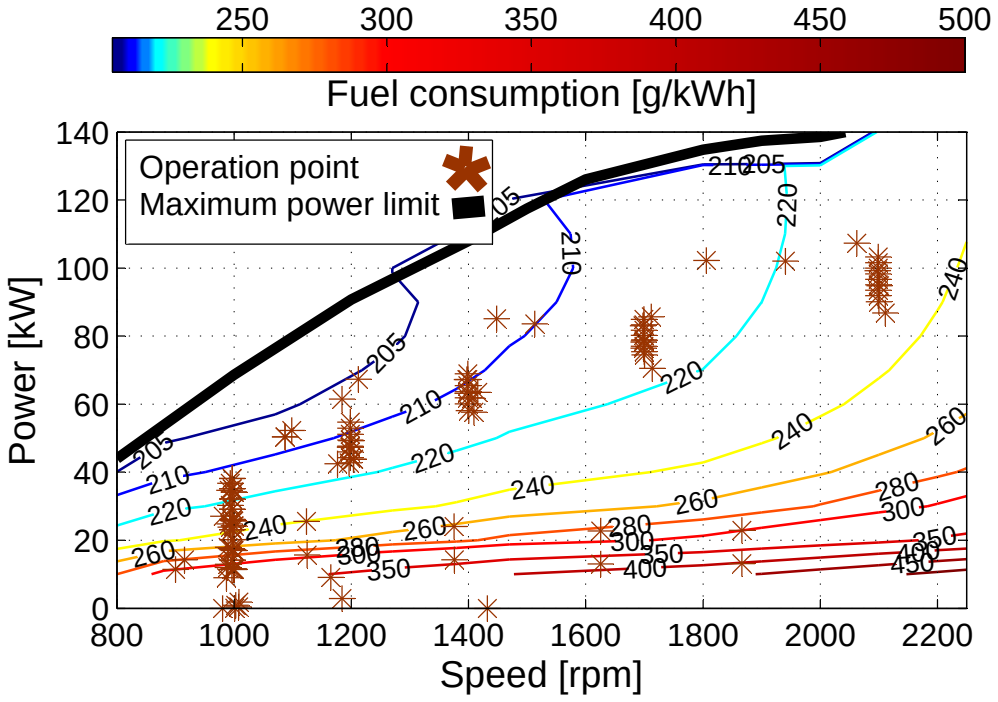

Figure 23: Operation points of the diesel engine in the variable speed use on the fuel consumption map.

The proposed rule-based speed control for an engine is not suitable for all types of loading. For instance, an engine might overload due to an abrupt high load step. Such a load can occur in a vehicle suddenly stopping and re-starting traction while already moving. On the other hand, the proposed engine speed control is suitable for loading which is ramped up during a longer time-period. Fig. 24 illustrates changes of operation areas with the proposed rule-based speed controller for an engine. This figure shows how static speed states are changed with high torque values to higher speeds, and, on the contrary, with low or regenerative torque values to lower speeds.

The context of the proposed speed control is based on an idea of using an engine with predetermined constant speeds on the low fuel consumption area, rather than using an engine with continuously varying speed as proposed in Publication II. The engine plant model speed transition accuracies are studied in Publication III, and reviewed in Section 4.3.

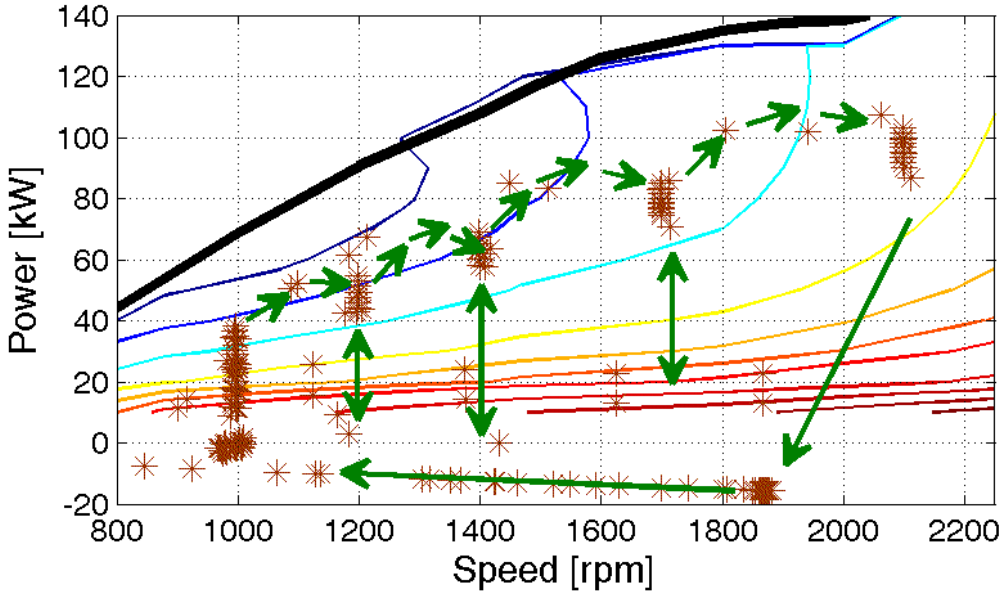

Figure 24: Operation principle of the proposed rule-based speed control of an engine.

3.12 Cumulative maximum errors of the proposed modeling method

The target of the proposed modeling method is to provide a feasible way to design a powertrain for a specific use. System-level plant models together enable design of powertrain energy management algorithms. However, there is a need for a full powertrain modeling error analysis in order to have a proper estimate of the designed EMS affect to fuel consumption and other characteristics. Thus, this sub-section concentrates on modeling and model parameter extraction accuracies for the diesel-electric powertrain with an active UC buffering.

Generally, the maximum error of a variable can be calculated with the partial differential equation, as

$$\Delta F = \left|\frac{\delta F}{\delta x_1}\right|\Delta x_1 + \left|\frac{\delta F}{\delta x_2}\right|\Delta x_2 \ldots + \left|\frac{\delta F}{\delta x_\mathrm{n}}\right|\Delta x_\mathrm{n}, \tag{56}$$

where F refers to the function of the variable, x_n refers to the n^{th} factor of the function F, and Δx_n to an error value for the n^{th} factor.

Therefore, in order to have an accurate fuel consumption modeling result, as $\Delta\dot{m}$, the proposed model is piecewise differentiated in relation to all changing parameters. Strictly speaking, the presented accuracy analysis considers only the static-state accuracies, and neglects accuracies in transients. The target to concentrate on the static accuracy gives an assumption that all errors for variables controlled with an integral term become equal to a measurement error.

Depending on the starting point of the simulations, the static error analysis

begins either on p_{mech} or p_{LOAD}. When the starting point is chosen at p_{mech}, then speed and torque of traction motors are considered to be known accurately. However, p_{LOAD} is considered to be known if the starting point is on an intermediate circuit side.

The accuracy of an electric drive efficiency mapping η_{ED} can be derived, as

$$\Delta\eta_{\mathrm{ED}} = \left|\frac{\delta\eta_{\mathrm{ED}}}{\delta\boldsymbol{\tau}_{\mathrm{EM}}}\right|\Delta\boldsymbol{\tau}_{\mathrm{EM}} + \left|\frac{\delta\eta_{\mathrm{ED}}}{\delta\omega_{\mathrm{EM}}}\right|\Delta\omega_{\mathrm{EM}} + \left|\frac{\delta\eta_{\mathrm{ED}}}{\delta u_{\mathrm{in}}}\right|\Delta u_{\mathrm{in}} + \left|\frac{\delta\eta_{\mathrm{ED}}}{\delta i_{\mathrm{in}}}\right|\Delta i_{\mathrm{in}}, \tag{57}$$

where

$$\eta_{\mathrm{ED}} = \frac{\boldsymbol{\tau}_{\mathrm{EM}} \cdot \omega_{\mathrm{EM}}}{u_{\mathrm{in}} \cdot i_{\mathrm{in}}},$$

thus

$$\Delta\eta_{\mathrm{ED}} = \frac{\omega_{\mathrm{EM}}}{u_{\mathrm{in}} \cdot i_{\mathrm{in}}}\Delta\boldsymbol{\tau}_{\mathrm{EM}} + \frac{\boldsymbol{\tau}_{\mathrm{EM}}}{u_{\mathrm{in}} \cdot i_{\mathrm{in}}}\Delta\omega_{\mathrm{EM}} + \frac{\boldsymbol{\tau}_{\mathrm{EM}} \cdot \omega_{\mathrm{EM}}}{u_{\mathrm{in}}^2 \cdot i_{\mathrm{in}}}\Delta u_{\mathrm{in}} + \frac{\boldsymbol{\tau}_{\mathrm{EM}} \cdot \omega_{\mathrm{EM}}}{u_{\mathrm{in}} \cdot i_{\mathrm{in}}^2}\Delta i_{\mathrm{in}}.$$

Table 7 gives accuracies for the efficiency mapping sensors. The accuracy of torque sensor is a datasheet value of *Dataflex 42/1000* (KTR), accuracies of tachometer speed measurements are given in [60], and electrical measurement accuracies are based on *Norma D6100* (LEM) datasheets.

Table 7: Measurement sensor accuracies for efficiency mapping of an electric drive.

$\boldsymbol{\tau}_{\mathrm{EM}}$ error [Nm]	n error at 30 rpm [%]	n error at 3000 rpm [%]	u_{in} error at 650 V [%]	i_{in} error [%]
± 5	± 0.025	± 0.05	± 0.181	± 0.1

Thus, efficiency mapping measurement accuracies are illustrated in Table 8 for low speed (30 rpm) with 1.0 kW shaft power, and for high speed (3000 rpm) with 100 kW shaft power.

Table 8: Efficiency mapping accuracies of an electric drive with low and high speeds, and motoring as well as regenerative powers.

$\boldsymbol{\tau}_{\mathrm{EM}}$ [Nm]	ω_{EM} [rad/s]	u_{in} [V]	i_{in} [A]	$\Delta\eta_{\mathrm{ED}}$ [%]
+ 318.3	+ 3.141	+ 650	+ 7.692	± 0.375
− 318.3	+ 3.141	+ 650	− 0.308	± **9.38**
+ 318.3	+ 314.1	+ 650	+ 181	± 1.62
− 318.3	+ 314.1	+ 650	− 130.8	± 2.24

Maximum errors of efficiency mapping remain high, due to a high error in torque measurement which covers ∼ 83 % of the maximum error, cf. with Eq. 57 and values

of Tables 7 and 8. The worst presented error in efficiency mapping accuracies, i.e. ± 9.38 %, refers to the case when low mechanical power is transferred to the intermediate circuit. However, the impact of the high error with low powers is small to the full cycle cumulative error value due to the fact that cumulation of small powers results to small energies. In other words, more dominant maximum error value examples during full drive cycle analysis are e.g. ± 1.62 % and ± 2.24 %.

Furthermore, cumulative error in an electric drive energy losses calculation is,

$$\Delta E_{\text{losses\_ED}} = \int_0^t \Delta\eta_{\text{ED}} \cdot p_{\text{mech}} \mathrm{d}t, \tag{58}$$

and thus, integral of $\Delta\eta_{\text{ED}}$ determines directly error percentage in $E_{\text{losses\_ED}}$.

Then, the accuracy of p_{LOAD} is described, as

$$\Delta p_{\text{LOAD}} = \left|\frac{\delta p_{\text{LOAD}}}{\delta \eta_{\text{ED}}}\right| \Delta\eta_{\text{ED}} = \begin{cases} p_{\text{mech}} \cdot \Delta\eta_{\text{ED}} \Big/ \eta_{\text{ED}}^2, & \text{if} \quad p_{\text{mech}} > 0, \\ p_{\text{mech}} \cdot \Delta\eta_{\text{ED}}, & \text{if} \quad p_{\text{mech}} < 0. \end{cases} \tag{59}$$

Accuracy of p_{LOAD} with motoring and regenerating powers, and both, 1.0 kW power at low speed, and 100 kW power at high speed, are given in Table 9. The results illustrate that absolute error values of the p_{LOAD} are dependent on the p_{mech} magnitude, and therefore, relative errors change depending on the sign of the load power.

Table 9: Accuracy of p_{LOAD} when the starting point of modeling is mechanical power.

p_{mech} [kW]	p_{LOAD} [kW]	Δp_{LOAD} [W]	$\Delta p_{\text{LOAD}}/p_{\text{LOAD}}$ [%]
+ 1.0[a]	+ 5.0	± 93.8	± 1.88
− 1.0[a]	− 0.20	± 93.8	± **46.9**
+ 100[b]	+ 118	± 2240	± 1.90
− 100[b]	− 85.0	± 2240	± 2.63

[a] At 30 rpm, [b] at 3000 rpm.

The worst presented relative error value ($\Delta p_{\text{LOAD}}/p_{\text{LOAD}}$) is high (± 46.9 %), as the absolute error deriving from efficiency mapping is high in contrast to p_{LOAD}. However, the relative error with low power has a minor impact on the full cycle cumulative error value in which error values close to the nominal power are dominant.

Then, as the intermediate circuit voltage is controlled with the PI-regulator, thus the actual value of u_{DC} is a constant. Therefore, the static error of $\Delta i_{\text{LOAD}}/i_{\text{LOAD}}$ equals to $\Delta p_{\text{LOAD}}/p_{\text{LOAD}}$. Furthermore, the PI-regulator ensures that,

$$i_{\text{LOAD}} = i_{\text{ES}} + i_{\text{AFE}}, \tag{60}$$

in the static-state, and thus, the energy storage system current i_{ES} needs to be solved. Figure 25 illustrates error paths which exist in the considered system. The

primary sources of error in simulations are efficiency mappings η_{ED} and $\eta_{\mathrm{DC/DC}}$, as well as measurements i_{es}, u_{uc}, and u_{DC}.

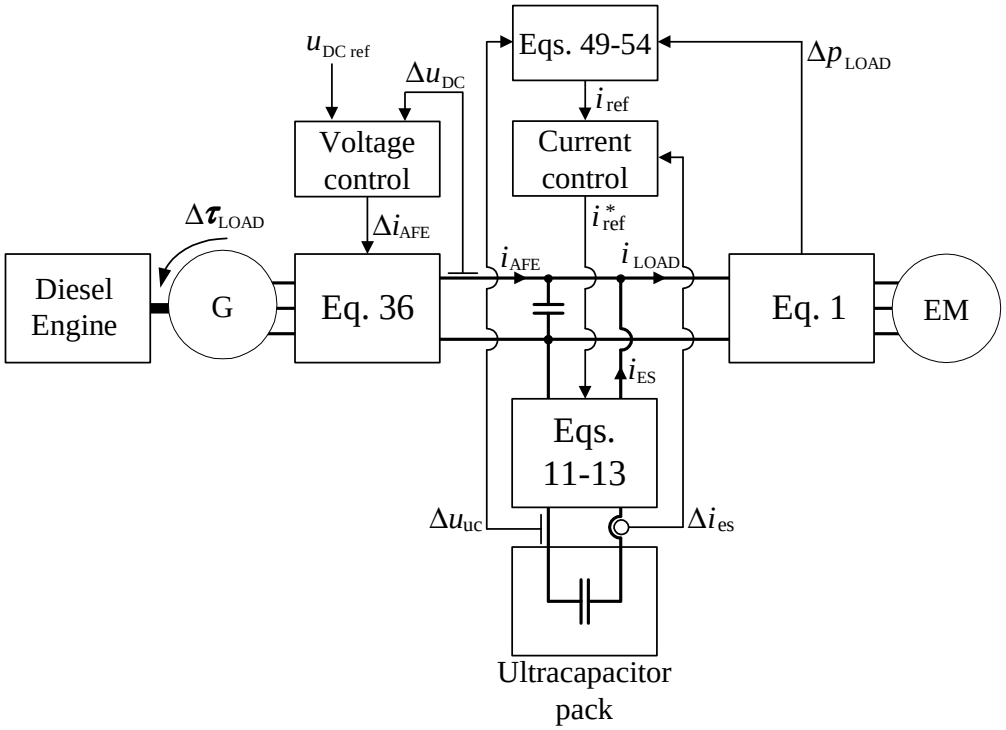

Figure 25: Error paths of the model-based design for the diesel-electric powertrain with an active UC buffering.

The accuracy of the energy storage system current is dependent on i_{es}, u_{es}, u_{DC}, and $\eta_{\mathrm{DC/DC}}$, as

$$\Delta i_{\mathrm{ES}} = \left|\frac{\delta i_{\mathrm{ES}}}{\delta i_{\mathrm{es}}}\right| \Delta i_{\mathrm{es}} + \left|\frac{\delta i_{\mathrm{ES}}}{\delta u_{\mathrm{es}}}\right| \Delta u_{\mathrm{es}} + \left|\frac{\delta i_{\mathrm{ES}}}{\delta u_{\mathrm{DC}}}\right| \Delta u_{\mathrm{DC}} + \left|\frac{\delta i_{\mathrm{ES}}}{\delta \eta_{\mathrm{DC/DC}}}\right| \Delta \eta_{\mathrm{DC/DC}}. \tag{61}$$

Therefore, the accuracy Δi_{ES} can be written, while discharging, as

$$\frac{u_{\mathrm{es}} \cdot \eta_{\mathrm{boost}}}{u_{\mathrm{DC}}} \Delta i_{\mathrm{es}} + \frac{i_{\mathrm{es}} \cdot \eta_{\mathrm{boost}}}{u_{\mathrm{DC}}} \Delta u_{\mathrm{es}} + \frac{u_{\mathrm{es}} \cdot i_{\mathrm{es}} \cdot \eta_{\mathrm{boost}}}{u^2_{\mathrm{DC}}} \Delta u_{\mathrm{DC}} + \frac{u_{\mathrm{es}} \cdot i_{\mathrm{es}}}{u_{\mathrm{DC}}} \Delta \eta_{\mathrm{boost}}, \tag{62}$$

and while charging, as

$$\frac{u_{\mathrm{es}}}{u_{\mathrm{DC}} \cdot \eta_{\mathrm{buck}}} \Delta i_{\mathrm{es}} + \frac{i_{\mathrm{es}}}{u_{\mathrm{DC}} \cdot \eta_{\mathrm{buck}}} \Delta u_{\mathrm{es}} + \frac{u_{\mathrm{es}} \cdot i_{\mathrm{es}}}{u^2_{\mathrm{DC}} \cdot \eta_{\mathrm{buck}}} \Delta u_{\mathrm{DC}} + \frac{u_{\mathrm{es}} \cdot i_{\mathrm{es}}}{u_{\mathrm{DC}} \cdot \eta^2_{\mathrm{buck}}} \Delta \eta_{\mathrm{buck}}.$$

In Eqs. 62, known error values are Δu_{es}, Δu_{DC}, $\Delta \eta_{\mathrm{boost}}$, and $\Delta \eta_{\mathrm{buck}}$. Accuracies of Δu_{es} and Δu_{DC} are considered to equal the overall accuracy of the voltage transducer

(Δu_{meas}) *AV100-750* (LEM), which changes from ± 0.7 % to ± 1.7 % at nominal voltage of 750 V depending on the considered temperature range, either constant +25 °C, or −40…+85 °C. The accuracies of efficiency mappings were derived in Section 3.4 to ± 0.5 % with look-up table data, and to ± 0.9 % based on a polynomial function. The accuracies of efficiency mappings do not consider temperature dependencies in any means. The unknown Δi_{es} is dependent on control algorithms, as described in Section 3.11. Furthermore, the Δu_{es} is a function of i_{es}, and thus errors have a cross-coupling. Therefore, Δu_{es} is simplified to the neighbourhood of u_{es} together with the overall measurement accuracy Δu_{meas}, as

$$\Delta u_{\mathrm{es}} = \Delta u_{\mathrm{uc}} = \Delta u_{\mathrm{uc1}} + \Delta u_{\mathrm{uc2}} = R_{\mathrm{uc}} \cdot \Delta i_{\mathrm{es}} + \Delta u_{\mathrm{meas}}, \tag{63}$$

and the integral part of Eq. 21 determines charge-discharge frequency error, as

$$\Delta d = \frac{(1/C_{\mathrm{uc}}) \cdot \int_0^t \Delta i_{\mathrm{es}} \mathrm{d}t}{2 \cdot (U_{\mathrm{max}} - U_{\mathrm{min}})}. \tag{64}$$

Thus, the error value Δi_{es} determines errors in energy storage voltage, and charge-discharge frequency.

Moreover, energy storage voltage affects to Δi_{es} due to feedback in control algorithms. However, the effect of Δu_{uc1} on Δi_{es}, cannot be taken into consideration, because of an existing algebraic loop. Thus, error Δi_{es} is considered to accumulate measurement accuracies of variables u_{es}, p_{LOAD}, and error Δi_{meas} in the converter current PI-control. The error in u_{DC} is neglected. The error analysis considers the accuracy of current measurement (Δi_{meas}) to equal with the overall accuracy of the current transducer *CT 50-T* (LEM), which is ± 0.1 % at nominal current of 50 A within temperature range of −25…+70 °C. Therefore, Δi_{es} is determined, as

$$\Delta i_{\mathrm{es}} = \left| \frac{\delta i_{\mathrm{es}}}{\delta u_{\mathrm{uc}}} \right| \Delta u_{\mathrm{uc}} + \left| \frac{\delta i_{\mathrm{es}}}{\delta p_{\mathrm{LOAD}}} \right| \Delta p_{\mathrm{LOAD}} + \Delta i_{\mathrm{meas}}. \tag{65}$$

In Eq. 65, the first partial derivative in respect of u_{uc} can be derived, as

$$\left| \frac{\delta i_{\mathrm{es}}}{\delta u_{\mathrm{uc}}} \right| \Delta u_{\mathrm{uc}} = \left| \frac{\delta [P \cdot (u_{\mathrm{DC\_ref}} - u_{\mathrm{DC}}) \cdot u_{\mathrm{DC}}/u_{\mathrm{uc}} + (p_{\mathrm{LOAD}} - p_{\mathrm{filter}})/u_{\mathrm{uc}}]}{\delta u_{\mathrm{uc}}} \right| \Delta u_{\mathrm{uc}},$$

in which the difference of $u_{\mathrm{DC\_ref}}$ and u_{DC} becomes zero, and the parallel controller, as

$$\left| \frac{p_{\mathrm{LOAD}}}{u_{\mathrm{uc}}^2} - \left(2 \cdot P_{\mathrm{MAX}} - \sum_{t_{\mathrm{i}}=t_{\mathrm{k-n-1}}}^{t_{\mathrm{n}}=t_{\mathrm{k}}} [p_{\mathrm{LOAD}}(t_{\mathrm{k}})/(n+1)] \right) \Big/ u_{\mathrm{uc}}^2 \right| \Delta u_{\mathrm{uc}}.$$

Then, the partial derivative in respect of load power gives,

$$\left| \frac{\left[p_{\mathrm{LOAD}}(t_{\mathrm{k}}) + \sum_{t_{\mathrm{k-n-1}}}^{t_{\mathrm{k}}} [p_{\mathrm{LOAD}}(t_{\mathrm{k}})/(n+1)] \cdot (1 - u_{\mathrm{uc}}/U_{\mathrm{max}}) \right] \Big/ u_{\mathrm{uc}}}{\delta p_{\mathrm{LOAD}}} \right| \Delta p_{\mathrm{LOAD}},$$

$$= \frac{\Delta p_{\mathrm{LOAD}}(t_{\mathrm{k}}) + \sum_{t_{\mathrm{k-n-1}}}^{t_{\mathrm{k}}} [\Delta p_{\mathrm{LOAD}}(t_{\mathrm{k}})/(n+1)] \cdot (1 - u_{\mathrm{uc}}/U_{\max})}{u_{\mathrm{uc}}}.$$

Therefore, Table 10 illustrates energy storage current error values depending on considered error sources. Eight different operation points with variance in p_{LOAD} value, power direction and energy storage voltage is used to give an overview of variance in error values. Five different error values for each of the operation points are presented, which refer to different error sources as: $\Delta i_{\mathrm{es1}}/i_{\mathrm{es}}$ considers $\Delta u_{\mathrm{uc}} = 0.7$ % and $\Delta p_{\mathrm{LOAD}} = 0.0$ %, $\Delta i_{\mathrm{es2}}/i_{\mathrm{es}}$ considers $\Delta u_{\mathrm{uc}} = 1.7$ % and $\Delta p_{\mathrm{LOAD}} = 0.0$ %, $\Delta i_{\mathrm{es3}}/i_{\mathrm{es}}$ considers $\Delta u_{\mathrm{uc}} = 0.0$ % and $\Delta p_{\mathrm{LOAD}} =$ Table 9, $\Delta i_{\mathrm{es4}}/i_{\mathrm{es}}$ considers $\Delta u_{\mathrm{uc}} = 0.7$ % and $\Delta p_{\mathrm{LOAD}} =$ Table 9, and $\Delta i_{\mathrm{es5}}/i_{\mathrm{es}}$ considers $\Delta u_{\mathrm{uc}} = 1.7$ % and $\Delta p_{\mathrm{LOAD}} =$ Table 9. In all cases, Δi_{meas} is considered to be 0.1 %.

The results of Table 10 show five different cases with different assumptions of the present situation. Case 1 refers to either the system modeling beginning from the intermediate circuit load (p_{LOAD}), or control error in the real system in which Δp_{LOAD} is measured accurately. The temperature is assumed to be +25 °C. In such a case, i_{es} error at a high load is in range of ± 0.52 %, and with a low load at ± 53 %. Case no. 2 is equal to Case 1 except that an assumption of temperature is changed to −40…+85 °C. In Case 2, comparable error values are ± 1.1 % with high, and ± 130 % with low-loads, respectively. Case no. 3 assumes errors of p_{LOAD} will be realized due to inaccuracies in the efficiency mapping of an electric drive. However, energy storage voltage measurement is considered to be ideal. In the third case, i_{es} error values vary within ± 4.8 % with high and low-loads, respectively. The fourth case assumes all measurement errors to realize in +25 °C ambient temperature, and thus, error values at a high load is in range of ± 5.3 % and with a low load at ± 58 %. The fifth case is similar to Case 4 with a difference in the ambient temperature range which is −40…+85 °C. Then, error values were within ± 5.9 %, and ± 134 %, respectively. The results show that an error may be significant at low loads, but decreases remarkably when high loads are transferred. In the worst error cases (bold font with red color), the regenerative power magnitude is negligible, i.e. − 0.2 kW, which is not possibly transferred to the ES system at all. Therefore, a realistic i_{es} maximum error with low loads is in range of ± 53… 134 %, and with high loads in the range of ± 0.35… 5.9 %. Furthermore, as stated before, high error values with low loads have a small impact on the full cycle cumulative error value in which error values close to the nominal power are dominant.

The moving average in Eq. 65, approx. halves ramp-up p_{LOAD} signals, and passes the long-time constant p_{LOAD} signals by multiplying those with a coefficient of one. The assumption of a ramp-up p_{LOAD} refers to acceleration of a vehicle from zero speed, and the period of constant power refers to acceleration or deceleration of vehicle with some initial speed. Table 10 presents error values referring to the long-time constant p_{LOAD} case. Furthermore, it is assumed that half of the positive load power is taken from the ES system and half from the primary source. On the contrary, all the regenerative power is considered to be charged to the ES system. An effect of this assumption can be seen in the differences between motoring and

regenerating i_{es} accuracies with high loads, for example, regenerative error values are smaller. In addition, this consideration assumes U_{max} to be 390 V, and U_{min} to 200 V, respectively.

Table 10: Energy storage current accuracies.

p_{LOAD} [kW]	u_{uc} [V]	i_{es} [A]	$\Delta i_{es1}/i_{es}$ [%]	$\Delta i_{es2}/i_{es}$ [%]	$\Delta i_{es3}/i_{es}$ [%]	$\Delta i_{es4}/i_{es}$ [%]	$\Delta i_{es5}/i_{es}$ [%]
+ 5.0	390	+ 6.4	± 53	± 130	± 3.9	± 57	± 133
+ 5.0	295	+ 8.5	± 53	± 130	± 4.8	± 58	± 134
− 0.2	200	− 1.0	**± 700**	**± 1700**	**± 70**	**± 770**	**± 1770**
− 0.2	295	− 0.70	**± 700**	**± 1700**	**± 60**	**± 760**	**± 1760**
+ 118	390	+ 150	± 0.52	± 1.1	± 3.9	± 4.3	± 4.9
+ 118	295	+ 200	± 0.52	± 1.1	± 4.8	± 5.3	± 5.9
− 85	200	− 430	± 0.35	± 0.7	± 4.0	± 4.3	± 4.6
− 85	295	− 290	± 0.35	± 0.7	± 3.4	± 3.6	± 4.0

Energy storage voltage maximum error based on Eq. 63 and Table 10 becomes ± 1.4 V... 3.3 V, for an UC module with capacitance of 17.8 F, R_{uc} of 65 mΩ, and U_{max} of 390 V. In Publication III, Hardware-in-the-Loop experiments were compared with simulations, and ± 1.0 V... 3.0 V accuracy in mean values were reached. The lower voltage error value refers to modeling with a variable capacitance, and the higher error to constant capacitance, respectively. It can be noticed that experimented mean error values are within the theoretically calculated maximum error value of ES voltage.

Then, the error of ES system current on the intermediate circuit as functions of Δi_{es}, Δu_{es}, Δu_{DC}, and $\Delta \eta_{DC/DC}$, described in Eq. 62, can be calculated. Furthermore, the error of AFE converter current is the sum of the load current and ES system current errors. The results are presented in Table 11 with two different cases, when Δi_{es} uses the values of Cases 1 and 4 from Table 10, u_{DC} is 650 V with accuracy of Δu_{meas}, and $\Delta \eta_{DC/DC}$ is ± 0.5 %.

Maximum error values in Table 11 refer to cases in which all partial errors are realized with their maximum values in the same direction. The minimum values refer to cases where the system loading were considered to be electrical, and the maximum values refer to mechanical starting points of the modeling, respectively. Furthermore, ambient temperature have been assumed to +25 °C. Considered error sources are efficiency mapping of an electric drive, ES current and voltage measurement errors for control of the ES system. In addition, this assessment included the DC-DC converter plant-model realization inaccuracies consisting of maximum errors in ES current and voltage, DC-link voltage, and efficiency mapping of the DC-DC converter. Resulted values are pessimistic, and for more descriptive error values the quantitative analysis should be used.

Furthermore, the highest error values in Tables 10 and 11 (bold font with red color) can be neglected, because such small powers are most likely not delivered through an ES system. In practice, auxiliary loads in the intermediate circuit are

Table 11: Energy storage system current Δi_{ES} and AFE converter current Δi_{AFE} accuracies on the intermediate circuit.

u_{uc} [V]	i_{es} [A]	$\eta_{\mathrm{DC/DC}}$ [a] [%]	$\Delta i_{\mathrm{es}}/i_{\mathrm{es}}$ [b] [%]	$\Delta i_{\mathrm{ES}}/i_{\mathrm{ES}}$ [b] [%]	$\Delta i_{\mathrm{AFE}}/i_{\mathrm{AFE}}$ [b] [%]
390	+ 6.4	95.6	± 53…57	± 55…59	± 57…61
295	+ 8.5	94.3	± 53…58	± 55…60	± 57…62
200	− 1.0	93.3	**± 699…768**	**± 701…771**	**± 750…820**
295	− 0.70	94.3	**± 699…757**	**± 701…759**	**± 750…810**
390	+ 150	97.5	± 0.52…4.3	± 2.4…6.3	± 4.3…8.2
295	+ 200	96.9	± 0.52…5.3	± 2.5…7.4	± 4.4…9.3
200	− 430	95.8	± 0.35…4.3	± 2.3…6.8	± 4.9…9.4
295	− 290	97.0	± 0.35…3.6	± 2.3…5.8	± 4.9…8.4

[a] see Appendix A, [b] variation in $\Delta i_{\mathrm{es}}/i_{\mathrm{es}}$, $\Delta i_{\mathrm{ES}}/i_{\mathrm{ES}}$, and $\Delta i_{\mathrm{AFE}}/i_{\mathrm{AFE}}$ refers to the cases 1 and 4 in energy storage current (i_{es}) accuracies.

higher than those regenerative powers in question, and thus in those cases, power control would not necessarily react at all.

The error in charge-discharge frequency bases on Eq. 64 which can be further derived to

$$\frac{\Delta d}{d} = \int_0^t \frac{\Delta i_{\mathrm{es}}}{i_{\mathrm{es}}} \mathrm{d}t. \tag{66}$$

Thus, the maximum error of d for low power operation is within ± 53…58 %, and for high power operation within ± 0.35…5.3 %, based on i_{es} values in Table 11.

Finally, load torque of an engine $\boldsymbol{\tau}_{\mathrm{load}}$ can be solved, which is based on AFE converter current i_{AFE} and efficiency mapping of an electric drive η_{ED}. An error in generator speed is considered to be zero due to a speed PI-controller for an engine. Load torque can be derived, as

$$\Delta \boldsymbol{\tau}_{\mathrm{load}} = \left| \frac{\delta \boldsymbol{\tau}_{\mathrm{load}}}{\delta i_{\mathrm{AFE}}} \right| \Delta i_{\mathrm{AFE}} + \left| \frac{\delta \boldsymbol{\tau}_{\mathrm{load}}}{\delta \eta_{\mathrm{ED}}} \right| \Delta \eta_{\mathrm{ED}}, \tag{67}$$

thus

$$\Delta \boldsymbol{\tau}_{\mathrm{load}} = \frac{u_{\mathrm{DC}}}{\eta_{\mathrm{ED}} \cdot \omega_{\mathrm{G}}} \cdot \Delta i_{\mathrm{AFE}} + \frac{u_{\mathrm{DC}} \cdot i_{\mathrm{AFE}}}{\eta_{\mathrm{ED}}^2 \cdot \omega_{\mathrm{G}}} \cdot \Delta \eta_{\mathrm{ED}}, \text{ when } i_{\mathrm{AFE}} > 0,$$

and

$$\Delta \boldsymbol{\tau}_{\mathrm{load}} = \frac{u_{\mathrm{DC}} \cdot \eta_{\mathrm{ED}}}{\omega_{\mathrm{G}}} \cdot \Delta i_{\mathrm{AFE}} + \frac{u_{\mathrm{DC}} \cdot i_{\mathrm{AFE}}}{\omega_{\mathrm{G}}} \cdot \Delta \eta_{\mathrm{ED}}, \text{ when } i_{\mathrm{AFE}} < 0.$$

The AFE-converter-generator combination efficiency mapping accuracies are based on sensor accuracies in Table 7, and derived for two different motoring operation points based on Eq. 57. Results are presented in Table 12.

Then, Eq. 67 with positive i_{AFE} results to relative errors of ± **180…190** % for low loads, and to ± **8.0…13.0** % for high loads, respectively. Finally, relative errors of fuel consumption are available, if

$$\frac{\Delta \dot{m}}{\dot{m}} \approx \frac{\Delta \boldsymbol{\tau}_{\mathrm{load}}}{\boldsymbol{\tau}_{\mathrm{load}}}, \tag{68}$$

Table 12: Efficiency mapping accuracies of the generator electric drive in considered operations points.

u_{DC} [V]	i_{AFE} [A]	ω_{EM} [rad/s]	$\boldsymbol{\tau}_{\mathrm{EM}}$ [Nm]	$\Delta\eta_{\mathrm{ED}}$ [%]
+ 650	+ 3.85	+ 314.1	+ 16.0	± 63.4
+ 650	+ 90.5	+ 314.1	+ 220	± 3.03

is assumed. Smaller error values correspond to cases with electrical load as the starting point, and maximum values refer to the mechanical starting point, respectively. The values assume ambient temperature to be in the range of +25 °C. Considered error sources are efficiency mappings of all power electronics devices and electric machines, current and voltage measurement errors for control of the system, and inaccuracies in realization of a DC-DC converter plant model. After all, presented accuracies still neglect the fuel consumption mapping accuracy of an engine.

Although, the relative error values for variables become high due to a cumulation of errors. It should be remarked that error values represent the maximum errors in which all errors are realized in the same direction, and thus, are the worst case values. More representative error values could be attained with quantitative analysis which is, however, excluded from this study.

Proposed sub-system models were in the beginning targeted to mean values with 20 Hz-bandwidth. Presented experiments and simulations (in Publications) show that low-frequency operation behavior can be predicted with proposed models. Furthermore, error analysis gives the theoretical maximum error value for predicted fuel consumption in static states. The presented maximum error values in fuel consumption are high due to a cumulation of errors in different sub-systems. Maximum error values can be decreased by considering quantitative analysis e.g. in efficiency mappings. Therefore, qualitative error analysis seems to be more reasonable when considering maximum errors of individual sub-system components.

The target of the proposed models was to predict system behavior in 20 Hz-bandwidth, which has been proven to some extent. Thus, proposed models enable design of EMSs only within this bandwidth, and faster behaviors are most likely not predicted with appropriate accuracy. Furthermore, the proposed modelling approach may not necessarily be used as the precision tool for fuel consumption predictions, as noticed in error analysis. Thus, the proposed simulation models suit the design of different energy management hierarchies by the Model- and Hardware-In-the-Loop principles.

An analysis of maximum errors of the proposed simulation method illustrates that small individual error values cumulate to a high total maximum error value in fuel consumption of a studied system. Thus, it is unclear what would be a sufficient accuracy of a sub-system model. For instance, an increase in error of the DC-DC converter efficiency mapping from ± 0.5 % to ± 0.9 % has a greater influence on fuel consumption error than on interface variables of the converter. Therefore, continuous improvement of simulation model accuracies can be considered to be good

practise. In future, such a procedure leads to knowledge of achievable accuracies in a sub-system and full-system models.

4 Summary of Publications

4.1 Publication I

The paper presents and analyses the first versions of simulation models which were realized for supervisory control software prototyping and optimization of a series-hybrid powertrain. Possible powertrain components are introduced and their system-level power control discussed. Furthermore, the initial state of ideas to control energy through a powertrain is discussed.

Fig. 26 presents the high level schematics of the designed system-level simulation model. The focus of the simulation tool was to realize the interfaces of sub-system models with real-value physical simulation components, such as resistors, inductors, capacitors, and current sources. Thus, current controllers had the highest bandwidths of phenomena to be modelled. The functionality of sub-system models were imitated with basic Simulink and State-flow blocks.

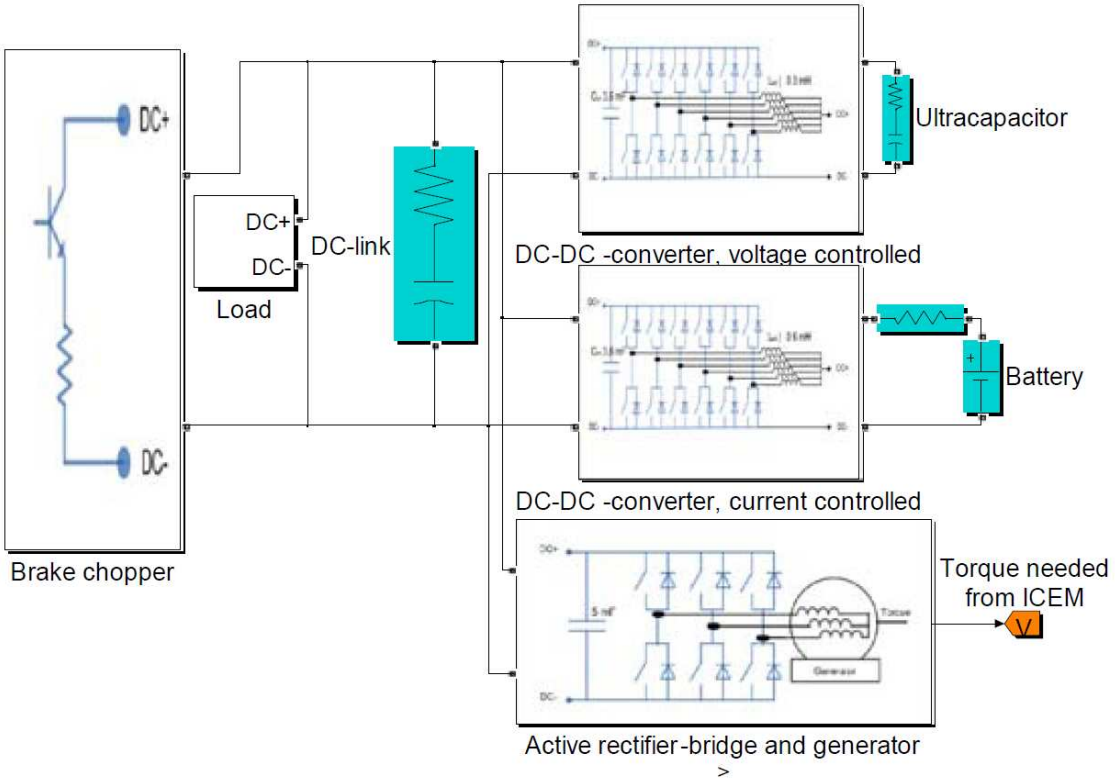

Figure 26: The series-hybrid powertrain simulation model realized with the SimPowerSystems and Stateflow library components.

In the first phase, the simulation method was already the backward calculation from a known load cycle to sources. The load was modelled with a controlled current source, the brake resistor with a voltage regulated current source, the battery pack had a current controlled DC-DC converter as an interface and the UC pack interface device was a voltage controlled DC-DC converter, respectively. Finally,

engine torque was calculated backward from the load regulated by the intermediate circuit voltage controller and the constant speed operation of the engine.

A merit of this study is that it brought to light the need for a simulation environment which would help with supervisory control prototyping and design of series-hybrid powertrains. Furthermore, the study discussed an approach to model the full series-hybrid powertrain system, and thus the value for others is on discussions of modeling and energy management ideas. Design of energy management hierarchies can be started with the presented and discussed modeling approach. Furthermore, use of this or nearly similar implementation would most likely lead to proper solutions in energy management designs. The advantage of this approach is on physical electric circuit components which better visualize the system for new engineers.

However, there were three essential reasons to further contribute to the series-hybrid powertrain design environment. The first was such that physical simulation tools are not executable on targeted digital signal processors, and thus those cannot be used for real-time calculations. The second reason is the license costs of extra Simulink^{TM} libraries for original equipment manufacturers. The third reason was that the approach aimed at overly accurate electrical phenomenon modeling for powertrain topology studies, thus increasing the full operation cycle simulation times. Increase in simulation times was due to the modeling of current regulators for controlled current sources, which have been assumed as ideal in the later phase of research. The proposed simulation method situated between proper approaches for the full powertrain and electrical-circuit models. This method was slow for the full powertrain modeling and inaccurate for the control design of internal controllers in the power electronics components. At this phase of research, it is not clear if the presented approach becomes beneficial in powertrain design issues with bandwidths higher than 20 Hz.

4.2 Publication II

The paper presents a model-based design of an energy management strategy for the diesel-electric powertrain buffered with the active UC pack. The proposed energy management is validated in Publication III and reviewed structure presented in Section 3.11. The indirect primary source power buffering method is investigated for the series-hybrid powertrain. The background for low-level controls of the proposed energy management was on the existing hardware, a current controlled DC-DC converter and a voltage controlled active rectifier.

This research adopts efficiency mappings of a DC-DC converter to plant models, and illustrates simulations of system-level models which were realized with basic Simulink blocks without utilization of physical SimPowerSystem components. Furthermore, the ES system cycle efficiency is introduced, which includes two times DC-DC converter and two times UC pack energy losses.

The UC buffered diesel-electric powertrain topology, under consideration of the study, was presented in Fig. 21. Load power reference for the model-based design study was the New European Driving Cycle which is shown in Fig. 27. Figs. 28 and

29 illustrate simulated currents, and Fig. 30 presents the energy storage voltage.

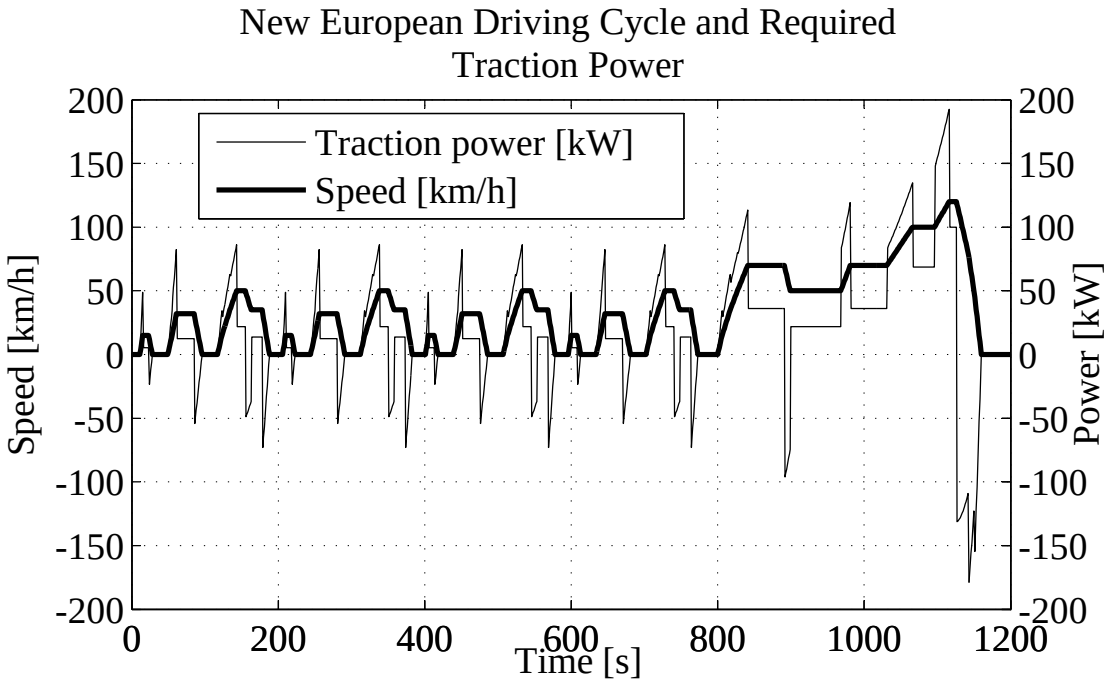

Figure 27: The New European Driving Cycle and required traction power.

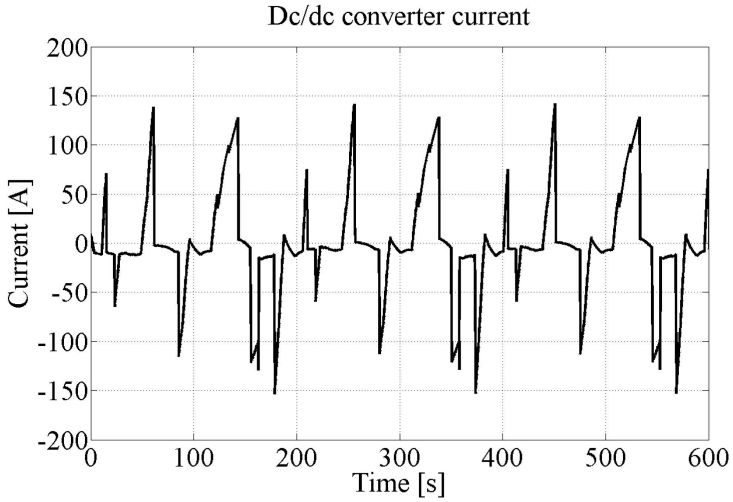

Figure 28: The simulated ES current with the NEDC.

The paper presented correctly directed simulation results for the powertrain operation with the NEDC which were validated in Publication III. The simulation study illustrated the VSDG decrease potential to be within 50...72 % of an original, while an ES system operates in a proper efficiency area. The decrease ratio

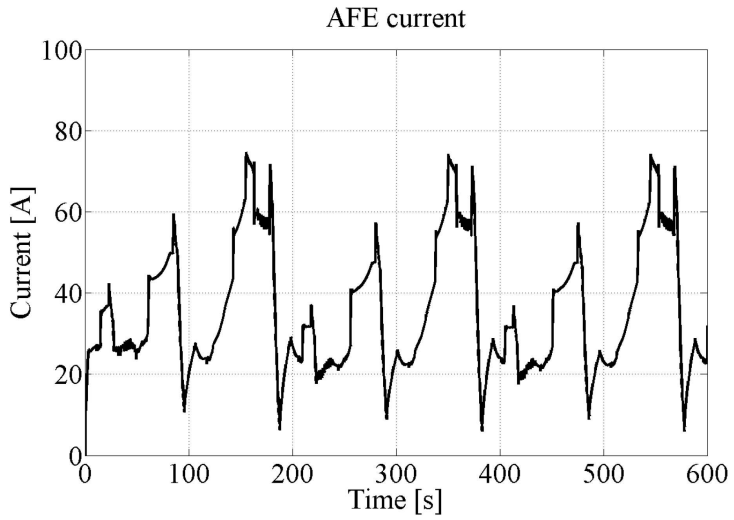

Figure 29: The simulated AFE converter intermediate circuit current with the NEDC.

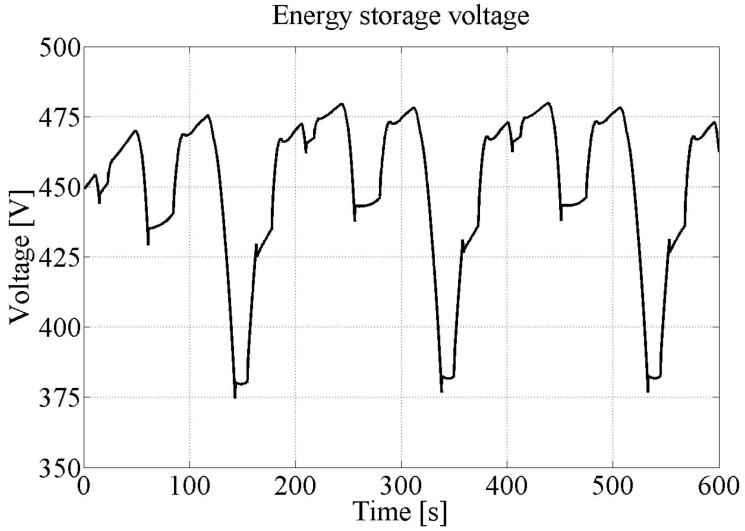

Figure 30: The simulated UC pack voltage with the NEDC.

depends on the drive cycle, and the sizing of the UC pack as well as DC-DC converter. Furthermore, the problematic nature of controlling power was noticed with only one energy management algorithm during overly high loads.

However, the proposed control algorithms had a flaw, although the right aspects of a well operating controller were presented. An error occurred in the choice of the DC-DC converter current direction, which in the presented form (Fig. 7) resulted in unstable operation. However, the described error did not have an impact on the presented results of the study due to the small proportional controller coefficient value for DC-link voltage stabilization after the chosen current direction, c.f. Table 2 in Publication II. Thus, correction to the algorithm was made in the validation

phase (Publication III), and review of the algorithm is presented in Section 3.11. Furthermore, derations of the DC-DC converter control were not implemented into the models in this phase of research, which can be noticed from simulations in Publication II. Moreover, the idea of an additional filtering of i_{AFE} (Fig. 8) could not be implemented into the target hardware (in Publication III) due to the low bandwidth of the DC-DC converter current regulator.

4.3 Publication III

The paper presents validation experiment results for the designed series-hybrid powertrain plant models. Furthermore, this paper focuses on modeling and energy management of the UC buffered diesel-electric powertrain.

First, information is gained on the accuracies of the designed simulation models. Figs. 31, 32, and 33 illustrate experiments in contrast to simulation results. These figures show that the mean values of variables can be predicted with the designed plant models. In addition, the study illustrates that the designed energy management (in Publication II) operates as intended. The study concludes that the proposed energy management interface enable all operation modes of a hybrid powertrain. Based on the information gained, precise descriptions of energy management algorithm interfaces have not been covered thoroughly for all powertrain topology cases.

Furthermore, it can be argued that the presented experiments with simulation comparisons are either the first or amongst the first, which can be found from the literature for the studied powertrain case. In addition, essential operation behaviors are pointed out with figures. Those figures and presented accuracies are valuable for peers working with the same or similar series-hybrid powertrain systems.

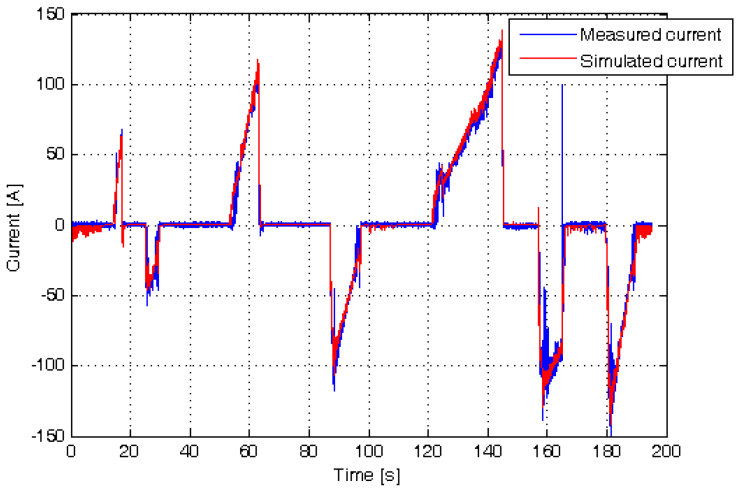

Figure 31: Comparison of the simulated and the experimented ES current with the proposed energy management algorithms.

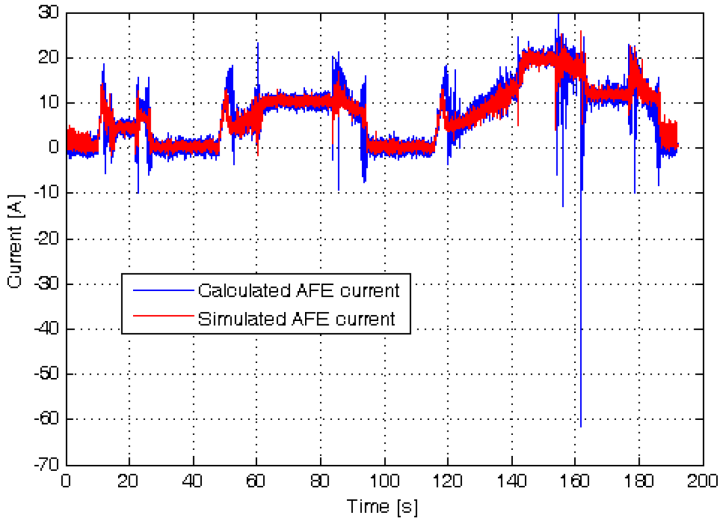

Figure 32: Comparison of the simulated and the experimented AFE current with the proposed energy management algorithms.

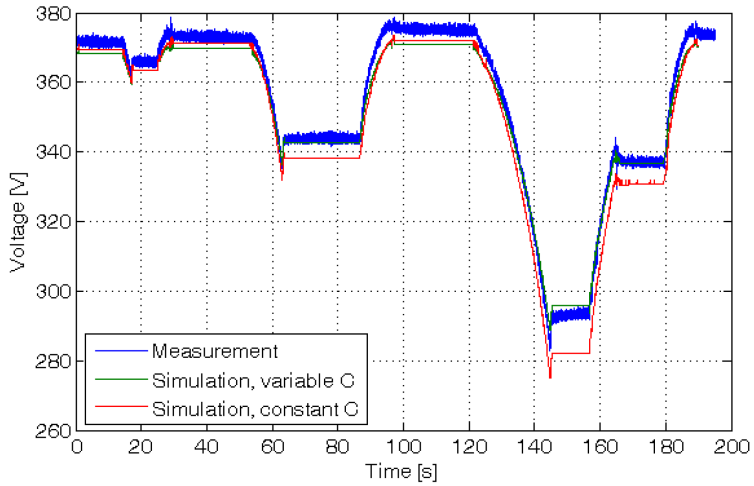

Figure 33: Comparison of the simulated and the experimented ES storage voltage with the proposed energy management algorithms. Comparison consist of variable and constant capacitance simulations.

A limitation of the study is that it only mentions the descriptions of simulation models, and thus neglects mathematical descriptions as well as the schematics of plant models. Thus, the study is difficult to reproduce for a new engineer, but most likely behind a moderate workload for an engineer with existing simulation tools and experimenting hardware. Moreover, a better choice for the DC-DC converter plant model validation would have been an intermediate circuit current and not an ES current. The intermediate circuit current would have also considered the accuracy of the plant model, and not only the accuracy of the energy management algorithm.

Review of Plant Models Accuracies

In autumn 2010, a new comparison was performed of modeling accuracies. Table 13 summarizes the accuracies which were achieved with the proposed simulation method. The static and dynamic accuracies are characterized as being good, intermediate, and low by referring to the behavior of a plant model, not to the plant model description. In addition, there was a revaluation of max, mean, and RMS errors between simulated and measured variables.

Table 13: The variable accuracies with the proposed backward modeling approach.

	u_{DC}	n_{VSDG}	i_{AFE}	u_{uc}	i_{es}
Static behavior	good	good	good	good	good
Dynamic behavior	low	good	intermediate	good	intermediate
Max error	-	∼90 rpm	∼80 A	3 V[a]...5 V[b]	∼150 A
Mean error	-	∼5 rpm	± 0.2 A	1 V[a]...3 V[b]	± 0.5 A
RMS error	-	∼9 rpm	∼3.0 A	3 V[a]...4 V[b]	∼6.0 A

[a] refers to the variable $\mathbf{C}_{\mathrm{uc}}$, [b] refers to the constant C_{uc}

Accuracies are the poorest when the simulation bandwidth, and simulated phenomenon bandwidths are the closest. Therefore, the DC-link voltage modelling accuracy is the poorest—specifically in transitions. However, mean error values are small as targeted at the beginning of this study, and therefore, the approach enables the energy management algorithm design for series-hybrid powertrains within 20 Hz-bandwidth.

4.4 Publication IV

The paper presents the experiments of two different power buffering cases with active control of an UC pack. First, the peak power cutting method is described, as well as an acceleration assistance and regenerative energy recuperation method. Furthermore, there is a presentation of efficiency maps of single power conversion through a DC-DC converter, single power conversion through an UC pack, and ES system cycle efficiency through twice a DC-DC converter and twice an UC pack. Finally, efficiency and fuel consumption maps are utilized for illustrations of the ES system and the VSDG operation areas with the proposed control algorithms.

The paper concentrates especially on the control and efficiencies of an ES system. Furthermore, described power control methods were applied to simulations of the diesel-electric powertrain with an active UC buffering. The simulations presented illustrate precisely the operation areas of a diesel engine and ES system in two different energy management cases, and show the downsizing potential of an engine. Based on the information attained, similar system level energy management comparisons have not been presented before for the studied series-hybrid powertrain case in the literature.

However, the simulated Figs. suggest that the proposed control for the system add divergent power transitions to the primary source, and controls the ES system

current with less sudden transients. Such a system operation may be unwanted due to operation of an engine. Based on the figures presented, it is not clear whether problems arise from the proposed energy management algorithms, sizing of a DC-DC converter, or sizing of an UC pack. Therefore, solutions to avoid transients in engine operation should be considered when reproducing similar work.

Fig. 34 shows the operation areas of the ES system on the two-quadrant efficiency map with two simulated cases. Green crosses refer to the operation points with the peak power cutting control method, and red circles refer to operation points with the acceleration assistance and regenerative energy recuperation method, respectively. Fig. 35 illustrates loading of the VSDG in conventional use, and in hybrid powertrain cases.

New similar research contributions could be made for different energy management strategies and algorithms. In those new contributions, emphasis could be on ensuring steady operation of an engine. Furthermore, load transient limitations for an engine should be specified as a base for the energy management design. Two interesting paths can be named for considerations of new energy management strategies and algorithms. First, a new algorithm structure with use of either a dynamic rate limiter or a high-pass filter to ramp-up an engine power reference, and to subtract an ES power reference based on load and engine power references. Second, change of the control strategy from the AFE converter regulated intermediate circuit voltage to the ES converter regulated voltage, respectively. In the second case, a tuning variable for an engine control would be torque.

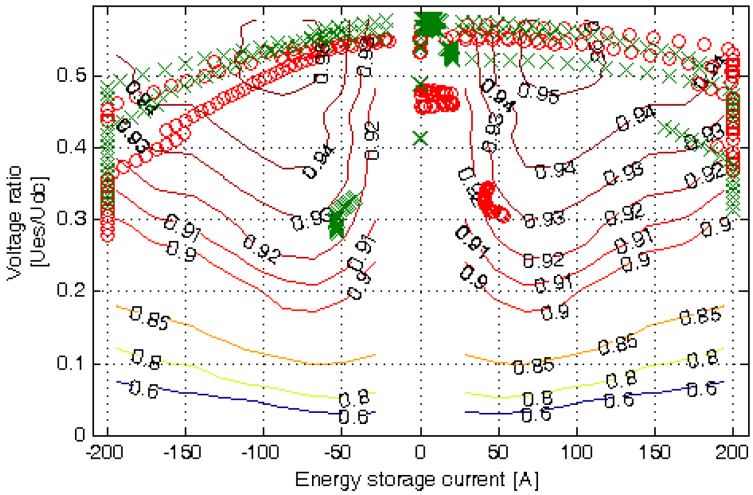

Figure 34: Operation points of the ES system during ECE-15 drive cycle simulations. Green crosses refer to the peak power cutting control method, and red circles refer to the acceleration assistance and regenerative energy recuperation method, respectively.

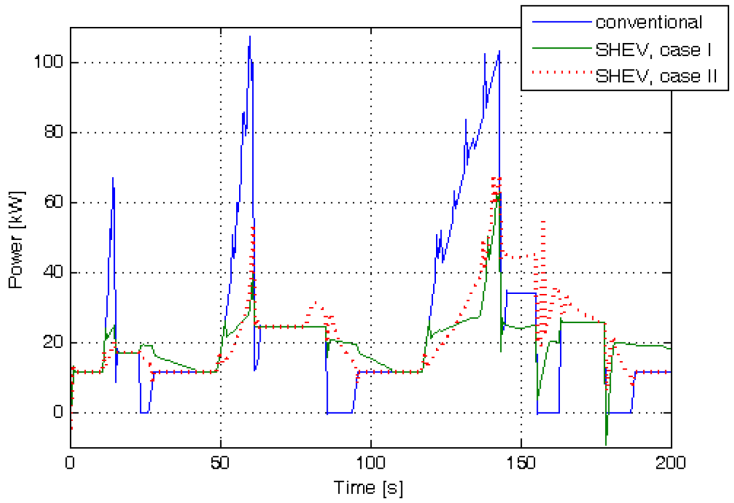

Figure 35: The loading of the VSDG in three simulation cases. The blue line refers to the conventional VSDG use, the green line refers to the peak power cutting control method, and the red dashed line refers to the acceleration assistance and regenerative energy recuperation method, respectively.

4.5 Publication V

A mutual comparison is presented of different powertrain topologies in a specific harbor straddle carrier usage in this paper. In the comparison, five different FC powertrain cases are considered. Powertrain cases are: FC and passive battery, FC with passive battery and active UC pack, FC with active battery and active UC pack, variable power operated FC with active UC pack, and constant power operated FC with active UC pack. Considered features in the comparison are weights, sizes, efficiencies, and initial as well as lifetime costs of each powertrain cases.

The paper presents mathematical descriptions of plant models to improve the repeatability of similar work and illustrates different powertrain cases with figures of simulated power flows. Furthermore, the knowledge attained of mutual differences between powertrain cases enables optimization of a duty vehicle powertrain for a specific purpose. For instance, a different topology optimizes a powertrain in respect to weight and size, than which optimizes a powertrain in respect to costs or in efficiency.

However, the whole comparison topic is wide and one conference paper cannot describe all the issues related to the work, e.g. specific control algorithms on each case. Therefore, more concentration is needed on describing energy management algorithms in each powertrain case through mathematical descriptions and schematic illustrations. Otherwise the repeatability of the work for other researcher or engineers may be difficult. Thus, future research directions include exact descriptions of energy management algorithms based on modelling principles presented in this study.

Furthermore, the study has only considered usage of the high energy density bat-

tery technology, and neglected possible use of high power density battery technology. The review presented in the next section adds the high power battery technology to the consideration of mutual differences between different powertrain cases.

4.6 Review for Comparisons of Fuel Cell Series-Hybrid Powertrain Topologies

This section reviews results of Publication V with respect to high power (HP) battery packs. In this categorization, the high energy (HE) battery refers to cases with continuous 1C charge and discharge currents, and with maximum 2C discharge current. The HP battery refers to cases with 6C continuous current for both charging and discharging, and 10C maximum current, respectively. The results in Publication V are calculated assuming use of the HE battery.

Five different powertrain topologies are considered (as in Publication V) with the following configurations:

- Case *a*: fuel cell, and passive battery, [Fig. 36 (a)]
- Case *b*: fuel cell, passive battery and active UC, [Fig. 36 (b)]
- Case *c*: fuel cell, active battery and active UC, [Fig. 36 (c)]
- Case *d*: fuel cell with active UC, variable FC power production, [Fig. 36 (d)] and
- Case *e*: fuel cell with active UC, limited FC power production. [Fig. 36 (d)]

Calculation parameters for the review are presented in Table 14. The results are calculated assuming 15 years lifetime of a powertrain.

Table 14: Weight, size, price, and lifetime parameters.

Component	Weight [Wh/kg]	Size [Wh/dm^3]	Price [$/kWh]	Lifetime [M]
HE battery	102	129	210 - 840	0.3[a]
HP battery	50	95.6	980 - 2800	0.3[a]
UC	2.3	1.6	2380 - 3220	1[b]
	[kW$_{peak}$/kg]	[kW$_{peak}$/dm^3]	[$/kW$_{peak}$]	[years]
FC	0.21 - 0.38	0.14 - 0.27	100	1.6
DC-DC	3.45	5.8	100	15
Brake resistor	13	6.6	5	15

[a] refers to a shallow cycle, [b] refers to a deep-discharge cycle

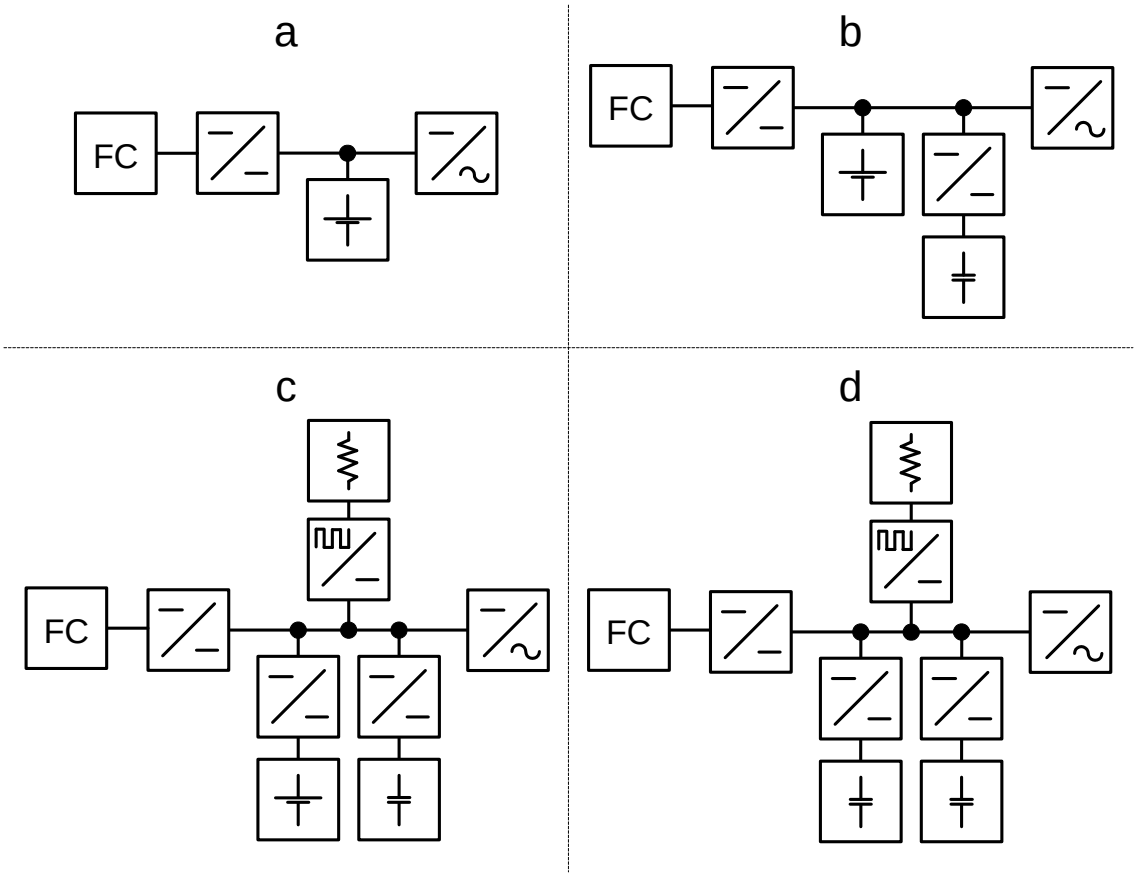

Figure 36: Schematics of studied powertrain topologies.

Lower price values of energy storages refer to mass manufacturing costs, and high price values refer to early market costs, respectively. Prices of FC and PE are somewhat the same as mass manufacturing costs estimated for 500k units yearly production.

Table 15 presents equivalent FC hybrid powertrains based on backward simulations from a known load cycle of a NRMM to sources. Results are based on simulations presented in Publication V.

Fig. 37 presents weight and size comparisons for different topologies with HE batteries, in cases *a*, *b*, and *c*. The UC buffered topologies are cases *d* and *e*, as well as *b* and *c* with UC peak power buffering only. Fig. 38 presents weight and size comparisons for the HP battery buffered topologies, respectively.

These figures show that the minimum weight and size are achieved with the fuel cell, passive HP battery topology. Almost equivalent weights and sizes respect to the HP case *a* are attained with HP cases *b* and *c*. However, if the HE battery is used, the weight and size order changes. Then, the minimum weights and sizes are achieved with cases *b* and *c*. Furthermore, the HE case *a* becomes significantly heavier and larger, and is comparable to UC buffered cases *d* and *e*. The heaviest and largest case is the *e* in which the FC source is operated continuously on maximum power region and buffered with UC packs. Therefore, weight and size mutual relations of

Table 15: Equivalent powertrains.

	Battery [kWh]	UC [kWh]	FC [kW_{peak}]	DC-DC [$\sum kW_{peak}$]	Resistor [kW_{peak}]
Case *a*, HE	189	0	75	75	0
Case *b*, HE	108	0.55	75	275	0
Case *c*, HE	108	0.55	75	386	157
Case *a*, HP	34	0	75	75	0
Case *b*, HP	19	0.55	75	275	0
Case *c*, HP	19	0.55	75	386	157
Case *d*	0	2.63	200	357	267
Case *e*	0	4.03	82	385	27

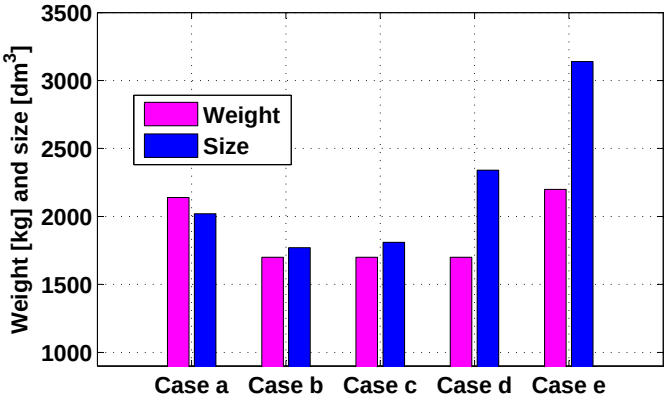

Figure 37: Weights, and sizes of different topologies, with the HE battery buffering.

different topologies are dependent on nominal current value which can be reached from a high power battery pack.

Figs. 39 and 40 present initial and lifetime costs calculated with new parameter values. Lifetime costs are average values within energy storage cost variance which is shown with error bars.

The figures show that the minimum costs are achieved with the case *e*, e.g. the maximum power region operated FC source buffered with UC packs, due to the low price of UCs. Note that the UC error bars are negligible. The second lowest price is attained with the case *d* which has a higher rated FC source. Battery based topologies will not ever achieve as low lifetime costs with shown parameter values. In battery based topologies, the cheapest is the HP case *b*, and the second cheapest is the HP case *c*. The most expensive topology is the HE case *a*.

Table 16 presents distribution of mass manufacturing costs in percentages between different powertrain components. The table illustrates the significant impact the battery has in each case on topology costs. Energy cost becomes more significant

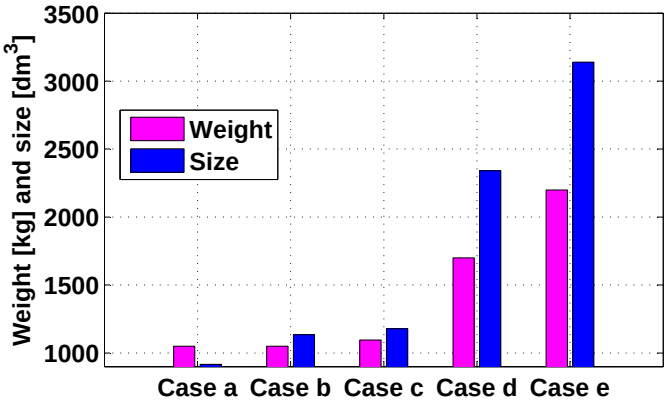

Figure 38: Weights, and sizes of different topologies, with the HP battery buffering.

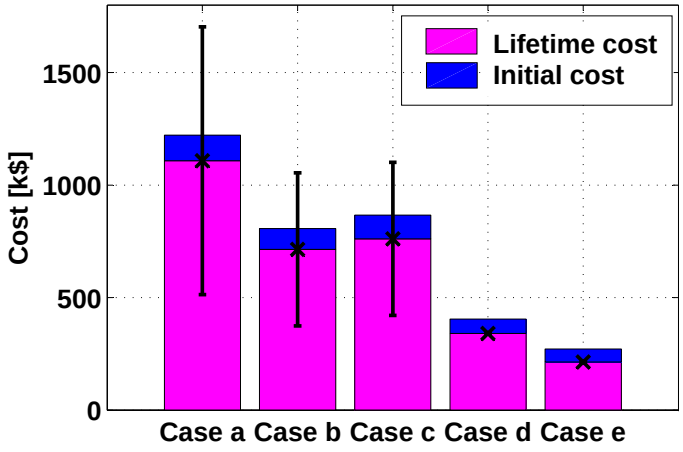

Figure 39: Initial and lifetime costs of different buffering topology cases, with the HE battery pack.

if battery size is decreased with the low-cost UC based peak power unit. The FC source price dominates on UC based topologies d and e, whereas UC and PE prices begin to have an impact.

Fig. 41 illustrates an iteration path which was used during the study. The first phase of the work refers to the general design of powertrain topology, control strategy, and energy management algorithms. The second phase refers to simulations with the present state of the model. After simulation, a comparison is made between reference power and realized power transfer. A comparable powertrain case is achieved when reference and actual powers are equal, in which case the characteristics of the powertrain can be calculated. In the case of derated load power transfer, either simulation parameters, such as designs of DC-DC converters, battery, UC pack, or FC source are reconsidered, or even the basis of the control strategy and the energy management are reconsidered.

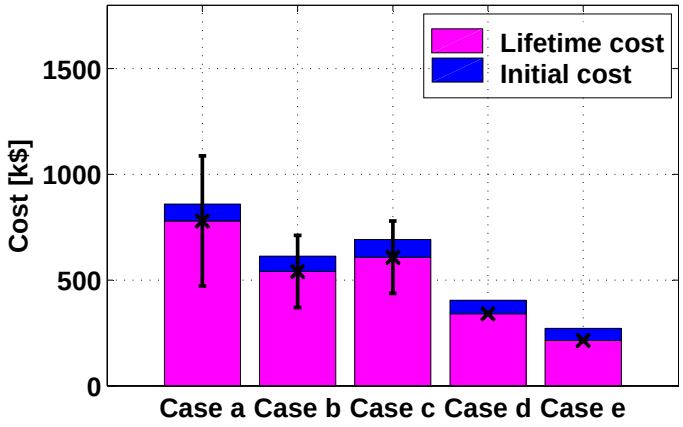

Figure 40: Initial and lifetime costs of different buffering topology cases, with the HP battery pack.

Table 16: Distribution of lifetime costs in percentages.

	Battery [%]	UC [%]	FC [%]	PE [%]	Energy [%]
Case *a*, HE	77.5	0.0	13.7	1.5	7.4
Case *b*, HE	60.9	1.1	18.9	7.4	11.8
Case *c*, HE	53.9	0.9	16.7	9.4	19.0
Case *a*, HP	69.9	0.0	14.9	1.6	13.6
Case *b*, HP	50.0	1.1	19.1	7.5	22.4
Case *c*, HP	42.3	0.9	16.1	9.1	31.7
Case *d*	0.0	5.5	55.5	11.0	28.0
Case *e*	0.0	13.8	36.8	18.6	30.9

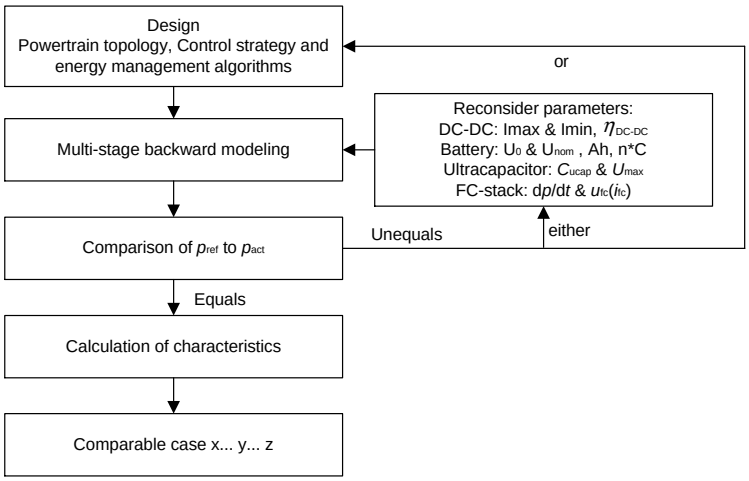

Figure 41: Iteration path to simulations to achieve comparable powertrains.

5 Conclusions

The main scope of the study is specifically on design, modeling, and energy management of series-hybrid powertrains for non-road mobile machineries. Contributions are made to find proper plant models for the model-based design of different series-hybrid powertrains in vehicles. This study proposed the use of certain system-level plant models for the design of series-hybrid powertrains, gave mathematical descriptions for plant models, and pursued an understanding of accuracy in a model-based design, with both based on theory and experiments. Furthermore, contributions were given, especially for energy management design in the diesel-electric powertrain with an active ultracapacitor pack as the energy storage. Finally, designed plant models were used for the comparison study between different FC powertrains. As a result, knowledge is gained of mutual differences between powertrain characteristics, such as weights, sizes, efficiencies, and costs.

A multi-stage simulation tool has been created for the engineering purposes of different series-hybrid powertrains. The modeling method and its use for powertrain comparisons, as well as energy management design, have been illustrated with examples. Thus, the work has value for students, researchers, and engineers aiming to reproduce similar work. Furthermore, designed powertrain models can be adopted to aid powertrain designers R&D, or for teaching purposes. Based on a comparison between simulations and experiments, as well as theoretical error analysis, the proposed multi-stage approach enables the energy management algorithm design for series-hybrid powertrains within 20 Hz-bandwidth. The motivation of this thesis is on the distribution of knowledge and on documentation needs of the proposed modeling method. Furthermore, the adoption of clean and renewable energy technologies requires similar studies as presented in this thesis.

This thesis illustrated thoroughly the design and operation of the energy management algorithm for the active UC pack buffered diesel-electric powertrain. Special care must be taken while implementation the proposed or similar energy management to the target hardware, due to the complexity of the full system. Despite promising energy management illustrations and experiments, some modifications to algorithms might be needed. Furthermore, implementation of this or any other energy management algorithm is vulnerable to issues arising from behaviors above 20 Hz-bandwidth.

This thesis provided knowledge on achievable accuracies with the proposed modeling method in the vehicle powertrain design. Furthermore, comparison procedure for different series-hybrid powertrains is described, and this research contributes to an understanding of mutual differences in the characteristics of different powertrain cases targeted to—specifically, the harbor straddle carrier application. Therefore, a comparison has been introduced of different series-hybrid powertrain topologies. However, mutual differences in powertrain comparison are sensitive to parameter changes, such as nominal battery current, as well as weights, sizes, costs of components. Thus, it might become beneficial to enact a similar powertrain comparison in parallel with design process of new hybrid powertrains.

New research contributions could be created, firstly, for the design of differ-

ent energy management strategies and algorithms in the active UC pack buffered diesel-electric powertrain. In those contributions, emphasis could be more on steady operation of an engine. Two interesting paths for those studies were mentioned in this thesis; first, that of changing the energy management algorithm, and secondly, changing the control strategy. In this context, changing the energy management algorithm refers to new algorithm structure, and changing of the control strategy refers to changing primary tuning variables in the energy management. Secondly, new research contributions are needed to give exact mathematical and schematic descriptions for different energy management algorithms in series-hybrid powertrain topologies. Algorithms should be implemented to the real hardware in order to avoid misleading errors. Such work is needed for knowledge transfer and documentation, as well as for adoption of clean and renewable energy technologies in the transportation sector. Thirdly, introduction of quantitative analysis is suggested for efficiency and fuel consumption mappings, in order to cumulate small error values in the resulted fuel consumption estimate.

References

[1] C. C. Chan *et al.*, "Electric, Hybrid, and Fuel-Cell Vehicles: Architectures and Modeling," *IEEE Trans. Veh. Technol.*, vol. 59, no. 2, pp. 589-598, Feb. 2010.

[2] M. Ehsani *et al*, "Hybrid Electric Vehicles: Architecture and Motor Drives," *Proc. IEEE*, vol. 95, no. 4, pp. 719-728, Apr. 2007.

[3] M. van Walwijk *et al.*, "Hybrid and Electric Vehicles − The Electric Drive Establishes a Market Foothold − Progress Towards Sustainable Transportation," IA-HEV, Angers, France, IA-HEV Annual report 2008, Feb. 2009.

[4] C. C. Chan, "The state of the art of electric, hybrid, and fuel cell vehicles," *Proc. IEEE*, vol. 95, no. 4, pp. 704-718, Apr. 2007.

[5] M. Åhman, "Primary Energy Efficiency of Alternative Powertrains in Vehicles," *Energy*, vol. 26, no. 11, pp. 973-989, Nov. 2001.

[6] A. F. Burke, "Batteries and Ultracapacitors for Electric, Hybrid, and Fuel Cell Vehicles," *Proc. IEEE*, vol. 95, no. 4, pp. 806-820, Apr. 2007.

[7] J. S. Lai and D. J. Nelson, "Energy Management Power Converters in Hybrid Electric and Fuel Cell Vehicles," *Proc. IEEE*, vol. 95, no. 4, pp. 766-777, Apr. 2007.

[8] D. W. Gao *et al.*, "Modeling and Simulation of Electric and Hybrid Vehicles," *Proc. IEEE*, vol. 95, no. 4, pp. 729-745, Apr. 2007.

[9] M. Guarnieri, "When Cars Went Electric, Part 1," *IEEE Ind. Electron. Mag.*, vol. 5, no. 1, pp. 61-62, Mar. 2011.

[10] M. Guarnieri, "When Cars Went Electric, Part 2," *IEEE Ind. Electron. Mag.*, vol. 5, no. 2, pp. 46-53, June 2011.

[11] M. Ehsani *et al.*, *Modern Electric, Hybrid Electric, and Fuel Cell Vehicles*. Boca Raton, FL: CRC Press LLC, 2005, pp. 13-19.

[12] E. H. Wakefield, *History of the Electric Automobile: Battery-Only Powered Cars*. Warrandale, PA: Society of Automotive Engineers, 1994.

[13] B. Cook, "Introduction to Fuel Cells and Hydrogen Technology," *Eng. Sci. and Educ. J.*, vol. 11, no. 6, pp. 205-216, Dec. 2002.

[14] F. J. Teago, "Electric Traction," *J. Institution of Elect. Engineers*, vol. 80, no. 482, pp. 181-189, 1937.

[15] H. F. Harvey and W. E. Thau, "Electric Propulsion of Ships," *Trans. Amer. Inst. of Elect. Engineers*, vol. XLIV, pp. 497-522, 1925.

[16] E. F. Weiser, "Braking Resistors and Control for Diesel-Electric Locomotives," *Trans. Amer. Inst. of Elect. Engineers*, vol. 66, no.1, pp. 229-232, 1947.

[17] A. Kusko, "Off-Highway Vehicles," *Proc. IEEE*, vol. 56, no. 4, pp. 600-604, Apr. 1968.

[18] J. Brenneisen *et al.*, "A New Converter Drive System for a Diesel Electric Locomotive with Asynchronous Traction Motors," *IEEE Trans. Ind. Appl.*, vol. IA-9, no. 4, pp. 482-491, July 1973.

[19] K. Rajashekara, "History of Electric Vehicles in General Motors," *IEEE Trans. Ind. Appl.*, vol. 30, no. 4, pp. 897-904, July/Aug. 1994.

[20] P. Thounthong and S. Raël, "The Benefits of Hybridization," *IEEE Ind. Electron. Mag.*, vol. 3, no. 3, pp. 25-37, Sept. 2009.

[21] M. C. Trummel, "Development History of the Hybrid Test Vehicle," *IEEE Trans. Veh. Technol.*, vol. VT-32, no. 1, pp. 7-14, Feb. 1983.

[22] R. von Helmolt and U. Eberle, "Fuel Cell Vehicles: Status 2007," *J. Power Sources*, vol. 165, no. 2, pp. 833-843, Mar. 2007.

[23] N. Stark. (2007, June 19). *Diesel Hybrid Rubber-Tired Gantry Crane in Service in Canada* [Online]. Available: http://www.greencarcongress.com/2007/06/diesel_hybrid_r.html. (accessed 11.7.2012).

[24] F. Baalbergen *et al.*, "Energy Storage and Power Management for Typical 4Q-Load," *IEEE Trans. Ind. Electron.*, vol. 56, no. 5, pp. 1485-1498, May 2009.

[25] S.-M. Kim and S.-K. Sul, "Control of Rubber Tyred Gantry Crane With Energy Storage Based on Supercapacitor Bank," *IEEE Trans. Power Electron.*, vol. 21, no. 5, pp. 1420-1427, Sept. 2006.

[26] S. Bogosyan *et al.*, "A Novel Validation and Estimation Approach for Hybrid Serial Electric Vehicles," *IEEE Trans. Veh. Technol.*, vol. 56, no. 4, pp. 1485-1497, July 2007.

[27] A. Emadi *et al.*, "Topological Overview of Hybrid Electric and Fuel Cell Vehicular Power System Architectures and Configurations," *IEEE Trans. Veh. Technol.*, vol. 54, no. 3, pp. 763-770, May 2005.

[28] Y. Gao and M. Ehsani, "Parametric Design of the Traction Motor and Energy Storage for Series Hybrid Off-Road and Military Vehicles," *IEEE Trans. Power Electron.*, vol. 21, no. 3, pp. 749-755, May 2006.

[29] A. Lidozzi *et al.*, "Ultracapacitors Equipped Hybrid Electric MicroCar," *IET Electric Power Applicat.*, vol. 4, no. 8, pp. 618-628, 2010.

[30] H. Shibuya and K. Kondo, "Designing Methods of Capacitance and Control System for a Diesel Engine and EDLC Hybrid Powered Railway Traction System," *IEEE Trans. Ind. Electron.*, vol. 58, no 9, pp. 4232-4240, Sept. 2011.

[31] M. B. Camara *et al.*, "Design and New Control of DC/DC Converters to Share Energy Between Supercapacitors and Batteries in Hybrid Vehicles," *IEEE Trans. Veh. Technol.*, vol. 57, no. 5, pp. 2721-2735, Sept. 2008.

[32] M. B. Camara *et al.*, "DC/DC Converter Design for Supercapacitor and Battery Power Management in Hybrid Vehicle Applications-Polynomial Control Strategy," *IEEE Trans. Ind. Electron.*, vol. 57, no. 2, pp. 587-597, Feb. 2010.

[33] P. Grbović *et al.*, "The Ultracapacitor-Based Controlled Electric Drives with Braking and Ride-Through Capability: Overview and Analysis," *IEEE Trans. Ind. Electron.*, vol. 57, no. 6, pp. 1954-1963, June 2010.

[34] L. Gauchia and J. Sanz, "A Per-Unit Hardware-in-the-Loop Simulation of a Fuel Cell/Battery Hybrid Energy System," *IEEE Trans. Ind. Electron.*, vol. 57, no. 4, pp. 1186-1194, Apr. 2010.

[35] W. Gao, "Performance Comparison of a Fuel Cell-Battery Hybrid Powertrain and a Fuel Cell-Ultracapacitor Hybrid Powertrain," *IEEE Trans. Veh. Technol.*, vol. 54, no 3, pp. 846-855, May 2005.

[36] W. Greenwell and A. Vahidi, "Predictive Control of Voltage and Current in a Fuel Cell-Ultracapacitor Hybrid," *IEEE Trans. Ind. Electron.*, vol. 54, no 3, pp. 846-855, May 2005.

[37] D. Feroldi *et al.*, "Design and Analysis of Fuel-Cell Hybrid Systems Oriented to Automotive Applications," *IEEE Trans. Veh. Technol.*, vol. 58, no. 9, pp. 4720-4729, Nov. 2009.

[38] J. Bernard *et al.*, "Fuel-Cell Hybrid Powertrain: Toward Minimization of Hydrogen Consumption," *IEEE Trans. Veh. Technol.*, vol. 58, no. 7, pp. 3168-3176, Sept. 2009.

[39] W.-S. Lin and C.-H. Zheng, "Energy Management of a Fuel Cell/Ultracapacitor Hybrid Power System Using an Adaptive Optimal-Control Method," *J. Power Sources*, vol. 196, no. 6, pp. 3280-3289, Mar. 2011.

[40] J. Moreno *et al.*, "Energy-Management System for a Hybrid Electric Vehicle Using Ultracapacitors and Neural Networks," *IEEE Trans. Ind. Electron.*, vol. 53, no. 2, pp. 614-623, Apr. 2006.

[41] A.R. Miller *et al.*, "Analysis of Fuel Cell Hybrid Locomotives," *J. Power Sources*, vol.157, no. 2, pp. 855-861, July 2006.

[42] N. Woonki *et al.*, "Light Fuel-Cell Hybrid Electric Vehicles Based on Predictive Controllers," *IEEE Trans. Veh. Technol.*, vol. 60, no. 1, pp. 89-97, Jan. 2011.

[43] M. Zandi *et al.*, "Energy Management of a Fuel Cell/Supercapacitor/Battery Power Source for Electric Vehicular Applications," *IEEE Trans. Veh. Technol.*, vol. 60, no. 2, pp. 433-443, Feb. 2011.

[44] L. Wang and H. Li, "Maximum Fuel Economy-Oriented Power Management Design for a Fuel Cell Vehicle Using Battery and Ultracapacitor," *IEEE Trans. Ind. Appl.*, vol. 46, no. 3, pp. 1011-1020, May 2010.

[45] Z. Yu *et al.*, "An Innovative Optimal Power Allocation Strategy for Fuel Cell, Battery and Supercapacitor Hybrid Electric Vehicle," *J. Power Sources*, vol. 196, no. 4, pp. 2351-2359, Feb. 2011.

[46] X. Zhang *et al.*, "Wavelet-Transform-Based Power Management of Hybrid Vehicles with Multiple On-board Energy Sources Including Fuel Cell, Battery and Ultracapacitor," *J. Power Sources*, vol. 185, no. 2, pp. 1533-1543, Dec. 2008.

[47] A. Hentunen *et al.*, "Full-scale Hardware-in-the-Loop Verification Environment for Heavy-Duty Hybrid Electric Vehicles," in *Proc. Electric Vehicle Symp.*, Shenzhen, China, 2010.

[48] S. C. Oh, "Evaluation of Motor Characteristics for Hybrid Electric Vehicles Using the Hardware-in-the-Loop Concept," *IEEE Trans. Veh. Technol.*, vol. 54, no. 3, pp. 817-824, May 2005.

[49] F. U. Syed *et al.*, "Derivation and Experimental Validation of a Power-Split Hybrid Electric Vehicle Model," *IEEE Trans. Veh. Technol.*, vol. 55, no. 6, pp. 1731-1747, Nov. 2006.

[50] L. Guzzella and A. Sciarretta, *Vehicle Propulsion Systems, Introduction to Modeling and Optimization*, 2nd ed. Berlin Heidelberg, Germany: Springer-Verlag, 2007.

[51] M. Broy *et al.*, "Engineering Automotive Software," *Proc. IEEE*, vol. 95, no. 2, pp. 356-373, Feb. 2007.

[52] B. K. Powell *et al.*, "Dynamic Modeling and Control of Hybrid Electric Vehicle Powertrain Systems," *IEEE Control. Syst. Mag.*, vol. 18, no. 5, pp. 17-33, 1998.

[53] L. Shi and M. L. Crow, "Comparison of Ultracapacitor Electric Circuit Models," in *Proc. Power and Energy Society General Meeting – Conversion and Delivery of Electrical Energy in the 21st Century*, 2008 ©IEEE. doi: 10.1109/PES.2008.4596576.

[54] O. Tremblay *et al.*, "A Generic Battery Model for the Dynamic Simulation of Hybrid Electric Vehicles," in *Proc. IEEE Vehicle Power and Propulsion Conf.*, Arlington, TX, 2007 ©IEEE. doi: 10.1109/VPPC.2007.4544139.

[55] *Matlab Simulink*™ *Help* [Online]. Available: http://www.mathworks.com/help/toolbox/physmod/powersys/. (accessed 22.12.2011).

[56] S.-C.Tsai and M. R. Goyal, "Dynamic Turbocharged Diesel Engine Model for Control Analysis and Design," SAE Technical paper 860455, 1986, doi: 10.4271/860455.

[57] S. Pasricha and S. R. Shaw, "A Dynamic PEM Fuel Cell Model," *IEEE Trans. Energy Convers.*, vol. 21, no. 2, pp. 484-490, June 2006.

[58] J. Jia *et al.*, "Modeling and Dynamic Characteristic Simulation of a Proton Exchange Membrane Fuel Cell," *IEEE Trans. Energy Convers.*, vol. 24, no. 1, pp. 283-291, Mar. 2009.

[59] M. Ceraolo *et al.*, "A General Approach to Energy Optimization of Hybrid Electric Vehicles," *IEEE Trans. Veh. Technol.*, vol. 57, no. 3, pp. 1433-1441, May 2008.

[60] R. Bonert, "Design of a High Performance Digital Tachometer with a Microcontroller," *IEEE Trans. Instrum. Meas.*, vol. 38, no. 6, pp. 1104-1108, Dec. 1989.

A Appendix

Table A1: The efficiency mapping data of the DC-DC converter in charge mode.

u_{ratio}	30A	50A	70A	85A	107A	126A	146A	170A	196A
0.01	0.632	-	-	-	-	-	-	-	-
0.02	0.711	0.711	0.748	0.748	-	-	-	-	-
0.03	0.750	0.803	0.796	0.804	-	-	-	-	-
0.04	0.791	0.832	0.837	0.839	-	0.753	-	0.422	0.137
0.05	0.812	0.854	0.859	0.861	0.824	0.808	-	0.690	0.322
0.06	0.839	0.868	0.874	0.877	0.852	0.862	0.859	0.742	0.693
0.07	0.852	0.880	0.886	0.888	0.874	0.880	0.883	0.793	0.878
0.08	0.862	0.889	0.895	0.898	0.886	0.893	0.890	0.845	0.882
0.09	0.870	0.896	0.903	0.905	0.899	0.895	0.897	0.896	0.886
0.10	0.877	0.902	0.909	0.911	0.910	0.897	0.900	0.910	0.898
0.11	0.882	0.908	0.914	0.916	0.912	0.915	0.908	0.914	0.910
0.12	0.888	0.912	0.919	0.921	0.917	0.919	0.916	0.918	0.915
0.13	0.893	0.916	0.923	0.924	0.923	0.925	0.923	0.922	0.920
0.14	0.897	0.920	0.926	0.929	0.927	0.930	0.928	0.925	0.924
0.15	0.901	0.923	0.930	0.932	0.930	0.932	0.930	0.930	0.927
0.16	0.904	0.926	0.932	0.935	0.932	0.933	0.932	0.933	0.930
0.17	0.907	0.929	0.935	0.937	0.934	0.936	0.936	0.935	0.932
0.18	0.909	0.931	0.937	0.940	0.937	0.939	0.940	0.938	0.938
0.19	0.913	0.933	0.939	0.942	0.940	0.941	0.942	0.940	0.940
0.20	0.915	0.935	0.941	0.944	0.942	0.944	0.943	0.942	0.942
0.21	0.918	0.937	0.944	0.946	0.944	0.946	0.945	0.941	0.941
0.22	0.922	0.939	0.945	0.948	0.946	0.948	0.948	0.948	0.941
0.23	0.924	0.941	0.947	0.949	0.943	0.945	0.951	0.955	0.948
0.24	0.927	0.942	0.949	0.951	0.948	0.951	0.953	0.950	0.954
0.25	0.928	0.943	0.949	0.952	0.953	0.956	0.957	0.951	0.951
0.26	0.929	0.941	0.950	0.954	0.952	0.952	0.954	0.952	0.952
0.27	0.930	0.946	0.952	0.955	0.954	0.954	0.955	0.954	0.952
0.28	0.931	0.947	0.954	0.957	0.955	0.955	0.957	0.955	0.954
0.29	0.932	0.948	0.954	0.957	0.956	0.956	0.958	0.956	0.955
0.30	0.932	0.950	0.956	0.958	0.957	0.958	0.958	0.958	0.957

Table A2: The efficiency mapping data of the DC-DC converter in charge mode. Continuing from the previous page.

u_{ratio}	30A	50A	70A	85A	107A	126A	146A	170A	196A
0.31	0.933	0.951	0.957	0.959	0.957	0.959	0.959	0.959	0.958
0.32	0.934	0.952	0.957	0.960	0.959	0.960	0.961	0.961	0.959
0.33	0.935	0.953	0.958	0.961	0.960	0.961	0.961	0.961	0.960
0.34	0.936	0.954	0.959	0.962	0.961	0.962	0.963	0.962	0.961
0.35	0.936	0.955	0.960	0.963	0.962	0.963	0.963	0.963	0.961
0.36	0.937	0.956	0.961	0.963	0.963	0.964	0.964	0.964	0.962
0.37	0.937	0.957	0.962	0.965	0.964	0.965	0.964	0.964	0.963
0.38	0.938	0.958	0.962	0.965	0.965	0.965	0.965	0.965	0.964
0.39	0.939	0.958	0.963	0.966	0.966	0.966	0.966	0.966	0.965
0.40	0.940	0.959	0.964	0.966	0.966	0.967	0.967	0.967	0.966
0.41	0.941	0.959	0.965	0.967	0.966	0.967	0.968	0.967	0.966
0.42	0.941	0.960	0.966	0.968	0.967	0.969	0.969	0.968	0.967
0.43	0.942	0.961	0.966	0.969	0.969	0.969	0.969	0.969	0.968
0.44	0.942	0.962	0.967	0.969	0.969	0.969	0.970	0.970	0.968
0.45	0.943	0.962	0.967	0.970	0.970	0.970	0.970	0.970	0.969
0.46	0.944	0.963	0.968	0.970	0.970	0.970	0.970	0.971	0.970
0.47	0.944	0.963	0.969	0.971	0.971	0.971	0.971	0.972	0.970
0.48	0.945	0.964	0.970	0.971	0.971	0.972	0.972	0.972	0.971
0.49	0.946	0.965	0.970	0.972	0.972	0.973	0.973	0.973	0.972
0.50	0.947	0.965	0.970	0.973	0.973	0.973	0.973	0.973	0.972
0.51	0.947	0.966	0.971	0.973	0.973	0.974	0.970	0.972	0.968
0.52	0.948	0.966	0.972	0.974	0.972	0.974	0.974	0.974	0.971
0.53	0.949	0.967	0.972	0.974	0.974	0.975	0.975	0.975	0.974
0.54	0.950	0.968	0.973	0.975	0.975	0.976	0.976	0.976	0.974
0.55	0.951	0.968	0.973	0.975	0.975	0.976	0.976	0.976	0.975
0.56	0.952	0.969	0.974	0.976	0.976	0.977	0.976	0.976	0.975
0.57	0.953	0.970	0.975	0.976	0.977	0.977	0.977	0.976	0.976
0.58	0.955	0.971	0.975	0.977	0.977	0.973	0.975	0.976	0.976
0.59	0.956	0.971	0.976	0.977	0.977	0.973	0.975	0.976	0.976

Publication I

M. Liukkonen, A. Hentunen, J. Suomela, and J. Kyyrä, "Functional Simulations of Power Electronics Components in Series-Hybrid Machinery for the needs of OEM," in *Proc. Nordic Workshop on Power and Industrial Electronics* (Norpie 2008), Espoo, Finland, June 9-11, 2008.

Functional Simulations of Power Electronics Components in Series-Hybrid Machinery for the needs of OEM

Matti Liukkonen, Ari Hentunen, Jussi Suomela and Jorma Kyyrä

***Abstract*— This paper proposes method for rapid control prototyping of the series-hybrid transmission system. The rapid control prototyping needs simulation submodels from all system components in order to develop supervisory control software. The same simulation models can also be used to optimize the drive train. The target framework for the rapid control prototyping method is the original equipment manufacturer (OEM), where the objective is to build devices from subcontractor's components. The machinery industry, as a target group, uses high power ratings for the creation of motion, which leads to high voltage and current values used in the system. Therefore, prototyping is started with careful simulations. This paper also seeks to create a general idea about the structure of the series-hybrid power transmission and assists the start of the process for designing the supervisory control.**

***Index Terms*—functional simulation, power electronics, series-Hybrid drive train**

I. INTRODUCTION

HEAVY machinery such as harbor straddle carriers, loaders for underground mines and forestry harvesters are conventionally powered with the internal combustion engine (ICE). The ICE is traditionally connected to the mechanical or hydraulic power transmission. Work cycles of such machinery are often such that the fuel economy of the machine could be increased considerably by hybridizing the drive train. Buffered electric power transmission allows energy regeneration and optimization of the diesel operation.

The driving force behind the hybridizing of heavy machinery is the fuel economy. As a side-effect, better fuel economy results in lower emissions and equipments life-cycle costs. In some cases, it is also possible to downsize the engine, because the engine no more has to be sized for peak-power [1]. Another important aspect is the drastically increased amount of available electric power. In the heavy machinery there often exist subsystems which could benefit from the on-board electric power plant and electric energy storage. For example, the belt-driven cooling fan could be replaced with an electric motor driven fan. The speed of the fan could then be adjusted freely, because there is no mechanical coupling between the ICE's shaft and the fan. When cooling is not needed, energy could be saved by shutting the fan off. Additionally, the electric power transmission provides better traction and actuator control than the traditional power trains.

A hybrid electric vehicle is drive-by-wire by nature and needs a sophisticated vehicle control system. The control system collects data from subsystems, and based on the data and driver's requests, it gives control references to the subsystems. Because of the complexity of the system, model-based software development is widely adopted in the industry.

Model-in-the-loop (MIL) simulations provide fast and flexible development of the system level power management. Simulations provide also useful information in the concept design phase and can be used in the component selection of the subsystems.

In order to perform model-in-the-loop (MIL) simulations for the vehicle control system, functional models of the subsystems are needed. A functional simulation model describes the basic behavior and operational limits of a component or a subsystem. The models should have the same I/O interface as the real components. The models should also simulate real variables, such as voltages, currents and engine speed, with enough accuracy. Too high accuracy results in very slow model execution, and too low accuracy results in inaccurate data, thus corrupting the simulation results. Therefore, a good balance between accuracy and model execution time is desirable.

In this paper, functional models of the main components of the series-hybrid system are presented. MATLAB is used as a modeling environment. The framework of the study and development is the heavy machinery original equipment manufacturer (OEM) industry [2].

II. SIMULATION OF SERIES-HYBRID SYSTEM

The series-hybrid drive train connects primary energy sources to energy storages and loads via the dc voltage link. Therefore, power electronic devices are needed to separate

M. Liukkonen is with Helsinki University of Technology, Department of Electrical Engineering, P.O. Box 3000, FI-02015 TKK, Finland (phone: +358 9 451 2446; e-mail: mjliukko@cc.hut.fi).

A. Hentunen is with the same contact information as the corresponding author (e-mail: ari.hentunen@tkk.fi).

J. Suomela is with Helsinki University of Technology, Department of Automation and Systems Technology, P.O. Box 5500, FI-02015 TKK, Finland (e-mail: jussi.suomela@tkk.fi).

J. Kyyrä is with the same contact information as the corresponding author (e-mail: jorma.kyyra@tkk.fi).

different voltage potentials between energy storages and to control the power flow through the drive train. Furthermore, power electronic devices are needed for motion control with the electric motors.

Figure 1 represents possible components used in the series-hybrid drive train. The internal combustion engine or the fuel cell stack is used as a primary energy source. As a secondary energy storage can be used, for example, ultracapacitor module, battery, fly-wheel or a combination of these, depending on the application. Methodologies for designing appropriate power transmission system are presented in papers [1], [3] - [6].

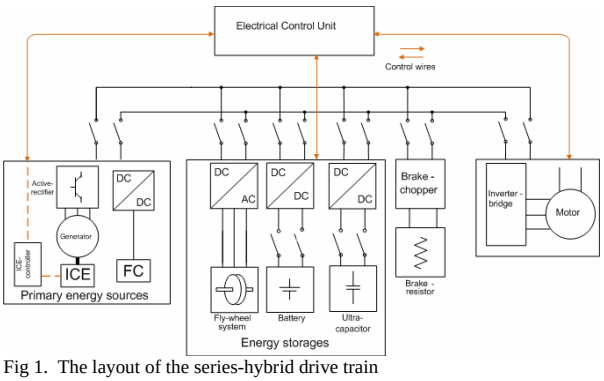

Fig 1. The layout of the series-hybrid drive train

The connection from the generator-set to the dc voltage link is made with an active rectifier, which enables adjustment of the output voltage in the dc voltage link part. As a result, it is possible to force the generator-set to work along the maximum efficiency line, in co-operation with the speed control and the active rectifier control [7]. The connection from the fuel cell stack to the dc voltage link is made with a unidirectional dc/dc converter. In contrast, the battery and the ultracapacitors are connected to the dc voltage link using bi-directional dc/dc converters [8]. The fly-wheel is connected to the dc voltage link through an inverter.

The simulation models presented in this paper are made with the MATLAB/Simulink software. Further, the simulation libraries SimPowerSystems and Stateflow are used to generate the simulation subcomponent models of the series-hybrid system. The SimPowerSystems library components are used for modeling the hardware in the series-hybrid drive train, and the Stateflow library is used for producing the control logic of the subsystems in the simulation model.

Modeling of the series-hybrid power transfer system should reach 20 Hz-bandwidths accuracy, which is enough for the system level control design. The accuracy is ensured by using correct capacitance and inductance values in the interfaces of power electronic component submodels. With regard to the transferred current levels, this bandwidth carries electrical transients caused by capacitors, inductors and the equivalent series resistances. The bandwidth enables the power electronic switches to be left out from the submodels, and the models are built over the current control loop. The functioning of the power-semiconductor switches is taken into account with the PI-regulators, which limits the maximum value of control signal. In additionally, the simulation models are run with a discrete solver of the MATLAB/Simulink, in which the sampling time of the models is close to the switching frequencies of the power electronic devices.

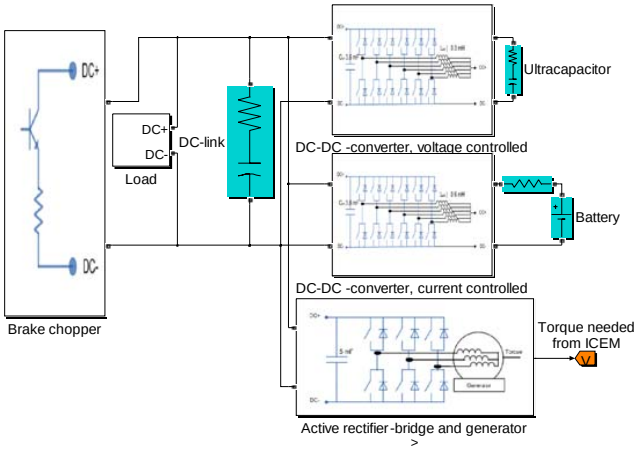

Fig. 2. The series-hybrid system simulation model realized with the SimPowerSystems and Stateflow library components.

The simulation model of the series-hybrid system includes submodels of the current and the voltage controlled dc/dc converters, the brake chopper, the load consumption data and the active rectifier-generator combination. Accurate simulation model from the internal combustion engine have been left

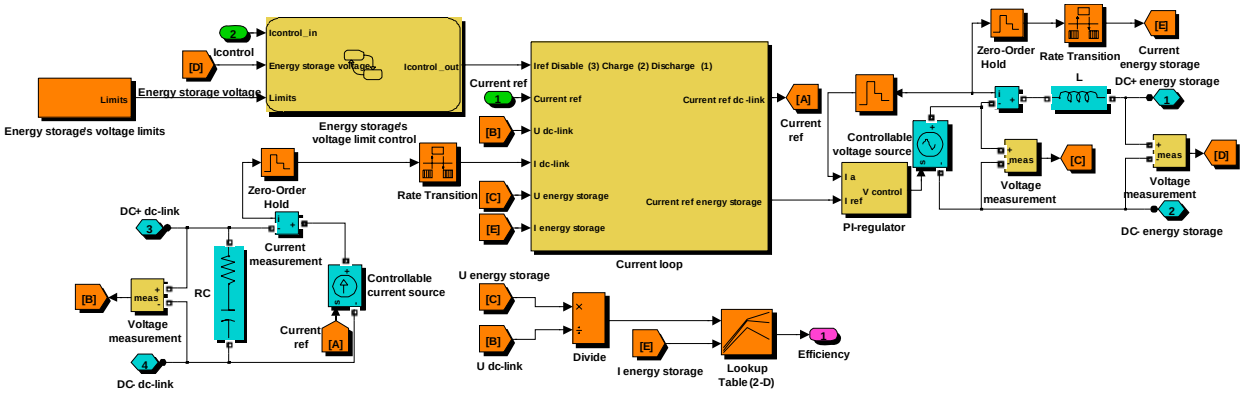

Fig. 3. The simulation model of the current controlled dc/dc converter

out of study for the simplicity. Therefore, the simulation model solves the required torque from the internal combustion engine, which gives information from the rating necessary.

A. Modeling of the Current Controlled DC/DC Converter

Modeling of the dc/dc converters is based on the current control loop. The dc/dc converters are presumed to transfer the current ideally from one voltage level to the other, because the consideration of transfer losses in transferred current would be difficult. The current control loop in the dc/dc converter simulation model will be as follows.

1. Given current reference is generated to the wanted direction
2. Transferred power is measured
3. Solved current is taken from the opposite direction

The difference between current transfers can be neglected because of a short sampling time in the simulations.

The interfaces of the dc/dc converters are modeled using the capacitance and the inductance components found in the SimPowerSystems library. The current reference coming from the superior control is generated and directed through to the inductance port with the controllable voltage source connected to PI-regulator.

Superior to the current control loop, the dc/dc converter has Stateflow block, which contains the voltage value limits of energy storage. If either the maximum or the minimum limit overpasses, then the signals coming from the superior control are disabled. The maximum voltage level is defined by the nominal voltage of the energy source and the minimum voltage is determined by the point at which the power transfer efficiency in the dc/dc converter collapses.

Information of the power transfer losses in the dc/dc converter

Information of the dc/dc converter's transfer losses is based on the measured efficiency map. The dc/dc converter's efficiency is defined by the transferred current and the conversion rate of the voltages between upper and lover voltage levels. The efficiency map is included into the simulation model as a lookup table, which gives the state of the power transfer at the time.

B. Modeling of the Voltage Controlled DC/DC Converter

The voltage controlled dc/dc converter is used in fast low level control/stabilization of the dc-link voltage. This converter is typically used with ultracapacitors [4]. The simulation model from the voltage control has been implemented between the current control and the superior control of the system. This control has been made using the Stateflow block.

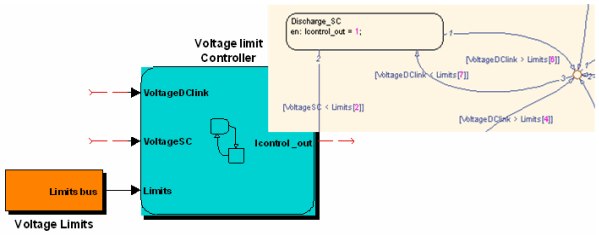

Fig. 4. The voltage control limits build on top of the current control loop with the Stateflow block.

In addition to the voltage limits in energy storage side, the voltage controlled dc/dc converter has a tolerance-band control in the dc voltage link port. The dc-link's tolerance-band control ensures that the dc-link's voltage does not collapse or increase in sudden load transients. After the voltage changes to the maximum or the minimum control value, the current is transferred via the dc/dc converter to stabilize it. The current direction depends in which, maximum or minimum, limit value dc-link's voltage overpasses. The current transfer stops after the voltage overpasses the hysteresis of the limit in question. The voltage controlled dc/dc converter enables the smooth loading of other energy sources, which is suitable for their operation. Therefore, other energy sources should be controlled to remove loading from the voltage controlled converter and to maintain the dc-link's voltage within its voltage tolerance band [9].

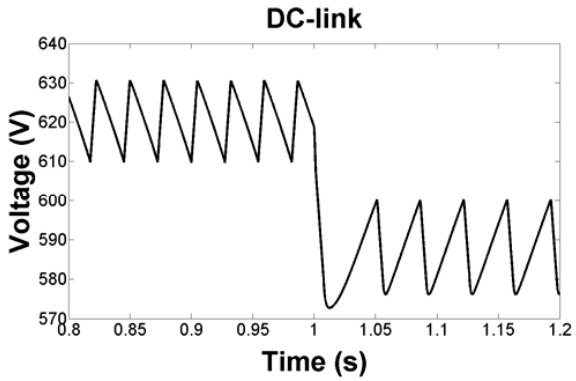

Fig. 5. The voltage control limits illustrated with constant current reference.

C. Modeling of the Active Rectifier

The active rectifier allows controlling of the output voltage of the dc-link's port. The active rectifier is modeled in a similar way as the dc/dc converters, which includes the ideal power transfer, the interface capacitance and the controllable current source. The output in the dc-link's port is voltage regulated, and the output voltage is calculated using the internal combustion engine's speed state value and also the voltage reference, which come from the superior control. The transferred power to the dc-link is measured and the necessary torque to maintain the speed reference of the internal combustion engine is solved. The generated transfer losses will be modeled using the efficiency data inside the lookup table.

Permanent magnet generator

The permanent magnet generator is modeled by taking into account the approximate efficiency value and the inertia of the rotor. The efficiency of the generator increases the torque value necessary from the internal combustion engine. The inertia of the rotor affects the speed states of the internal combustion engine.

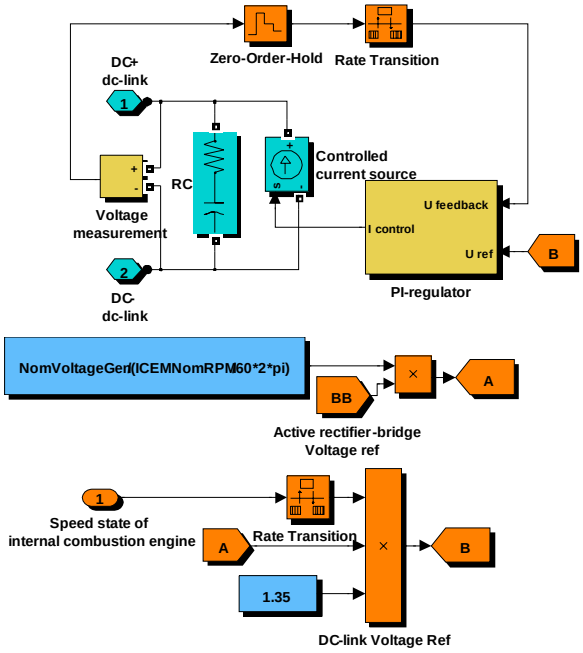

Fig. 6. The simulation model of the active rectifier

Solving the needed torque from the internal combustion engine

Modeling of the internal combustion engine is problematic because it operates behind its own electrical control unit. Therefore, the model of generator-set is superficial and includes only the inertia of the internal combustion engine and the speed control loop from which the required torque is solved. The torque is solved from the transferred power and from the speed state of the internal combustion engine and up rated with the efficiency value of the generator. The speed control loop, with the P-regulator, adjusts the required torque with the production of inertia as well as with the speed state adjustment signal.

D. Modeling of the Inverter load

The loading of the series-hybrid system is modeled using the recorded power consumption data. The heavy machinery's power consumption data can be recorded from the parameter values of the inverter in the machinery, which has electric drive train. The real power data gives information from rating of the secondary energy storages, the dc/dc converters as well as rating of the ICE. If the apparent power is used instead of the real power, the simulation offers information also from the necessary dc-link capacitance. The measured data can be driven out from the dc-link with the controllable current source. The inverters real power data is needed designing a supervisory control for different power flow directions and operation points. The other approach for the simulation of the load is to generate an approximate load curve with the signal builder block.

E. Modeling of the Brake chopper

The brake chopper is modeled using the current source parallel with the dc-link. The current source is controlled with a PI-regulator which is controlled with the dc-link voltage. As a functionality of the brake chopper, the current sources power transfer is limited by the maximum power, which can be dissipated into the brake resistor. The brake chopper enables when the dc-link's voltage overpasses the activation limit.

F. Modeling of the Power Sources

The ultracapacitors and the battery are modeled simply with an internal resistance, capacitance and with the energy storages initial condition. In reality, the equivalent circuit is more complex, but for the OEM needs this modeling level is sufficient. The supervisory control of the series-hybrid power transmission does not necessarily need information from voltage balance between subcomponents of the energy storage [10].

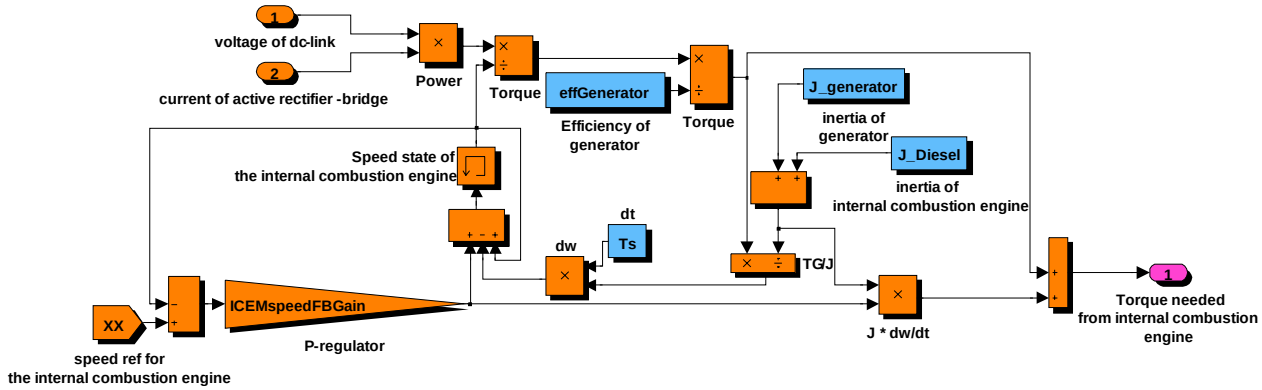

Fig. 7. The simulation model of the generator-set in the series-hybrid system

G. *Converting the Simulation Model to S-function*

The simulation model of the series-hybrid system is realized using the SimPowerSystems as well as the Stateflow components, which do not belong to basic Simulink libraries. Therefore, it is worthwhile to generate the S-function from the simulation model with the MATLAB/real-time workshop. The S-function belongs to the basic Simulink library, and after compilation, no other Simulink libraries are needed. This is an advantage because then the OEM does not necessarily need to have the same Simulink libraries as the university.

III. SYSTEM LEVEL POWER TRANSFER CONTROL

The power transfer in the series-hybrid system is realized through the dc voltage link. The first, requirement is to create algorithms for controlling the energy storages with the dc/dc converters and the internal combustion engine within the allowable control limits. For example, with the dc/dc converter, the voltage drop over the energy sources series resistance enforces the down rating of the current while operating near the energy sources maximum and minimum voltage levels [9]. Furthermore, the energy storages maximum voltage and power transfers efficiency's collapsing defines these voltage limits.

The second, requirement is to create algorithms and control logic for transferring power through the dc-link with stabilized dc-link voltage. Control with a stabilized dc-link voltage leads to minimized losses in the internal resistance of dc-links capacitor bank. It should be possible to transfer power from any source to any secondary energy storage. Information about the suitability of the controls is also gained from the torque curve of the ICE.

The third, requirement is to create the supervisory control for the series-hybrid power transmission. Several control strategies have been presented in the latest research papers. Simple control strategies are torque boost, in which an ultracapacitor module is used as support while accelerating and as storage while decelerating. Another simple control strategy is peak shaving, which smoothens loading from the ICE during continuous run with the ultracapacitor module. The need for slightly more complicated supervisory control strategies arises when a battery is included in the drive train. More sophisticated supervisory control strategies are presented in papers [6], [7], [10] and [11]. One interesting strategy, for example, is the Equivalent Consumption Minimization Strategy (ECMS) [7].

IV. TEST BENCH

The supervisory control for controlling the hybrid power transmission needs to be tested with the corresponding test setup. The testing is made with the test bench built in the automotive laboratory. The test bench includes an active rectifier-bridge (P_{cont} 310 kW) connected to a power grid, which can be used to simulate the active rectifier connected to the generator-set in the hybrid drive train. The dc/dc converter (P_{cont} 90 kW) and the ultracapacitor module (17,8F, U_{nom} 390V) are used for energy buffering in the test bench. The loading of the dc-link is created with an inverter (S_{cont} 120 kVA), which is connected to the induction motor (P_{cont} 67 kW). The induction motor is used against the dynamometer, which transfers power back to the power grid. The dynamometer has a continuous power limit of 120 kW. Parallel to the dc-link is the brake chopper, for which the power dissipation is rated as 60 kW. At the moment, the series-hybrid power transmission test bench is lacking Li-ion batteries as the

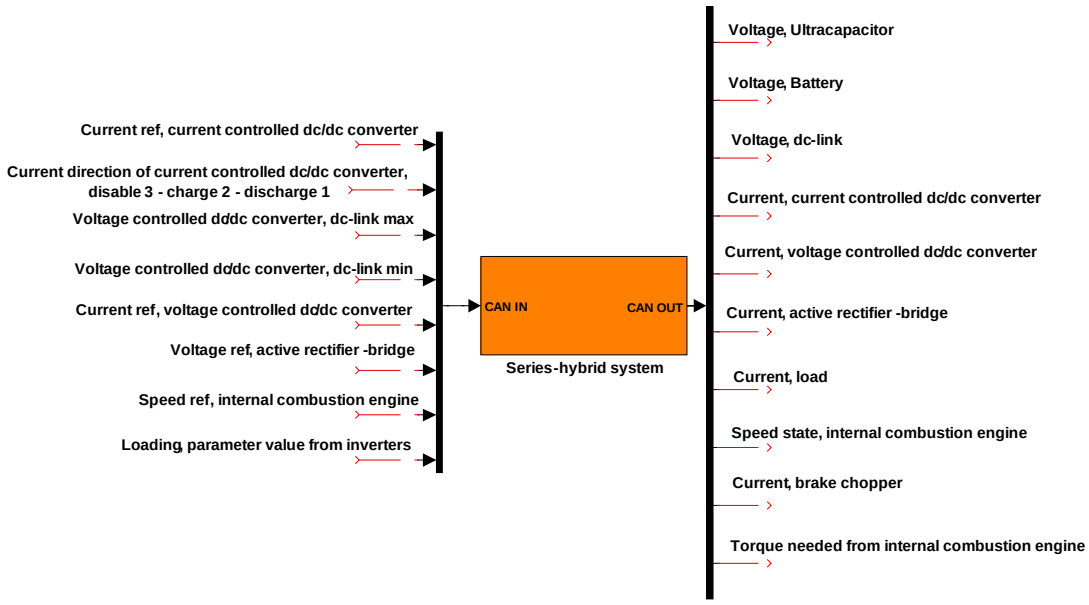

Fig. 8. S-function generated from the series-hybrid transmission simulation model and its control interfaces.

other secondary energy storage.

The series-hybrid power transmission system's components are connected to CAN-bus to Beckhoff industrial I/O interface, which is controlled with the dSPACE prototyping hardware MicroAutoBox. The dSPACE MicroAutoBox can be used to compile the Simulink models to C-code and also as the software platform [12].

Fig. 9. The test bench in the automotive laboratory

V. SIMULATION EXAMPLES

The simulation model is introduced with the control principle, where an ultracapacitor module is used for the power generation in fast load transients, whilst the battery current is ramped up to support the internal combustion engine [4]. The active rectifier is used for raising the dc-link voltage over the voltage controlled converters control limit. After disabling the ultracapacitors, the load current is supplied from the active rectifier and the battery.

The voltage controlled dc/dc converter is used with a 580 V minimum voltage level with 20 volts of control hysteresis. Its current is controlled with the quadratic function of the dc-link voltage. The current controlled dc/dc converter, which controls the battery, has a linear current reference as a function of the dc-link voltage, starting from the same dc-link voltage limit as the voltage controlled converter. Likewise, the control of the active rectifier is started from the same control limit and the voltage reference is ramped up as a function of the dc-link voltage.

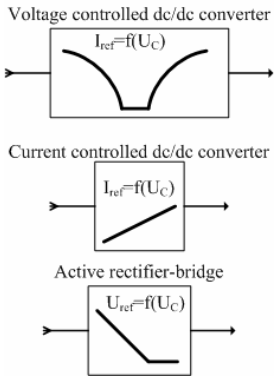

Fig. 10. The control functions in the example simulation

VI. FUTURE WORK

In the future, the series-hybrid power transmission systems control algorithms generation will be continued and the testing of the control logics is started with the hardware.

The test bench will be finalized with the lithium-ion battery energy storage connected via the current controlled dc/dc converter to the dc-link of the series-hybrid system's test bench. The active rectifier connected to the power grid is replaced with a combination of the generator-set and the active rectifier.

Efficiency measurement results from the dc/dc converter and from the inverter are included in the simulation model. As a result, the simulation model gives information for the rating of the liquid-cooling system.

Different supervisory control strategies will be simulated and tested in the test bench. In particular, strategies based on the inverter's power transfer parameter will be considered. Strategies with one and two current controlled energy sources, both voltage and current controlled energy sources are also investigated. Furthermore, it is possible to test different kinds of predictive control strategies, if proper data from the machinery's working cycle is available.

VII. CONCLUSIONS

This paper proposed a way to model the functionality of power electronic components in the series-hybrid drive train. For the generation of the simulation models the MATLAB/Simulink software with SimPowerSystem and Stateflow libraries were used. The model targeted to 20 Hz-bandwidths accuracy. The simulation models aim is to provide the possibility for early phase software design in the series-hybrid power transmission system, and is also a way to optimize the ratings of the secondary energy storages.

The construction and the operation principles of the sub-model components were presented and the route for the supervisory control generation was briefly described. The operation of the series-hybrid drive train was introduced with the control principle in which ultracapacitors were used for fast transient buffering while the battery and the internal combustion engine were used during steady state loading.

REFERENCES

[1] R. M. Schupbach, J. C. Balda, "Design methodology of a combined battery-ultracapacitor energy storage unit for vehicle power management", *IEEE Conf. Power Electronics Specialist*, vol. 1, pp. 88-93, Jun. 2003.

[2] K. E. Kadri, A. Djerdir, A. Berthon, "Hybrid energy sources for heavy truck: simulation and behavior" *Conf. EPE-PEMC 2006*, pp. 1395-1400, Aug. 2006.

[3] J. Bauman, M. Kazerani, "A comparative study of fuel-cell-battery, fuel-cell-ultracapacitor, and fuel-cell-battery-ultracapacitor vehicles" *IEEE Trans. on Vehicular Technology*, vol. 57, no. 2, pp. 760-769, Mar. 2008.

[4] R. M. Schupbach, J. C. Balda, "The role of ultracapacitors in an energy storage unit for vehicle power management", *IEEE Conf. Vehicular Technology*, fall 2003.

[5] W. Gao, "Performance comparison of a fuel cell-battery hybrid powertrain and a fuel cell-ultracapacitor hybrid powertrain" *IEEE Trans. on Vehicular Technology*, vol. 54, no. 3, pp. 846-855, May. 2005.
[6] M. J. Kim, H. Peng, "Combined control/plant optimization of fuel cell hybrid vehicles", *Proceedings of the American Control Conference*, pp. 496-501, Jun. 2006.
[7] P. Pisu, G. Rizzoni, "A supervisory control strategy for series hybrid electric vehicles with two energy storage systems" *IEEE Conf. Vehicle Power and Propulsion*, Sep. 2005.
[8] J. Lai, D. J. Nelson, "Energy management power converters in hybrid electric and fuel cell vehicles", *Proceedings of the IEEE*, Vol. 95, No. 4, pp. 766-777, Apr. 2007.
[9] P. Thounthong, S.Raël, B. Davat, "Control strategy of fuel cell and supercapacitors association for a distributed generation system", *IEEE Trans. on Ind. Electronics*, vol. 54, no. 6, pp. 3225-3233, Dec. 2007.
[10] J. Schiffer, O. Bohlen, R. W. D. Doncker, D. U. Sauer, "Optimized energy management for fuelcell-supercap hybrid electric vehicles", *IEEE Conf. Vehicle Power and Propulsion*, pp. 341-348, Sep. 2005.
[11] A. A. Ferreira, J. A. Pomilio, G. Spiazzi, L. A. Silva, "Energy management fuzzy logic supervisory for electric vehicle power supplies system" *IEEE Trans. on Power Electronics*, vol. 23, no. 1, pp. 107-115, Jan. 2008.
[12] (dSpace news) T. Schöberl, F.-G. Grein. (2008, Jan). Title. Experience the hybrid drive [internet]. Available: http://www.ceanet.com.au/Portals/0/downloads/Userstory/2008_1_customers_magna_steyr_en.pdf

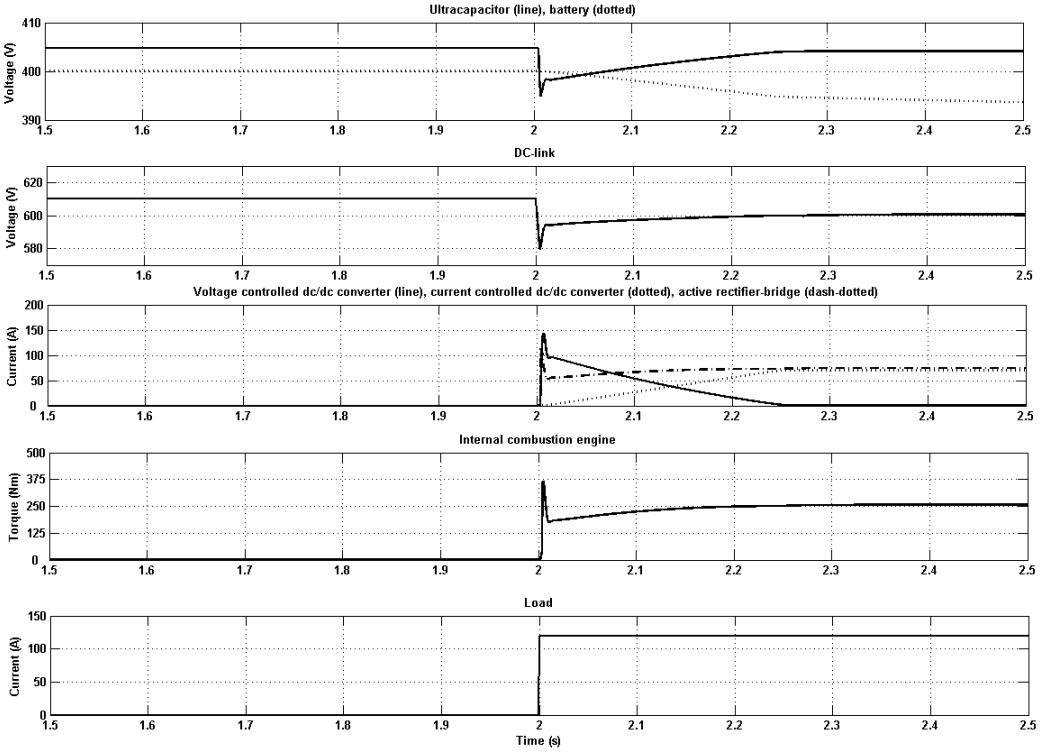

Fig. 11. Simulation results with the represented control principle.

Publication II

M. Liukkonen, A. Hentunen, J. Suomela, and J. Kyyrä, "Low-pass Filtered Power-flow Control in Series Hybrid Electric Vehicle," in *Proc. 24th Electric Vehicle Symposium* (EVS24), Stavanger, Norway, May 13-16, 2009.

Errata:

In Figs. 4 and 6 the y-axis should be:

$$u_{\text{ratio}} = u_{\text{es}}/u_{\text{DC}}.$$

Fig. 7 proposes the DC-DC converter current direction D to be chosen by incorrect way, and Fig. 8 presents an algorithm which was corrected based on later studies. Section 3.11 in this thesis, presents the correct algorithm structure validated by experiments.

EVS24
Stavanger, Norway, May 13-16, 2009

Low-pass Filtered Power-flow Control in Series Hybrid Electric Vehicle

Matti Liukkonen [1], Ari Hentunen [1] Jussi Suomela [2], Jorma Kyyrä [1]

[1] *M. Liukkonen is with Helsinki University of Technology, Department of Electrical Engineering, P.O. Box 3000, FI-02015 TKK, Finland (e-mail: matti.j.liukkonen@tkk.fi; ari.hentunen@tkk.fi; jorma.kyyra@tkk.fi).*

[2] *J. Suomela is with Helsinki University of Technology, Department of Automation and Systems Technology, P.O. Box 5500, FI-02015 TKK, Finland (e-mail: jussi.suomela@tkk.fi)t*

Abstract

This paper presents a low-pass filtered power-flow control strategy for a series hybrid electric vehicle (S-HEV) with an energy buffer. The proposed control aims to decrease the maximum power values from the primary energy source and, secondly, to reduce the engine-generator dynamics at sudden load changes (from low loads at low speed to high loads). In case of variable speed diesel generator (VSDG) set downsizing reduces the emissions and the fuel consumption. The proposed control strategy is introduced with two different driving cycles, both, for the urban and the sub-urban areas. The energy losses, caused by the energy buffering, and the sizing of heavy duty vehicle's series hybrid drive train are gained as a result.

Keywords: Low-pass filtered power-flow control, heavy duty vehicles, plant optimization, series hybrid electric vehicle, simulation

1 Introduction

THIS study is part of a duty vehicles hybridization project. Heavy duty vehicles typically have very machine and task specific cycles, which are difficult to generalize. Therefore, the well known Braunschweig and New European Driving (NEDC) cycles have been used in order to provide new information about power losses in supercapacitor (SC) buffered series HEV driveline. The study, which is made for the duty machines, can also be utilized for heavy duty road vehicles such as trucks and busses.

Usefulness of the hybrid electric driveline depends on the load cycle. Therefore, this paper presents a low-pass filtered power-flow control [5], [7]-[9], [11], [16] with two different load profiles, which argues for both convenient and inconvenient cycles. As a result, the study offers confirming data for reducing the size of the primary energy source compared to other research [8], as well as, sizing and power losses, in both, in the SC and in the dc/dc converter of the system [6].

It has been shown that bad dynamical properties of the system for the VSDG, as in conventional drive train, can be considerably improved by implementing power electronic converters with an energy buffer [12]. The low-pass filtered power-flow control reduces dynamic requirements from the primary energy source.

The presented low-pass filtered power-flow control also seeks methods to reduce the deep discharge cycles from the SC, which causes limited life-time in very cyclic applications. In order to achieve sufficient lifetime of supercapacitors, it should be avoided to use the full operation range of the SC (50% to 100% state of charge, SOC), which has a limited lifetime of 1 million cycles.

2 Introduction

2.1 Topology

The series hybrid drive train is presented in Fig. 1. The VSDG generates ac current to the active front end converter (AFE), which converts the ac current to the dc current and stabilizes the dc link voltage. The AFE regulates the dc link voltage to 650 V in the proposed system. The energy storage (ES), in this case a supercapacitor module, is connected via the dc/dc converter to the dc link. The inverter is connected to the dc link and is used directly from Power Management System (PMS) for the traction control purposes.

The proposed variables for the power-flow control are the load power to the inverters, the speed of the vehicle, the dc link voltage and the energy storage voltage [9], [10]. The load power can be considered as a measured or as a feedforward value [4]. The control signals for the power-flow control are the dc link voltage reference, which would be controlled from the PMS, feedforward power flow for the AFE, the dc/dc converter's current and the speed of the VSDG [2] [12]. VSDG is controlled within optimal operation area [14] [16]. The system topology, the control signals and variables are shown in Fig. 1.

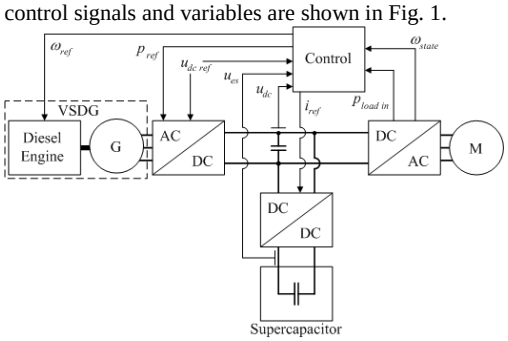

Fig. 1 The system topology, the control signals and control variables for the supercapacitor buffered series-hybrid electric transmission.

2.2 Propulsion power in the Driving Cycles

The required propulsion power from the electric transmission is determined based on the system constraints as maximum acceleration, rated and maximum vehicle velocity, and vehicle gradability. The propulsion power calculation is straightforward with the following equations. First, the total traction force is solved:

$$F(t) = C_0 mg + \frac{1}{2}\rho C_d A_F v(t)^2 + ma(t) \quad (1)$$

where $F(t)$ is the traction force as a function of time, C_0 is the static friction coefficient, m is the mass, g is the gravitation, ρ is the air density, C_d is the air friction coefficient, A_F is the cross-sectional area, $v(t)$ is the current velocity according to time, and a is the acceleration as a function of time. Then, the propulsion power $P(t)$ as a function of time is:

$$P(t) = F(t)v(t) \quad (2)$$

Therefore, solving of the propulsion power starts from the driving cycle, which gives the current speed and the acceleration as a function of the time. In the simulations we use the NEDC and the Braunschweig cycles to demonstrate the behavior of the presented control, as in reference [7]. Table I shows the environment and the vehicle parameters used to simulate the required propulsion power.

TABLE I
Environment and vehicle parameters in simulations [1]

Symbol	Quantity	Value
C_0	static friction coefficient	0,013 s^2/m^2
m	mass	10 000 kg
g	gravitation	9,81 m/s^2
ρ	air density	1,29 kg/m^3
C_d	air friction coefficient	0,3
A_F	cross-sectional area	8 m^2

Fig. 2 illustrates the speed and the required propulsion power for the NEDC and Fig. 3 represents the same variables for the Braunschweig cycle. These figures depict how the propulsion power reaches its highest values in the end of the acceleration and the regenerative power at the start of the deceleration.

The NEDC represents both, the urban and the sub-urban area cycles. As from the Fig. 2 can be seen, the change point of the urban and the sub-urban areas in the NEDC is in the 800 seconds. The Braunschweig cycle simulates only the urban area operation with shorter accelerations and decelerations contrary to NEDC.

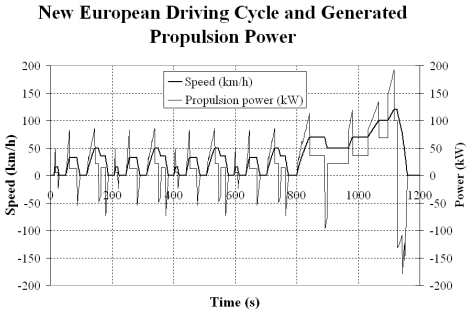

Fig. 2 The New European Driving Cycle and the required propulsion power (duration 1160 s, length 11.0 km, average speed 34.2 km/h, max speed 120 km/h, share of idle 22.4%).

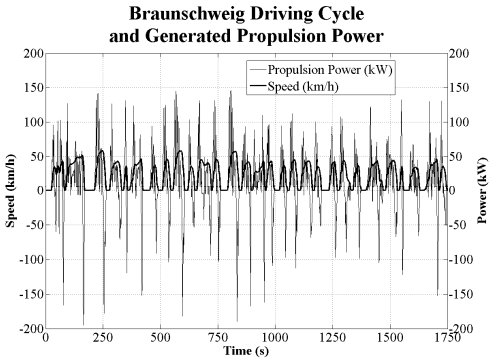

Fig. 3 The Braunschweig driving cycle and the required propulsion power (duration 1740 s, length 10.9 km, average speed 22.5 km/h, max speed 58.2 km/h, share of idle 25%).

The following simulations are made to illustrate how the maximum propulsion power can be reduced with the low-pass filtered power-flow control in different driving cycles, and which are its drawbacks.

Besides the propulsion power calculated from the driving cycles, the simulated cases are assumed to consume constant power to auxiliary devices of the vehicle. Constant power is simply added to propulsion power. In these simulation cases proper constant power consumption would be e.g. 10 kW, which is later used in the simulations.

2.3 Power losses in simulations

The power transfer efficiencies have a significant role in order to define the usefulness of S-HEV driveline. In this paper, the power losses deriving from power-flow filtering in dc/dc converter and supercapacitor module are considered. This is realized with measurement based efficiency maps from the dc/dc converter and ESR value of a commercial supercapacitor module. The power losses in other converters and electric machines of studied system are left out of the scope, though; they are still modeled with the same hybrid simulation modeling principle.

Inverters, rectifiers and traction motors, are modeled based on hybrid simulation modeling of converters and electric machines. These models are built with the efficiency maps received from the manufacturer. In hybrid simulation models, the transferred power through the power train is scaled with the efficiency value of the operation point of the device in question.

Simulations concentrate only on system level power transfer. Therefore, typical behavior of the supercapacitors electrochemical characteristics is left out of consideration and simulations only consider electrical characteristics of the energy storage. Although supercapacitors resistance and capacitance are state of charge dependent, supercapacitor modules are simulated with constant equivalent series resistance and capacitance [13]. Also, leakage currents of supercapacitors are neglected.

2.4 Hybrid Simulation model of the dc/dc converter

Dc/dc converter's transient behavior is neglected in the simulations, which causes a small error to the supervisory control simulations by the step response of modern dc/dc converter. Therefore, dc/dc converters are assumed to be ideal and the simulation steps are pushed longer.

The power losses during the converter's operation are defined with the measured efficiency data. Efficiency values from the converter's different operation points are used to calculate the power losses in the dc/dc converter and in the SC module during the energy buffering [3]. In the simulations, when operation point exceeds the limit of the efficiency map, the end value of the map is used. Preceding approach is widely called as a hybrid simulation model.

Fig. 4 shows the efficiency map of the buck-boost dc/dc converter as a function of the transferred current and the ratio between upper and lower voltage levels. The figure represents charge operation and it is based on the measurements done for the dc/dc converter which has interleaved inductor phases and 120 amps nominal current.

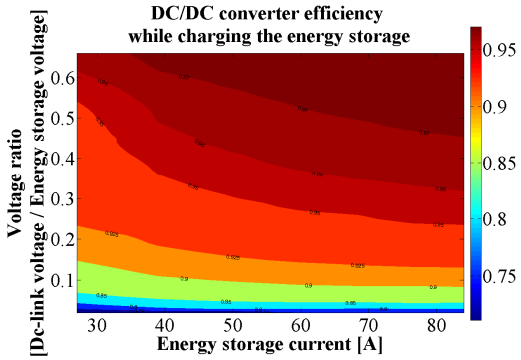

Fig. 4 The measured efficiency map of the dc/dc converter during charge operation.

The total power transfer efficiency from the dc link side is solved from the efficiency maps of the charge and discharge operations of the dc/dc converter, and also with the equivalent series resistance (ESR) of the supercapacitor module. One efficiency map of the energy storage according to ESR losses is shown in Fig. 5. The efficiency map from the ESR losses is calculated with the equation:

$$\eta = \frac{u_{sc} - R_{ESR} * i_{sc}}{u_{sc}}$$

where η is the efficiency, u_{sc} is the voltage of the SC module, R_{ESR} is the equivalent series resistance attained from the datasheet [15] and i_{sc} is the current of the SC module.

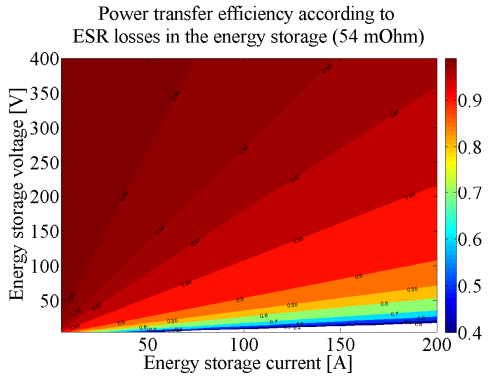

Fig. 5 The power transfer efficiency according to ESR losses in the energy storage.

Accuracy of solving the power losses in a supercapacitor module is reduced when the losses are calculated only with ESR value of the dc resistance. This is because the capacitance of a supercapacitor is very frequency dependent [13]. Therefore, assumption with supercapacitor power losses modeling is that converters transfer only dc current and power losses caused by converters switching frequencies are neglected. So, the simulated power losses in the supercapacitor module are considered to be the minimum that can be realized. Previous further speeds up system level modeling, while more accurate modeling of losses with higher frequency components make simulations unnecessary complicated.

Fig. 6 represents the total power transfer efficiency of the energy buffering. Figure is done by multiplying efficiency maps from the dc/dc converter and from the supercapacitor module with each other. So, the figure takes into account charge and discharge operations of the dc/dc converter and the ESR of the supercapacitor module. This figure is based on both theoretically calculated and experimentally measured efficiency values.

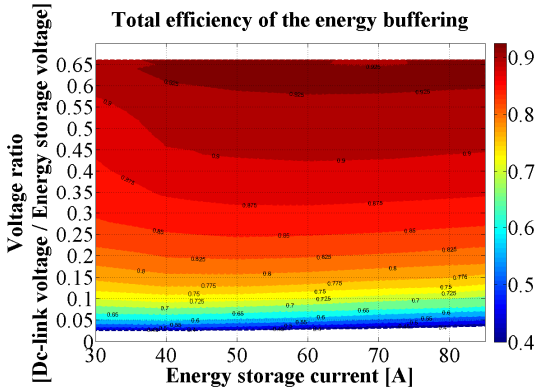

Fig. 6 The total power transfer efficiency map from the dc link side according to theoretical calculations and experimental measurements.

3 Presented power-flow control

3.1 Power-flow control in the dc link

The low-pass filtered power-flow control, which is previous presented in studies [5], [7]-[9], [11], can be implemented above the system shown in Fig. 1. It can be generalized into two parts. The first is the peak power shaving control algorithms and the second is the low-pass filtered power-flow control, which is build on the top of the first one. The low-pass filtered power-flow control simply makes the peak power shaving limits to move.

3.1.1.1 The Peak Power Shaving control

The proposed peak power shaving control is based on the minimum and the maximum power limits. These limits can also be used to specify the converter's current direction. The power limits are compared with the subtraction to the measured load power, and the result is saturated either with the normal or with the dynamic saturation. The minimum power limit is creating an inverse of the correct power buffering value; therefore it is needed to take absolute value from power buffering signal. The saturation values for the peak power shaving are from the zero to the maximum desired, and for the power buffering from the maximum buffered power to the power which triggers the buffering. The previous signals are next divided by the state value of the dc link voltage for to achieve the peak shaving and buffering current references. By adding them together, we attain dc/dc converter's current reference in the dc link side. Then, the error value from dc link's voltage is added to the current reference with the proportional gain for to more stabilize the dc links voltage. In the end, the current reference is shifted to ES's voltage level, in case where the dc/dc converter is designed to control the current in the ES's side.

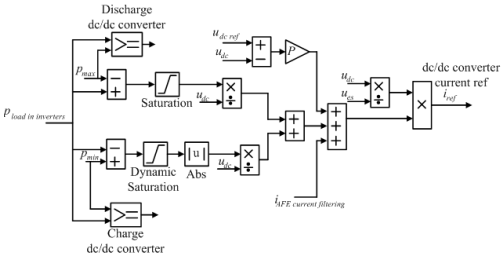

Fig. 7 The Peak Power Shaving control.

3.1.1.2 The low-pass Power-flow control

The low-pass power-flow control, which is shown in Fig. 8, is built on the top of the peak power shaving control. In the proposed control strategy, the idea is to make the maximum and the minimum power limits to move as a function of the load power and the voltage of the ES.

First, the state value of the load power is determined and brought to the supervisory control. Second, the discrete finite impulse response (FIR) filter averages the load power. This could also be made with several filters with different time constants [11]. According to the simulations it is suggested that the power is averaged with the time of the longest acceleration during the driving cycle [7]. In this paper filtering is done with only one time constant, which is 20 seconds. Third, the filtered power is weighted with 2 - 1/75000*$p_{filtered}$ function. This function priories the power buffering to take place in low loads instead of times of high loads.

In contrast to filtered load power value, energy storage's voltage determines the power level, which needs to be generated by the primary energy source. Previous is realized with a function, which gets high power values at low energy storage's SOC and vice versa. In the simulations this function was formulated as 75000 – 750/5*v, and it is only scaled with maximum energy storage's voltage level value between different simulation cases. In principle, this function creates power limit plane which defines either to cut peak powers or buffer the power from the VSDG. In addition, weighted function from energy storages voltage is filtered with 2 seconds time constant, which is also used to filter the variation of the power limit plane.

In the low-pass filtered power-flow control, the next step is to multiply prioritization function from the filtered load power and the power level created by energy storage's voltage. The result creates a weighted power limit plane as a function of filtered load power and energy storages voltage. Then; the hysteresis are added to the created power limit plane. These hysteresis are used to create delay between dc/dc converter's charging and discharging control signals. After hysteresis, control schemes from Fig. 7 and Fig. 8 interconnect. The proposed power limit plane has built-in maximum voltage limit for the SC.

Fig. 8 also presents algorithm, which filters more the AFE current. This AFE current filtering is also added to dc/dc converter current reference, shown in fig. 7, with the proportional gain value. The AFE current filtering component is calculated from the state value of the AFE current, filtered value of the AFE current and with multiport switch, which takes in consideration of present current direction in dc/dc converter. Filtering of the AFE current was done with 20 seconds time constant.

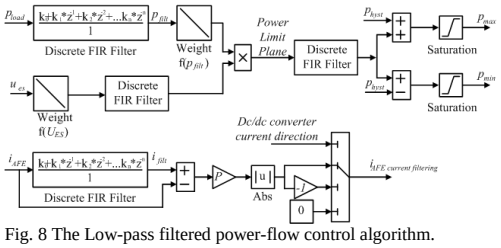

Fig. 8 The Low-pass filtered power-flow control algorithm.

The system without a load is driven automatically to high SOC value, if the power limits are kept high compared to the present state of the load power. This provides SOC to be adequate for the next acceleration. Fig. 9 presents the PLP set by the weighted variables.

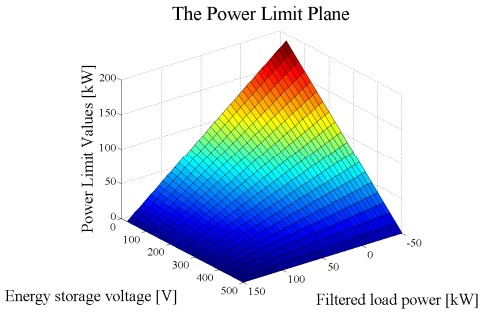

Fig. 9 The power limit plane set by weighted values from energy storage's voltage and the filtered power.

Table II presents the parameter values which were used in the introduced control.

TABLE II
Current controller parameters in the simulations

Symbol	Quantity	Value / function
P	Proportional gain in fig. 7	0,25
P	Proportional gain in fig. 8	0,5
i_{ref}	Dc/dc converter's current ref in the energy storage side	--
$f(p_{filt})$	The weighting function for the filtered power	$2 - 1/75000*p_{filtered}$
$f(U_{ES})$	The weighting function for the energy storage voltage	$75000 – 750/5*v$

3.2 The flowchart of the proposed power-flow management

Fig. 10 represents the startup flowchart for the proposed power-flow management. In the beginning, the system is in rest. After the auxiliary power is switched on, the VSDG is started and the supercapacitor module is charged to the specified level. Then, the dc link voltage is regulated with the AFE to 650 V level. After the activation of the dc link voltage regulation, the low-pass power-flow control begins to operate.

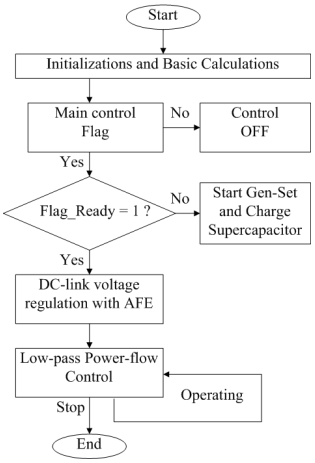

Fig. 10 The flowchart of the proposed power-flow management algorithm.

3.3 Control of Active Front End converter in the simulations and generation of operation points of the Diesel Engine

In the proposed control, the dc link voltage is stabilized with the active front end converter. AFE get its control signals from the supervisory control as a dc link voltage reference and as a transferable power to the dc link. The voltage reference was set to 650 V during the simulations and the power reference was calculated from the static traction power component of equations 1 and 2. So, feedforwarded power reference was calculated without the term, which included acceleration.

In the used AFE simulation model, limited maximum current as a function of the generator speed specifies the maximum counter torque of the VSDG simulation model. As a VSDG simulation model was used one-dimensional model of the diesel-engine. The difference between the VSDG maximum torque and the limited counter torque of the AFE define dynamical torque, which is used for the speed change of the VSDG. The control strategies of the variable speed diesel generating systems were further studied in [14].

The speed reference for the VSDG can be obtained with several different strategies [14]. Proposed control in the simulations formulates the VSDG speed reference from the transferred power of the AFE. Created operation points in one simulation of this control strategy are shown in Fig. 11. Figure presents generated power of the VSDG as a function of the speed of the VSDG with red crosses. Period between operation points was half second. In

addition, the figure includes maximum power curve of the VSDG simulation model (black curve) the maximum power of AFE specified by its counter torque (blue curve) and specific fuel consumption curves of the used VSGD simulation model.

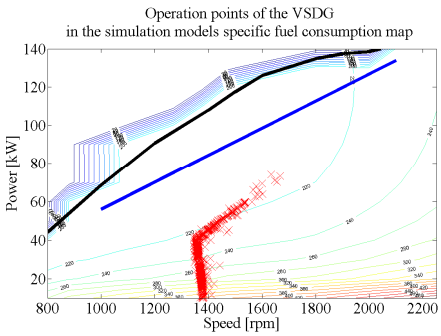

Fig. 11 The variable speed diesel generator operation points at the start of one simulation case with Braunschweig driving cycle and 31,5 F energy storage.

Operation points of the VSDG during simulation are determined by equation:

$$\frac{d\omega}{dt} = \frac{T - T_L}{J} \qquad (5)$$

where $d\omega/dt$ is differential speed change, T is torque of the VSDG, T_L is counter torque of the AFE and J is inertia of the gen-set shaft. In the simulations, inertia of the simulated VSDG was assumed to be 1 kgm^2 and the initial speed of the VSDG was 1400 rpm.

4 Simulations

The simulations are done with the 5 combinations of the capacitance value of the SC module and its maximum voltage level. The results from the simulations are tabulated and simulation figures from Case I are shown. Table III represents the SC dimensioning in different simulation cases. Energy storage's nominal values are based on manufacturer data. In these simulation cases supercapacitors are considered as built-in modules, which include cells, connections between cells, voltage balancing circuits, packaging and cooling [15].

TABLE III
Dimensions of the energy buffer in different simulation cases [15]

Quantity	Values Case I	Values Case II	Values Case III	Values Case IV	Values Case V
Capacitance (F)	31,5	42	63	12,6	25,2
ESR (mΩ)	34	25,5	17	85	42,5
Maximum Voltage (V)	500	375	375	625	625
Weight (kg)	464	348	522	290	580
Usable energy (kWh)	0,82	0,62	0,92	0,512	1,03
Continuous current (A)	300	300	450	150	300
Maximum current (A)	1500	1500	2250	750	1500
Modules (series / parallel)	(4 / 2)	(3 / 2)	(3 / 3)	(5 / 1)	(5 / 2)
Cells (series / parallel)	(188 / 2)	(141 / 2)	(141 / 3)	(235 / 1)	(235 / 2)
Initial Voltage (V)	450	337,5	337,5	562,5	562,5

* The efficiency map of the dc/dc converter is extrapolated in simulation cases where the maximum voltage value rises higher than 400 V.

The simulation figures present the total load current, the dc/dc converter current, the AFE current, the energy storages voltage and the dc link voltage, which are variables of proposed control algorithm.

4.1 The simulation figures with NEDC

The load current, which was drawn from the dc link, was solved with equations 1, 2 and with dc link voltage state. In addition, current change rate were limited not to reach infinite value and to imitate proper ramp times of power converters. The load current, in case I, is shown in Fig. 12 during three rounds of ECE cycle.

4.1.1.1 Simulations with the ECE cycle

Figures 12 – 15 presents three rounds of simulations with ECE cycle. This means 600 seconds long simulation.

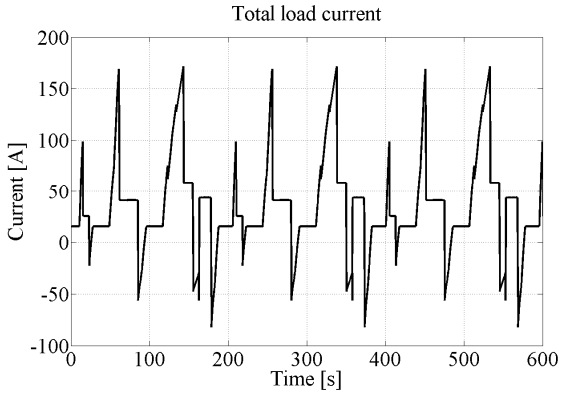

Fig. 12 The simulated load current, which was solved from the traction power and from constant power consumption during three rounds of ECE cycle.

In this study presented control scheme creates dc/dc converter current, which is shown in Fig. 13. This dc/dc converter current is presented in energy storage voltage level.

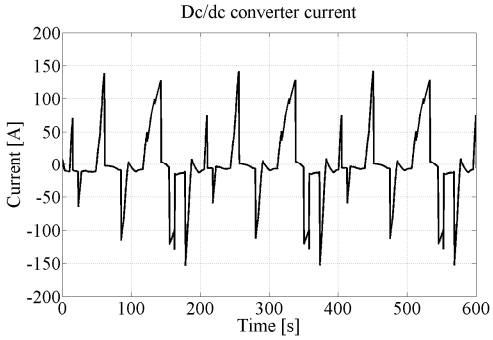

Fig. 13 The simulated dc/dc converter current, in case I, during three rounds of ECE cycle.

The simulated active front end converter current in the dc bus is shown in fig. 14. The figure shows a result of low-pass power filtering with dc/dc converter and simultaneous dc link voltage regulation of the AFE.

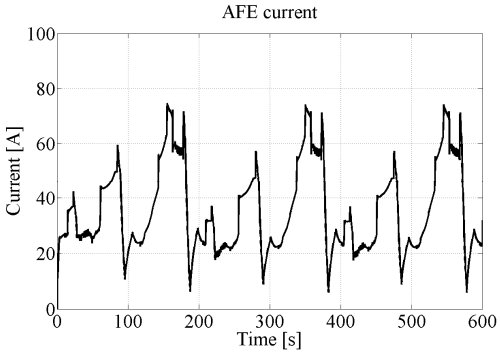

Fig. 14 The simulated AFE current, in case I, during three rounds of ECE cycle.

The simulated energy storage's voltage is shown in fig. 15. In simulation case I, the energy storage's capacitance was assumed to be 31,5 Farads and the ESR 34 mΩ.

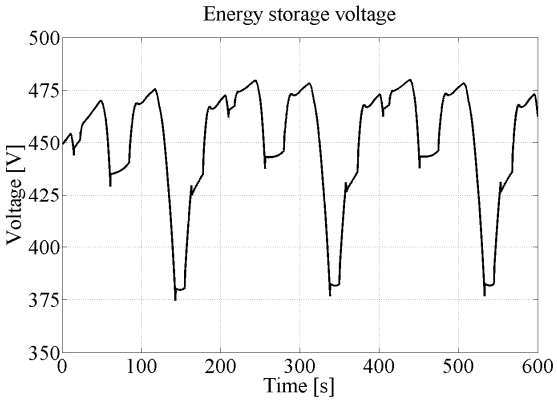

Fig. 15 The simulated supercapacitor module voltage, in case I, during three rounds of ECE cycle.

The dc link voltage was regulated in the simulations with the AFE, which got controls as a voltage reference and as a feedforward power transfer value. The simulated dc link voltage value is presented in fig. 16. In the simulations, the dc link capacitance was chosen to 40 mF, which directly affects to the variation of the dc link voltage.

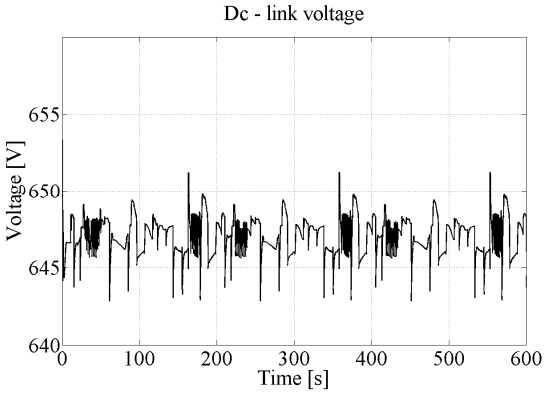

Fig. 16 The simulated dc link voltage, in case I, during three rounds of ECE cycle.

4.1.1.2 Simulations with the New European Driving Cycle

Next, the simulation results with the NEDC after 800 seconds are shown.

Figure 17 shows the dc/dc converter current during sub-urban part of the NEDC. In the end of the simulation figure can be seen the current spike, which is caused by energy storages voltage drop.

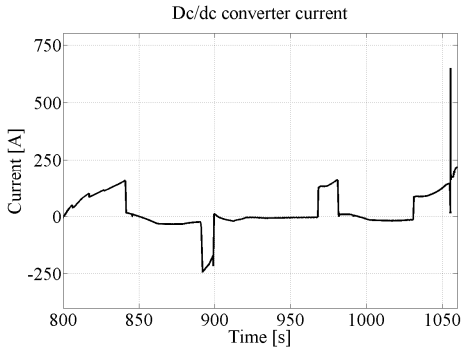

Fig. 17 The simulated dc/dc converter current, in case I, during NEDC sub-urban part.

The figure 18 shows the energy storages voltage, which causes failure of the simulated series hybrid power transfer during sub-urban part of NEDC. From the figure we can see that energy storages voltage drops to zero after 1050 secons of simulation.

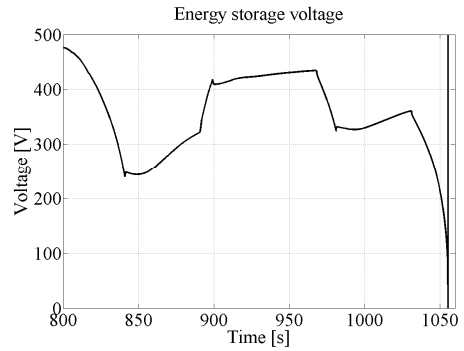

Fig. 18 The simulated supercapacitor module voltage, in case I, during NEDC sub-urban part.

4.2 The simulation figures with Braunschweig driving cycle

Simulations with the Braunschweig driving cycle were performed as NEDC. Following are shown simulation figures from control variables during Braunschweig driving cycles. Here only 400 seconds are shown to make pictures clearer, although results are obtained with 1800 seconds simulation. Fig. 19 represents the total load current, which was solved from Braunschweig driving cycle and from the constant power consumption.

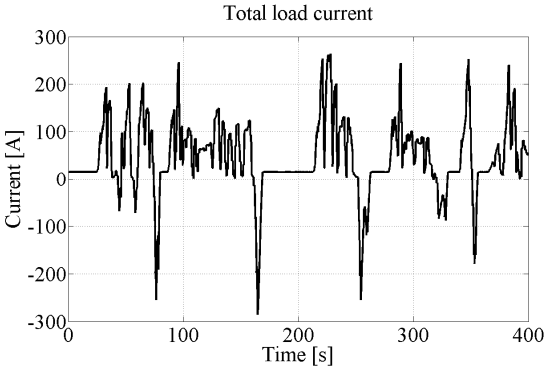

Fig. 19 The simulated load current, which was solved from the traction power and from constant power consumption for the 400 first seconds.

Fig. 20 shows the dc/dc converter current in the ES voltage level.

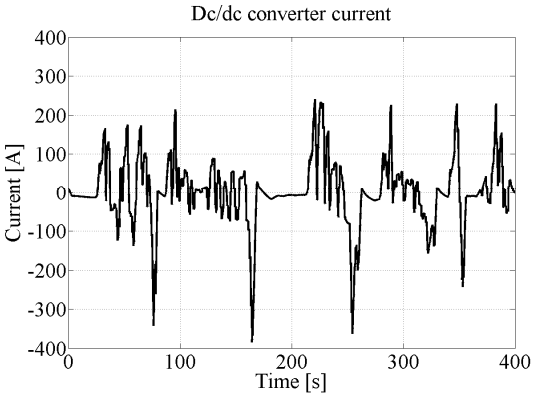

Fig. 20 The simulated dc/dc converter current, in case I, with Braunschweig driving cycle.

The active front end converter current was result of low-pass filtered power – flow control and regulation of the dc link voltage. The AFE current is shown in fig. 21.

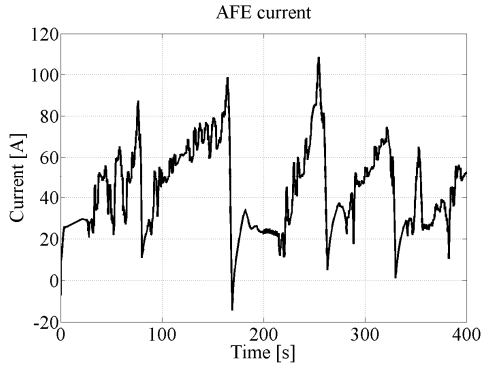

Fig. 21 The simulated AFE current, in case I, in the beginning of Braunschweig driving cycle.

In the Braunschweig driving cycle the ES voltage varied almost between nominal and half of the nominal value. This can be seen from fig. 22.

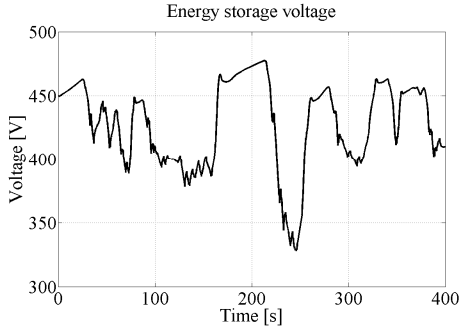

Fig. 22 The simulated supercapacitor module voltage, in case I, with the Braunschweig driving cycle.

The dc link voltage, which was also one of the control variables in the proposed control, is shown in fig. 23.

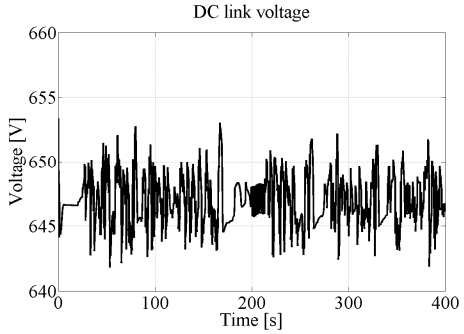

Fig. 23 The simulated dc link voltage, in case I, with the Braunschweig driving cycle.

4.3 The simulation results for both driving cycles

Following tables IV and V present the simulation results from the ECE and the Braunschweig cycles low-pass power filtering. These tables consists data from peak power decrease of the primary energy source, energy losses during low-pass power filtering and rating of dc/dc converter and supercapacitor module.

The maximum propulsion power in ECE cycle was 96,2 kW, which includes both the traction power and the constant power consumption. Similar value for the Braunschweig cycle is 156 kW.

TABLE IV

Simulation results with 4 rounds of ECE cycle

Quantity	Case I	Case II	Case III
Maximum power from the VSDG, [%] of the maximum load	60,9 %	59,9 %	59,4 %
Energy losses in the dc/dc converter, average value during 4 simulation rounds	525 Ws	684 Ws	693 Ws
Energy losses in the supercapacitor ESR	230,1 Ws	353 Ws	209 Ws
ES maximum current	156 A	158 A	155 A
ES rms current	31,3 A	31,0A	31,7 A
Voltage after 4 ECE cycles	439 V	333 V	328 V

	Case IV	Case V
Maximum power from the VSDG, [%] of the maximum load	72,6 %	60,3 %
Energy losses in the dc/dc converter, average value during 4 simulation rounds	542 Ws	517 Ws
Energy losses in the supercapacitor ESR	526 Ws	215 Ws
ES maximum current	157 A	157 A
ES rms current	31,2 A	31,4 A
Voltage after 4 ECE cycles	524 V	506 V

TABLE IV

Simulation results of Braunschweig cycle

Quantity	Case I	Case II	Case III
Maximum power from the VSDG, [%] of the maximum load	53,4 %	60,0 %	50,8 %
Energy losses in the dc/dc converter, average value during 4 simulation rounds	910,2 Ws	1235 Ws	1120 Ws
Energy losses in the supercapacitor ESR	628 Ws	1043 Ws	579 Ws
ES maximum current	387 A	400,0 A	383 A
ES rms current	55 A	54,9 A	55,4 A
Voltage after 4 ECE cycles	429 V	316 V	313 V

	Case IV	Case V

Maximum power from the VSDG, [%] of the maximum load	*	54,4 %
Energy losses in the dc/dc converter, average value during 4 simulation rounds	*	883 Ws
Energy losses in the supercapacitor ESR	*	573 Ws
ES maximum current	*	390,0 A
ES rms current	*	54,9 A
Voltage after 4 ECE cycles	*	495 V

* The energy storages' voltage dropped to zero with the proposed control parameters.

The performed simulations suggest that in urban areas and with very cyclic driving cycles it is possible to decrease peak powers to half of their original values. This peak power reduction can be done with several ways. The proposed low – pass filtered power flow control efficiency is dependent from the control parameters and from the dimensions of the energy storage. By increasing the amount of series coupled supercapacitor cells we can decrease energy losses in the dc/dc converter and in the ES. On the other hand, by paralleling supercapacitor cells or modules, we can decrease energy losses in the energy storage. Paralleling of supercapacitors naturally increases the capacity of the energy storage, which affects the stability of the power – flow control and also to the energy losses of the dc/dc converter.

5 Conclusion

The simulations suggest that the low-pass power control can achieve near 50 % down rating of the maximum power from the primary energy source, while in same time the energy storage's voltage fluctuates within 50 % of its maximum value. Previous conclusion is related to vehicles that are moving only in urban areas or have very frequent accelerating decelerating cycles. The low-pass power-flow control is not that effective when changed to sub-urban areas, where high power demand for energy storage charging and for traction purposes together comes with the delay. In cases of higher power peaks, as in sub-urban area driving cycles, more capacitance in energy storage is needed.

Simulations with different driving cycles suggest that the highest decrease for the primary energy source peak power is achieved in driving cycle with short accelerations and decelerations. Previous conclusion can be made by comparing simulation results from ECE, NEDC and Braunschweig driving cycles.

Energy losses generated by the low – pass power filtering algorithm is depended on the control parameters and from the dimensions of the supercapacitor module. Simulations clearly showed the benefit of paralleling supercapacitor modules, which decreases the ESR, and thereby the losses in the supercapacitor module. Also, the maximum operation voltage of the supercapacitor module showed its expected advantage when dc/dc converter energy losses are considered.

As a drawback, in the simulations, proposed control algorithm couldn't manage the peak power of the NEDC when driving cycles speed achieved 120 km/h. In addition, in this control algorithm the VSDG is used to charge the energy storage, which leads to unwanted generation of power transfer losses. However, this study was made to demonstrate possibilities to cut peak power values from the primary energy source.

In the case of Fuel Cell (FC) based systems, the very high cost of FC stacks makes it very important to reduce their nominal power [2]. This also can be achieved by low-pass filtered power flow control with long time constant, when only average power of the load is supplied to the dc link.

6 Acknowledgements

This study has been carried in HybDrive and HybLab projects financed by TEKES and TKK/MIDE, respectively.

REFERENCES

[1] I. Husain, *Electric and Hybrid Vehicles, Design Fundamentals.* CRC Press LLC, the United State of America, 2003.

[2] M. Ceraolo, A. Donato, G. Franceschi, "A General Approach to Energy Optimization of Hybrid Electric Vehicles", *IEEE Trans. on Vehicular Technology*, Vol 57, pp. 1433-1441, May 2008.

[3] M. Liukkonen, A. Hentunen, J. Suomela, J. Kyyrä, "Functional Simulations of Power Electronics Components in Series-Hybrid Machinery for the needs of OEM", *Nordic Workshop on Power and Ind. Electronics*, Jun. 2008.

[4] H. Yoo, S. K. Sul, Y. Park, J. Jeong "System Integration and Power-Flow Management for a Series Hybrid Electric Vehicle Using Supercapacitors and Batteries", *IEEE Trans. on Industry Applications*, Vol 44, pp. 108-114, Jan.-Feb. 2008.

[5] C. Andersson, "Observations on Electric Hybrid Bus Design", *Licentiate thesis, Dep. of Ind. Electrical Eng., Lund University*, pp. 65-80, 2001.

[6] R. Barrero, X. Tackoen, J. Van Mierlo, "Analysis and configuration of supercapacitor based energy storage system on-board light rail vehicles", *EPE-PEMC 2008 conference*, pp. 1512-1517, 1 – 3 Sept. 2008.

[7] Y. Cheng, J. Van Mierlo, P. Lataire, G. Maggetto, "Test Bench of Hybrid Electric Vehicle with the Super Capacitor based Energy Storage", *IEEE International Symposium on Ind. Elec.*, pp. 147-152, 4 – 7 Jun. 2007.

[8] Y. Cheng, J. Van Mierlo, P. Van den Bossche, P. Lataire, "Energy Sources Control and Management in Hybrid Electric Vehicles", *EPE-PEMC 2006 conference*, pp. 524-530, Aug. 2006.

[9] Y. Cheng, J. Van Mierlo, P. Van den Bossche, P. Lataire, "Super Capacitor based Energy Storage as Peak Power Unit in the Applications of Hybrid Electric Vehicles", *The 3rd IET International Conference on Power Elect., Machines and Drives*, pp. 404-408, Mar. 2006.

[10] M. J. Kim, H. Peng, "Combined control/plant optimization of fuel cell hybrid vehicles", *Proceedings of the American Control Conference*, pp. 496-501, Jun. 2006.

[11] J. Bauman, M. Kazerani, "A Comparative Study of Fuel-Cell-Battery, Fuel-Cell-Ultracapacitor, and Fuel-Cell-Battery-Ultracapacitor Vehicles", *IEEE Trans. On Vehicular Technology*, vol. 57, no. 2, pp. 760-769, Mar. 2008.

[12] J. Leuchter, V. Řeřucha, Z. Krupka, P. Bauer, "Dynamic Behavior of Mobile Generator Set with Variable Speed and Diesel Engine", *IEEE Conf. Power Electronics Specialists*, pp. 2287-2293, Jun. 2007.

[13] E-M Isola, J. Kyyrä, M. Bergelin, J. Keskinen, "Models of Supercapacitors and Their Charging Behavior", *IEEE Conf. P E Sp*, pp. 2x-2y, Jun. 2007.

[14] Z. Chlodnicki, W. Koczara, N. Al-Khayat, "Control Strategies of the Variable Speed Generating Systems", *IEEE Conf. EUROCON 2007*, pp. 1301-1309, Sep. 2007.

[15] Maxwell Product Guide, http://www.maxwell.com, Maxwell Technologies SA, Switzerland, 2009.

[16] E. Schaltz, A. Khaligh, P. O. Rasmussen, "Investigation of Battery/Ultracapacitor Energy Storage Rating for a Fuel Cell Hybrid Electric Vehicle", *IEEE Conf. Vehicle Power and Propulsion*, Sep. 2008.

7 Authors

Matti Liukkonen is an undergraduate with nearly finished M.Sc. (Eng.) degree in electrical engineering from the Helsinki University of Technology (HUT), Espoo, Finland.

In 2008, he wrote his master's thesis from "Functional Simulations of Power Electronics Components in Hybrid Machinery".

Since 2007, he has been working as research assistant in a project related to simulation and control of series hybrid power transfer in HUT.

From 2005 to 2007, he was working as a research assistant in R&D department in ABB, Drives Oy, Finland, and also in Corporate Research, ABB Switzerland Ltd.

Ari Hentunen received his M.Sc. degree in electrical engineering from the Helsinki University of Technology (HUT), Finland, in 2005. From 2005 to 2007, and since 2008, he has been working as a researcher at HUT. During 2007–2008 he worked at Patria Land & Armament as an R&D engineer in the field of model-based software development. His main research projects are in the field of hybrid electric work machines and DC/DC converters.

Jussi Suomela is senior research scientist and project manager in Department of Automation and Systems Technology in Helsinki University of Technology TKK since 1992. His main research areas are hybrid electric vehicles and field and service robotics. He received his doctoral degree from TKK in 2004.

Jorma Kyyrä (M'94) received the M.Sc., Lic.Sc., and D.Sc. degrees from Helsinki University of Technology (HUT), Espoo, Finland, in 1987, 1991, and 1995, respectively.

He has worked at the university since 1985 in various positions. Since 1996, he has been Associate Professor of Power Electronics and since 1998 Professor of Power Electronics. His research interests include power converters, modelling of converters, power factor correction, and distributed power systems. He is the Director of the Institute of Intelligent Power Electronics, IPE, HUT, Executive Director of the Research Foundation, HUT, since 2003.

Dr. Kyyrä was Vice-Chairman of the Finland Section from 1995 to 2004 and since 2003 has been a Board Member of the IEEE Nordic Education Chapter.

In 2008, he was nominated as Dean of Faculty of Electronics, Communications and Automation, in Helsinki University of Technology.

Publication III

M. Liukkonen, A. Hentunen, and J. Suomela, "Validation of quasi-static Series Hybrid Electric Vehicle Simulation model," in *Proc. IEEE Vehicle Power and Propulsion Conference* (VPPC 2010), Lille, France, Sept. 1-3, 2010.

Validation of quasi-static Series Hybrid Electric Vehicle Simulation model

Matti Liukkonen*, Ari Hentunen* and Jussi Suomela*
*Aalto University School of Science and Technology, Espoo, Finland
Email: matti.j.liukkonen@tkk.fi

***Abstract*—This paper presents validation measurements of a series hybrid electric vehicle (SHEV) drive line with an ultracapacitor energy buffer. The backward functional quasi-static power transfer plant models in SHEV are discussed and compared against validation measurements. The full power measurement equipment and equipment under tests (EUT) are presented. A traditional road cycle is used to imitate duty vehicles loading in the plant models validation tests. Finally, an energy management algorithm and its behavior are presented, and results are concluded.**

I. Introduction

THIS study is part of a duty vehicles hybridization project. Hybridization of vehicles and mobile machines aim to decrease emissions and fuel consumption by exploiting kinetic and potential energy of the system, downsizing the primary energy source's power rating, and by generating the primary power with the most efficient means.

Design of a hybrid vehicle or a mobile machine is a very complicated task. Therefore, profound research relating to energy storing, hardware design and supervisory control is needed. This study focuses on hybridization of heavy mobile machines. Thus, the study concentrates on the SHEV drive line topology with a variable speed diesel generator (VSDG), or optionally in the future a fuel-cell (FC) stack, as the primary energy source. [1]

In order to achieve all advantages of the SHEV drive line, proper energy management is needed. Therefore, backward functional quasi-static causal plant models [1] of power transfer components in the SHEV have been developed with Matlab Simulink™ [2]-[3]. Plant models of SHEV components are developed for the rapid control prototyping (RCP) of energy management algorithms [4]. The design of reliably energy management algorithms requires test facilities, where operation of algorithms can be verified before implementation in the target system [5]-[6].

The contribution and novelty of this article is on introducing modeling accuracy of the used simulation method against the behavior of real full-scale hardware, and on essential discussions of full-scale hardware features. Also, conclusions about the behavior of the used hard-computing algorithm for the load-based energy management are made.

The paper is organized as follows. Section II introduces the modeling principles of each power transfer component with the case example comparison between the simulation and the measurement, as well as presents error analysis. Section III presents a discussion of the used energy management algorithm, and section IV concludes the paper.

II. Development of SHEV plant models

The presented work had its pre-studies published in [2]-[3]. An introduction to the SHEV drive line is presented in Fig. 1, which is an example of an ultracapacitor module (UC) power buffered SHEV drive line. The abbreviations in the figure represent generator (G), active front end converter (AC/DC, AFE), dc-dc converter (DC/DC), inverter (DC/AC) and traction motor (EM). The control signals and actual values are speed reference (ω_{ref}) for the VSDG electronic control unit, power limits of the AFE ($\vec{p}_{\mathrm{limit}}$), the dc link voltage reference for the AFE ($u_{\mathrm{dc\ ref}}$), actual ultracapacitor module voltage (u_{es}), actual dc link voltage (u_{dc}), current reference for the DC/DC (i_{ref}) and actual load power (p_{load}).

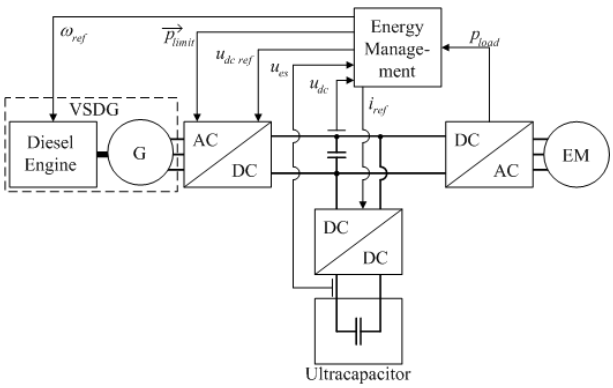

Fig. 1. The SHEV drive line with the ultracapacitor module for power buffering.

A. General simulation parameters and starting point

The target of the developed plant models for the SHEV drive line is to envisage 20 Hz-bandwidths events accurately. Furthermore, the designed system level model should be fast to provide efficient energy management RCP [4]. Therefore, backward functional modeling from the imposed load cycle towards the primary energy sources power delivery is appropriate [1].

The starting point of simulation models is to choose a proper simulation time-step, which in the presented cases is 1 ms. The previous fundamental time-step is justified by possible response times of the current control loop in power electronics (PE), for instance, an AFE converter [7]. Furthermore, accurate modeling of a change-over switching in PE components would lead to very low system level simulation times. For this reason, the current control loops of PE components are neglected and it is assumed that PE and EM components transfer the demanded current. Other regulators in different plant-models are operating causality with their input and output delays. Furthermore, the choice of the simulation time-step enforces the plant-models to the functional in the sense of a power electronics description.

In the backward simulations for the SHEV drive line practical starting points are either on the mechanical load of the EMs or the load currents of the inverters. The previous choice is dependent on the available load data. In the case of the mechanical load cycle data, we are able to derivate losses in the EMs and AC/DCs as well as scale loading to electric in the dc link side. This can be achieved with the measurement based efficiency charts in the torque and speed plane, as shown for EM in [5].

In this simulation model validation, the loading is regarded as electrical and derived from the ECE-15 cycle. Figure 2 presents power control targets for both the FC [8] and the VSDG powered SHEVs. The difference between these two cases is on the source current during the cycle's regenerative energy. The shown current waveforms are for the load (i_{load}), the energy storage (ES) (i_{ES}) and the AFE (i_{AFE}).

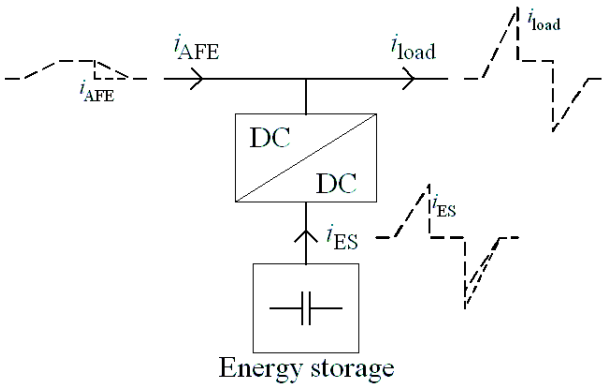

Fig. 2. The control problem of the hybrid power control; sketched targets of control and used measuring setup for the dc-dc converter plant model validation.

B. Measurement equipment and EUTs

Measuring hardware and software of this validation consisted of *dSPACE MicroAutoBox 1401/1505/1507* and *dSPACE ControlDesk* produced by *dSPACE* GmbH, respectively [9]. The measuring time-step for all variables was 10 ms.

The load current measurement was performed with an *LEM/Norma D6100* power analyzer with its triaxial shunts for 6 to 300 A current. The accuracy of the current measurement with the previous shunts is +/-0.1 %. The voltage u_{dc} was measured with the device's terminal with an accuracy of 0.05 %. [10]

The current transducer for the dc-dc converter current measurements was an *LA 305-S* and manufactured by *LEM*. The specific current transducer has a frequency bandwidth (-3dB) of DC to 100 kHz, overall accuracy of +/-0.8 % and less than 0.1 % error due to non-linearity [11].

The voltage transducer in u_{es} measurements was an *AV100-750*, which is also manufactured by *LEM*. The specific voltage transducer has a frequency bandwidth (-3dB) of DC to 13 kHz with less than 0.1 % error due to non-linearity [11].

The EUTs in the validation tests were as follows: The AFE converter *NXA_0460 5*, which is a product of Vacon Plc, regulated the dc link voltage around 650 V and supplied the primary source current i_{AFE}. The dc-dc converter between the dc link and the UC module was produced by MSc Electronics [13], with nominal current of 120A, maximum current of 200A and minimum current of 20A in the ES voltage level. The UC module was a product of *Maxwell technologies*®, with a nominal capacitance of 17.8 F and maximum voltage of 390 V [14].

C. Loading of the test system

In the simulation validation tests the load of the dc link was created with inverter, which was controlling one side of an EM dynamometer. The load current (i_{load}) was realized with speed control mode of a loading EM and torque control mode with the cascaded power controller of a traction motor. The traction motor power reference was ECE-15 drive cycle based. The structure of the used dynamometer is described in [5].

Figure 3 presents the speed pattern of the ECE-15 drive cycle, measured load current of the EM dynamometer and the AFE current in the dc link voltage level, as well as the ES current in the energy storage's voltage level.

The measured load current was used also as a loading of the dc link in the simulation model validation. This was done because modeling of the load would be very complicated and is not necessary for the power management design in non-predictive load-power-based-causal control. The ES current is the result of the supervisory control algorithms for the dc-dc converter in current control mode, and the AFE current is a derivative of the load current and the ES current.

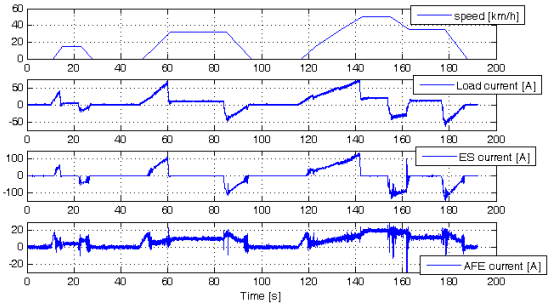

Fig. 3. Speed pattern of the ECE-15 drive cycle, the measured load current, the ES current and the resulting AFE current.

D. Functional plant model of the dc-dc converter

The PE converters typically reach to very high efficiency values in their best operation area. On the contrary, the efficiency of the PE converter can degrade significantly, if an inappropriate operation area is used. Therefore, with the previous presumption from the simulation time-step it is necessary to simulate the dc-dc converters with a combination of a measurement based efficiency map and a functional description.

The efficiency of dc-dc converter in general depends on the transferred current and the voltage conversion ratio. Hence, in the study [3] have been investigated efficiencies, which can be reached in power transfer with the previous variables.

The essential functionalities and dynamical properties which can be programmed on the dc-dc converter plant model are current control response time, minimum current, current ripple or noise, conduction event of the change-over switches' anti-parallel diode, quadruple point voltage controller and power losses according to the operation point.

Figure 4 shows how the plant model follows the original EUTs´ current with the same loading (i_{load}) in the simulation model as in the measurement. The measurement setup is as shown in Figure 2. The dc-dc converter current is presented in the ES voltage level and it corresponds to the ES current.

It can be seen from Figures 4 and 5 that there is some difference and variance between the simulated plant models´ current and the EUTs´ current, but it is convenient that the energy content of the difference is vanishing. The maximum current difference is 150 A, the mean error is -0.32 A and the rms error is 5.7 A. Furthermore, the mean error scale is near to the linear error and the rms error is near to the overall error of the sensor in the measuring range.

The largest differences between the measured and the simulated currents can be noticed near the minimum current (20 A) of the dc-dc converter (1), the highest regenerative current values (2) and during the shut off of the regenerative current (3). The previous numbers refer to areas in the scale-up Figure 5.

Points 2 and 3, in Figure 5, come up because of the energy management algorithm and the AFE voltage regulator is acting to stabilize the dc link voltage. The exact behavior of the AFEs´ voltage regulator is difficult to reproduce with the used functional simulation method. Therefore, the dc link voltage variation interacts with the measurement result. The dc link voltage drop at point 3 can be seen in Figure 6. The dc link voltage drop in this case was enforced with the low generating power limit of the AFE. The dc link voltage drop against the generating power limit could not be reproduced with the used simulation approach.

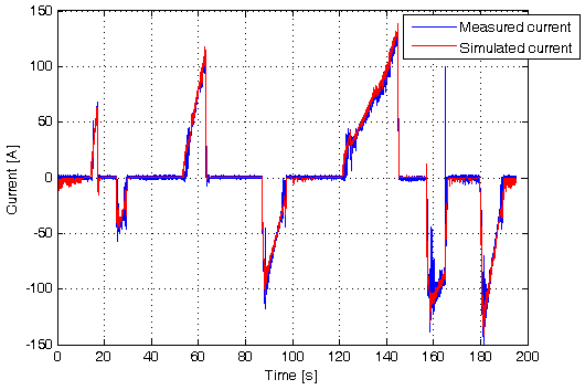

Fig. 4. The overview of the measured and the simulated dc-dc converter currents.

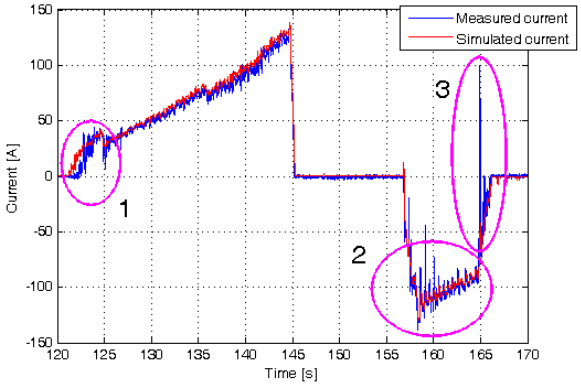

Fig. 5. The scale-up of the measured and the simulated dc-dc converter current.

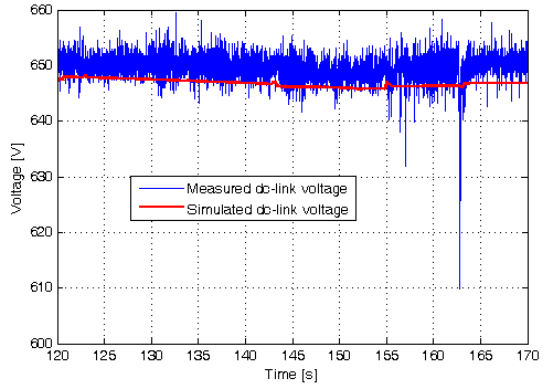

Fig. 6. The measured dc link voltage during the simulation model validation.

E. *Functional plant model of the AFE*

The active-front-end converter in the system level model is modeled with the efficiency map in the torque and speed plane, and also with the voltage regulator, which controls dc-current to the dc link. Losses of the generator are taken into account respectively. Change of voltage regulator type and parameters affect how power transfer is realized. In the developed AFE functional plant model the considered aspects of the voltage regulator are the stiffness of the voltage in the dc link side, as well as the control response time.

In the presented simulation model validation measurements the AFE took power directly from the power distribution network. Even though the power limit of the AFE was set to low (15.7 kW ~24 A) to prevent too strong supply, still the dc link voltage variation was low. Under stable conditions the dc link voltage was around 650 V +/-10 and in some transients, which are pointed out in Figure 6, the dc link voltage dropped down to 610 V. This affected the dc-dc converter current shown in Figures 4 and 5.

The next figures present the indirectly measured current of the AFE compared against the corresponding simulated current. The AFE current was achieved by calculating the difference between the load current and the dc-dc converter current due to practical reasons. First, Figure 7 presents the overview of the AFE current, and Figure 8 presents the scale-up of the current transients.

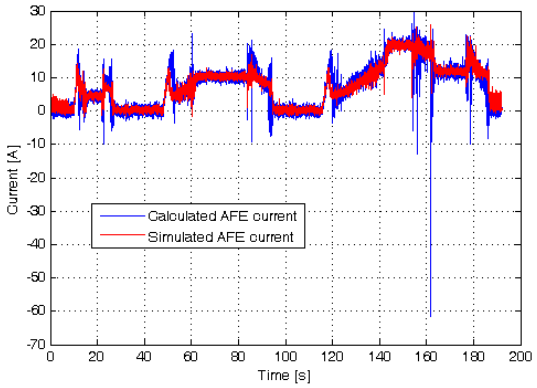

Fig. 7. The calculated and the simulated current of the AFE.

The scale-up figure shows the affect of the dc-dc converter minimum current (1), the accuracy of the load current sharing algorithm (2) and how current flows to the dc link from the AFE, if the generating power limit is not changed (3 and 4). The previous areas are shown in the scale-up figure. The maximum current difference, between the measured and simulated AFE current, is 79.8 A, the mean error is -0.19 A and the rms error is 3.0 A. The mean error is comparable to linear measurement accuracy and rms error to overall accuracy as earlier in the current measurement.

The size of load-step for the AFE in area 2, shown in Figure 8, depends on the pattern of the loading and energy management algorithm's parameters. So, the loading conditions should be taken under consideration in the energy management algorithm in order to optimize load sharing during the acceleration event.

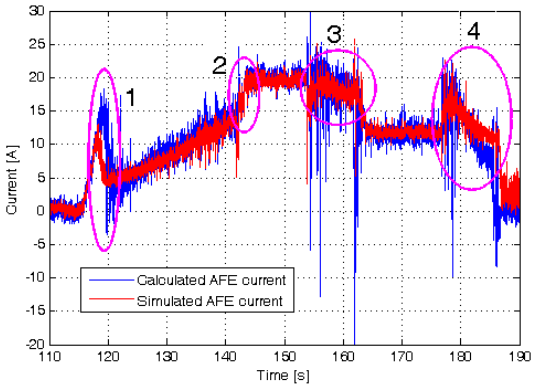

Fig. 8. The scale-up of the measured and the simulated current of the AFE.

F. *Modeling of the ultracapacitor module*

An UC simulation model is based on equivalent series resistance (R_{dc}) and measured capacitance variation as a function of ES voltage and current. The function for simulating the ES voltage is shown in Equation 1, where C_{es} represents the capacitance of the ES, i_{es} represents ES actual current and Δt represents the discrete time-step of simulations

$$u_{es}(R_{dc}, C_{es}(u_{es}, i_{es})) = R_{dc} i_{es} + \Delta t * i_{es} / C_{es}(u_{es}, i_{es}). \quad (1)$$

The figure below presents two different cases from the simulated and the measured voltage variation of the UC module with charging, discharging and static events. One simulation case is for constant nominal capacitance of the UC module, and other is for variable capacitance model simulation. The simulated cases of UC voltages are the integrals of the simulated dc-dc converter current.

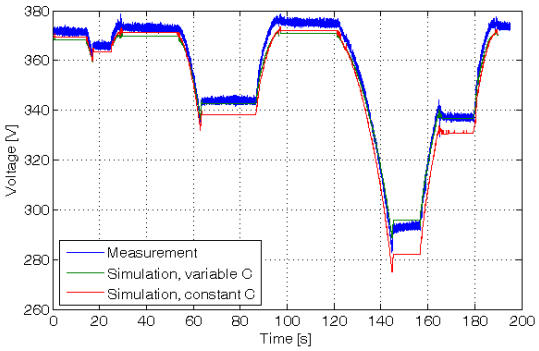

Fig. 9. Two different simulation cases from the UC modules´ voltages ($C_{constant}$ and $C_{variable}$) and the measured voltage with the same ES current.

Reasonable simulation accuracy is achieved even with the nominal capacitance of the UC module (error values: max 14 V, mean 4.8 V and rms 5.6 V), but smaller error values are achieved with the measured capacitance variation based model (max 8.4 V, mean 1.7 V and rms 3.0 V). Still, the mean error is approximately a decade larger than linear measurement error in measuring range.

G. *Modeling of the diesel engine*

The simulation model validation with measurements has been divided into testing of the electrical energy management and testing of the VSDG responses. This section presents a comparison of the simulation and logged parameter values from the VSDG electronic control unit. Realized loading of the VSDG has been used as a load torque in the simulation model. Both, the load-step and speed-reference-step responses are considered.

The diesel engine simulation model includes Newton's second law for rotational dynamics, the PI-controller for speed, the rate limiter for the speed reference, idle losses as a function of speed and calculation of fuel consumption from the PI-controller's fuel injection output and actual speed. The diesel engine under comparison is a 49 DTAG, and it is manufactured by AGCO SISU POWER [15].

Figure 10 presents the actual load torque during the load-step response test, a comparison between the simulated and the logged speed, as well as the speed reference. An accurate simulation of the speed response in load-steps depends on the PI-controller parameters. With the used PI-controller parameters the speed error values were as follows: max 91 rpm, mean 4.9 rpm and rms 8.8 rpm. These values are determined from an evaluation run of 300 seconds. The high maximum error is caused by misalignment between simulated and measured transients. Otherwise, the measurement accuracy is dependent on the features of the target equipment.

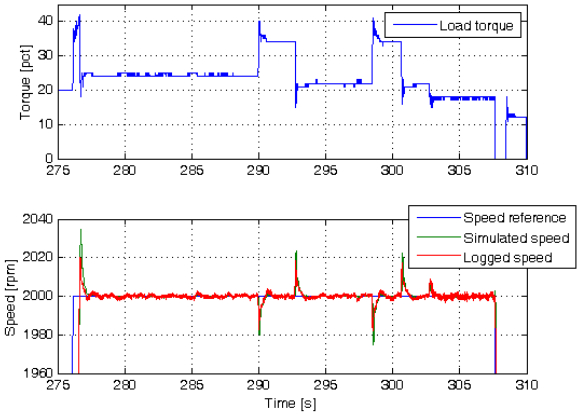

Fig. 10. The comparison between the simulation model and the measurement in the load-step response test.

Figure 11 presents the speed-reference-step responses for acceleration as well as for deceleration.

In the acceleration event the step-response depends on the speed reference rate limiter and the over-shoot depends on the PI-controller parameters. In the deceleration event the step-response depends on the inertia of the shaft, idle losses and the loading. In the previous case the loading can be seen from Figure 10 and in the latter case the loading was zero.

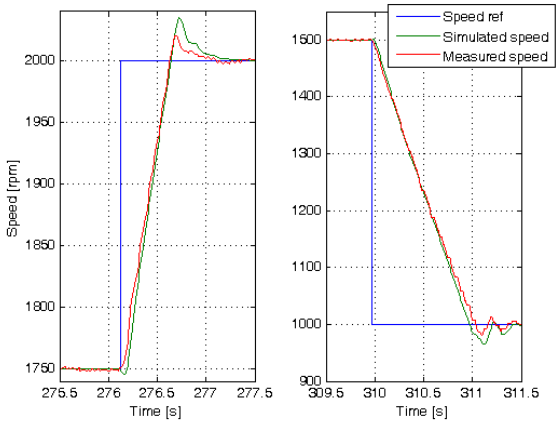

Fig. 11. The comparison between the simulation model and the measurement in the speed-reference-step test.

III. Energy Management Algorithm

This section presents a hard-computing algorithm, which was used for energy management of the SHEV system model in the validation tests with one ES. The presented energy management is targeting to peak power shaving from the primary energy source.

The energy management algorithm's (Fig. 12) inputs are, as defined with context of Fig. 1, $u_{\mathrm{dc\ ref}}$, u_{dc}, p_{load} and u_{es}. The output of the algorithm is i_{ref}. The moving average of the algorithm had unity coefficients and was calculating a 20 seconds average from the load power. The weight vector w_1 changes actual power to a per-unit value and w_2 defines the power which should be generated with the VSDG as a function of the actual ES voltage. The positive-linear function prevents filtered power calculation from going negative, and, therefore, all regenerative power is included in the load sharing algorithms output. The P-controller from the dc link voltage stabilizes the dc link and can be used for charging the ES.

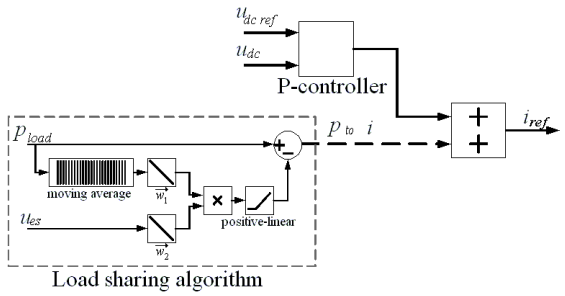

Fig. 12. Hard-computing algorithms for energy management in the SHEV drive line

We can discover that the proposed hard-computing algorithm is capable to realize all operation modes presented in [16] for the series hybrid drive train. Therefore, the study suggests that the power management of the SHEV drive line can be designed using the discussed hard-computing algorithms with use of finite-state machines or soft-computing algorithms.

Figure 13 specifies operation modes, which are realized with the proposed algorithm. Pure electric and engine modes come naturally, as well as pure ES charging mode. Hybrid mode (1) operates while the presented algorithm is running. Engine traction and ES charging mode (2) can be achieved, for example, with the change of voltage reference or the algorithm's weight vector w_2. Regenerative braking mode (3) operates with the algorithms nature, when the power limits of the AFE are controlled to zero. Hybrid ES charging mode (4) realizes when the algorithm is running and the power limits of the AFE are controlled appropriately.

In Figure 13, the dc link voltage drop in the operation area 2 is due to a voltage reference change for the proposed algorithms P-controller in order to charge the ES. Correspondingly in operation area 3, the drop is caused by the parallel current controllers of the algorithm regulating the current reference simultaneously.

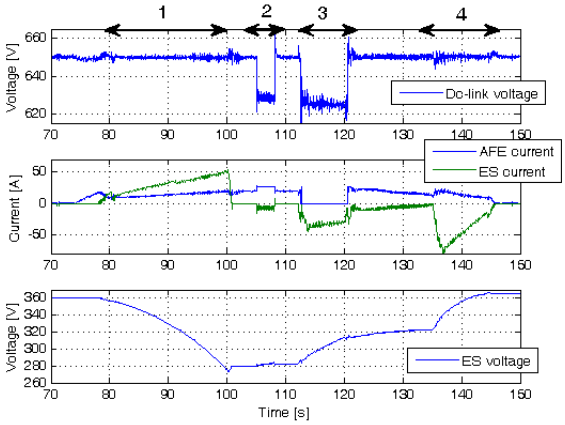

Fig. 13. The simulation figure presents different operation mode areas in the hybrid drive.

IV. Conclusion

This study discussed realization of backward functional quasi-static causal plant models of the SHEV, the verified simulation methods' accuracy with the introduced full-scale hardware and the proposed load-based energy management algorithms for the SHEV. In addition, relevant full-scale hardware features for RCP plant-models were discussed.

The used simulation method derivates accurately the mean values, as well as rms values, of all modeled variables. On the other hand, some transients of variables could not be reproduced as in cases which were caused by unknown regulator parameters, simplifications of models or misaligned control moments respect to validation. Therefore, maximum errors during transients remain high. However, the simulation accuracy is on a good level for a complex system. This can be justified with the insignificant energy content of the mean error values. Besides, the represented measuring errors are not significant compared to the simulation errors.

The proposed load-based hard-computing algorithm shows promising results for use in the SHEV energy management. However, realization of hybrid mode in peak power shaving during acceleration and deceleration is dependent upon the load pattern. Therefore, further study could be made to improve the algorithm to adapt in to different load pattern conditions. In addition, all required operation modes for the SHEV drive line energy management were described in the simulation with the proposed algorithm.

This study's aim is on duty vehicles hybridization, which have diverse and in some cases very repetitive load cycles. The previous brings opportunities for the energy management design.

Acknowledgment

This study has been carried out in HybDrive, TopDrive and HybLab projects financed by the Finnish Funding Agency for Technology and Innovations (Tekes) and Multidisciplinary Institute of Digitalization and Energy (MIDE) of Aalto University School of Science and Technology, respectively.

References

[1] C. C. Chan, A. Bouscayrol and K. Chen, "Electric, Hybrid, and Fuel-Cell Vehicles: Architectures and Modeling," IEEE Trans. Veh. Technol., vol. 59, no. 2, pp. 589-598, Feb. 2010.

[2] M. Liukkonen, A. Hentunen, J. Suomela and J. Kyyrä, "Functional Simulations of Power Electronics Components in Series-Hybrid Machinery for the needs of OEM," presented at the NORPIE, Nordic Workshop on Power and Ind. Electronics, Espoo, Finland, Jun. 9-11, 2008.

[3] M. Liukkonen, A. Hentunen, J. Suomela and J. Kyyrä, "Low-pass Filtered Power-flow Control in Series Hybrid Electric Vehicle," presented at the EVS24 Int. Battery, Hybrid and Fuel Cell Electric Vehicle Symp., Stavanger, Norway, May 13-16, 2009.

[4] M. Broy, I. H. Kruger, A. Pretschner and C. Salzmann, "Engineering Automotive Software" Proc. of the IEEE, vol. 95, no. 2, pp. 356-373, Feb. 2007.

[5] A. Hentunen, J. Suomela, A. Leivo, M. Liukkonen and P. Sainio, "Hardware-in-the-Loop Verification Environment for Heavy-Duty Hybrid Electric Vehicles," IEEE Vehicle Power and Propulsion Conf., Lille, France, Sep. 1-3, 2010, unpublished.

[6] Y. Cheng, J. V. Mierlo and P. Lataire, "Research and test platform for hybrid electric vehicle with the super capacitor based energy storage," European conf. on Power Electron. and Applications, Aalborg, Denmark, Sep. 2007.

[7] M. Gokasan, S. Bogosyan and D.J. Goering, "Sliding Mode Based Powertrain Control for Efficiency Improvement in Series Hybrid-Electric Vehicles," IEEE Trans. on Power Electron. vol. 21, pp. 779-790, May 2006.

[8] J. V. Mierlo, Y. Cheng, J.-M. Timmermans and P. V. Bossche, "Comparison of Fuel Cell Hybrid Propulsion Topologies with Super-Capacitor," Power Electron. and Motion Control Conf. EPE-PEMC, Portorož, Slovenia, Aug. 2006.

[9] dSPACE homepage. [Online]. Available: http://www.dspace.de/

[10] Norma D6000 specification description. [Paper].

[11] LEM homepage. [Online]. Available: http://www.lem.com/

[12] Vacon homepage. [Online]. Available: http://www.vacon.com/

[13] MSc Electronics homepage. [Online]. Available: http://www.mscelectronics.fi/

[14] Maxwell Technologies homepage. [Online]. Available: http://www.maxwell.com/

[15] AGCO Sisu Power homepage. [Online]. Available: http://www.agcosisupower.com/

[16] M. Ehsani and Y. Gao, "Hybrid Drivetrains," in Handbook of Automotive Power Electronics and Motor Drives, Boca Raton, FL: T&F, 2005, ch. 1, sec. 3, pp. 37-53.

Publication IV

M. Liukkonen, A. Hentunen, and J. Suomela, "Analysis of the Ultracapacitor Module in Power Buffering," in *Proc. 4th European Symposium on Super Capacitors and Applications* (ESSCAP 2010), Bordeaux, France, Oct. 21-22, 2010.

Analysis of the ultracapacitor module in power buffering

Matti Liukkonen, Ari Hentunen, Jussi Suomela

Aalto University School of Science and Technology, Otakaari 5, 02015 Espoo, Finland
E-mail: matti.j.liukkonen@tkk.fi

Abstract

This paper presents efficiency analysis of the power buffering in common voltage bus systems. Operation of the power buffering is briefly described with the power control experiments. The efficiency measurement setup and performed measurements from the charging and discharging events of the ultracapacitor module with the dc-dc converter are presented. As a result, the efficiency map of the dc-dc converter is gained and losses of the ultracapacitor module energy storage are differentiated. In addition, the efficiency map of the full charging and discharging cycle of the energy storage system is attained and the capacitance variation of the ultracapacitor module in the dc-dc converters operation area is presented. The operation areas of the energy storage system and variable speed diesel generator (VSDG) in series hybrid electric vehicle (SHEV) application are investigated in simulation case studies.

1. Introduction

This study is part of a duty vehicles hybridization project. Hybridization of vehicles and mobile machines aims to decrease emissions and fuel consumption by exploiting the kinetic and potential energy of the system, downsizing the primary energy source's power rating, and by generating the primary power with the most efficient means.

Design of a hybrid vehicle, non-road mobile machinery (NRMM) or other hybrid power system is a very complicated task. Therefore, profound research relating to energy storing, hardware design and supervisory control is needed. This study focuses on the system efficiency of peak power buffering in common voltage bus systems. The system efficiency study utilizes the measured data, since it is not feasible to use too accurate system level models with a semiconductor switching events. The functional approach in system level models provides possibility to solve power train's total efficiency efficiently. Also, characteristics of an ultracapacitor (UC) module in system level are considered [1].

The contribution and novelty of this article is in introducing the power buffering from the Original Equipment Manufacturer's (OEM's) from the NRMM industry point of view. This consists of presented measurements, analysis and case simulations for the UC module based power buffering in SHEV drive lines. Efficiency maps from charging, discharging, and full cycle are presented for the three-phase interleaved boost converter, [2] and [3]. Also, losses of the UC module are differentiated from the measurements. Furthermore, as a case example the operation area of an energy storage system in peak power buffering is described on a two-quadrant efficiency map and the affect of the dc-dc converter control strategy on the VSDG's possible operation area is compared. This study completes the SHEV modeling studies presented in [4] and [5].

2. Power buffering in common voltage bus systems

Two different power control cases are presented in this chapter: case 1 presents the peak power cutting method and the case 2 presents the acceleration assistance and regenerative energy recuperation method. In addition, the latter can be separated into two sub cases depending on the source current during the regenerative load current. The current patterns and scheme of the experiment setup of these two power control cases are shown in Figure 1.

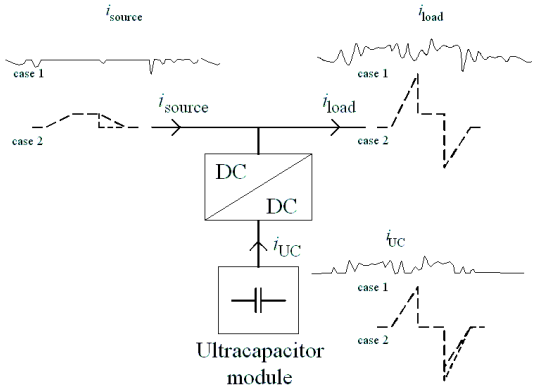

Fig. 1. The power control targets for two different cases: peak power cutting and acceleration assistance / regenerative energy recuperation.

2.1 Peak Power Cutting

Figure 2 presents the peak power cutting measurement. The dc-dc converter was controlled in the presented experiment with a constant power limit of 45 kW. After the load power exceeded the power limit value, the dc-dc converter discharged the UC module with a margin of the load power and power limit value. The continuous current of the dc-dc converter was ~80A, which limited the continuous power of the ultracapacitor module to around 15 kW. The minimum power limit, which is used for

charging of the ultracapacitor module, operates respectively during regenerative or low loads.

As features, the used dc-dc converter has overshot the reference current in the beginning of the discharge operation and minimum current limit (27 A), which alters the used power limit values with a variable depending on the UC module's voltage. In the shown figure the minimum transferred power was ~5 kW.

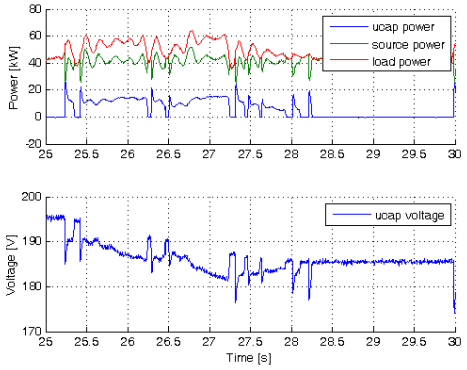

Fig. 2. The peak power cutting control method with the ultracapacitor module. The dc-dc converter with 80A continuous energy storage current is controlled when the load exceeds the maximum power limit.

2.2 Measurement setup in Peak Power Cutting experiments

The scheme of measurement setup is shown in Figure 1. The measuring hardware and software for this experiment consisted from dSpace *MicroAutoBox 1401/1505/1507* (MABX) and dSpace *Controldesk* produced by *dSpace* GmbH, respectively [6].

The load power was calculated from the dc link voltage and the dc link current to load which were measured with *AV100-750* and *HTFS 400-P* sensors. The ultracapacitor module's voltage and current were measured with *AV100-750* and *LA 305-S* sensors, respectively. All the used sensors are products of *LEM* [7].

The source power is calculated from the previous measured variables. The source was an active front end converter (AFE) *NXA_0460 5* (Vacon Plc.), which regulated the dc link voltage and supplied the source current. [8]

The load was an electric drive system ELFA produced by Siemens [9]. The inverter (G650 D440/170/170) and electric machine (1PV5135-4WS28) of the loading system was operating against the NRMM's disc brake on its shaft.

The dc-dc converter was a product of *MSc electronics Plc.* and the model was *MSc200DCDC750* [10]. The UC was a product of *Maxwell technologies*®, with a nominal capacitance of 17.8 F and maximum voltage of 390 V [11].

2.2 Acceleration assistance / regenerative energy recuperation

Figure 3 presents the power control measurement with the acceleration assistance / regenerative energy recuperation method in the SHEV powertrain. Implementation, comparison to simulations and error estimation are presented in [4]. The hardware for the experiment is described in detail [2]. The presented power control experiment describes how primary source current can be ramped up in common voltage bus systems with the full-scale power transfer hardware for the primary energy source's needs, [12] and [13]. The figure shows the load current, the Ucap current, the source current and the Ucap voltage during an ECE-15 based load cycle.

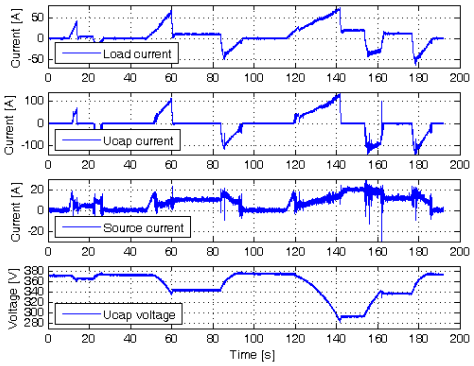

Fig. 3. The acceleration assistance / regenerative energy recuperation control method with the ultracapacitor module. The figure presents an experiment which was realized in the full-scale hardware-in-the-loop verification environment.

Previous experiments with the different types of load cycles illustrate how an UC module is a practical choice for power buffering in different applications.

3. Efficiency measurements

3.1 Measurement setup

Equipment under tests (EUTs) includes the ultracapacitor module (17.8F, 390V) and the dc-dc converter. As a change for the previously described measuring setup all measurement sensors were replaced with a power analyzer. Figure 4 illustrates the schematic from the measurement setup.

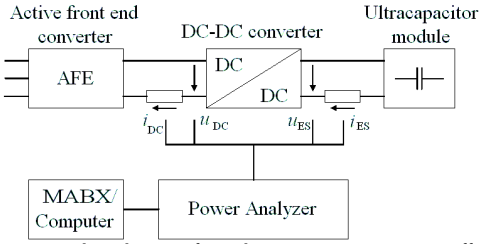

Fig. 4. The schematic from the measurement setup in efficiency measurements.

The used power analyzer was *LEM/Norma D6100* with its triaxial shunts for 6 to 300 A current measurements. The measuring accuracy for voltage channels in the frequency range of 0 to 15 Hz are ± (0.15 + 0.03) % for reading and range, respectively. The measuring accuracy for current shunts is ± 0.1% within a frequency range of 0 to 100 kHz [14].

Measurement data acquisition was performed via an RS-232 cable and the control of the dc-dc converter in the tests was performed with the MABX.

3.2. Measurements

Efficiency measurements were performed in the following means. The UC was charged and discharged repeatedly from zero voltage to its maximum voltage and back to zero voltage. The UC current was kept constant in one charge – discharge cycle, and afterwards the reference current was changed for the next repetition. The dc link voltage was kept within 650 to 655 volts with the AFE, according to the averaged dc link voltage measurement data.

Figure 5 illustrates the UC voltage measurement data with different charging and discharging currents. The legend represents the average ES rms current values during charge – discharge operations.

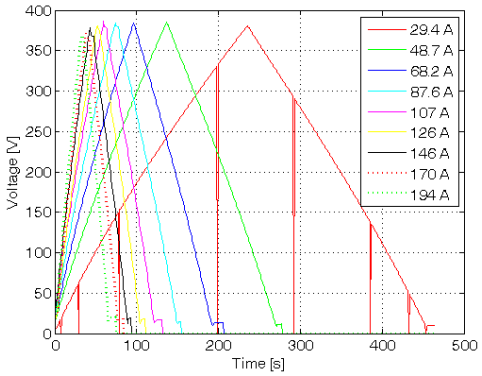

Fig. 5. Charging and discharging of the ultracapacitor module with different constant currents.

All measured variables in each charge – discharge cycle were the voltages in the energy storage and the dc link side, as well as the currents from both voltage potentials, respectively. All variables were taken as rms values. The measurement points are illustrated in Figure 4.

Measurement data sampling frequency in the power analyzer was fixed at 70 kHz. In addition, the measuring device averaged measured values over a 0.934 seconds time frame with a digital filter to avoid efficiency values from varying and to prevent an excess amount of data.

3.2. Measurement analysis

The measured data provides directly the efficiency maps of the dc-dc converters charge and discharge operations. The efficiency values (η) in different operation points are functions of the ES current (i_{ES}) and the voltage ratio (u_{ratio}) between the ES and the dc link. The efficiency maps for charge and discharge operations are calculated as in (1),

$$\eta(u_{ratio}, i_{ES}) = \frac{u_{out} \cdot i_{out}}{u_{in} \cdot i_{in}}. \quad (1)$$

The in and out subscripts refer to power transfer directions.

Efficiency values corresponding to particular ES current and voltage ratio in two digits accuracy are averaged. This way the realized charge efficiency map is presented in Figure 6. Measurements were performed in two sets, firstly from zero current to 90 A, and ,secondly, from zero current to 200 A. Both measurement data sets are utilized in the results.

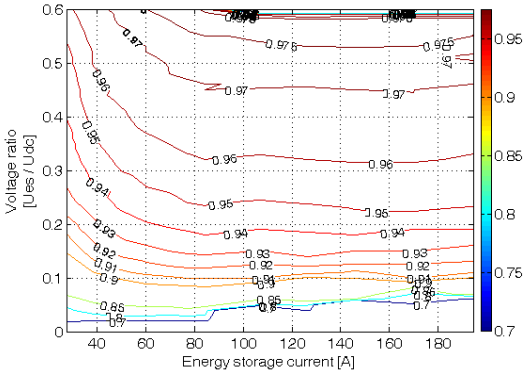

Fig. 6. The efficiency map of the dc-dc converter during charge operation.

The total power buffering efficiency can be derived from the measurement results as in (2),

$$\eta(u_{ratio}, i_{ES}) = \frac{p_{out}(u_{ratio}, i_{ES})}{p_{in}(u_{ratio}, i_{ES})} \cdot \frac{T_{out}}{T_{in}}. \quad (2)$$

In Equation 2, p_{out} refers to instantaneous power on the dc link side towards the dc link and p_{in}, respectively, towards the ES. T_{out} refers to the total discharge time of the ES and T_{in} to the total charge time of the ES. In addition, u_{ratio} is used without the voltage drop over the equivalent series resistance (ESR) of the ES.

The previous equation leads to the full power buffering cycle efficiency according to the ES operation points. The full power buffering cycle efficiency map is presented in Figure 7.

Further, from the measurement data can be derived also the variable capacitance map over the UC module operation area. The variable capacitance map can be derived as in (3),

$$C(u_{ES}, i_{ES}) = \frac{I \cdot \Delta t}{\Delta U}. \quad (3)$$

In Equation 3, C refers to capacitance, I to rms current, Δt to time change and ΔU to change of voltage. The variable capacitance map is presented in Figure 8.

The modeling of the UC can be realized with the variable capacitance map and the ESR value of the module, [1] and [4].

The efficiency of the UC module, with the used dc-dc converter, can be derived from the total efficiency map by subtracting the charging and discharging losses of the dc-dc converter, and by assuming the UC module's efficiency equal in charge and discharge operations, as contained in Figure 9.

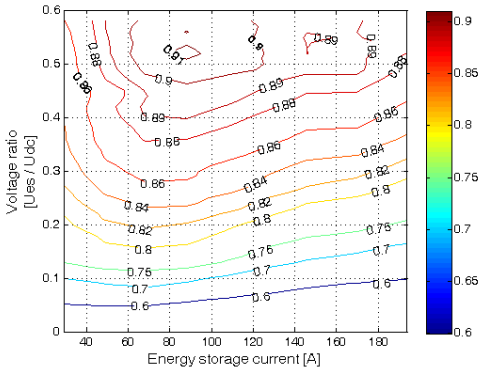

Fig. 7. The full power buffering cycle efficiency map, which consists of twice the losses from the dc-dc converter and the ultracapacitor module.

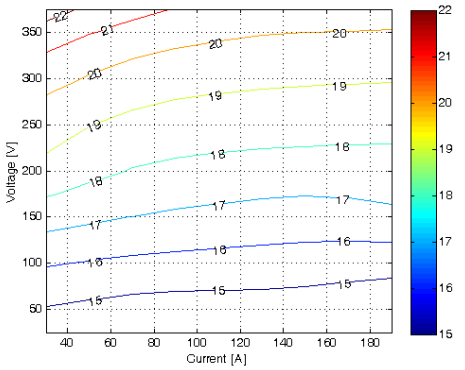

Fig. 8. The variable capacitance map of the ultracapacitor module as a function of the ES current and the voltage ratio.

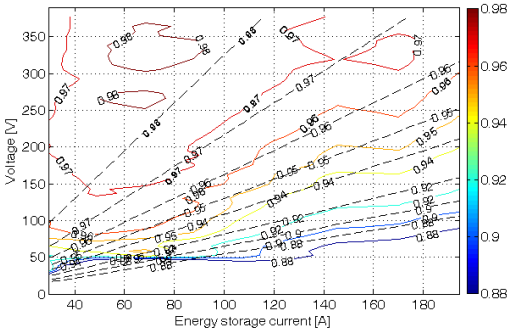

Fig. 9. The comparison between theoretical and measured efficiency map of the ultracapacitor module in either charge or discharge operations. The theoretical efficiency pattern is drawn with black dashed lines and the measured efficiency pattern with colored lines, respectively.

Figure 9 can be compared to the efficiency contour pattern created by pure ESR losses for the UC module. The efficiency contours created by 65 mΩ resistance [11] is drawn in the background with black dashed lines as in (4),

$$\eta(u_{ES}, i_{ES}) = \frac{u_{ES} \cdot i_{ES} - ESR \cdot {i_{ES}}^2}{u_{ES} \cdot i_{ES}}. \qquad (4)$$

The presented figure suggests that UC module's losses are mainly caused by the dc current in the ESR of the UC module and the ripple current component of the dc-dc converter has only minor or insignificant effects on low ES currents. The change in the trend of the efficiency pattern of the UC module can be seen with less than 50 A values.

4. Simulations

An introduction to the simulated SHEV drive line is presented in Figure 10, which is an example of an ultracapacitor module power buffered SHEV drive line. The abbreviations in the figure represent generator (G), active front-end converter (AC/DC, AFE), dc-dc converter (DC/DC), inverter (DC/AC) and traction motor (EM). The control signals and actual values are speed reference (ω_{ref}) for the VSDG electronic control unit, power limits of the AFE ($\vec{p}_{limit}$), the dc link voltage reference for the AFE ($u_{dc\ ref}$), actual ultracapacitor module voltage (u_{es}), actual dc link voltage (u_{dc}), current reference for the DC/DC (i_{ref}) and actual load power (p_{load}).

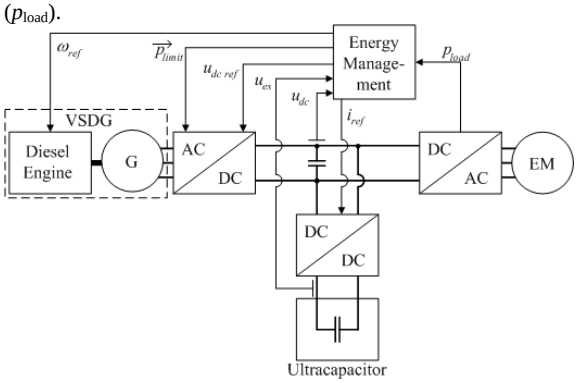

Fig. 10. The SHEV drive line with the ultracapacitor module for power buffering.

Simulations illustrate how the operation points of the primary energy source and energy storage differ after hybridization from the conventional electric drive line. In the shown example, the drive line is considered to provide power for the ECE-15 drive cycle, with peak power equal to the diesel engine's maximum. The operation area of the conventional VSDG use and hybrid power control method cases I and II are illustrated in Figure 11. The figure shows the operation points of the conventional electric drive line and the SHEV drive line with the UC module

ratings of 17.8F and 390V. In the figure blue stars refer to operation points with the conventional VSDG use, green crosses refer to operation points in the SHEV drive line with power control case I and red circles refer to operation points with power control case II. Operation points are drawn on the static fuel consumption map (g/kWh), which is not exact during transitions. In addition, the black line depicts the maximum power of the VSDG, and the VSDG is assumed to operate with the speed reference as a function of transferred power.

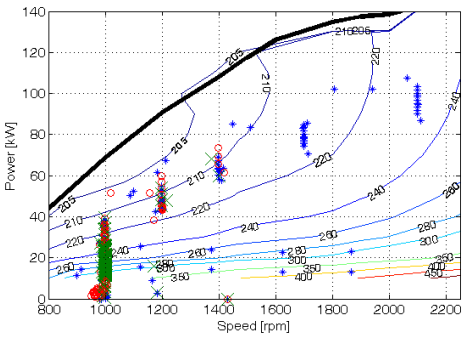

Fig. 11. Operation points of the conventional VSDG and with the SHEV drive line during the ECE-15 drive cycle. The figure illustrates the primary source's downsizing with two different power control methods. Blue stars refer to the operation points with the conventional VSDG use, green crosses refer to the operation points in the SHEV drive line with the power control case I and red circles to the case II, respectively.

Both SHEV drive line power control cases decrease the maximum power to approximately two thirds of the original. In addition, the power control case I provides the possibility to move the operation points of the VSDG from low load and low speed to higher load with low speed when compared against case II.

Figure 12 presents the VSDG's power in the each simulation case, in the time domain.

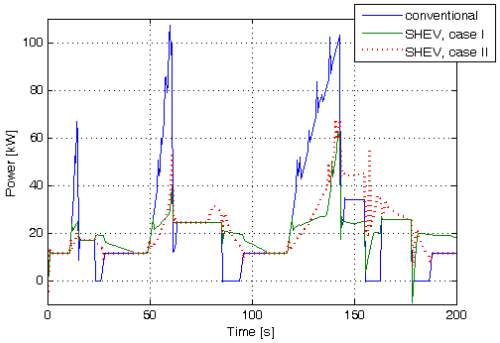

Fig. 12. The loading of the VSDG in three simulation cases. The blue line refers to the conventional VSDG use, the green line refers to the SHEV drive line with the power control case I and the red dashed line refers to the case II, respectively.

Figure 13 depicts the operation points of the energy storage system on the top of its total efficiency map. The figure is two quadrant, such that the positive current is towards energy storage and negative current is towards the load. Figure 13 is derived by taking the square root from the full power buffering cycle efficiency map. The dc-dc converter is considered to transfer the current within its maximum current limit 200 A. Green crosses refer to the operation points with power control case I and red circles refer to the operation points with power control case II.

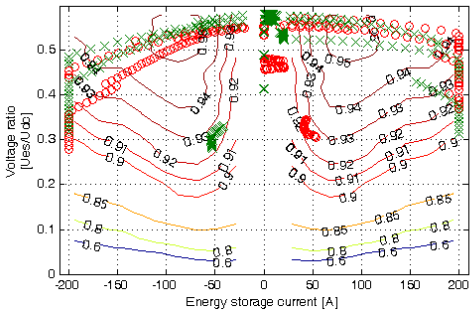

Fig. 13. Operation points of the ultracapacitor module in the SHEV drive line during the ECE-15 drive cycle. Green crosses refer to the operation points in the SHEV drive line with the power control case I and red circles to the case II, respectively. The positive current is towards the UC module.

Figure 13 illustrates that the energy storage system containing the dc-dc converter and the UC module operates mostly in area with 90 to 95 percent efficiency when power conversion efficiencies either from the dc link to the energy storage or to opposite direction is considered.

Figure 14 presents the UC module's current in two power control cases, in the time domain.

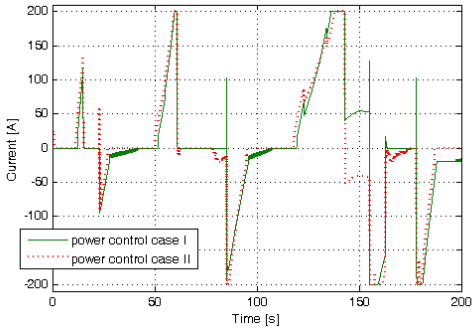

Fig. 14. The ultracapacitor module's currents in the SHEV drive line during the ECE-15 drive cycle presented in the time domain. The green line refers to values of the SHEV drive line with the power control case I and red dashed line to the case II, respectively. The positive current is towards the load.

4. Conclusions

This study describes two different power control methods for the SHEV drive line with experiments. Also, the efficiency measurement setup and efficiency

measurements for the energy storage system are described and results of the measurements are analyzed. The study is concluded with case simulations from the operation areas of the energy storage system and the VSDG in the SHEV drive line in contrast to conventional use. The approach to the system level models is a functional, which utilizes measurements presented in the study. The functional approach to system level modeling provides the efficient method to solve the power train's total efficiency.

Acknowledgments

This study has been carried out in the HybDrive, TopDrive and HybLab projects financed by the Finnish Funding Agency for Technology and Innovations (Tekes) and the Multidisciplinary Institute of Digitalization and Energy (MIDE) of Aalto University School of Science and Technology, respectively.

References

[1] W. Lajnef, J.-M. Vinassa, O. Briat, S. Azzopardi, E. Woirgard, "Characterization methods and modelling of ultracapacitors for use as peak power sources", *Journal of Power Sources*, vol. 168, n°2, pp. 553-560, June 2007.

[2] A. Hentunen, J. Suomela, A. Leivo, M. Liukkonen and P. Sainio, "Full-Scale Hardware-in-the-Loop Verification Environment for Heavy-Duty Hybrid Electric Vehicles", in *Proc. Electric Vehicle Symposium (EVS 25)*, Nov. 5-9, 2010, Shenzhen, China. (in press).

[3] L. Fleischli, S. Lemofouet and A. Rufer, "Multichannel DC-DC Converter's Efficiency Optimisation by variable Number of active Channels", *IECON 2006 – 32nd Ann. Conf. on IEEE Ind. Electron*., pp. 2581-2586, 6-10 Nov. 2006, Paris, France.

[4] M. Liukkonen, A. Hentunen and J. Suomela, "Validation of quasi-static Series Hybrid Electric Vehicle Simulation model", in *Proc. IEEE Vehicle Power and Propulsion Conference*, Sep. 1-3, 2010, Lille**,** France.

[5] M. Liukkonen, A. Hentunen, J. Suomela and J. Kyyrä, "Low-pass Filtered Power-flow Control in Series Hybrid Electric Vehicle", in *Proc. Electric Vehicle Symposium (EVS 24)*, May 13-16, 2009, Stavanger, Norway.

[6] dSPACE homepage. [Online]. Available: http://www.dspace.de/

[7] LEM homepage. [Online]. Available: http://www.lem.com/

[8] Vacon homepage. [Online]. Available: http://www.vacon.com/

[9] Siemens electric drive system ELFA. [Online]. Available: http://www.siemens.com/elfa

[10] MSc Electronics homepage. [Online]. Available: http://www.mscelectronics.fi/

[11] Maxwell Technologies homepage. [Online]. Available: http://www.maxwell.com/

[12] P. Thounthong, B. Davat, S. Raël and P. Sethakul, "Fuel Cell High-Power Applications", *IEEE Industrial Electronics Magazine*, Vol. 3, n°1, pp. 32-46, Mar., 2009.

[13] P. Thounthong and S. Raël, "The Benefits of Hybridization", *IEEE Industrial Electronics Magazine*, Vol. 3, n°3, pp. 25-37, Sep., 2009.

[14] Norma D6000 specification description. [Paper].

Publication V

M. Liukkonen, A. Lajunen, and J. Suomela, "Comparison of Different Buffering Topologies in FC-hybrid Non-Road Mobile Machineries," in *Proc. IEEE Vehicle Power and Propulsion Conference* (VPPC 2011), Chicago, IL, USA, Sept. 6-9, 2011.

Errata:

Eq. 5 should be:

$$u_{\mathrm{uc}} = \frac{1}{C_{\mathrm{uc}}} \int_0^t i_{\mathrm{uc}} \mathrm{d}t - R_{\mathrm{uc}} i_{\mathrm{uc}} + U_{\mathrm{uc\_initial}}. \tag{5}$$

Comparison of Different Buffering Topologies in FC-hybrid Non-Road Mobile Machineries

Matti Liukkonen, Antti Lajunen and Jussi Suomela
Aalto University School of Electrical Engineering, Espoo, Finland
E-mail: matti.liukkonen@aalto.fi

***Abstract*-This paper presents powertrain comparison for fuel cell hybrid non-road mobile machinery. The objective of this study is to investigate the feasibility of different fuel cell hybrid powertrain topologies. This study concentrates on hybrid powertrain topologies which are generated from the fuel cell source output to loading inverters inputs. The compared features of different powertrains are efficiency, weight, size, cost and lifetime costs, as well as, benefits and disadvantages. The study considers fuel cell hybrid topologies with different active and passive connections of a battery pack, an ultracapacitor pack or the both. The comparison of different powertrain topologies requires a validated simulation tool, specific power control algorithms for each topology, knowledge of the target application and several iteration rounds for simulations.**

I. INTRODUCTION

The main objective of this study is to investigate the fuel cell system (FCS) suitability as the primary energy and power source for the non-road mobile machinery (NRMM). In this context, the FCS properties such as efficiency, weight, size, initial and lifetime costs, and operating requirements are evaluated. The focus is on the fuel cell hybrid applications therefore different powertrain topology options are introduced and their characteristics evaluated [1].

For introducing the fuel cell system as a part of hybrid powertrain in a NRMM application, the most relevant fuel cell (FC) hybrid topologies were defined. In this context, the topology means the main component configuration in the powertrain system. This system usually includes the primary power and energy source (engine, fuel cell…), energy storage (battery, ultracapacitor, flywheel…), drive system such as electric motors, and other loads (work hydraulics, auxiliary devices…). Based on expertise knowledge and a literature study, five different FC-hybrid cases were chosen to be analyzed.

As mentioned before, special focus is given for different energy buffering solutions. For FC-hybrid applications, an important part of the hybrid system is the energy storage. Depending on the application, they are used for storing energy for short or longer period of time. Basically, the need for energy capacity can be evaluated based on the operation requirements. Moreover, these requirements typically depend on the load cycle which describes the power need during a certain period of time or distance.

Fuel cells have been successfully implemented in different road vehicle applications such as passenger cars (Honda FCX, MB F-CELL…) and city buses (MB Citaro, Van Hool…). Also, some application of non-road mobile machinery has been developed such as forklifts, loaders, tractors and locomotives [2]-[6]. Currently, all the fuel cell powered vehicles or NRMM are still in prototype phase because of the high production costs, lower performance and limited access to refuelling pure hydrogen.

II. RESEARCH METHOD

This study compares different fuel cell powered series-hybrid buffering topologies for NRMM with the aid of system level simulation studies. System control strategies are developed for the each defined topology while a load cycle is specific for the studied mobile machine. The simulation model was developed and validated during previous hybridization research projects [7]-[8]. The backward modeling methods accuracy was proven to be on sufficient level.

This research concentrates especially on the Heavy Mobile Port Equipment load cycle. Studied topologies are simulated with the particular power control and their powertrain efficiency, approximate powertrain weight, size, initial and lifetime costs, and operating requirements are analysed, with targeted 15 years of operation. Therefore, starting points for solving the feasibility of different powertrain topologies are the Heavy Mobile Port Equipment load cycle, the FC-stack and the battery pack operational limits. The target of power control in each powertrain topology is to keep the FC-stack load changes within 2.5 kW/s, which ensures the maximum lifetime of the FC-stack [9].

III. SYSTEM LEVEL ANALYSIS

A. Load cycle

The studied Heavy Mobile Port Equipment has conventionally an electric powertrain with a high voltage DC-link and power sources. Therefore, it has been possible to acquire traction and hoist loading data from inverters. The traction and the hoist loading data consist from several separate loading units, which are assumed as sum from the point of common coupling. The full data acquisition from the vehicle consists of powertrain variables with 0.5 seconds interval from the 5312 seconds period. Table I presents operation percentages for different load power levels. Power levels in the table are per unit (p.u.) values from the maximum load.

978-1-61284-247-9/11/$26.00 ©2011 IEEE

TABLE I
THE TRACTION, THE HOIST AND THE SUM POWER HISTOGRAMS FROM THE TOTAL DATA ACQUISITION PERIOD.

Bin [p.u.]	Traction power [%]	Hoist power [%]	Sum power [%]
Min power	-0.681 pu	-0.900 pu	-0.900 pu
-0.873	0	0.02	0.02
-0.764	0	0	0.01
-0.655	1.4	0.06	1.3
-0.546	2.5	0.07	2.3
-0.437	1.5	0.2	1.7
-0.328	1.9	0.7	2.6
-0.218	1.9	0.5	2.4
-0.109	2.9	1.0	3.4
0	36.0	92.1	32.7
0.109	8.0	1.5	7.1 [a]
0.218	4.1	1.1	4.7 [a]
0.328	7.4	1.1	8.1 [a]
0.437	7.0	0.7	7.4 [a]
0.546	4.5	0.5	4.9 [a]
0.655	3.6	0.4	3.9 [a]
0.764	2.8	0.06	3.0 [a]
0.873	8.9	0	8.9 [a]
0.983	5.6	0	5.6 [a]
1.092	0.01	0	0.01 [a]
Max power	1 pu	0.716 pu	1 pu

[a] The positive part of the sum power with the additional constant load make a positive load E_{+load} from the DC-link.

B. Studied powertrain topologies

Four different powertrain topologies presented in Fig. 1 are considered in this study with the following configurations:

A. Case *a* : fuel cell and battery,
B. Case *b* : fuel cell, passive battery and active ultracapacitor,
C. Case *c* : fuel cell, active battery and active ultracapacitor pack and
D. Case *d* : fuel cell with active ultracapacitor packs.

Furthermore, topology case *d* is divided into two different cases based on the control strategy. In comparison, the case *d* refers to topology *d* with actively DC-link voltage controlled ultracapacitor (UC) packs and varying FC power production. In addition, the case *e* refers to topology *d* with both voltage and current controlled ultracapacitor packs and constant FC power production, see Section VI.

The case *a* consists of a high voltage FC-stack, a current controlled unidirectional FC-converter, a high voltage battery pack and load inverters. The battery pack was dimensioned for the particular load cycle. Dimension of the battery pack is impacted by the maximum allowable charging current, which is a restrictive factor for the battery pack sizing in this topology. The sizing of the battery pack can be achieved based on FC-source control, battery pack voltage (u_{bat}), and the load cycle.

The case *b* can be controlled such a way that the active ultracapacitor pack limits the maximum and the minimum current of the battery pack approximately within the nominal current value (C, Ah/h), as well as, it limits the battery pack's power transients.

The case *c* consists of a FC-stack with its converter, secondary storages, a battery pack and an UC pack, with their converters and a brake resistor with its brake chopper. The benefits of the topology originate from the increased amount of degrees of freedom in energy storages control and sizing. The fundamental reason for the lower powertrain efficiency is the battery pack DC-DC converter losses, which occur increasingly if the vehicle is operated during the start-up phase of the FC-source.

The case *d* has UC packs as its energy storage. The DC-link voltage controller for the UC packs was a proportional; when the motoring load decreases the DC-link voltage and the regenerating load increases the DC-link voltage. In this case, the FC-source is controlled such a way that it follows the load power against its power transition limit of 2.5 kW/s.

The case *e* can be designed such a way that the current controlled UC pack averages the load power, the FC-source operates on its maximum power region and the voltage controlled UC pack stabilizes the DC-link and provides power in transients. This topology with current and voltage controlled ultracapacitor packs topology gives a low cost but relatively high weight and size option for the powertrain.

C. Finding of equivalent powertrain sizing

In the backward powertrain design the reference load power must be derated if the load power causes instability to the DC-link. This might be due to the saturation of power transfer components to their maximum limits and it is a sign of a too high load or a weak design. In order to compare different powertrain cases against each other, the designer must ensure that they are able to provide the same energy, and the peak power, to the load, as well as, receive the regenerative power. This inspection is done by integrating the positive and the negative load powers, and by comparing those to integrations of the reference value. Disparity in comparison is a sign of lacking performance and gives a reason for a new iteration round of powertrain component sizing. Powertrains cannot be equally compared until they reach the same performance.

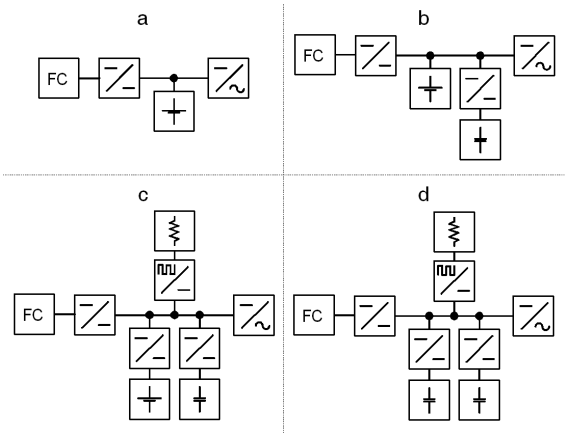

Fig. 1. Schematics of studied powertrain topologies.

D. Definition of the powertrain efficiency

This study investigates power transfer efficiencies between the primary source output and load inputs. Therefore, the efficiency from the fuel cell stack electrical output to electrical inputs of inverters is considered. The efficiency of the powertrain (η_{pt}) is defined as

$$\eta_{pt} = E_{+load} / (E_{+load} + E_{p\_conversion\_losses} + E_{brake\_resistor}), \quad (1)$$

where E_{+load} represents a positive load from the DC-link, which contains the positive part of the sum power and the constant load from the DC-link for auxiliaries. The constant load in this study was 0.065 pu. $E_{p\_conversion\_losses}$ is a sum of the power losses integration in the FC-converter, energy storage converters and the equivalent series resistance (ESR) power losses in energy storages. $E_{brake\_resistor}$ refers to the power losses in the brake resistor.

IV. MODELING

A. Modeling of the FC-stack

This study uses a static *ui*-curve model for a FC-stack. The FC-stack is modeled as a current-dependent voltage source, i.e., $u_{fc} = f(i_l)$, where u_{fc} is the output voltage of the FC-stack and i_l is current from the low-voltage side of the boost converter. The fuel cell stack *ui*-curve imitates the output voltage of a typical commercial fuel cell stack.

B. Modeling of energy storages

1. Battery pack

A generic Li-ion battery model was used in this research. The Li-ion battery pack discharge characteristics ($i^* > 0$) is modeled as in (2), and charge characteristics ($i^* < 0$) as in (3), respectively.

$$u_{bat}(it, i^*, i_{bat}) = U_0 - K \cdot Q / (Q - it) \cdot i^* - K \cdot Q / (Q - it) \cdot it + A \cdot \exp(-B \cdot it) - R_{bat} \cdot i_{bat}. \quad (2)$$

$$u_{bat}(it, i^*, i_{bat}) = U_0 - K \cdot Q / (it + 0.1 \cdot Q) \cdot i^* - K \cdot Q / (Q - it) \cdot it + A \cdot \exp(-B \cdot it) - R_{bat} \cdot i_{bat}. \quad (3)$$

In equations 2 and 3, u_{bat} is nonlinear output voltage (V), it is extracted capacity (Ah), i^* is low frequency current dynamics (A), i_{bat} is battery current (A), U_0 is the maximum voltage value of the linear area (V), K is polarization constant (Ah^{-1}), Q is maximum battery capacity (Ah), A is exponential voltage (V), B is exponential capacity (Ah^{-1}) and R_{bat} is constant ESR (Ω) of the battery pack. The study uses an estimate value for battery resistances, since resistance varies based on operation and environmental parameters. The battery resistance is calculated as

$$R_{bat} = U_{nom} / C \cdot 0.01, \quad (4)$$

where U_{nom} is the minimum voltage of the battery packs linear voltage area. In other words, Equation 4 means 1% power losses on the battery pack with the 1C value for the both charge and discharge conditions. [10]

2. Ultracapacitor pack

The ultracapacitor pack output voltage modeling with moderate accuracy [7] can be performed as

$$u_{uc} = (1 / C_{ucap}) \cdot \int i_{uc} \cdot dt + R_{uc} \cdot i_{uc}. \quad (5)$$

In equation 5; u_{uc} is ultracapacitor pack output voltage (V), C_{ucap} is ultracapacitor pack capacitance (F), i_{uc} is ultracapacitor pack current (A) and R_{uc} is constant ESR (Ω).

3. Energy storage losses

In general, the energy losses in both battery and ultracapacitor packs ($E_{losses\_energy\_storage}$) are calculated as

$$E_{losses\_energy\_storage} = R \cdot \int i_{es}^2 \cdot dt. \quad (6)$$

C. Modeling of the DC-DC converter

The efficiency of the DC-DC converter depends on the energy storage current (i_{es}) and the voltage conversion ratio (u_{ratio}). In the study [8], DC to DC power conversion efficiencies in the energy storage system with different i_{es} and u_{ratio} values have been investigated. Here, the voltage conversion ratio is expressed as

$$u_{ratio} = u_{es} / u_{DC}, \quad (7)$$

where u_{es} refers to the energy storage side voltage and u_{DC} to the DC-link voltage, respectively.

Modeled functionalities and dynamical properties on the DC-DC converter plant model are following; current control response time ($\tau_{DC/DC}$), minimum and maximum current limits (I_{min}, I_{max}) and power losses according to the efficiency mapping of an operation point. Furthermore, in the current control mode the DC-DC converter plant model is controlled with the current reference ($i_{|ref|}$) and with the current direction D (+1, 0 or -1). Therefore, the DC-DC converter plant model can be expressed, as in (7) to (11),

$$i_{ref} = D \cdot i_{|ref|}, \text{ when } I_{min} \le i_{|ref|} \le I_{max}, \quad (8)$$

$$i_{es} = i_{bat} = i_{uc} = 1 / (\tau_{DC/DC} \cdot s + 1) \cdot i_{ref}. \quad (9)$$

Equations 8 and 9 apply, because the classical boost converter topology under consideration regulates the energy storage current. Therefore, the energy storage system's DC-link current (i_{ES}) can be expressed, during discharging (10) and charging (11), respectively.

$$i_{ES} = i_{es} \cdot \eta_{boost}(i_{es}, u_{ratio}) \cdot u_{ratio}. \quad (10)$$

$$i_{ES} = i_{es} / \eta_{buck}(i_{es}, u_{ratio}) \cdot u_{ratio}. \quad (11)$$

Equations 10 and 11 use the DC-DC converter efficiency mapping $\eta(i_{es}, u_{ratio})$ with values from 0 to 1.

V. Evaluation Parameters

A. Calculation parameters

In order to compare differences between buffering topology cases, weight, size, price and lifetime parameters need to be fixed. Chosen parameter values are presented in Table II.

The weight and size calculations use manufacturers' data and reference sources. The FC-stack is considered as two cases; 75 kW and 150 kW with weights of 350 kg and 400 kg, and size 0.55m^3 for the both. The brake chopper weight and size is neglected.

In the lifetime column, unit M (million) refers to the shallow cycle lifetime for the battery and to the deep discharge cycle for the UC pack, unit y refers to years, respectively. In this research an average lifetime of FC-stack in test use during the last decade were considered. The battery and power electronics component (PE) lifetimes are targets, and the UC pack lifetime is a datasheet value.

TABLE II
Weight, Size, Price and Cycle Life Parameters for Calculations.

Comp.	Weight	Size	Price	Life-time	Refs
Bat.	102 Wh/kg	129 Wh/dm^3	500 $/kWh	0.3M	[11], [12], [13]
UC	2.3 Wh/kg	1.6 Wh/dm^3	2800 $/kWh	1M	[11]
FC	0.21 – 0.38 kW/kg	0.14 – 0.27 kW/dm^3	80 $/kW	1.6y	[14], [15], [16]
DC-DC	3.45 kW_{peak}/kg	5.8 kW_{peak}/dm^3	25 $/$kW_{peak}$	15y	[17], [18]
Brake res.	13 kW_{peak}/kg	6.6 kW_{peak}/ dm^3	5[a] $/$kW_{peak}$	15y	[19]

[a] estimate

Calculated battery capacities in the cases *a* and *b* are 189 and 108 kWh with U_0 670 – U_{nom} 614 V, and in the case *c* 108 kWh with 330 – 307 V area, respectively. The UC pack capacities in the cases *b* and *c* is 16 F, in the case *d* 76 F and in the case *e* 100 F with U_{max} of 500 V in all cases.

B. Component lifetime estimation

In principle, an energy storage life expectancy can be calculated out of the load cycle frequency, if the FC-source power production is kept constant and secondary energy storages' buffer the load variation. This is true in all other cases than the case *d*, in which the FC-stack is operated against its allowable power transition limit and produced power varies. Therefore, the study utilizes the modeled charge-discharge cycle count for the energy storage lifetime calculations. The cycle count is a rough visual approximation from the charge-discharge frequency of the energy storage.

C. Powertrain initial and lifetime cost estimations

Prospected powertrain cost and lifetime cost estimations are based on values presented in Table II. Values are based on targeted mass production costs. The energy price is considered as 0.1 $/kWh [11]. The electric machine and the inverter costs are not included in the cost calculations, since the design is done for a conventional diesel series-hybrid powertrain.

Energy content for the cost calculations of the battery pack (E_{bat}) is calculated as in (12), and for the UC pack (E_{uc}) as in (13), respectively.

$$E_{bat} = (U_0 + U_{nom}) / 2 \cdot Q. \quad (12)$$

$$E_{uc} = 1 / 2 \cdot C \cdot U_{max}^2. \quad (13)$$

where U_{max} refers to the maximum voltage of the ultracapacitor pack.

The maximum (kW_{peak}) and average power (kW) values of DC-DC converters, brake choppers, and the FC-source are attained from the powertrain modeling, presented in Section VI. Therefore, all needed data is achieved and the powertrain lifetime costs can be calculated as

$$S_{lifetime} = t_{ref} / t_{lifetime\_1} \cdot S_1 + t_{ref} / t_{lifetime\_2} \cdot S_2 + \ldots + (1 - \eta_{pt}) \cdot P_{avg} \cdot S_{energy} \cdot t_{ref}, \quad (14)$$

where $S_{lifetime}$ is the expected buffering topology cost within the examined time span, t_{ref} is the examined time span (15 years), $t_{lifetime\_n}$ refers to the nth component's expected lifetime, S_n refers to the nth component price, P_{avg} refers to the average FC-source power and S_{energy} refers to the energy costs.

VI. Power Flow Waveform Examples

This section presents examples of the power flow waveforms of the different buffering topologies. Figures from 2 to 5 present power flows at the point of common coupling of the DC-link. Figures refer to a short period of the full modeled loading cycle.

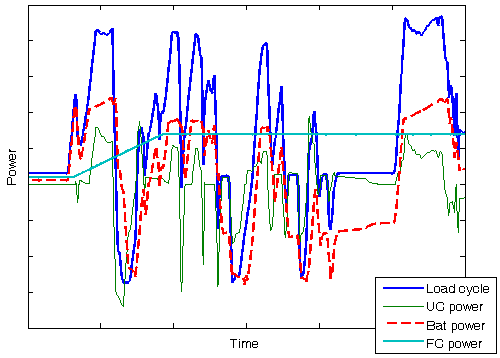

Fig. 2. The power flow waveform example from the case *b*.

In figures, the blue colored, continuous and widened waveform is the actual backward model loading data based on the original reference value from the Heavy Mobile Port Equipment. Other waveforms are case dependent and descriptions are in the legends of the figures. The grid, axis scales and units have been purposely left out from the figures.

Cases *a*, *b* and *c* operate the FC-source on the maximum power region due to the battery pack in topology. Cases *d* and *e* operate the FC-source against power transition limit, as can be seen from Figs. 4 and 5, respectively.

Cases *b* and *c* have slightly different targets for a battery pack current limitations. The case *b* compensates energy depletion in the UC pack with the battery pack current limitation ability, and case *c* does not compensate the UC pack depletion, respectively.

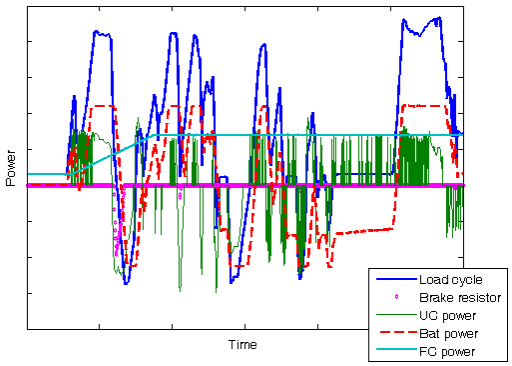

Fig. 3. The power flow waveform example from the case *c*.

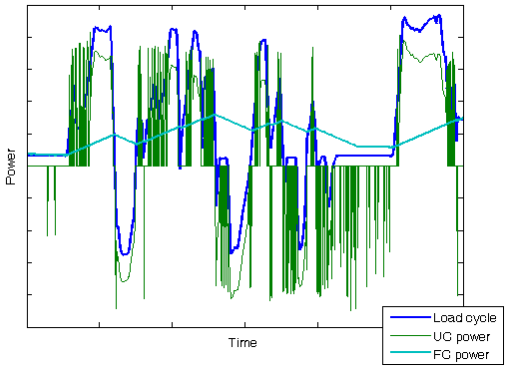

Fig. 4. The power flow waveform example from the case *d*.

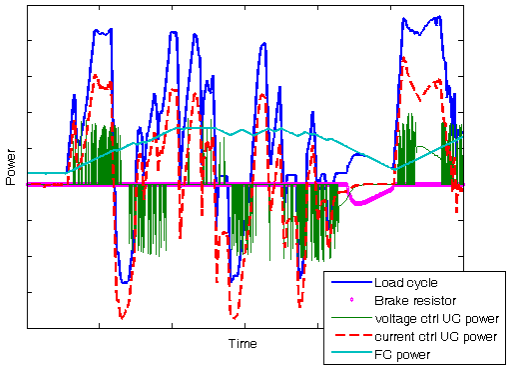

Fig. 5. The power flow waveform example from the case *e*.

VII. RESULTS

This section presents results of different buffering topologies in comparison. Fig. 6 shows how weight and size are dependent on the choice of the buffering topology. Fig. 7 presents efficiencies and power losses of the different buffering topology cases and Fig. 8 presents initial and lifetime costs. Furthermore, lifetime cost percentages are distributed between different components in Table III.

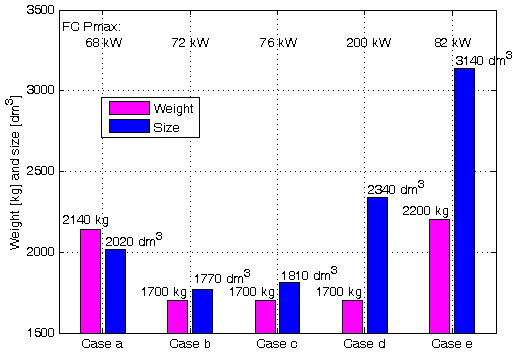

Fig. 6. Weights, sizes and max. FC-stack powers of different topologies.

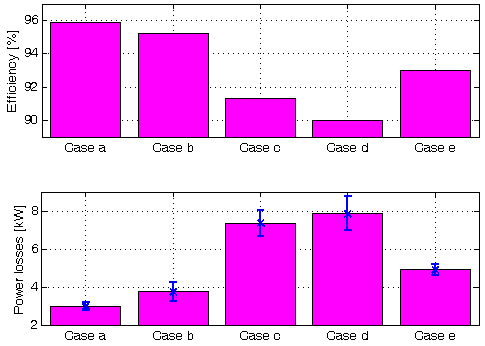

Fig. 7. Efficiencies and power losses of different buffering topology cases.

The lowest weight is achieved in the cases *b*, *c* and *d* while the weight of the cases *a* and *e* are around 25-30% higher than the lowest weight.

The minimum size is achieved in the cases *b* and c with proper choice of the battery and the UC pack. A battery or an UC only buffering in the cases *a*, *d* and *e* increases sizes, thus the UC only buffered topologies have the highest volume.

The efficiency maximum is reached with the case *a*, due to the fewest DC-DC conversions on the primary energy path. The case *b* has slightly lower efficiency, since peak powers are taken via the DC-DC conversion. The case *c* introduces DC-DC conversion for the battery pack, and hence increases significantly power losses with respect to the case *b*. The case *d* is vulnerable to FC-converter efficiency and the case *e* finds its powertrain efficiency between cases *b* and *c*.

Cost calculations favor the UC pack only buffering topologies, while the relation to the battery based topologies

depend increasingly on calculation parameters. FC and energy costs become significant in the cases *d* and *e*.

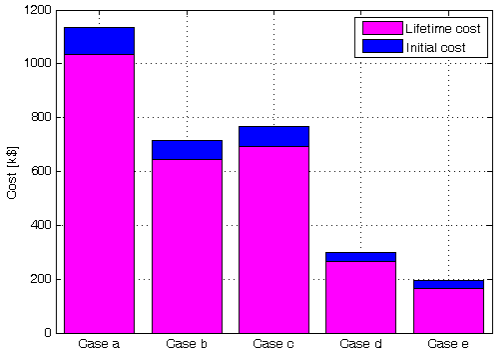

Fig. 8. Initial and lifetime costs of different buffering topology cases.

TABLE III
DISTRIBUTION OF LIFETIME COSTS IN PERCENTAGES.

Case	Bat	UC	FC	PE	Energy
a	91%	-	5%	<1%	3%
b	83%	1%	8%	1%	7%
c	78%	<1%	9%	1%	11%
d	-	5%	57%	4%	34%
e	-	20%	37%	6%	37%

VIII. CONCLUSIONS

This research compares five different fuel-cell hybrid topology cases with the load cycle which is specific for the Heavy Mobile Port Equipment. Each of the topologies has their own benefits and disadvantages.

It can be said that the feasibility of the battery pack based powertrains are very dependent on allowed charging and discharging currents of high energy battery cells. In the fuel cell battery topology the influence of double C values is the largest by almost halving size, weight and lifetime costs.

Feasibility of presented topologies is very dependent on the DC-DC converter efficiencies. Therefore, calculated powertrain efficiency gives valuable feedback and reason to reconsider the design of DC-DC converters. This is the case e.g. in buffering topology cases *c* and *d*, in which power losses might cause powertrain option to become impractical.

This study was conducted as a full iterative process. Such a process may not expectedly find the global maximums but points near of those. Optimization targets for different topologies could, with attained knowledge, be considered.

It should be remembered that the proposed efficiency values are dependent on the load cycle, the powertrain topology and the system control, and therefore, those cannot be generalized. Also, calculated cost values are sensitive to current trends and future prospects, and should not be considered as targets, but as reference values in the presented comparison. Therefore, results are interrelated and should not be extracted from the context. Results of this study describe a powertrain characteristics for NRMMs which duty-cycle is repetitive for long periods of time.

ACKNOWLEDGMENT

This study has been carried out in the TopDrive project financed by the Finnish Funding Agency for Technology and Innovations (Tekes) and the Multidisciplinary Institute of Digitalization and Energy (MIDE) of Aalto University School of Electrical Engineering, respectively.

REFERENCES

[1] W. Gao, "Performance Comparison of a Fuel Cell-Battery Hybrid Powertrain and a Fuel Cell-Ultracapacitor Hybrid Powertrain," *IEEE Transaction on Vehicular Technology*, vol. 54, no. 3, pp. 846 – 855, May 2005.

[2] L.L. Gaines, A. Elgowainy and M.Q. Wang, "Full Fuel-Cycle Comparison of Forklift Propulsion Systems," Center for Transportation Research, Argonne National Laboratory, October 2008. [Online]. Available: http://www.transportation.anl.gov/pdfs/TA/537.pdf.

[3] D. Barnes, "Fuel Cell Powered Front-End Loader Mining Vehicle," *2005* Annual Progress Report, DOE Hydrogen Program. [Online]. Available:http://www1.eere.energy.gov/hydrogenandfuelcells/pdfs/vib3_slattery.pdf.

[4] Press release, *New Holland Agriculture, New Holland's drive concept of the future*, 6 October 2009.

[5] A.R. Miller, J. Peters, B.E. Smith and O.A. Velev, "Analysis of fuel cell hybrid locomotives," *Journal of Power Sources*, vol.157, no. 2, pp. 855-861, July 2006.

[6] T. Furuya, K. Kondo and T. Yamamoto, "Experimental Study on a PEMFC Fed Railway Vehicle Motor Drive System," *IEEE Industry Applications Conference*, Tampa, FL, 8-12 October 2006, pp.1249 – 1252.

[7] M. Liukkonen, A. Hentunen and J. Suomela, "Validation of quasi-static Series Hybrid Electric Vehicle Simulation model," in *Proc. of the IEEE Vehicle Power and Propulsion Conference*, Lille, France, Sep. 1-3, 2010.

[8] M. Liukkonen, A. Hentunen and J. Suomela, "Analysis of the ultracapacitor module in power buffering," presented at *the 4th European Symposium on Super Capacitors & Applications (ESSCAP'10)*, Bordeaux, France, Oct. 21-22, 2010.

[9] P. Thounthong, B. Davat, S. Raël and P. Sethakul, "Fuel Cell High-Power Applications," IEEE Industrial Electronics Magazine, Vol. 3, no. 1, pp. 32-46, Mar., 2009.

[10] Matlab Simulink™ Help. [Online]. Available: http://www.mathworks.com/help/toolbox/physmod/powersys/ref/battery.html.

[11] G. Passier et al., "Status Overview of Hybrid and Electric Vehicle Technology," IEA International Energy Agency. TNO report MON-RPT-033-DTS-2007-02955, Nov. 2007. [Online]. Available: http://www.ieahev.org/pdfs/annex_7/annex7_hev_final_rpt_110108.pdf

[12] K. Smith, "Battery System Life and Cost Modeling (NREL)," FY2009 Annual Progress Report for Energy Storage R&D, pp. 76-79, Jan., 2010. [Online]. Available: http://www1.eere.energy.gov/vehiclesandfuels/index.html.

[13] M. Anderman, "The Plug-In Hybrid and Electric Vehicle Opportunity," Advanced Automotive Batteries, April 2010.

[14] J. Sinha, S. Lasher and Y. Yang, "Cost Analyses of Fuel Cell Stacks/Systems," U.S. Department of Energy (DOE) Hydrogen Program Annual Progress Report 2009, pp. 931-936, Nov., 2009. [Online]. Available: http://www.hydrogen.energy.gov/index.html.

[15] Ballard homepage. [Online]. Available: http://www.ballard.com/.

[16] I. Staffell, "Review of PEM fuel cell performance", University of Birmingham. [Online] Available: http://www.fuelcells.bham.ac.uk/documents/Review_of_PEMFC.pdf.

[17] "FreedomCAR and Vehicle Technologies Program, Multi-Year Research and Development Plan", U.S. Department of Energy, Nov. 2003. [Online]. Available: http://www1.eere.energy.gov/vehiclesandfuels/index.html.

[18] J.W. Dixon and M.E. Ortúzar, "Ultracapacitors + DC-DC Converters in Regenerative Braking System," IEEE AESS Systems Magazine, pp. 16-21, Aug., 2002.

[19] Hipas homepage. [Online]. Available: http://www.hipas.net/.